

Strain Gradients and Magnetoresistance in Microstructured 3D Topological Semi-metals

Présentée le 7 décembre 2023

Faculté des sciences et techniques de l'ingénieur
Laboratoire des Matériaux Quantiques
Programme doctoral en science et génie des matériaux

pour l'obtention du grade de Docteur ès Sciences

par

Jonas De Jesus DIAZ GOMEZ

Acceptée sur proposition du jury

Prof. D. Grundler, président du jury
Prof. Ph. J. W. Moll, Prof. H.-A. Klok, directeurs de thèse
Prof. J. M. De Teresa, rapporteur
Prof. F. von Rohr, rapporteur
Prof. J. Ph. Brantut, rapporteur

To my parents.

Acknowledgements

During the course of my doctoral studies I have had the great pleasure to meet many people whose help, support and kindness made the work presented in this thesis possible. To all of them I would like to express my deepest gratitude.

First and foremost, I would like to thank my supervisor Philip Moll for giving me the chance to work in his group. His guidance, willingness to help at all times and creative approach to science were enlightening to me and taught me a great deal.

I would also like to express my sincere gratitude to Carsten Putzke, whose invaluable insights, supervision and support in technical and scientific matters were essential for the realization of this thesis.

During this thesis I was fortunate to work with many collaborators from different institutions. I would like to thank Chandra Shekhar from the Max Planck Institute for Chemical Physics of Solids, and Nityan Nair and James Analytis from the University of California, Berkeley for providing excellent single crystals of Cd_3As_2 . My research on this material benefited greatly from the input and insightful discussions with Roni Ilan from the Tel Aviv University and Dmitry Pikulin from Microsoft Station Q. Similarly, I would like to thank Paul Canfield from Iowa State University for growing wonderful crystals of the material PtSn_4 . The DFT calculations of this material performed by Qun Yang from the Weizmann Institute of Science were essential to interpret the experimental data. I sincerely thank her for her illuminating work.

At EPFL I also had the great luck of being able to access excellent research infrastructure and expert technical support. I would like to thank everyone from the CIME team, especially Lucie Navrátilová, for their efforts in maintaining the FIB instruments and for giving me the necessary training. From the ISIC platform, I want to thank Rosario Scopelliti and Farzaneh Fadaei for their immense help in the X-ray characterization of single crystals. I'm also very grateful for the wonderful work of the mechanical workshop at the Institute of Materials, lead by Pierre-André Despont. I would like to thank the CMi team for their assistance and

training, in particular, Rémy Juttin for his help in refining the recipe for Au sputtering. From the administrative staff at the EPFL Institute of Materials, I would like to give special thanks to Crystelle Demierre, Corinne Farquharson-Grandjean and Susanne Rodrigues da Silva for their professional and diligent assistance.

I am immensely grateful to the members of the MQM and QMAT groups: Xiangwei, Amelia, Maja, Mark, Hungwei, Mathieu, Sonya, Guillaume, Maarten, Josh, Toni, Tino, Kim and Kent. It was an absolute pleasure to work and learn from them. I would like to thank Josh for his help in the fabrication and data analysis of PtSn₄ microstructures. A special mention goes to two other members: Xiangwei and Amelia. I am very lucky to have shared most of my doctoral studies with them. Their kindness and support helped me get through the often difficult path of research, and their friendship is one of the most valuable rewards I obtained from this experience.

I also want to thank the friends I made along the way and with whom I shared many joyful occasions: Fabian, Thomas, Andrea, Alejandra, Luciano and Nathy.

Finally, I want to thank those closest to me: my parents, Carmen and Jonas, and my brother Carmelo and his wife Dalia; my girlfriend Maria and her parents, Eva and Mihai. Their unconditional support and love are the main reason I'm still standing.

Abstract

Three-dimensional topological semimetals have emerged as strong candidates to probe new fundamental physical phenomena that could be exploited to develop next generation electronics. However, many aspects of their electronic properties remain unclear. This thesis addresses mainly two of them: (i) the interplay between their lattice deformations and charge carrier dynamics and (ii) the possible origin of their magnetoresistive behaviour. This is done by investigating the transport properties of microstructures fabricated with the focused ion beam. The results are presented in three main parts:

In the first part, I describe the development of an apparatus for the controlled application of strain gradients at cryogenic temperatures. This is achieved by mechanically bending 3D crystalline cantilevers. A simple sample design aimed at transport characterization under strain is adopted. The bending apparatus is also fitted to a rotator probe for the simultaneous application of strain gradients and the rotation with respect to the applied magnetic field. Strain gradients exceeding $1.3\% \mu\text{m}^{-1}$ are achieved at a surface strain value of $\approx 0.65\%$. Moreover, the results establish that the quantum transport characteristics of the cantilevers are unaltered by the large strain gradients, demonstrating that no plastic deformation is induced.

In the second part, I apply the newly developed technique to explore the effects of strain gradients on the Dirac semimetal Cd_3As_2 . This material hosts novel electron orbits, called Weyl orbits, that combine bulk chiral states coming from Landau quantization with Fermi arc states that are located on the surface. Theoretical models that treat strain gradients in the framework of pseudo-electromagnetic fields predict that the periodicity of the Weyl orbits is sensitive to strain gradients. Despite features of the experimental data compatible with some of the expected effects of pseudo-fields, the results reveal a more complicated experimental scenario with important aspects that cannot be easily captured by the available simplified models.

In the final part, I investigate the transport properties of the Dirac nodal arc semimetal PtSn_4 . This material is characterized by its extremely large magnetoresistance at low temperatures. There has been an intense debate on whether such behaviour is connected to its peculiar electronic structure that contains a short Dirac node line in momentum space associated

to graphene-like surface states. By fabricating the first microstructures of this material, I study the transport behaviour for currents applied along all main crystallographic directions. While for some directions the usual extremely large magnetoresistance is observed, for one particular direction the magnetoresistance is suppressed. An inspection of the complex Fermi surface shows that this suppression is associated to the existence of open orbits in one of the branches. The presence of the open orbits is very sensitive to the magnetic field orientation. These results suggest a semi-classical origin for the characteristic large magnetoresistance observed in this material.

Key words: topological, semimetal, strain, magnetoresistance, micro-fabrication.

Résumé

Les semi-métaux topologiques tridimensionnels ont émergé comme prometteurs pour examiner de nouveaux phénomènes physiques fondamentaux qui pourraient être exploités pour développer la génération future de l'électronique. Cependant, de nombreux aspects de leurs propriétés électroniques restent peu claires. Cette thèse aborde principalement deux : (i) la relation entre leurs déformations de réseau cristallin et leur dynamique de porteur de charge et (ii) l'origine possible de leur comportement magnétorésistif. Ceci est effectué en investiguant les propriétés de transport de microstructures fabriquées avec la machine à faisceau d'ions focalisé, focused ion beam (FIB). Les résultats sont présentés en trois parties principales :

La première partie porte sur le développement de l'appareil pour la soumission contrôlée à des gradients de déformation à des températures cryogéniques. Ceci est réalisé en fléchissant mécaniquement des cantilevers cristallins 3D. Un design simple d'échantillon visant la caractérisation de transport sous déformation est adopté. L'appareil de flexion est également intégré dans une sonde de rotateur pour la soumission à des gradients de déformation et la rotation simultanées en relation avec le champ magnétique auquel le cantilever est soumis. Des gradients de déformation excédant $1.3\% \mu\text{m}^{-1}$ sont réalisés à une valeur de déformation de surface de $\approx 0.65\%$. En outre, les résultats établissent que les caractéristiques du transport quantique des cantilevers ne sont pas modifiées par les grands gradients de déformation, ce qui démontre qu'aucune déformation plastique n'est induite.

La deuxième partie porte sur l'application de la technique nouvellement développée pour explorer les effets de gradients de déformation sur le semi-métal Dirac Cd_3As_2 . Ce matériau abrite de nouvelles orbites d'électrons qu'on appelle orbites de Weyl. Elles combinent des états chiraux provenant de la quantification de Landau avec des états d'arc Fermi situés sur la surface. Les modèles théoriques qui traitent de gradients de déformation dans le cadre de champs pseudo-électromagnétiques prédisent que la périodicité des orbites de Weyl est sensible aux gradients de déformation. Malgré des aspects de données expérimentales compatibles avec certains des effets attendus des pseudo-champs, les résultats révèlent un scénario expérimental plus complexe avec des aspects importants qui ne peuvent pas être facilement saisis par les modèles simplifiés existants.

La dernière partie examine les propriétés de transport du semi-métal nodal arc Dirac PtSn₄. Ce matériau se caractérise par sa grande magnéto-résistance à des températures basses. Il y a eu des débats intenses sur la question si un tel comportement est lié à sa structure électronique particulière qui contient une courte ligne nodale Dirac dans l'espace réciproque associée à des états de surface qui ressemblent au graphène. En fabriquant les premières microstructures de ce matériau, on étudie le comportement de transport pour les courants appliqués dans toutes les directions cristallographiques principales. Tandis que pour certaines directions la grande magnéto-résistance habituelle est observée, pour une direction particulière la magnéto-résistance est supprimée. L'examen de la surface de Fermi complexe montre que cette suppression est liée à l'existence d'orbitales ouvertes dans l'une des branches. La présence de ces orbitales ouvertes est très sensible à l'orientation du champ magnétique. Ces résultats suggèrent une origine semi-classique pour la grande magnéto-résistance caractéristique observée dans ce matériau.

Mots clés : topologique, semi-métal, déformation, magnéto-résistance, micro-fabrication.

Contents

Acknowledgements	i
Abstract (English/Français)	iii
List of figures	xi
List of tables	xv
1 Introduction	1
2 Focused ion beam micromachining	5
2.1 Introduction	5
2.2 General principles and features of the FIB instrument	6
2.2.1 Ion sources	6
2.2.2 Ion-solid interactions	9
2.2.3 FIB-induced deposition	11
2.3 Basic control parameters of the FIB	11
2.4 FIB artifacts	13
2.4.1 Curtaining	13
2.4.2 Amorphization and ion implantation	15
2.4.3 Differential sputtering	16
2.4.4 Redeposition	16
2.5 Fabrication of microstructures for transport measurements	17
2.5.1 Lamellae preparation from a single crystal	18
2.5.2 Glue-mounted microstructures	22
2.5.3 Free-standing microstructures	27
2.6 Conclusions and outlook	31
3 Experimental methods	33
3.1 Introduction	33
3.2 AC transport measurements	34
3.2.1 Working principle of the lock-in amplifier	34
3.2.2 Electrical set-up for transport measurements of microstructures	35
3.3 Low temperature and high magnetic fields	39
3.3.1 Physical properties measurement system (PPMS)	39

3.3.2	Other systems used	40
3.4	X ray characterization	41
3.4.1	MultiWire Laue back-reflection diffractometer	42
3.4.2	SuperNova single crystal diffractometer	43
3.5	Finite elements simulations	46
4	Theoretical background	49
4.1	Introduction	49
4.2	Band theory fundamentals	50
4.3	Band crossings and topological invariants	51
4.3.1	Berry phase	52
4.3.2	Weyl semimetals	54
4.3.3	Dirac semimetals	54
4.3.4	Bulk-boundary correspondence	55
4.4	Electronic transport under external fields	55
4.4.1	Drude model	55
4.4.2	Semi-classical equations of motion	57
4.4.3	Magnetoresistance basics	58
4.4.4	Landau quantization	59
4.4.5	Shubnikov-de Haas oscillations	61
4.4.6	Weyl Orbits	64
4.5	Pseudo-magnetic fields induced by strain	65
5	Mechanical bending set-up for microstructures	69
5.1	Introduction	69
5.2	Sample design and fabrication for bending experiments	71
5.3	Bending apparatus	74
5.3.1	Bending without rotation	74
5.3.2	Probe for bending and rotation	82
5.4	Conclusions and outlook	89
6	Mechanical bending of Cd₃As₂ cantilevers	91
6.1	Introduction	91
6.2	Cd ₃ As ₂ material characteristics	93
6.3	Experimental results	94
6.3.1	Angle dependence of quantum oscillations without bending	94
6.3.2	Bending without rotation	101
6.3.3	Bending and rotation	105
6.4	Conclusions and outlook	108
7	Transport measurements in PtSn₄ microstructures	111
7.1	Introduction	111
7.2	PtSn ₄ material characteristics	112

7.3	Experimental results	113
7.3.1	Magnetoresistance and Kohler scaling	113
7.3.2	Resistivity anisotropy	115
7.3.3	Sondheimer oscillations	118
7.3.4	Suppression of magnetoresistance	120
7.4	Conclusions and outlook	130
8	Summary and outlook	131
	Publications	135
	Bibliography	151
	Curriculum Vitae	153

List of Figures

2.1	Schematic of the basic components of a SEM/FIB dual system	7
2.2	Two kinds of ion sources for the FIB	8
2.3	Spot size as a function of beam current for Ga-FIB with a LMIS and a P-FIB with a ICP source	9
2.4	Ion-solid interactions during FIB processing	10
2.5	FIB-assisted deposition process	11
2.6	Basic control parameters and milling patterns of the FEI Helios G4 system . . .	14
2.7	Curtaining effect on a PtSn ₄ lamella	15
2.8	Amorphization damage in Si from both Ga-FIB and P-FIB at different accelerating voltages	16
2.9	Transport device from a parent PtSn ₄ crystal	17
2.10	Lamella extraction process flow using the FIB	21
2.11	Lamella extraction procedure for the material CoSi	22
2.12	Set-up for the transfer of extracted lamellae	23
2.13	The lamella <i>ex situ</i> transfer process	25
2.14	Au coating and placing of the contact wires	26
2.15	Process flow of the FIB microstructuring procedure for glue-mounted samples	27
2.16	SEM image of a PtSn ₄ free-standing microstructure	28
2.17	Main steps in the lamella <i>in situ</i> transfer process to a thin membrane	30
3.1	Lock-in amplifier working principle	36
3.2	Schematic diagram of electrical configurations used for transport measurements	38
3.3	Technical drawing of the PPMS system	41
3.4	MWL120 Multiwire back-reflection Laue system	44
3.5	Crystal orientation with the Laue system	45
3.6	Agilent SuperNova diffractometer system	46
3.7	X-ray characteritaion of single lamellae	47
3.8	Finite element method	48
3.9	COMSOL simulation of a microstructure	48
4.1	Schematic band structure of a normal metal and Wely and Dirac semimetals . .	51
4.2	Berry phase and paths in the Brillouin zone	52
4.3	Fermi arcs in Weyl semimetals	56

4.4	Magnetoresistance and Fermi surface shape	59
4.5	Main differences between the Landau quantization of non-topological (parabolic band) and topological (linear band) fermions	62
4.6	Quantum oscillations from Weyl orbits	65
4.7	Pseudo-magnetic fields in graphene	66
4.8	Fermi arc states as the zeroth Landau level of a pseudo magnetic field	68
5.1	Different approaches for producing strain gradients	70
5.2	Sample design for transport measurements under large strain gradients	72
5.3	Main steps in the fabrication of cantilevers	73
5.4	Working mechanism of the attocube nano-positioners	75
5.5	Sample holder for the mechanical bending set-up	77
5.6	Transport behaviour of Cd ₃ As ₂ cantilevers without bending	78
5.7	Approach and bending procedure	80
5.8	Quantum oscillations before and after maximum bending	82
5.9	Probe with mechanical rotator and attocube nanopositioner to perform bending experiments	83
5.10	Piezo-resistive cantilever from torque magnetometry chip	84
5.11	Bending and rotation mounting and bending procedure	85
5.12	Rotation and bending for sample 3	87
5.13	Nanopositioner step size characterization	88
6.1	Effect of pseudo-magnetic fields on the Weyl orbits	92
6.2	Pseudo-magnetic field \mathbf{B}_5 created in a bent slab of a WSM or DSM	93
6.3	Crystal structure and electronic characteristics of Cd ₃ As ₂	95
6.4	Quantum oscillations of Sample 1 for <i>in-plane</i> rotation.	97
6.5	Quantum oscillations at different temperatures for the field direction $\mathbf{B} \parallel 100$	98
6.6	Quantum oscillations of Sample 1 for <i>c-axis</i> rotation	100
6.7	Quantum oscillations of Sample 1 during bending	101
6.8	LK fitting of quantum oscillations for unbent and bent Sample 1	102
6.9	FFT of quantum oscillations for the bending without rotations experiments.	103
6.10	Comparison of the F_{Weyl} change from bending and rotation experiments	104
6.11	A simple model for the evolution of F_{Weyl} during bending	105
6.12	Thinning down of Sample 3	106
6.13	Quantum oscillations of the thinned down sample 3 at zero bending	107
6.14	Quantum oscillations of the thinned down sample 3 with a bending angle $\theta = 25^\circ$	108
6.15	Quantum oscillations of thinned down sample 3 for different bending and rotation angles.	109
7.1	Crystal structure and electronic characteristics of PtSn ₄	113
7.2	Glue-mounted PtSn ₄ microstructure	114
7.3	Transverse magnetoresistance as a function of temperature and field magnitude and direction	115

7.4	Shubnikov-de Haas oscillations for two different field directions	116
7.5	Temperature dependence of the resistivity along different crystallographic directions	117
7.6	Magnetoresistance as a function of field magnitude and direction from the "U" structure at 2K	118
7.7	Sondheimer oscillations in a PtSn ₄ microstructure	119
7.8	Staircase structure designed for SOs experiments	121
7.9	Mean free paths extracted from Sondheimer oscillations	122
7.10	Free-standing microstructure	122
7.11	Magnetoresistance as a function of field magnitude and direction for the free-standing microstructure	123
7.12	Magnetoresistance around B <i>b</i>	125
7.13	Two-axis rotation study of a PtSn ₄ macrocrystal	126
7.14	Angular dependence of the magnetoresistance at 0.5K of a PtSn ₄ macrocrystal .	127
7.15	Magnetoresistance as a function of temperature and field magnitude and direction for the staircase microstructure	128
7.16	Band structure and Fermi surface of PtSn ₄	129



List of Tables

5.1	Devices fabricated and the final thickness of their flexures	74
6.1	Main parameters of the two principal samples discussed	99
7.1	Main experimental SdH frequencies and corresponding cyclotron effective masses	116

1 Introduction

The study of novel electronic states of matter using the concepts of topology has proven to be a very fruitful enterprise in material science. The understanding of phenomena like the integer quantum Hall effect (IQHE) in terms of a topological invariant [1, 2], the development of notions of order that go beyond symmetry-breaking considerations [3, 4], and the effort to classify new quantum states according to their topological character [5] have all become new paradigms in the search for fundamental organizing principles of matter. Experimentally, the enterprise has been bolstered significantly by the isolation of graphene and by the realization of 2D and 3D topological insulators (TIs). These materials became fertile platforms for the observation of physical effects characteristic of topologically non-trivial matter, like the presence of dissipationless edge states, ultrahigh electronic mobilities and extremely large magneto-resistance (XMR), among others [6, 7]. More recently, another class of topologically non-trivial materials have received a lot of attention: 3D Topological semimetals (TSMs) [8–10]. Their electronic band structure can be thought of as a 3D version of graphene and they have indeed shown some of the same extraordinary behaviour. Furthermore, TSMs exhibit additional features in their band structures, such as one dimensional nodal rings or tilted cone-like electronic dispersion, as well as hosting new fermionic excitations, topologically distinct to those observed in graphene or TIs [11–13]. These characteristics have made this class of materials very promising candidates for a large variety of electronic applications that range from quantum computing to magnetic storage and high-efficiency energy conversion [14, 15].

A key challenge in the field of topological matter is the study of devices at the microscale. Not only is this scale very relevant for some of the potential technological applications but, as it is often the case with many newly synthesized materials, clean crystalline samples are usually available only in micrometer sizes. The exploration of TSMs at the micrometer and sub-micrometer scale is one of the main objectives in this thesis. The characterization of samples at these scales also allows for the identification of different transport regimes as the geometrical dimensions of the samples are reduced and become comparable to some of the main physically relevant length scales, like the mean free path, phase coherence length or

cyclotron radius. In the case of 2D materials and thin films, the advancement in the fabrication processes of transport devices has pushed the field into very high levels of precision down to the nanometer scale, mainly thanks to sophisticated lithographic and deposition techniques [16]. These techniques have also been applied to study 1D and 2D TSMs nanostructures like nanowires and nanoplates. Although they have shown some of the same behaviour as bulk samples, the nanostructures tend to suffer from a reduction of sample quality, the appearance of band gaps and limited possibilities of geometrical manipulation [17–19]. Until very recently, a high level of fabrication precision had been somewhat lacking in the case of 3D materials. One of the most successful fabrication techniques trying to fill that void is the focused ion beam (FIB) [20]. As the name indicates, the FIB uses a beam of electromagnetically focused ions to mill away material locally at any desired position. The beam spot size can range from tenths of nanometers to several micrometers depending on the settings used. Deposition can also be done *in situ* by using ion-assisted chemical deposition [21]. These capabilities make the FIB an ideal tool for the micromachining of transport devices, as it allows to carve complex shapes over the target crystal and to deposit materials that can form good electrical and mechanical contacts. This is particularly well suited for measurements of novel materials, for which 3D samples can be cut along different crystal directions with dimensions extending from millimeter down to nanometer scale.

One physical consequences of going to the microscale is the appearance of strain effects that can become quite significant even in 3D materials. Just like in other solid materials, the electronic properties of TSMs are intimately related to their lattice degrees of freedom, making it possible, in principle, to use elastic deformations to explore their electronic band structure. In this regard, one of the aims of this thesis is to show the possibility of detecting and manipulating novel electronic states of TSMs by using strain. The use of strain to probe novel electronic states in quantum materials has become a very powerful strategy in recent experimental research. For example, unidirectional strain techniques have established themselves as a valid way to tune quantum states in many classes of materials, such as electronic nematics [22], unconventional superconductors [23], or complex magnets [24]. Unidirectional strain has also been shown to push systems into different topological ground states [25], for example, by prompting a transition to a fully gapped quantum spin Hall insulator [26], inducing topologically non-trivial surface states [27] or changing the sign of a band gap [28]. Not only unidirectional strain can couple to topologically non-trivial matter but also strong strain gradients have been linked to unique phenomena in TSMs. For example, flat Landau levels with a gap compatible with the emergence of an effective magnetic field of the order of hundreds of Tesla have been observed in graphene [29] and artificial 2D graphene systems [30]. The strength of this effective magnetic field is determined by different intrinsic degrees of freedom, which are able to produce drastic band structure effects similar to those caused by external electromagnetic fields, while still preserving time-reversal symmetry [31]. In the case of 3D materials the harnessing of strain gradients to probe topological properties is a challenging but promising strategy.

The potential of TSMs to exhibit novel topological, strain-sensitive properties at the microscale

is related to their particular band structure. Weyl semimetals (WSMs) are a class of TSMs characterized in the bulk by linear dispersion bands that touch at pairs of separate points, termed Weyl nodes. Near these points, the bands can be described by the Hamiltonian $H = \chi \hbar v_F \mathbf{k} \cdot \boldsymbol{\sigma}$, where v_F is the Fermi velocity, $\boldsymbol{\sigma}$ are the Pauli matrices and \mathbf{k} is the wave vector. Each node is distinguished by a new quantum number called chirality, $\chi = \pm 1$, which describes whether the spin is locked parallel or anti-parallel to the momentum. This number is a conserved quantity in these systems and constitutes a new degree of freedom to encode and process information. Just like semiconductor technology is based on the manipulation of the charge degree of freedom, or spintronics on the spin degree of freedom, chirality can be used to produce current channels between regions with imbalances in the number of electrons of a given chirality. Moreover, chirality conservation protects the electrons against back-scattering (this would involve a spin flip), making electron mobilities extremely high. One of the challenges towards the creation of electronic devices that take advantage of this new degree of freedom is the detection and manipulation of chiral states. Strain can be a way to probe and control such states since it can couple to the Weyl nodes and alter their separation in momentum space. Lattice deformations can be modelled by introducing a space dependant node separation \mathbf{k}_0 that couples to the nodes of different chirality with an opposite sign: $H = \pm \hbar v_F (\mathbf{k} \pm \mathbf{k}_0) \cdot \boldsymbol{\sigma}$ [32–34]. This is analogous to the coupling of a particle of charge q and momentum \mathbf{p} to a vector potential \mathbf{A} : $H \propto (\mathbf{p} - q\mathbf{A})^2$. Just like we can obtain the magnetic field through $\mathbf{B} = \nabla \times \mathbf{A}$, we can interpret $\mathbf{B}_5 = \nabla \times \mathbf{k}_0$ as a pseudo-magnetic field, originated from the application of strain gradients, that acts on fermions of opposite chirality with an opposite sign. If similar effects can be observed in 3D TSMs, it would not only mean that strain can be used to explore chiral degrees of freedom but that in doing so it would manifest electronic behaviour impossible to access with conventional magnetic field technology.

Due to their topological nature, the conducting states of TSMs are not limited to the bulk but also extend to the surface. The projections of the nodes on the surface of the Brillouin zone are connected by states called Fermi arcs. Changes in the separation of the nodes will also lead to changes in the extension of these surface states. In TSMs under external magnetic fields electrons can form closed orbits called Weyl orbits, composed of chiral bulk sections (associated to the zeroth Landau level) and Fermi arc sections on the opposite surfaces of the material. Since these orbits involve the Fermi arcs, they are susceptible to changes in the separation of the Weyl nodes coming from strain. Weyl orbits were first confirmed experimentally by Moll et al [35] on FIB microstructured devices of Cd_3As_2 , where they were associated to additional frequencies on the frequency spectrum of the quantum oscillations (QOs). Key factors in this observation were the correct crystallographic alignment of the devices and the reduction of their thickness to dimensions comparable to the electronic mean free path (otherwise Weyl orbits would be destroyed by scattering), which highlights the necessity of precise fabrication capabilities. The finding of these orbits suggests a path to probe electronic topological states and identify charge transfer through Fermi arcs using transport measurements.

Another property of 3D TSMs that has attracted a lot of interest is the sensitivity of their

transport behaviour to the application of an external magnetic field. In particular, large, non-saturating transverse magnetoresistance (MR) in the order of $10^5\%$ - $10^6\%$ at low temperatures and fields of around 10T has become one of the primary features observed in these materials [10, 12]. Naturally, this drastic change in the resistance could be very useful in different technological applications such as magnetic field sensors and magnetic data storage. The origin of such a large MR has been a matter of intense debate but no universal mechanism has been accepted as ultimately responsible. For some TSMs, it's been argued that the application of a magnetic field and its consequent breaking of time-reversal symmetry leads to a suppression of the back scattering protection present at zero field [36]. Interesting information regarding the large MR behaviour can be obtained from its field dependence. Typically, the MR of TSMs follows a power law $MR \propto B^n$, with the exponent n ranging from 1 to 2 [10, 12]. Linear MR has been associated to a classical effect originating from mobility fluctuations in disordered systems [37] but also to a quantum effect when the quantum limit is reached [38]. Quadratic and sub-quadratic MR have been usually associated to the known semi-classical mechanism of electron-hole compensation from closed pockets in a two-band system. The picture is further complicated by the often complex shape of the Fermi surface of some TSMs, which can lead to additional effects in the MR like the presence of open orbits. The challenge in this active topic is to disentangle topological from non-topological effects as well as establishing if the phenomenological similarities observed in many TSMs can be captured within a single universal mechanism or if material-specific models must be invoked in each case.

The work done in this thesis represents an effort to exploit the fabrication possibilities offered by FIB microstructuring in order to explore, characterize and manipulate novel electronic states exhibited in TSMs that would be otherwise impossible to measure using other techniques. The rest of the thesis is organized as follows: chapter 2 describes the main working principles of the FIB, with particular emphasis on its use for the fabrication of transport devices and the possibilities of sample fabrication under different strain conditions. Chapter 3 describes the principal experimental techniques used for the characterization and measurement of the fabricated samples. Chapter 4 introduces the main theoretical concepts necessary throughout the thesis for the understanding and interpretation of the main results. In chapter 5 I introduce an experimental set-up for the controlled application of strain gradients by mechanically bending FIB-machined, 3D crystalline microcantilevers. A simple sample design tailored for transport characterization under strain at cryogenic temperatures is proposed. Chapter 6 presents the experimental findings of bending microcantilevers of the TSM Cd_3As_2 . These results are compared to the predicted presence of strain-induced pseudo-magnetic fields. Chapter 7 is devoted to the TSM PtSn_4 . The first ever microstructures of this material were fabricated and its transport properties are compared to measurements of macroscopic crystals. Finally, chapter 8 summarizes the main results of the thesis and provides an outlook for the continuation of research in the field.

2 Focused ion beam micromachining

2.1 Introduction

Since its development in the 1970's, and its early use in the integrated circuit industry for photomask repair, the focused ion beam has become an important tool for microanalysis and microstructuring in a wide range of technological applications and fields. For example, in the semiconductor industry it is still commonly used for circuit editing, failure analysis and rapid prototyping. In material science, a popular use for the FIB is the preparation of thin samples to be studied by transmission electron microscopy (TEM) and the creation of detailed 3D tomographic models of the specimens of interest thorough the so called "slice and view" procedure.

More recently, the fabrication and machining capabilities of the FIB have been exploited to study the electric and magnetic properties, down to the micrometer scale, of novel crystalline materials that would be very hard or impossible to investigate using other lithographic techniques. These materials, typically called quantum materials since they exhibit striking properties whose origin is quantum mechanical, include, among many others, unconventional superconductors like Sr_2RuO_4 [39], heavy fermion compounds like CeIrIn_5 [40], and more importantly for the subject of this thesis, topological materials like the already mentioned PtSn_4 [41] and Cd_3As_2 [35]. The FIB-machining of 3D microstructures from these compounds has lead to a new level of precision and sophistication in the design of devices fabricated from a parent single crystal, previously unreachable by, for example, manual wiring and polishing of macrocrystals. Although this approach is still in its early stages, it is quickly establishing itself as the new standard for the creation of high quality samples in the field of 3D quantum matter. In this chapter I will introduce some of the working principles of the FIB instrument with an emphasis on how it can be used to fabricate microstructures of quantum materials designed for the investigation of electrical transport properties.

2.2 General principles and features of the FIB instrument

Most modern commercially available instruments are dual systems combining both a FIB and a scanning electron microscope (SEM) sharing a common sample chamber. A schematic illustration of some of the main components of these systems is presented in figure 2.1, together with a photograph of the FEI Helios G4 instrument located at the the Interdisciplinary Centre for Electron Microscopy (CIME) in EPFL. As can be seen there, the electron column is typically mounted vertically while the ion column is mounted at an angle of around 50° (52° for the FEI system in figure 2.1 (b)). Naturally, having both columns allows for the simultaneous SEM imaging of the sample as it is treated with the ion beam, which is not possible in instruments with a single ion column. The sample is held on a five-axis stage to enable precise alignment of the selected region at the point of coincidence of the two beams. The five-axis stage allows for displacement in the (x,y,z) directions of the sample chamber, as well as concentric rotation with respect to the vertical axis of the stage, and tilting of the stage towards the ion beam column. The instrument is also provided with a gas injection system (GIS) with which to locally deposit metallic or insulating materials on the target surface via FIB-induced deposition (FIB-ID) (this process will be discussed in 2.2.3). Additionally, many systems are nowadays equipped with a sharp needle, typically made of tungsten, that serves as an *in situ* micromanipulator capable of moving in the (x,y,z) coordinates of the chamber as well as rotating around its own axis. Combined with the FIB deposition, this micromanipulator allows for the transferring of samples within the FIB, expanding the mounting and milling possibilities for the fabrication of transport devices. Modern systems are also typically equipped with a detector for energy dispersive spectroscopy (EDS) to analyse the characteristic X-ray spectrum from the sample atoms that are excited by the electron beam. A software is then used to identify and quantify the abundance of the detected elements, making it possible to quickly study the chemical composition of the samples.

2.2.1 Ion sources

The shape and overall quality of the focused beam depends on the ion source used. FIB ion sources are designed to have a small source diameter, a large brightness (defined as current per unit acceleration bias) and a small energy spread across the ions in the beam. These parameters influence the beam current and the diameter of the focused beam. The most common type of source used is the liquid metal ion source (LMIS), which is shown schematically in figure 2.1 (a). In it, a reservoir containing the source metal, typically Ga, is connected to a sharp tungsten needle with a radius of just a couple of micrometers. An induction coil surrounding the reservoir is used to melt the metal, producing a liquid that wets the needle. Using the extractor electrode, a high voltage of around 10kV is produced that induces an electrostatic force on the liquid. This force, combined with the surface tension of the liquid, leads to the formation of a very sharp cone, called Taylor cone, whose tip has a radius of around 2nm-5nm. Thanks to the electric field provided by the extractor electrode,

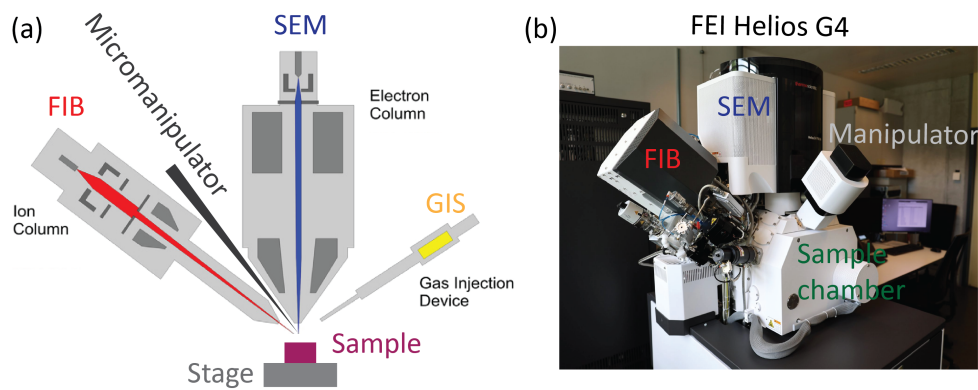


Figure 2.1: **Schematic of the basic components of a SEM/FIB dual system.** (a) The main features include the electron and ion column for imaging and milling, respectively, and the micromanipulator and gas injection system for material deposition. The sketch is based on [42]. (b) Optical image of the Xe based FEI Helios G4 instrument at the Interdisciplinary Centre for Electron Microscopy (CIME) in EPFL.

ions are emitted via field ionisation. One big advantage of this design is that the source is self-sharpening since the shape of the cone is maintained by the reservoir as the ions are continuously emitted. Although several metals such as Al, In, Au, or Bi (as well as other alloys) can be used as source material, Ga is usually preferred for a number of reasons: it has a relatively low melting temperature of around 30 °C that is easy to achieve, a relatively high ion mass, low volatility, low vapour pressure and a long lifetime due to the non-reactivity with the tungsten tip.

One important limitation of the Ga LMIS is that the maximum attainable current is limited to approx. 100nA. For larger currents, there is a breakdown of the Taylor cone and due to spherical aberrations coming primarily from the energy spread of the beam due to space charge effects, the beam size increases, meaning that the LMIS rapidly becomes less useful as the current increases. This, in turn, means that the rate of removed material is also limited. The desire for larger material removal rates with smaller and more stable high-current beams lead to the development of the inductively coupled plasma (ICP) source in 2006 [43], which is shown schematically in figure 2.1 (b). This source is formed by a reservoir of an inert gas that is inductively coupled to a radio frequency (RF) antenna. The electromagnetic field generated by the antenna accelerates the electrons and creates a dense plasma by ionising the gas. An extraction electrode is then used to move the resulting ions through an aperture and into the rest of the FIB column. Typically, xenon is used over other inert gases like argon, given its high mass and favorable performance parameters such as higher milling rate and lower energy spread.

The ions beams resulting from these two different sources show some important differences. In terms of beam profile, the beam from the LMIS, which is mainly limited by spherical aberrations, produces a wide, flat beam closer to a Gaussian profile, while the ICP source,

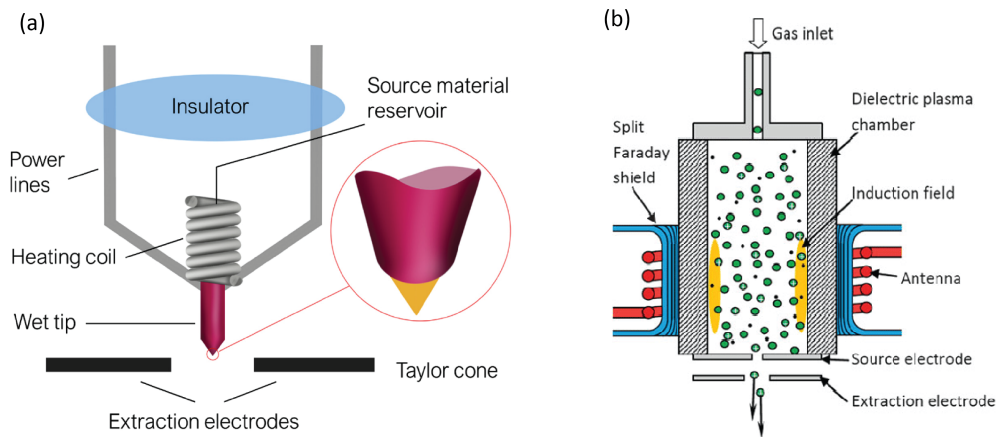


Figure 2.2: **Two kinds of ion sources for the FIB.** (a) Liquid metal ion source (LMIS). (b) Inductively coupled plasma source (ICP). The sketches are taken from [47] and [48], respectively.

which generates more collimated ions, produces a narrow, sharp beam but with larger beam tails [44]. In terms of spot size, figure 2.3 shows a comparison between both sources for the same ion accelerating voltage. For currents smaller than 10 nA, the Ga-FIB provides a stable beam spot smaller than the P-FIB one. However, for bigger currents the Ga-FIB spot size increases rapidly, resulting in smaller current density and hence smaller rate of material removal. In this range, the P-FIB clearly outperforms the Ga-FIB and can reach stable currents of up to 2.5 μ A with a very high milling rate [45]. With this into consideration, the Ga-FIB is usually the better option for milling very fine features in a microstructure, while the P-FIB is more suitable for large scale removal of material. In addition to this, the use of the P-FIB also has the advantage of avoiding the implantation of Ga ions into the sample and reducing the extension of the damage layer created by the ion beam (these effects will be discussed in more detail later in this chapter). At the CIME in EPFL, both a Zeiss AURIGA crossbeam FIB with a Ga-LMIS and the already mentioned FEI Helios G4 with a Xe-ICP source were used for the fabrication of the microstructures studied in this thesis.

It is worth mentioning that another kind of source has also been developed recently: the gas field ionisation source (GFIS) [46]. The basic component in this design is a tip that is sharpened down to a "trimer" of atoms. The tip is positively biased against a counter electrode and then the source gas, typically He, is made to flow in its vicinity, ionising it via field ionisation. Very small beam sizes in the sub-nm scale have been achieved with this source, opening the way to ultra-high imaging and milling. The drawback is the limited maximum beam current of around 5 pA and the potential higher contamination with the very light He atoms.

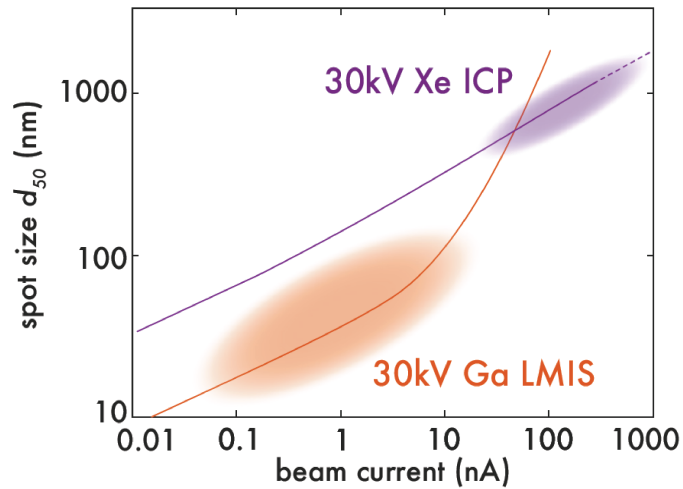


Figure 2.3: **Spot size as a function of beam current for Ga-FIB with a LMIS and a P-FIB with a ICP source.** The spot size d_{50} indicates the effective central beam diameter containing 50% of the ion current. Figure based on [43].

2.2.2 Ion-solid interactions

As the beam of accelerated ions hit the target surface and losses its kinetic energy, a number of physical and chemical processes such as ion backscattering, atomic sputtering and sample heating can take place (see figure 2.4 (a)) [47, 49–52]. The presence of these processes will depend on the nature of the interaction between the impinging ions and the target material, and can have important consequences when fabricating microstructures for transport experiments.

The kinetic energy from the ions is transmitted to the target material through both elastic and inelastic interactions. The elastic interactions are dominated by the transfer of energy between the incoming ions and the nuclei of the target atoms, triggering a collision cascade where the atoms in the sample can be displaced and give raise to the creation of interstitial vacancies and amorphous regions around the area of irradiation. If the energy transferred to the atoms close to the surface is greater than their binding energy, they get ejected or sputtered from the material. This is the main mechanism for material removal with the FIB. Additionally, elastic collisions may result in the ions themselves getting ejected back from the substrate after one or multiple collisions, in a process referred to as backscattering. On the other hand, ions can also lose all the energy and remain embedded in the substrate, in a process called ion implantation. This process is important since it can lead to appreciable changes in the chemical composition of the surface of the material. Charged ions from the material itself, named secondary ions (SI) as opposed to the primary ions from the beam, can also be emitted in the collision cascade and can be in fact used for compositional analysis in secondary ion mass spectrometry.

The inelastic interactions are dominated by the transfer of energy from ions to the electrons in

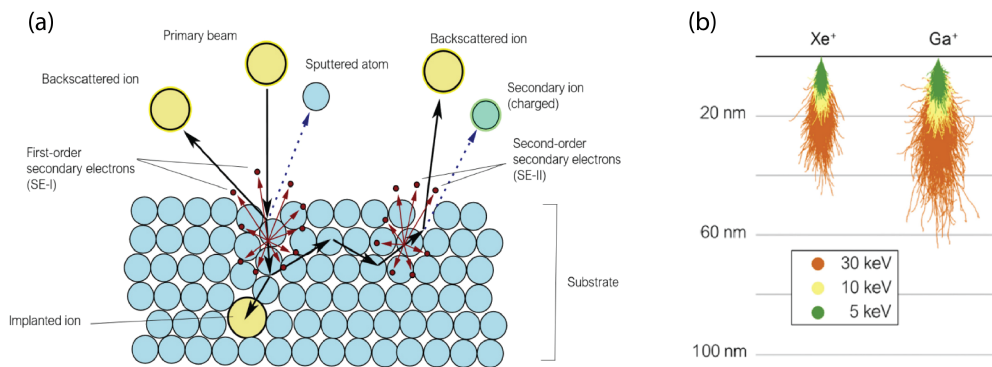


Figure 2.4: **Ion-solid interactions during FIB processing.** (a) Scheme of interactions of primary ions generating secondary electrons (SE) and a collision cascade of substrate atoms. (b) SRIM simulations of trajectories in a Si substrate of Xe⁺ and Ga⁺ ionic species under different acceleration voltages, highlighting the interaction volume in each case. Figure taken from [47].

the sample and leads to the appearance of the so-called secondary electrons (SE) as ionization products, emission of electromagnetic radiation, and, in the case of metallic materials, in the creation of plasmons and phonons. As depicted in figure 2.4 (a), SE are usually divided in SE-I or first order SE if they are generated close to the area of irradiation, and SE-II or second order SE if they are generated in regions further away, from primary ions that had been previously scattered.

Computational simulations of ion-solid interactions are generally performed with a program called SRIM (Stopping Range of Ions in Matter) [53]. The inbuilt Monte Carlo calculation uses quantum mechanical models for the ion interactions and statistical algorithms to allow ions and atoms to hop between successive collisions, thus simulating the collision cascade, and calculating the changes in energy and trajectory happening at each instance. The final results are obtained after a large number of instances are simulated. A SRIM simulation requires incident ion angle, energy and weight, as well as sample depth and constituent material as input parameters. Important information can then be obtained regarding a number of processes such as phonon production, ion backscattering, extent of ion implantation and the collision cascade and sputtering yield. A typical SRIM simulation of the trajectories in a Si substrate under different acceleration voltages and ionic species is shown in figure 2.4 (b). As the ion energy increases, both the range and the collision cascade size grow, with heavier ions having a smaller range, as can be seen in figure 2.4 (b) for the case of the heavier Xe ions compared to the lighter Ga ions. Sputtering yield is also favored for heavier ions and higher energies although for too high energies ions can penetrate too deeply to allow the displaced target atoms to escape.

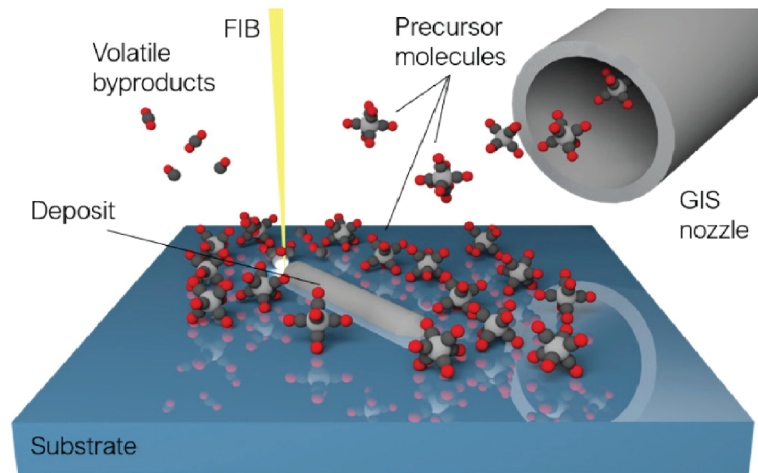


Figure 2.5: **FIB-assisted deposition process.** A precursor gas is injected by the gas injection system (GIS) and adsorbed on the sample surface. Ion bombardment dissociates the precursor gas into volatile and nonvolatile components. The volatile fragments are pumped away, leaving behind the non-volatile conductive matrix as a deposition. Figure taken from [47].

2.2.3 FIB-induced deposition

One of the very useful capabilities of the FIB is to deposit different materials on the desired target surface. The basic mechanism behind this process is shown in figure 2.5. A precursor material stored in a reservoir is heated until sublimation and the resulting gas is delivered to the chamber through a nozzle located close to the target sample. Several precursor gases are used depending on the material to be deposited (mostly organometallic compounds like $W(CO)_6$ or $CpPtMe_3$) [21]. Typically, W, Pt and C are used for deposition. Once the precursor gas is adsorbed on the surface then it is irradiated with the ion beam and the volatile byproducts are pumped away while the heavier atoms are deposited on the surface. However, the material deposited is not a pure metal but an amorphous mixture of different components. Some studies, for example, have reported that for a Ga-FIB deposited layer of Pt the actual composition is 72% C, 18% Pt and 10% Ga [54]. Furthermore, the deposited layers typically show resistivities that can be up to three orders of magnitude higher than the pure metals. This limits their use as electrical contacts but, as will be shown in later sections, combined with the sputtering of a Au layer, deposited strips of Pt, for example, do serve as strong mechanical and chemically inert bonds for microstructures as well as helping to create good Ohmic contacts.

2.3 Basic control parameters of the FIB

The FIB fabrication process involves adjusting a number of parameters according to the characteristics of each material and microstructure design. Two main aspects to take into consideration when using the FIB are the beam size and the way in which we scan the beam during patterning. The profile and size of the beam depends, among other parameters, on the

chosen values for the current and accelerating voltage [21]. The characteristics of the beam affect the sharpness of the cuts and the milling rate during patterning. In the FIB machine, a pattern is defined by a set of pixels at certain positions. In a single pass, each pixel is exposed to the beam during a given time interval (known as the dwell time, defined below). Several passes are required for the completion of a pattern. Some of the main FIB parameters to take into account during the fabrication process are the following (although there is some variation from system to system, the same or similar functionalities are typically found in all systems) :

- **Current** : it quantifies the number of ions delivered per unit of time. The beam diameter will increase for higher currents but also the milling rate. This is why large currents are better suited for cutting large, broad features, while small currents are used to cut small, detailed ones.
- **Voltage** : it is the voltage used to accelerate the ions along the column. The higher the voltage, the further the ions penetrate the sample, thus increasing the sputtering yield. The spot size will tend to decrease for higher voltages.
- **Scan type**: determines the way in which the beam is scanned over the pattern. There are two main types:
 - **Raster**: The beam moves from left to right, then it is blanked and goes to the left again to continue the pattern.
 - **Serpentine**: The beam goes from left to right, then it is blanked and then continues from right to left in the next line.
- **Pattern type**:
 - **Rectangle**: this is one of the most commonly used patterns given its versatility. Whether using the raster or serpentine scanning, the patterning is completed through several passes that extend over the whole rectangular area. If the cut is not too deep, the resulting milled region shows a cross section with a flat bottom surface.
 - **Regular Cross Section (RCS)**: this pattern can be scanned using two methods: i) Multipass: similar to the Rectangle pattern, it processes the whole pattern with several passes. ii) Stair step: the pattern is created as a compilation of rectangles with specified overlap between them, resulting in a stair-step cross section cut. This last scan option is suitable for fast removal of material.
 - **Cleaning Cross Section (CCS)**: this pattern is processed line by line in the scan direction. After one line is milled, the beam advances to the next line without returning to previous lines, unless it is manually set to do so. This possibility of repeating a line several times is advantageous when polishing the side walls of the microstructures without producing excessive redeposition.

- **Line, Circle, Polygon and Bitmap:** although less common, these patterns can also be used for milling and deposition. As will be explained in the next section, the Polygon pattern is mainly used to remove Au evenly from the top of the Au coated sample. In the case of Bitmap patterns, they allow to mill more complex shapes and are useful to label samples. One of the disadvantages of Polygons and Bitmap patterns is that the scan path will depend strongly on the particular shape of the pattern. If the shutter is not quick enough to blank the beam, the irregular scan path can lead to undesired beam trails on parts of the sample that were not intended to be milled.
- **Dwell time :** the time the beam spends on a single pixel during the scan of the pattern.
- **Refresh time :** it is the time that must elapse between consecutive passes of the beam. This parameter is particularly relevant when using the FIB for deposition since too small a value can lead to milling instead of deposition.
- **Overlap:** typically expressed in (%), it sets the beam diameter overlap. It can be positive or negative depending on a particular application. A higher overlap increases the irradiation density, favoring more even milling. This can be useful when making highly polished surfaces.
- **Blur and Defocus:** Both of these options essentially defocus the ion beam, which can be beneficial during deposition on large areas, for example.

2.4 FIB artifacts

The interaction of the ion beam with the target material can lead to a number of artifacts or undesirable effects on the materials surface, potentially altering its physical and chemical structure. Careful tuning of the beam parameters can help reduce and sometimes eliminate some of these effects. The following are some of the most common FIB artifacts observed when fabricating microstructures:

2.4.1 Curtaining

When milling a surface with the FIB, it's not uncommon to observe the formation of vertical stripes or ripples indicating an uneven removal of material. This "curtaining" effect is caused by the spatial variation of the milling rate of the target sample and the resulting modulation of the current density by forward scattering of the ions. Such a variation is usually related to the presence of an inhomogenous surface with materials of variable milling rates. For example, porous samples exhibit particularly deep curtaining effects downward from the pores due to a higher milling rate attacking the bottom of the pore [56]. In general, the presence of curtaining depends heavily on the material targeted. There are several ways to reduce curtaining effects,

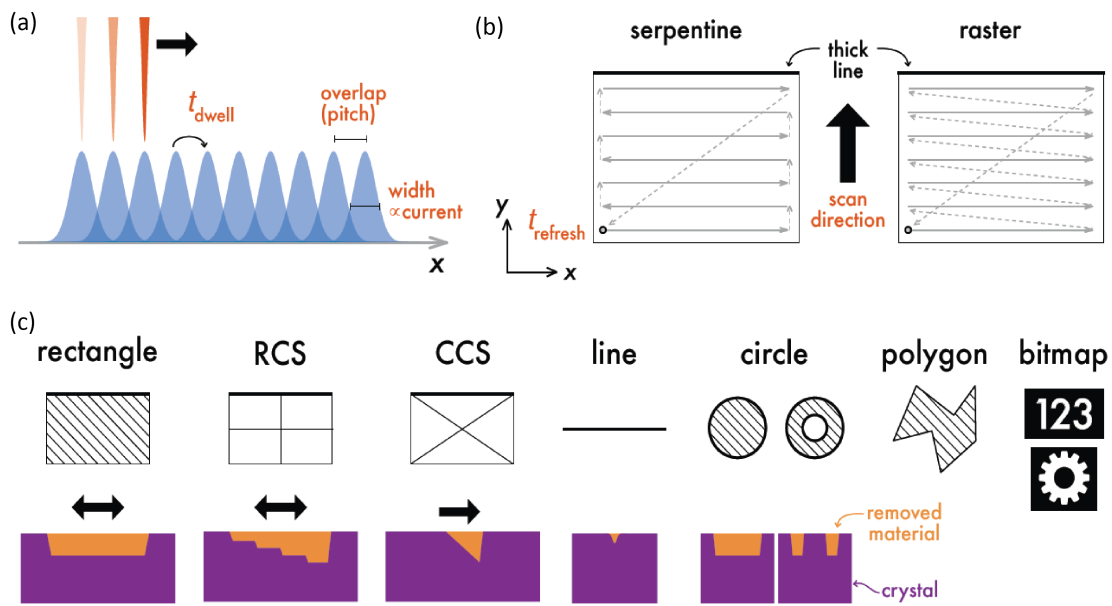


Figure 2.6: **Basic control parameters and milling patterns of the FEI Helios G4 system** . (a) The ion beam remains at each pixel of the pattern a t_{dwell} amount of time. The pitch refers to the separation of two beam spots, which depending on the beam diameter will also result in a given beam overlap (usually expressed in beam percentage). (b) Different scan types for a given pattern: serpentine and raster. In both cases a time $t_{refresh}$ is elapsed between consecutive passes of the pattern. (c) Basic patterning types available in the FEI user interface. See main text for detailed description. The bottom row shows the respective cross section of the patterns with the orange region representing the volume that is milled away. Figure taken from [55].

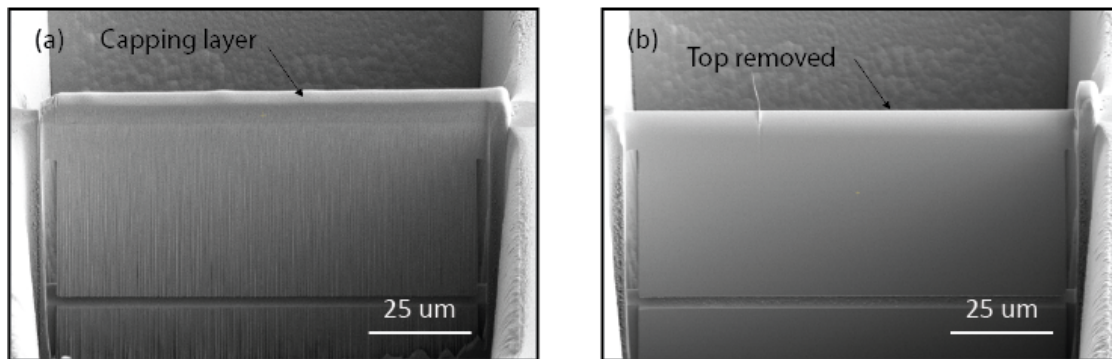


Figure 2.7: **Curtaining effect on a PtSn_4 lamella.** (a) Even with a Pt capping layer deposited on top of the lamella, curtaining can still persist. (b) After removing the top of the lamella (including the deposited layer) a smooth surface can be obtained.

including: polishing the surface with a low current; using a special "rocking stage" where the sample is moved back and forth while milling; depositing a thick layer of a hard material like Pt or C before polishing the surface; and finally, removing altogether the rough part of the sample and then polishing. As an example, the last of these options was used to polish one of the materials studied in this thesis: PtSn_4 . As can be seen in figure 2.7 (a), even after depositing a thick layer of Pt on top, the polishing of the lamella resulted in pronounced curtaining. Only after removing completely the top part of the lamella, this artifact could be eliminated and a smooth surface was obtained (figure 2.7 (b)).

2.4.2 Amorphization and ion implantation

When the ion beam hits the target surface not all the sample atoms are ejected, some of them are displaced within the material altering its crystallinity and producing an amorphous layer [57, 58]. This amorphization is limited by the penetration depth of the ions and, as can be seen in figure 2.8, its size depends, among other factors, on the accelerating voltage and ion mass. As expected, higher voltages and lighter ion species lead to larger damage layers. A related effect is the implantation of ions in the target material, already mentioned in 2.2.2, which happens when the beam ions get stuck in the sample after losing all their energy in the ion-sample interaction. In general, the damage layer created by the FIB using typical settings for the machining of microstructures extends only a couple of nanometers. Regarding its influence in the transport properties of the fabricated devices, such a layer can usually be ignored since its resistance contribution is negligible most of the times (one important exception is discussed in the next section) and it doesn't damage the bulk extensively as to, for example, suppress quantum oscillations from the quantization of the bulk Fermi surface. More interestingly, the damage layer does not affect the signal from quantum orbits that are partially extended on the surface of FIB microstructures [35].

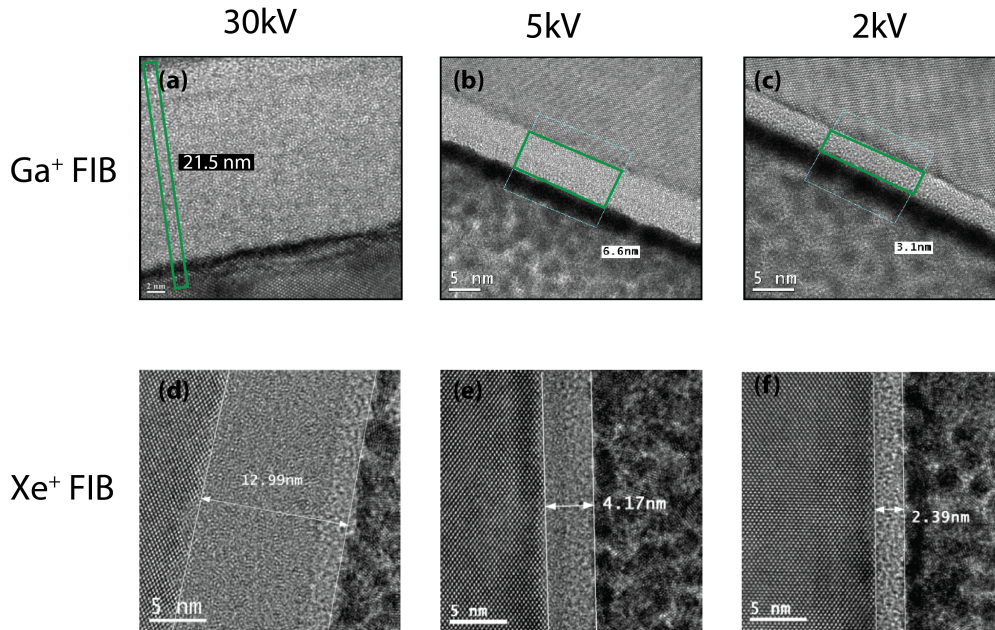


Figure 2.8: **Amorphization damage in Si from both Ga-FIB and P-FIB at different accelerating voltages.** Milling with the heavier Xe^+ ion produces less damage than with the lighter Ga^+ ion of the same energy. As expected, the amorphous damage decreases considerably with decreasing accelerating voltage. Figure taken from [58].

2.4.3 Differential sputtering

The sputter rate of different atoms in the material might not be the same, which means that some elements can be preferentially sputtered in comparison to others. This can lead to modifications in the chemical composition of the surface. For example, in the mono-arsenide family $(\text{Nb,As})(\text{As,P})$ it has been shown that FIB irradiation of the crystalline bulk produces a surrounding amorphous layer rich in Nb (Ta) since As (P) is preferentially sputtered away. This has very important consequences regarding the transport properties of the irradiated sample since the amorphous layer actually becomes superconducting at low temperatures [59].

2.4.4 Redeposition

When exposing a surface to the ion beam, not all the target atoms are ejected and pumped away, some of the atoms that are sputtered can land back on the target surface forming a region of redeposited material [49]. This effect limits the practical width-to-depth ratio of the trenches that can be milled. Furthermore, in the microstructuring of transport devices, redeposited material can affect the final geometry of the device and also create undesired shortcuts. One way to mitigate these effects is to run the milling patterns in parallel to evenly remove the material and then carefully polish the faces of the microstructure with a small current. In general, the amount of redeposited material depends on the type and geometry of pattern used as well as the energy on the incoming ions.

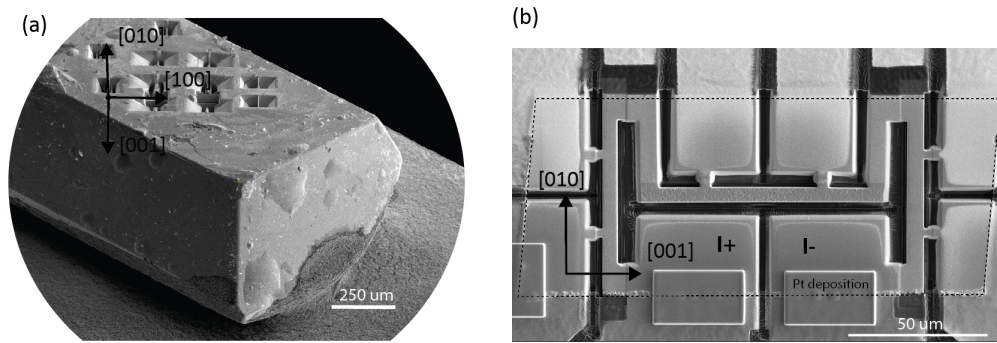


Figure 2.9: **Transport device from a parent PtSn_4 crystal.** SEM images of (a) PtSn_4 macrocrystal with its corresponding crystallographic directions and (b) a typical "U" transport device machined from the extracted lamella (highlighted by the dotted line).

2.5 Fabrication of microstructures for transport measurements

In this section I will describe the main steps necessary to use the FIB to fabricate a transport device from the material of interest. Given the versatility of the FIB, the procedure to design and fabricate a device will ultimately depend on the physics that is meant to be explored with such a device. In this section I will concentrate on the fabrication processes that are most relevant for the work done in this thesis. The main goal is to take in consideration the FIB features and characteristics described so far to fabricate a sample according to the general criteria of functionality of a transport device. These criteria include, amongst others, the presence of well defined voltage contacts and current paths (for example, by avoiding shortcuts), the minimization of bulk damage to the sample and the reduction of parasitic capacitive and/or inductive couplings that could distort the voltage signal from the device. Thanks to the fabrication precision of the FIB, these criteria can be met to a much larger degree than with typical preparation methods for 3D quantum materials. Figure 2.9 shows a usual starting and final point in the FIB fabrication process. Beginning with a parent crystal, in the case of figure 2.9 (a) it is PtSn_4 , whose crystallographic directions have been previously determined, a lamella is extracted and transferred to a suitable substrate. Such a lamella (highlighted in figure 2.9 (b)) forms the basis of the transport device, which in this case consists of three pairs of voltage contacts along two different crystallographic directions to perform four-point measurements. Such a device is typically referred to as a "U" structure and is designed to measure precisely the resistivity anisotropy along the different directions. The same kind of measurement would be almost impossible to make using the macrocrystal and manually-mounted electrical contacts. Notice that Pt patches were deposited on some contacts to improve electrical connection and low current milling was used to accurately narrow the voltage contacts and shape the corresponding bars where the device's current flows. This makes it possible to greatly reduce the cross-sectional area of the device, which translates into achieving very high current densities of around 1 MA/m^2 (about 100 times larger than could be obtain with the macrocrystal) and hence very large voltage signals.

2.5.1 Lamellae preparation from a single crystal

As mentioned before, the first stage common to most FIB processes for the fabrication of transport devices is the cutting of a lamella from the parent crystal. The procedure is very similar to the one used for the preparation of TEM lamellae and has been applied to a large number of different quantum materials [20]. The following steps can be performed to successfully carve a lamella that is suited for device micromachining:

- **Placing the parent crystal on the SEM stub:** The first step is to have the single crystal of the desired material mounted on the SEM stub using an adequate conductive adhesive. For this thesis, two adhesives were typically used for this purpose: Silver Conductive Adhesive 503 (12686-15) from EMS, and 4929N from DuPont. The first one is a conductive paint that contains high purity silver flakes, shows good adhesion to most substrates and dries relatively fast; the second one is a viscous paste that needs to be thinned down to the desired consistency. It also has a high metallic silver content and tends to dry slightly faster than the EMS paint. Its advantage is that by controlling the amount of thinner, it is usually possible to obtain very fine droplets or films that are more suitable for very small crystals. In both cases, the main purpose is to have a firm mechanical adhesion to the SEM stub to avoid spacial displacements, and to electrically ground the crystal to avoid undesirable aberrations from the accumulation of charge. Before mounting the crystal, it is necessary to identify the desired crystallographic directions, for which X-ray diffraction methods can be used. Ideally, the crystal should be mounted with the desired crystallographic face as flat as possible on the SEM stub in order to have the beam of ions striking perpendicularly on its surface (at 52° in the case of the FEI P-FIB system). Small angle misalignments, whether from slightly irregular crystal faces or minute uneven mounting, can still be handled either by using pre-tilted SEM stubs or by correcting the tilting angle of the stage. However, if the crystal shape is so irregular that no correction is possible within the limits of the stage movement, it's necessary to expose the desired crystallographic face first by using other means. These could include, for example, mechanical polishing or, as will be discussed later in this section, preliminary cuts with the FIB.
- **Capping layer deposition:** Once the crystal is properly mounted and the desired crystallographic face is exposed, it is necessary to choose a region of the crystal from which to cut the lamella. The aim is to choose a clean, smooth and flat surface with as few defects or miss growths as possible, thus guaranteeing the best quality for the lamella. Although it's not always strictly necessary, it is usually very convenient to deposit a rectangular capping layer, a couple of micrometers thick, where we aim to carve the lamella in order to protect the crystal's surface. By making the top surface more homogeneous, this can greatly reduce the effects of curtaining and also allow to use higher currents to mill the material adjacent to where the lamella is located. Carbon and platinum are two common options but the exact recipe will depend on the material and the dimensions of the lamella to cut. For deposition, it is usually recommended to use a low accelerating

FIB voltage, as well as a relatively low dwell time and large refresh time to avoid milling the crystal instead of depositing the desired capping layer. For the Pt deposition in the FEI P-FIB system some typical values are 12kV of accelerating voltage, $t_{dwell} = 100$ ns and $t_{dwell} = 1$ ns. A general rule of thumb to choose the appropriate current value I is $I \approx 4 \cdot \text{area}(\frac{pA}{\mu m^2})$. For instance, if the Pt layer to be deposited is $20\mu m \times 100\mu m$ large, then the empirical formula suggests using a beam current of around 8 nA.

- **Cutting of the trenches:** To cut the lamella we use two RCS patterns delimiting the deposited capping layer or the region where the lamella will be (see figure 2.10 (a)-(d)). These two patterns will mill the so-called trenches, between which the lamella stands. The final result should look like figure 2.10 (d). The milling of the trenches should be done as quickly as possible by selecting high beam currents. This means that we have to leave a considerable space between the two patterns delimiting the trenches to account for the beam diameter. Otherwise, we risk having a lamella that is too thin or not having a lamella at all. For example, if we use a current of $2.5 \mu A$ at 30kV with a beam radius of approx. $8 \mu m$, we should leave $\approx 26 \mu m$ between the patterns to end up with a lamella that is around $10 \mu m$ thick. This leave us with enough material to further polish the lamella, whose final thickness is typically around $5-6\mu m$. The final thickness will naturally depend on the desired application but leaving at least $2\mu m$ of extra material on each side of the lamella for polishing is recommended. Both the depth and width of the RCS pattern and ultimate cut will determine the final depth of the lamella. In general, the width of the RCS pattern should at least be $\sqrt{3}x$ the desired lamella depth.
- **Undercut:** To liberate the lamella from the crystal we perform an undercut, which is a cut at as high of an angle as possible with respect to the surface of the crystal (typically more than 60°). The schematic of this cut is presented in figure 2.10 (e)-(f). In the case of the FEI P-FIB, the undercut is done at a tilting angle of -10° , which is the smallest one available. Two small bridges on the top of the lamella are left uncut to keep it in place. When drawing the rectangle patterns for the undercut, it is convenient to make them overlap at the corners of the lamella, as shown schematically in figure 2.10 (e). In this way, we make sure that the beam goes through the crystal at these points. The patterns for the undercut are typically $5\mu m$ wide for the bottom pattern and $3\mu m$ wide for the lateral ones and a current of around 15-60 nA is used. Naturally, these values depend on the final thickness of the lamella, and could be increased if required until a U-shaped cut in the lower side wall of the trench is visible, indicating that the beam has milled through the crystal.
- **Polishing:** after cutting the trenches, the lamella's cross section is typically trapezoidal because of the beam profile (especially when using the P-FIB), that is, thicker at the bottom than at the top, and with rough surfaces due to curtaining. To have smooth and parallel faces on which to fabricate our device, we use the beam to polish the surface of the lamella at a tilting angle of $52^\circ + \theta$. The value of θ depends on the target material and the beam settings used. Whatever the kind of FIB, polishing should be done preferably

with a pattern that allows line by line control. In the case of the FEI systems, the CCS pattern is the most suitable one (see figure 2.10 (g)-(h)). To find the optimal value of θ , we begin with a small value of θ , for example, 1° , and polish one face of the lamella. We then tilt the stage back to 0° to check if it is possible to see the bottom of that face. If it's not, then the angle is right and we should only begin to see the bottom of the lamella when we tilt the stage to around $0.5-1^\circ$. If, on the other hand, we can still see the bottom at 0° , then the lamella's cross section is still trapezoidal and we must increase the angle θ and repeat the above procedure. 15-60 nA is a good range of currents for polishing. Before the pattern is finish, it is recommended to repeat the last line 5-10 times to make sure that the surface is really clean and the bottom of the lamella doesn't change. When polishing, having the capping layer on top can be very beneficial to obtain smooth surfaces. However, as already shown in figure 2.7 (a), in some cases not even that is enough to guarantee a successful polish. Another possibility is to completely remove the top of the lamella using a similar stage setting as the undercut. For the material PtSn₄ that was usually the better strategy (see figure 2.7 (b)). One small disadvantage of this option is that the top of the lamella typically shows a "bullet" profile instead of a sharp rectangular edge.

- **Cut the bridge:** In the final step, one of the small bridges holding the lamella is milled away and the other one is reduced to about $1\mu m^2$ in cross section. The smaller this bridge, the easier it will be to break and transfer the lamella, however, it shouldn't be too small since the lamella could fall off and be lost.

It was mentioned before that in case of irregularly shaped crystals, it is not always possible to mount the desired crystallographic face flat on the SEM stub and that some other step must be taken before carving the lamella. In this paragraph I discuss one such case, where the high milling rate available with the P-FIB is exploited to expose the desired crystallographic faces of the material. The situation is presented in figure 2.11. The material in question is CoSi, a topological semi-metal with a cubic crystal structure that was investigated during the course of this thesis and whose process of crystallographic orientation and FIB-cutting was optimized for the extraction of lamellae along the crystallographic directions of interest . A SEM image of a typical as-grown crystal is shown in figure 2.11 (a). The crystals are usually not too big and the crystal faces tend to grow along the [111] and equivalent directions, as revealed by X-ray diffraction. However, the directions of interest are the [001] and equivalent. The (111) faces form an octahedron, while the (001) faces form a cube. An illustration of these two kinds of crystallographic faces is presented in figure 2.11 (b). Based on that sketch, it is possible to devise a simple procedure to use the P-FIB to cut the crystal at the right angles to expose the (001) faces. Figure 2.11 (c) shows the angle between the relevant two directions. By taking the edge of one of the octahedron faces as reference and making a cut at $17^\circ + 2^\circ$ tilt, the (001) face can be exposed. The extra 2° were taken to have a more parallel face. The result is shown in figure 2.11 (d), where a maximum current of $2.5\mu A$ at 30kV was used. After this first cut, the crystal was then mounted with the freshly cut face flat on a substrate. The substrate was then

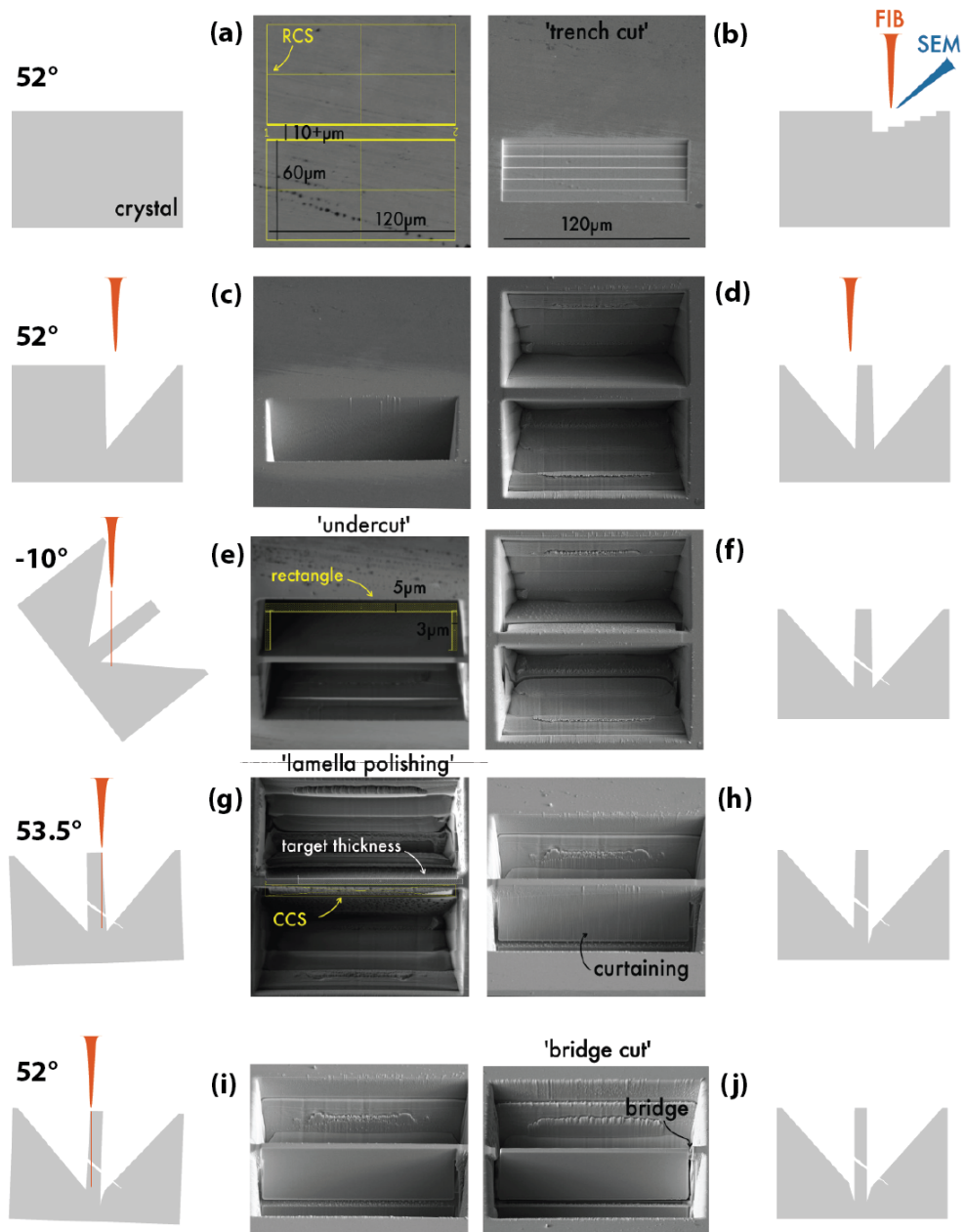


Figure 2.10: **Lamella extraction process flow using the FIB.** (a)-(d) First, two trenches are milled with the FIB at normal incidence to the crystal. Depending on the material, the deposition of a capping layer where the lamella will be located can be beneficial. (e)-(f) Next, the undercut of the lamella is performed, (g)-(h) followed by the polishing of both lamella surfaces using the beam at grazing angles (a typical value of 53.5° is shown). (i)-(j) Finally, a thin bridge is left behind to hold the lamella to the crystal. Figure taken from [55].

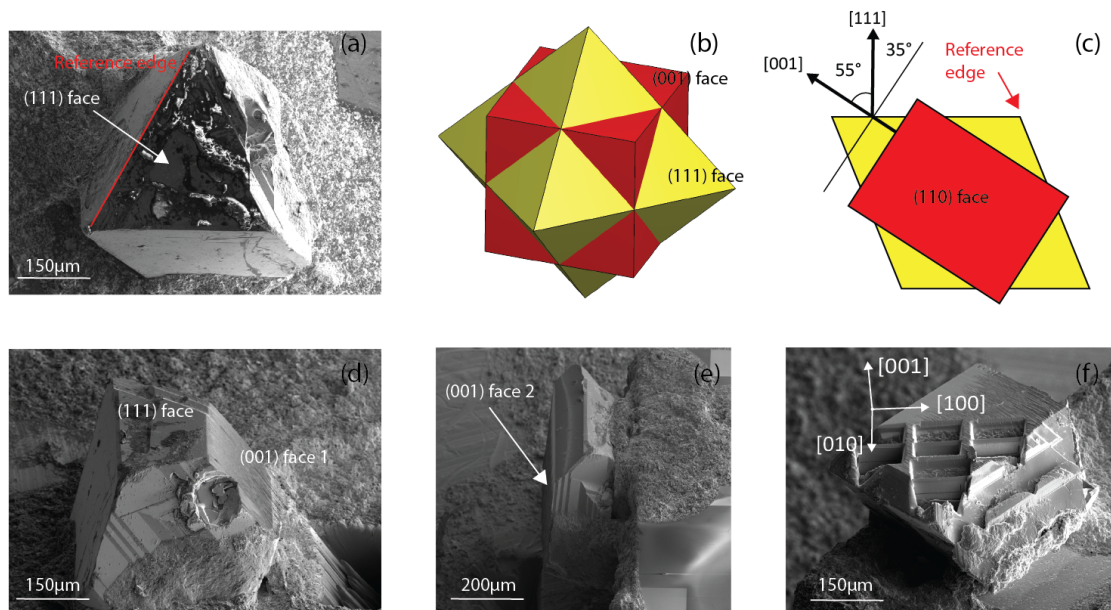


Figure 2.11: **Lamella extraction procedure for the material CoSi**. Thanks to the high milling rate of the P-FIB, it is possible to mill entire faces of as-grown crystal in order to extract lamellae along the desired crystallographic directions. (a) SEM image of a typical CoSi crystal. CoSi has a cubic crystal structure and usually the crystal faces grow along the $[111]$ directions. (b) Schematic illustration of the (111) crystal faces and the (001) faces that are meant to be exposed. (c) Angle between the normal directions of the aforementioned faces. (d) and (e) SEM images of the crystal after P-FIB milling. (f) SEM images of the resultant crystal with lamellae cut along the $[001]$ crystallographic directions.

mounted horizontally on a SEM stub and a second cut was made at $52^\circ + 2^\circ$ with the same beam settings as before. The result is shown in figure 2.11 (e). Next, the substrate is mounted vertically, thus exposing the (001) face of the crystal flat with respect to the SEM sub. Finally, the lamellae are cut at 45° from the octahedron reference edge, as shown in figure 2.11 (f).

2.5.2 Glue-mounted microstructures

2.5.2.1 Lamella transfer

After polishing the surfaces of the lamella and cutting the bridge, the lamella can be extracted *ex situ* from the parent crystal and transferred to a suitable substrate (typically sapphire or Si/SiO₂) with pre-fabricated electrical contacts. The main goal of the transfer procedure is to safely break off the remaining bridge of the lamella, secure the holding of the lamella, and transfer it to glue it down to the desired substrate. A set-up used for this purpose is shown in figure 2.12. It consists of a 3-axis hydraulic micromanipulator with a magnetic base that can be solidly fixed on a steel base. This is important to reduce any undesired vibrations that could hinder the transfer process. A wooden pole with a small Kapton tip attached to it is mounted on the arm of the micromanipulator. The Kapton tip is shaped as a loop with

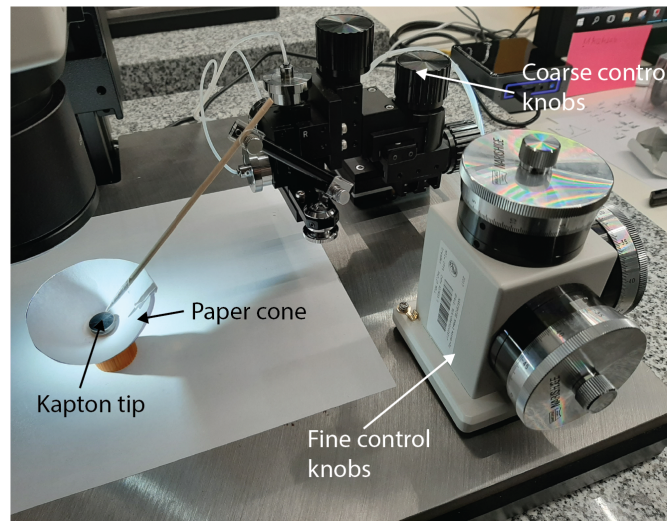


Figure 2.12: **Set-up for the transfer of extracted lamellae.** The parent crystal is approached by a small Kaptop tip mounted on a wooden pole. The pole is attached to a 3-axis hydraulic micromanipulator with a magnetic base that can be fixed on the solid stainless steel base. The Kaptop tip is used to break the bridge and capture the lamella. The SEM stub with the crystal is surrounded with a clean paper cone in case the lamella disattaches from the Kaptop tip.

different diameters available (usually we used one of $20\mu m$). The idea is to carefully approach the crystal with the Kaptop tip and use it to capture the lamella via electrostatic forces. The crystal is mounted on a SEM stub and is surrounded by a paper cone. This makes finding the lamella easier in case of loosing it during the transfer process.

The main steps in the *ex situ* transfer process are shown in figure 2.13. The first step is to use the micromanipulator to approach the lamella and position the Kaptop tip close to where the remaining bridge is located (figure 2.13 (b)). With a gentle push, it is possible to break the bridge, after which the electrostatic forces should be strong enough to secure the lamella to the tip. It's likely that the lamella flies away, in which case it is necessary to look for it in the area surrounding the crystal and the internal surface of the paper cone. It's also likely that while approaching the lamella it is attached to the Kaptop tip in irregular ways. The optimal way to attach the lamella to the tip is shown in figure 2.13 (c). It should be attached to the tip with its short axis as flat as possible and its long axis with a slight tilting downwards, such that one of the short sides is the lowest point. The next step is to move the lamella to the center of the substrate. Before lower it down, we must first create a thin film or small droplet of glue to firmly attach the lamella to the substrate. We use the two-component Araldite® rapid epoxy for the glue, which provides a working time of around five minutes before it starts to dry. An eyelash attached to a wooden pole or a glass rode with a very fine tip can be used to produce the glue droplet. The droplet should be big enough to comfortably fit the whole of the lamella, such that all sides are in contact with glue, but not too big and thick as to risk sumerging the lamella. It is recommended to flatten the droplet as much as possible to avoid having a very steep droplet profile, which would make it more difficult to place the lamella flat.

After creating the droplet we proceed to carefully lower the lamella on top of it. The procedure to do this is presented in figure 2.13 (d). Once the lamella comes in contact with the epoxy, the surface tension will pull it into the glue droplet so there is no need to push it too much. Ideally, the final result should show a fully submerged lamella except for the top surface, with a smooth transition from the substrate to the edges of the lamella. Figure 2.13 (e) and (f) show some images of the transfer procedure on an actual lamella. After the lamella is in place, the epoxy is cured by heating it to 140 °C for one hour.

2.5.2.2 Au sputtering and electrical contacting

After transferring the lamella to the substrate, it is necessary to create Ohmic electrical contacts from the lamella to the pre-defined electrical contacts of the substrate. We achieve this by sputtering a metallic layer over an area covering the lamella and contacts. The first step in this process is to create a mask with Kapton tape to expose only the desired area during the sputtering process. The sputtering recipe typically includes an initial low energy etching of 120 s to clean the surface of the lamella, followed by the deposition of a sticking layer of 3nm of Ti, and a final layer of 200nm of Au (other metals like Pd were also used in this thesis). Figure 2.14 shows the result of a sputtering step. Having deposited the metallic layer, the next step is to attach wires to the pre-defined electrical contacts, which are meant to be used as voltage and current leads for the transport experiments. To this end we use a two-component silver epoxy (Epotek® EE129-4), which provides very good electrical and mechanical connection. It requires curing at 150 °C for one hour. The DuPont 4929N paint can also be used for contacting purposes although its mechanical bonding is weaker than the H20E. Usually, the wires used for electrical contacting are made of high purity silver with with a small diameter ($\approx 25 \mu\text{m}$), although for particular purposes like high magnetic field measurements, twisted pairs of copper wires can also be used (see figure 2.14). Once the metallic layer is deposited and the wires are attached, the sample is ready for the final microstructuring in the FIB.

2.5.2.3 FIB microstructuring

In the following I describe the main steps in the microstructuring process taking a "U" shape device as an example. Figure 2.15 shows a schematic illustration of the process flow.

- **Drawing the desired pattern:** in this step we design the pattern that we want to mill into the lamella, leaving some extra space in the design to account for the beam diameter and the additional polishing step to be carried out later. It is recommended to extend the cuts well beyond the edges of the lamella to guarantee that we mill all the way through the material and avoid any possible electrical shortcuts. This is particularly important on the side of the undercut since the bottom of the lamella could be wider than the top (due to the slope of the undercut cross section) and remain "hidden" in the glue. We should try to maximize the area of the contacts, aiming for an area of at least $10\mu\text{m} \times 10\mu\text{m}$.

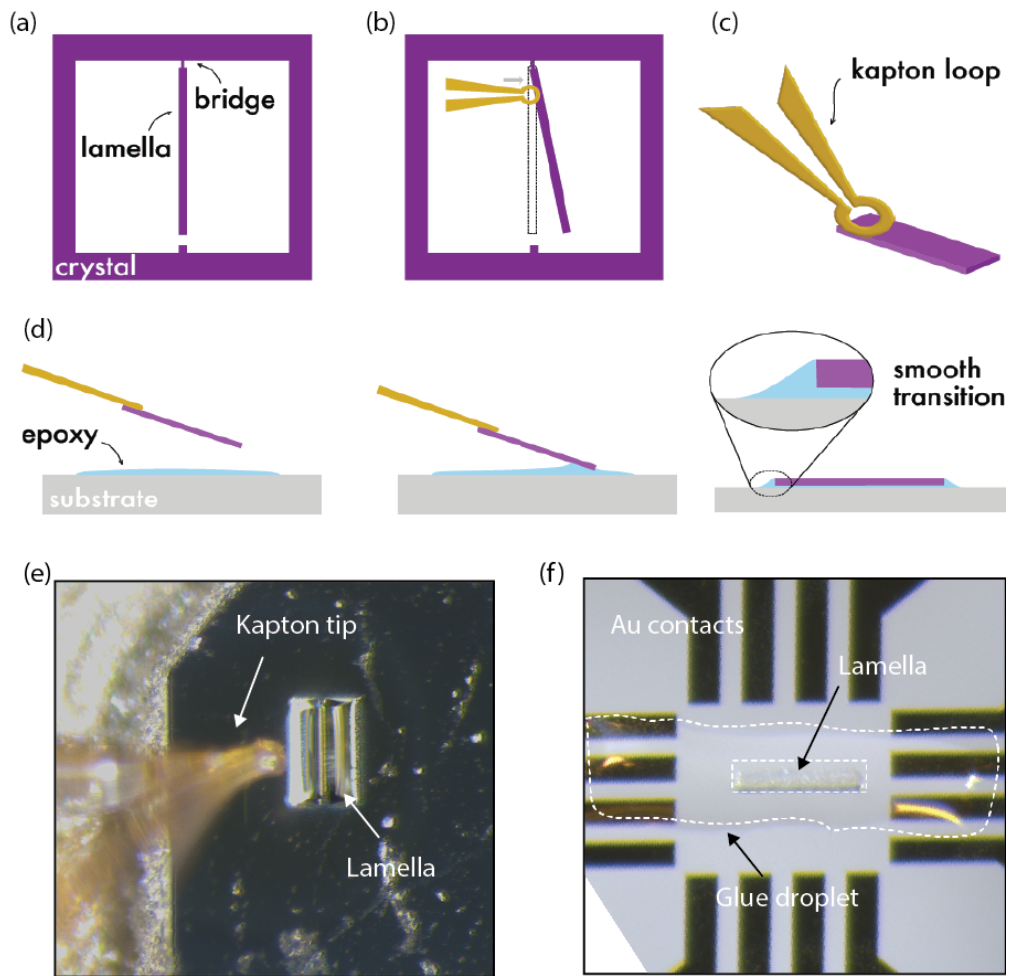


Figure 2.13: **The lamella *ex situ* transfer process.** (a) Top view of a finished lamella. (b) With a gentle push, the Kapton tip is used to break the bridge connecting the lamella to the parent crystal. Ideally, the lamella should stay electrostatically attached to the tip. (c) Optimal positioning of the lamella for transferring. (d) Sequence of steps to lower the lamella into the epoxy droplet. It is important to create a smooth transition from the glue droplet to the top edges of the lamella. (e) Photograph of a Kapton tip approaching a finished lamella. (f) Photograph of a lamella after it was lowered into the epoxy droplet. (a)-(d) are taken from [55].

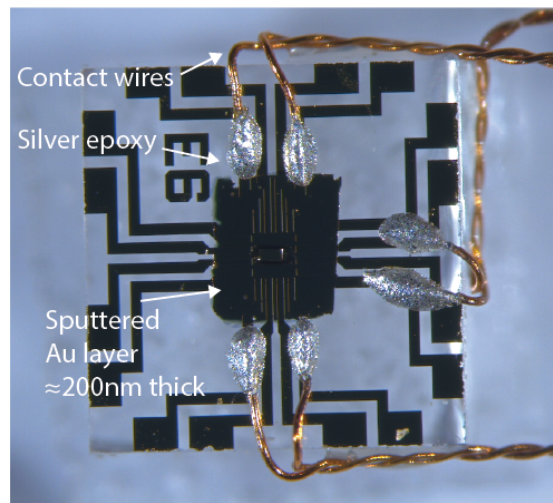


Figure 2.14: **Au coating and placing of the contact wires.** After transferring the lamella, a Au layer is deposited by sputtering and wires are attached with silver epoxy to form electrical contacts.

- **Au removal from top of the lamella:** after defining the pattern of the device, we need to remove the Au from those areas where current will flow, while keeping Au on top of the contacts. Usually, a polygon pattern is used to create the appropriate pattern shape. The optimal FIB settings for a smooth removal of Au depend on the target material, but in most cases it is recommended to use small accelerating voltages and currents. Ideally, one should observe an even removal of Au over the pattern with a clear contrast change once the whole layer is depleted. For some materials, including PtSn_4 and Cd_3As_2 , the top irradiation during the Au removal can lead to a roughening of the surface of the lamella. The avoidance of this effect might require further tuning of the beam parameters although it might be difficult to eliminate completely.
- **Milling the pattern:** to mill the final pattern we usually choose small currents but not so small as to make the patterning excessively long. 30kV and currents in the range of 1nA-7nA are suitable for patterning. Too large a current would mean a large beam diameter that could remove too much Au from the contacts or mill through undesired parts of the device, specially if fine features (like the voltage narrow nozzles) are involved. It is important to check that the milling is done until the glue or substrate beneath the lamella is clearly visible. The patterns in this step are milled in parallel to minimize re-deposition.
- **Polishing the faces of the microstructure:** using the same principle as in the polishing section, we smooth the faces of our device to achieve homogeneous and well defined current paths along the parts of the device we are actively measuring. CCS patterns with small currents are the better option.
- **Removing Au to define electrical contacts:** to define individual electrical contacts to

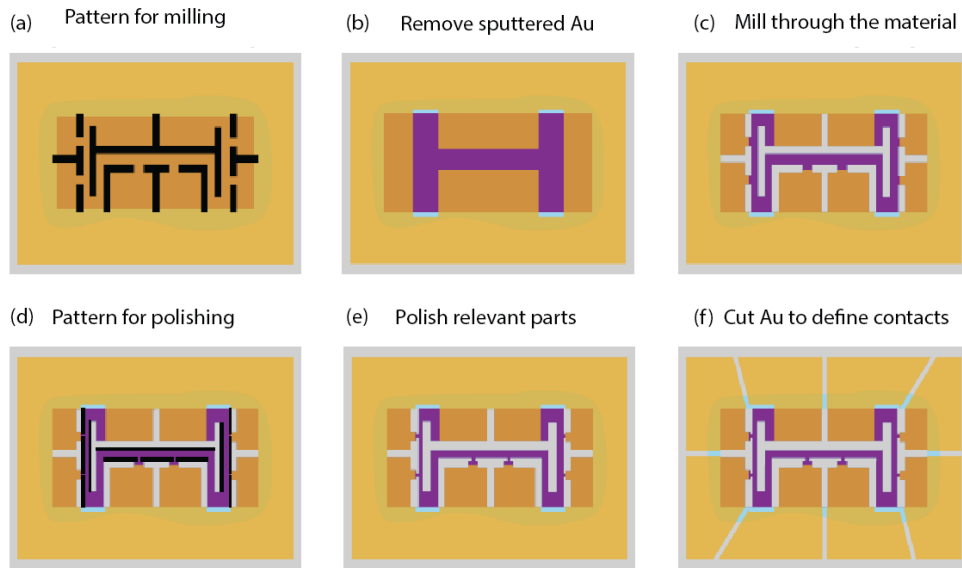


Figure 2.15: **Process flow of the FIB microstructuring procedure for glue-mounted samples.** (a) The first step is to create the desired pattern for milling (shown in black), which in this case is a "U" microstructure. (b) Next, the sputtered Au layer is removed from the parts of the device where current flows, thus avoiding undesired shortcuts. (c) After this, the pattern from (a) can be milled. (d) and (e) The sections of the device being measured are polished and the voltage contacts are narrowed down. (f) Finally, Au is further removed to define the current and voltage contacts associated to each wire. Figure taken from [55].

the attached wires, we must remove parts of the Au layer. Close to the sample we should use small currents (4nA) to avoid damaging the microstructure but farther away from it we can use higher currents to speed up the process (60nA).

- **Label the microstructure and measure relevant dimensions:** finally, it is important to clearly label the microstructure by milling its name on the Au layer. For this, a Bitmap pattern is typically used. The final images of the device should be taken with high resolution and showing all the relevant dimensions, which are necessary for accurate resistivity measurements.

2.5.3 Free-standing microstructures

The procedure described in the previous section is a successful way to prepare microstructures for their physical characterization in transport experiments. However, the use of glue to fix the lamella to the substrate can have the disadvantage of subjecting the sample to a unknown strain landscape originating from the differential thermal contraction between the substrate and the material of interest. This can have important consequences in the transport behaviour of strain-sensitive materials (see, for example, [40]), which is particularly relevant for TMSs given the way in which strain gradients can potentially affect their electronic properties.

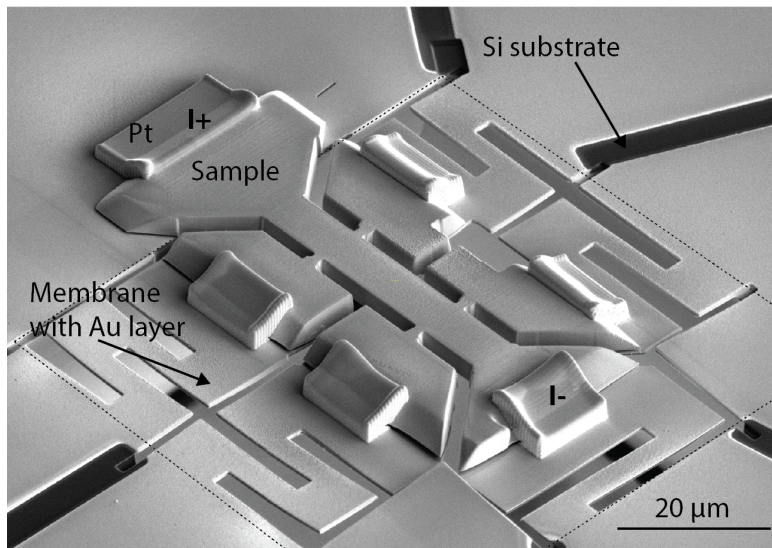


Figure 2.16: **SEM image of a PtSn_4 free-standing microstructure.** The PtSn_4 sample is suspended on a thin SiN membrane using FIB-deposited Pt contacts. The dotted line highlight the are covered by the thin SiN membrane. The meandering cuts are meant to serve as springs that release the accumulated strain.

In this section I present an alternative way to mount the sample that aims at minimizing the effects of strain by suspending the microstructure on free space and using a SiN thin membrane to form spring-like arms to contact the microstructure electrically. This free-standing mounting was used recently for the strain-sensitive material CsV_3Sb_5 [60] and was adapted and optimized in this thesis to explore potential strain effects on the TSM PtSn_4 . A typical six-point measurement device mounted in this way is presented in figure 2.16. The SiN membranes used for this design, also known as TEM windows, are commercially available and consist of a Si substrate with a central window where the thin membrane is located. Several window sizes and thicknesses are available, with the latter typically ranging from 10nm to 1000nm. The membrane used in figure 2.16 has a window size of $100\mu\text{m} \times 100\mu\text{m}$ and a thickness of 100nm. These kind of membranes are a standard element in many applications and have been shown to be chemically inert and mechanically robust. In the following I present the fabrication details of the free-standing devices, whose process flow is schematically presented in figure 2.17.

The preparation of the lamella is similar to the one previously described in section 2.5.1, with two main differences: there is no need to finely polish the lamella and the two bridges should be left uncut after the undercut. Once the lamella is prepared in this way, we use the micromanipulator to transfer it *in situ* to a copper grid or TEM holder (see figure 2.17 (a)). The first step to do this is to sharpen the tip of the micromanipulator by using relatively high currents (60nA) and rotating the micromanipulator around its axis to have a well defined conical tip. Next, we make a CCS pattern (15nA) to have the tip with a side ($3\mu\text{m}$ - $5\mu\text{m}$ long, for example) that is parallel to the face of the lamella. After this, we can approach the lamella

and use the FIB-induced deposition to weld it to the tip of the micromanipulator. Typically, the micromanipulator is attached on the upper left side of the lamella. After welding the tip, we proceed to cut the bridges and carefully lift the lamella without hitting the trenches. The micromanipulator is then retracted and we move the stage to where the TEM grid is located. There we attach the lamella using FIB deposition one more time and cutting the tip of the micromanipulator. In this position, we proceed to finely polish the lamella in the way described in section 2.5.1. Next, take the sample out of the FIB and flip the TEM grid horizontally to position the lamella for microstructuring (see figure 2.17 (b)). One advantage of having the sample on the TEM grid is the elimination of redeposition issues since the milled material is immediately pumped away. It is convenient to mill the edges of the lamella at a steep angle in order to have a smooth bevelled edge for the Pt deposition necessary in the later stages. For example, in the P-FIB system, milling at a tilt angle of 7° will create a 45° bevel. During this step, a small bridge is left uncut to hold the lamella to the TEM grid. One additional feature to consider when designing the microstructure pattern is to leave small bridges joining the different current and voltage contacts. This is done to secure the structural integrity of the sample during the transfer process (see figure 2.17 (h)). After milling the desired pattern, the lamella is again attached to the micromanipulator following the same general guidance as in the previous paragraph. It is very important that no part of the micromanipulator sits at a lower position than the bottom of the lamella. Once the lamella is welded to the micromanipulator, the bridge holding the lamella to the TEM grid is cut, the micromanipulator is retracted and we move the stage towards the membrane.

Before placing it into the FIB, a Au layer is deposited over the membrane and contact wires are attached to the substrate in the same way described in . Once inside the instrument, it is important to use a higher voltage and current for SEM imaging in order to have a clear contrast between the Si substrate and the thin membrane. Typical values used were 20kV and 1.6nA, respectively (compared to the usual 5kV and 0.8nA). These settings are crucial since the visualization of the membrane is not possible using the FIB but only the SEM. This requires a high degree of coincidence of both beams to confidently and precisely mill the patterns at the desired positions. The first of these cuts is shown schematically in figure 2.17 (c). It is a rectangular cut at the edge of the Si substrate that is meant to accommodate the central part of the six-point device. CCS patterns and currents in the range of 1nA-4nA are suitable for milling through the membrane. Using the CCS options is important since the line by line milling avoids having parts of the membrane curl up or potentially breaking away while milling and landing on undesired parts of the substrate. Once the rectangular cut is made, we can bring in the sample, carefully lower it down at the desired position and weld it to the substrate and membrane (see figure 2.17 (d) and (e)). A key point during this step is to have the lamella transferred as flat as possible onto the substrate. One possible strategy to help achieve this is to perform the transfer not at a tilting angle of 52° , where the substrate is nominally perpendicular to the ion beam, but at an angle a few degrees smaller, for example, 50° (the exact values will depend on the particular positions of the lamella and substrate). In this way, we can see when the part of the lamella farthest from the micromanipulator welding

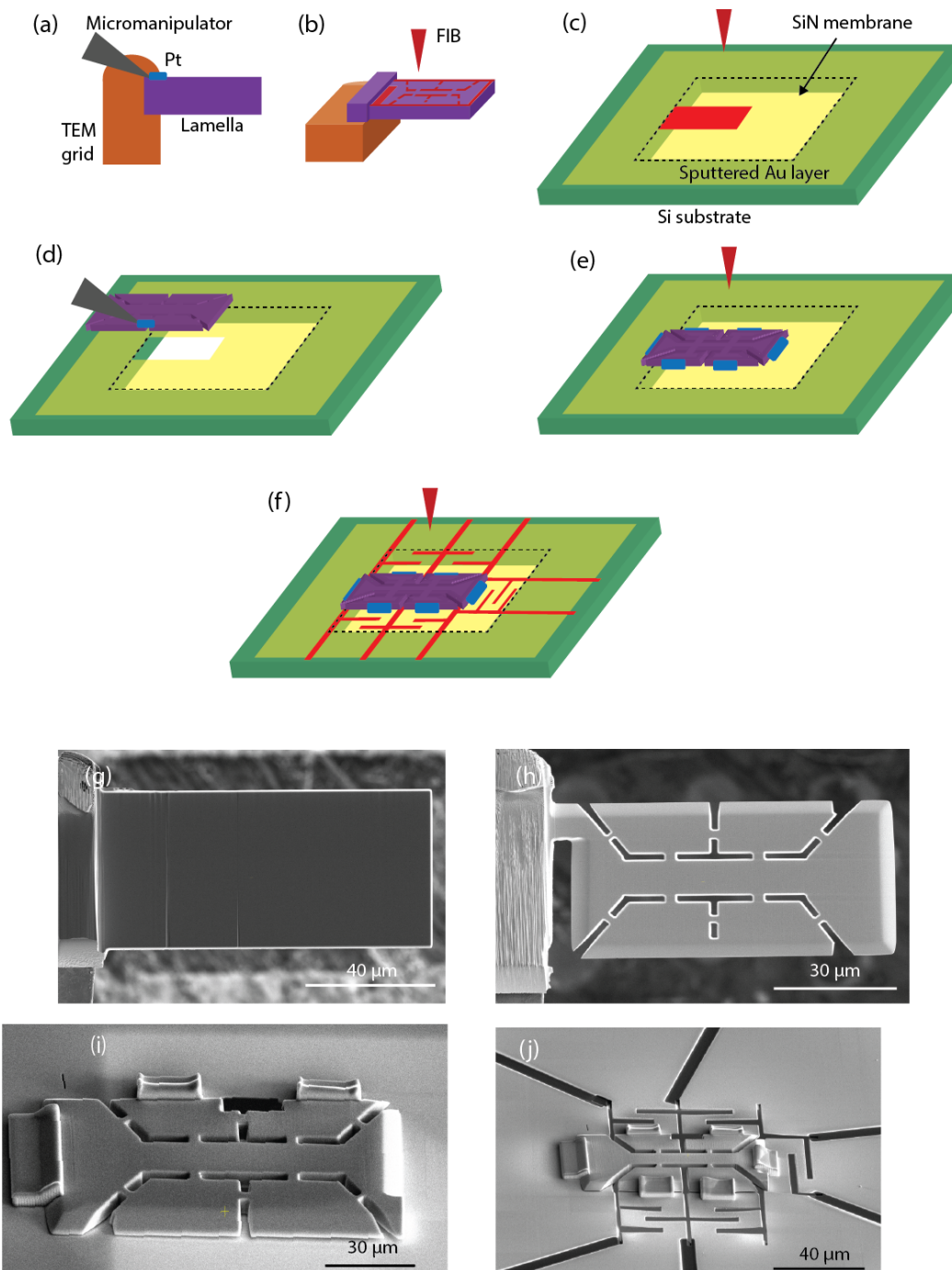


Figure 2.17: **Main steps in the lamella *in situ* transfer process to a thin membrane**. (a) The lamella is lifted from the parent crystal and attached to a TEM grid using the micromanipulator. (b) The TEM grid is placed horizontally and the desired pattern is milled through. After milling, the lamella is attached horizontally to the micromanipulator. (c) An opening is milled on the Au-sputtered membrane. (d) The sample is lowered down precisely on top of the opening milled in the previous step (e) attached to the substrate and membrane using FIB-deposited Pt contacts. (f) Finally, Au is removed to define current and voltage contacts. (g)-(j) SEM images of some of the steps described before for a PtSn₄ microstructure.

point first touches the substrate and we can make sure that the gap between lamella and substrate is gradually closed as we continue to lower the lamella and push it down onto the substrate. Although it is likely that a small gap remains between some parts of the sample and the membrane (see figure 2.17 (i)), reducing its size is advantageous to achieve a smooth and strong Pt deposition to weld down the sample. After having welded all the contacts, we can mill away the small bridges left for the structural integrity of the sample during transfer. Next, we can cut the patterns defining the spring-like arms on the membrane and finally, mill away the Au layer to delineate the electrical contacts (see figure 2.17 (f)).

2.6 Conclusions and outlook

In this chapter I introduced the FIB as a tool for the fabrication of microstructures. The versatility of this fabrication technique combined with the use of different sample mounting options as well as sample designs were exploited to address the main experimental questions explored during this thesis. Working transport devices made from the TSMs of interest were successfully fabricated and the control parameters of the FIB were optimized to minimize some of the artifacts associated with FIB machining, like surface curtaining and damage. In this sense, the work presented in this chapter represents a valuable addition to the class of materials and sample designs that can be investigated with the FIB, including, for example, the first ever PtSn₄ microstructures.

3 Experimental methods

3.1 Introduction

From an experimental point of view, the goal of this thesis is to study the electronic properties of FIB-machined microstructures of TSMs at low temperatures. This chapter provides a general description of the main experimental methods used to meet such a goal. I begin by discussing the working principle of the lock-in amplifier technique to perform AC electrical measurements, followed by a brief presentation of the bath-cryostat systems with superconducting magnets that were used to reach temperatures down to 1.5 K and magnetic fields up to 18 Tesla. These are well established techniques in the the field of electrical measurements at low temperatures and can be readily applied to FIB-machined microstructures. Furthermore, the use of microstructure provides several significant experimental advantages compared to typical macrocrystals. For example, by reducing the cross section of the current-carrying path in the microrstructures, much higher current densities can be reached without using excessively high currents, making higher signal to noise ratios easier to achieve without causing too much Joule heating (which is proportional to the square of the current). This is particularly relevant for some TSMs like PtSn_4 that are extremely good conductors at low temperatures, showing resistivities as low as $0.04 \mu\Omega \text{ cm}$ [61] . Similarly, the reduced dimensions of the microstructures make them less vulnerable to spurious effects such as undesired thermal or magnetic field gradients and eddy currents.

Later in the chapter I discuss the characterization of samples via X-ray diffraction techniques, including both parent macrocrystals and the lamellae extracted from them for subsequent micromachining. Here again, the use of the FIB to cut the lamellae along the desired crystallographic directions as well as to mount them for further X-ray screening allows for greater verification of the cristallinity of the sample, avoiding issues like the presence of flux inclusions or internal cracks that might not be easily detectable in a macrocrystal. Finally, I introduce the finite element method as a tool to simulate the electrical and mechanical situation in the microstructures. This tool has proven to be very helpful to understand the behaviour of the microstructures in realistic experimental conditions, shining light in aspects like the extend

of current jetting effects [62] or the role of the epoxy glue used to mount the lamellae to the substrates [55].

3.2 AC transport measurements

Electrical AC measurements constitute a fundamental characterization technique that can provide very valuable information about the band structure of a material and different electronic phenomena, such as scattering mechanisms and quantum oscillations, that are susceptible to exhibit potential topological-related effects. In this regard, the lock-in amplifier technique has become a powerful tool to apply AC currents to the sample of interest and detect the usually very small AC signal that can be buried in the background noise. In the following I will briefly describe the basic principles of this technique and give some details regarding the experimental set-up adopted for the electrical characterization of the microstructures.

3.2.1 Working principle of the lock-in amplifier

The lock-in measurement is based on the so called phase sensitive detection (PSD) where an excitation with a certain reference frequency is used to probe the sample and the lock-in is synchronized to detect the response of the sample at that exact reference frequency. In this way, noise signals at frequencies other than the reference one are rejected and do not affect the measurement. In the context of electrical characterization, the noise comes from different sources such as the ubiquitous $1/f$ electronic noise, thermoelectric voltages and the external noise created by motors, computer screens, or other electrical equipment in the vicinity of the experiment. Figure 3.1 shows a schematic depiction of a typical lock-in amplifier measurement. An sinusoidal excitation voltage signal $V_{ref}(t) = V_{ref}\sin(\omega_{ref}t + \theta_{ref})$, which serves as the reference signal as well, is generated by the lock-in amplifier internal oscillator (an external source can also be used) and applied to the sample. For resistivity measurements, a four-point configuration is adopted to avoid unwanted signals from the current leads mixing with the actual sample's response. The resultant signal coming from the sample $V_{sam}(t) = V_{sam}\sin(\omega_{sam}t + \theta_{sam})$ is first amplified by a differential amplifier and then multiplied by the reference signal. This is the key point in the PSD step since the resultant signal V_{PSD} has the following form:

$$V_{PSD}(t) = \frac{1}{2} V_{sam} V_{ref} \cos([\omega_{ref} - \omega_{sam}] + [\theta_{sam} - \theta_{ref}]) - \frac{1}{2} V_{sam} V_{ref} \cos([\omega_{ref} + \omega_{sam}] + [\theta_{sam} + \theta_{ref}]) \quad (3.1)$$

The first component depends on the difference in frequency ($\omega_{ref} - \omega_{sam}$) and the second on the sum ($\omega_{ref} + \omega_{sam}$). Using the condition $\omega_{ref} = \omega_{sam}$ the first component represents a DC component proportional to the signal of interest, while the second component can be filtered

out by a low pass filter. The filtered output V_{PSD1} will then be:

$$V_{PSD1} = \frac{1}{2} V_{sam} V_{ref} \cos(\theta) \quad (3.2)$$

where $\theta = \theta_{sam} - \theta_{ref}$ is defined as a phase difference. One way to eliminate the dependency on this parameter is to add a second mixer using a reference signal that is 90 degrees out of phase with $V_{ref}(t)$ (i.e. a cosine function). A similar procedure as that leading to equation 3.2 results in:

$$V_{PSD2} = \frac{1}{2} V_{sam} V_{ref} \sin(\theta) \quad (3.3)$$

By the virtue of knowing the magnitude of V_{ref} , one can determine the outputs of two phase sensitive detectors to obtain the components $X = V_{sam} \cos(\theta)$ and $Y = V_{sam} \sin(\theta)$, from which the magnitude and phase difference of the sample's signal can be computed as:

$$\begin{aligned} R &= \sqrt{X^2 + Y^2} \\ \theta &= \arctan\left(\frac{Y}{X}\right) \end{aligned} \quad (3.4)$$

The X and Y quantities are termed the "in-phase" and quadrature components, respectively. Notice that R measures the signal amplitude and does not depend on the phase between the signal and lock-in reference. Ideally, in the filtering step one would expect the filter to have full transmission only for the DC signal of interest and zero transmission for all other frequencies (see figure 3.1 (e)). Unfortunately, such idealized filters are impossible to realize in practice. In reality, all low-pass filters have a certain band of frequencies that are transmitted and are characterized by some roll-out function in the frequency spectrum. One simple approximation is the RC filter with the following transfer function [63]:

$$H(\omega) = \frac{1}{1 + i\omega\tau} \quad (3.5)$$

where ω is the frequency, $\tau = RC$ is the time constant, R the resistance and C the capacitance. By increasing the time constant, the bandwidth of the filter decreases and the output DC signal becomes more steady as fewer higher frequencies affect the measurement. However, the settling time of the RC filter also increases with increasing τ , which will slow down the output response. In general, the chosen value of τ is a compromise between obtaining a signal that is not too noisy and doesn't take too long to measure.

3.2.2 Electrical set-up for transport measurements of microstructures

In this thesis, the multichannel SynkTek MCL1-540 lock-in amplifier was used to perform the AC transport measurements. The frequency of the excitation signal was selected to avoid coupling to the main frequency of nearby power lines (50 Hz in Switzerland). Usual values chosen were 77 Hz and 177 Hz. These frequencies are located in a clean white noise region

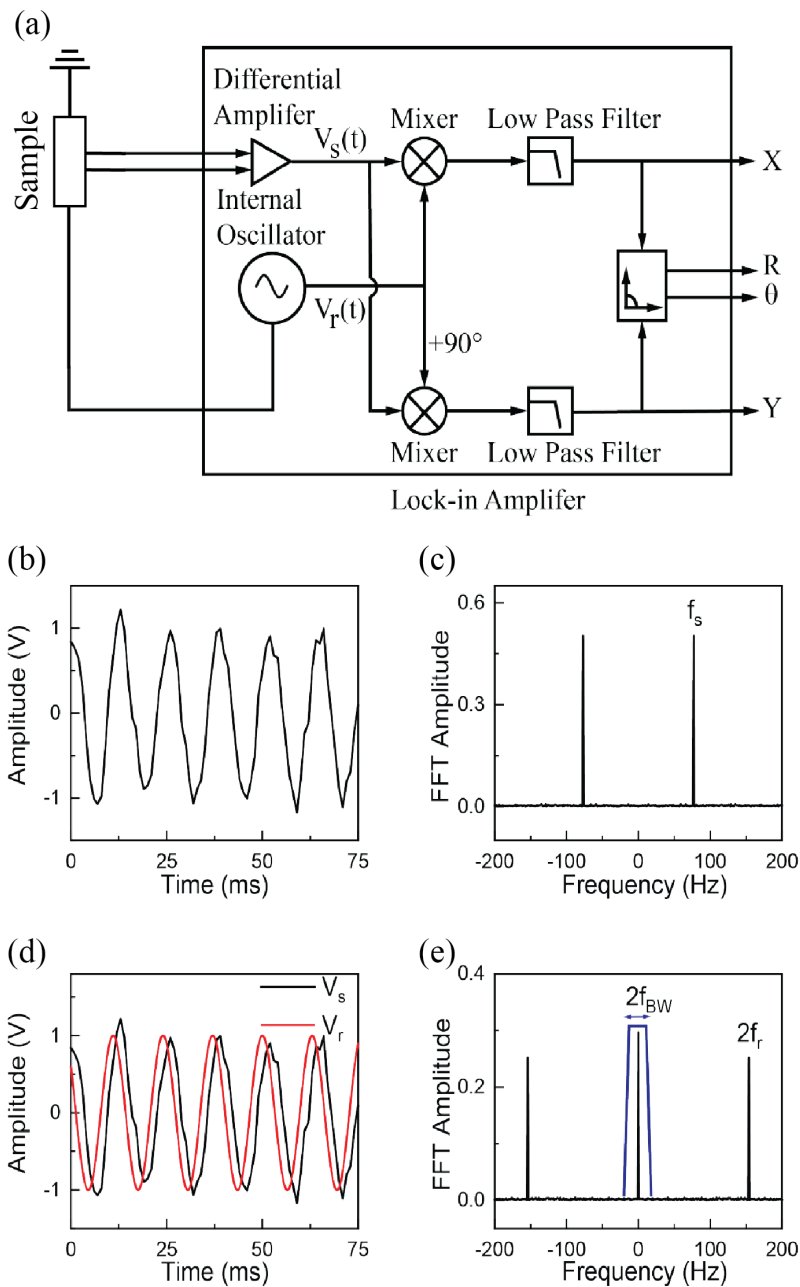


Figure 3.1: Lock-in amplifier working principle . (a) Schematic depiction of the main elements in a lock-in amplifier. See the text for further details. (b) An sinusoidal input signal displayed over time with a frequency of 77 Hz and superimposed noise (which for reasons of clarity has been chosen to be small in amplitude), and (c) its corresponding FFT. The peak at negative frequency is just a consequence of expressing a real sinusoidal in terms of complex exponentials. (d) An input signal V_s (black) and a reference signal V_r (red) of the same frequency. (e) FFT of the resultant signal after mixing (multiplying) the signals displayed in (d). The amplitude of the original input signal is related to the DC component, while the AC components must be excluded using filter with a narrow band of f_{BW} around zero. Image taken from [64].

above the $1/f$ noise. A typical time constant of 1s was also chosen with noise levels in the order of $10^{-9}\text{V}/\sqrt{\text{Hz}}$ commonly obtained. During the experiments, the value of the phase difference θ was checked to be close to 0° (or equivalently 180°). This is important since a value that departs too much from zero might indicate that the voltage signal coming from the sample is not completely resistive in nature but might be affected by spurious inductive or capacitive couplings.

Lock-in amplifiers can be used directly as a current source by combining its output voltage signal with a shunt resistor. If the shunt resistor is chosen to be of much higher resistance than that of the sample plus wiring, the current through the sample is approximately the ratio of the output voltage and the shunt's resistance. The model SynkTek MCL1-540 actually incorporates an output channel designed for current measurement based on this idea [65]. Furthermore, the model also allows for active AC regulation of the current using either a proportional–integral–derivative (PID) control loop or an exponential approach to the final value with a selectable weight factor. Figure 3.2 (a) shows the basic electric connections when using this AC regulation option to maintain a constant current through the sample in a four-point resistant measurement. This was the most common configuration for the transport experiments performed for this thesis. However, having an active regulation is not always the most favourable option. For example, if the sample exhibits big quantum oscillations, undesired modulations of the current could become prominent. In cases like this one, the configuration shown in 3.2 (b) was adopted, where an external shunt resistor is added to the circuit and no active AC regulation is chosen.

One issue that can persist when performing a four-point measurement with the lock-in technique is the existence of the so-called common mode errors, which come from undesired voltage signals common to both voltage leads in the four-point configuration. This voltage is still present in the output of the differential amplifier used to magnify the signal from the sample and its quantified by the common-mode rejection ratio, CMRR, of the amplifier, normally expressed in decibels. Typically, a common-mode signal of 100 mV is only cancelled to 1 part in 10^5 by an amplifier with a CMRR of 100 dB and so it will appear as if there is still a $1\mu\text{V}$ differential signal at the input. Common-mode voltages are more prominent when the sample is very conductive and the wiring to the cryostat is much more resistive. To combat this situation the configuration presented in figure 3.2 (c) was used. As before, a shunt resistor is used to regulate the applied current and another channel of the lock-in amplifier is used to measure the voltage drop across the shunt and calculate the current more accurately. The shunt is however coupled to the current channel via a transformer. This coupling helps minimizing the common mode errors in the measurements by providing a low impedance path to ground which prevents unwanted high frequency signals contained in the source voltage from reaching the transformer secondary.

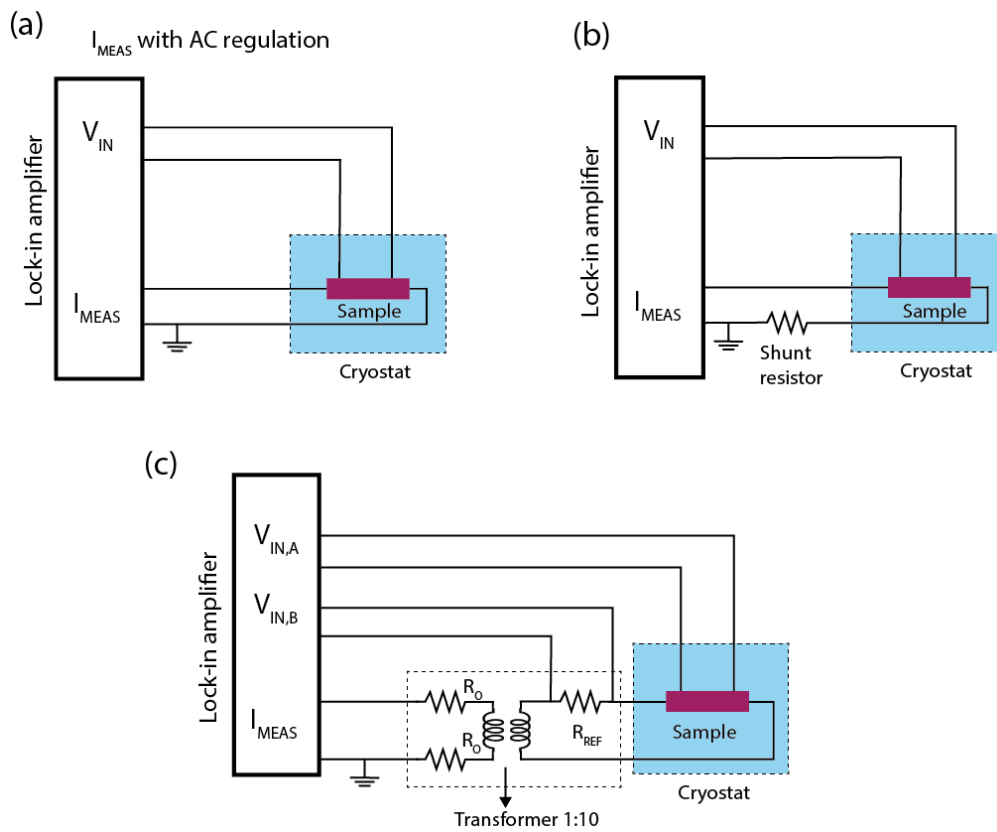


Figure 3.2: **Schematic diagram of electrical configurations used for transport measurements.** (a) SynkTek MCL1-540 active AC regulation option. (b) I_{meas} output connected to a highly resistive shunt resistor for sourcing current. (c) Incorporation of a transformer break-out box to reduce the effects of common mode errors. Typical values of the resistors were $R_0 = 500 \Omega$ and $R_{REF} = 10 \Omega$.

3.3 Low temperature and high magnetic fields

Since Kamerlingh Onnes first liquified helium more than one hundred years ago, the use of low temperatures has been crucial for the understanding of new ground states in quantum matter, ranging from superconductivity, to quantum Hall effects and other more recently observed topologically non-trivial states. Without low temperatures these effects would be smeared out by the surrounding thermal energy and become unobservable. Similarly, the use of high magnetic fields to probe many of these exotic states has become key for their understanding since coupling to electromagnetic fields is one of the ways in which electrons and other charge carriers can be manipulated. Standard cryogenic technologies are based on cryogenic liquids, mainly liquid N_2 and liquid He^3/He^4 , and can be categorized into three temperature zones:

- Liquid He^4 temperature zone, with a base temperature of about 1.5 K that can be reached by controlling the vapor pressure of the He^4 .
- Liquid He^3 temperature zone, with a base temperature of around 300 mK that can be reached by controlling the vapor pressure of He^3 .
- Dilution refrigerator temperature zone, with a base temperature of around 10 mK, that can be reached through the continuous dilution process of a He^3/He^4 mixture.

In this thesis, the vast majority of experiments were performed in the first zone, with a few additional ones performed in the last zone. This is why in the following I will concentrate on discussing He^4 based cryostats with a superconducting magnet, and only briefly mention the dilution refrigerator set-up later.

3.3.1 Physical properties measurement system (PPMS)

The physical properties measurement system (PPMS) from Quantum Design is a He^4 -based instrument with a base temperature of 2K and maximum magnetic field of 14T that is designed to perform electrical, magnetic and thermal measurements. It combines some automated features, like temperature and field control, with a considerable degree of flexibility to accommodate the particular needs of any given experiment. Figure 3.3 shows some the main parts of the instrument, including the Dewar containing the cryogenics and the internal probe hosting the magnet and the sample. Many of the same design principles for these parts are applied to the other system used during this thesis (see next section), which is why the PPMS serves here as a general example. Figure 3.3 (a) shows the schematic cross section of the PPMS Dewar. It includes an outer jacket of liquid nitrogen, sandwiched between superinsulation layers and the internal liquid helium He^4 bath. This nitrogen layer helps to reduce the helium consumption considerably. The principle for cooling is to continuously pump helium from the bath through an impedance assembly and into the cooling annulus. The helium vapor flows through the annulus at rates that are automatically controlled by the Model 6000 PPMS Controller, which incorporates the main pump, to achieve the desired temperature.

Figure 3.3 (b) shows a more detailed scheme of the cross section of the PPMS probe with some of its main components. The innermost region is the sample space contained in the sample chamber, which is itself surrounded by the cooling annulus. Vacuum and superinsulation prevent heat exchange between the sample chamber and the helium bath. The vacuum space between the outer and inner vacuum tubes contains reflective superinsulation to minimize radiative power loss into the helium bath. At the base of the sample chamber sits the 12-pin connector that contacts the puck where the sample is mounted. Two thermometers and a heater are immediately below the sample puck connector for optimal temperature control and monitoring. With this design and the accompanying software control, temperatures with a typical accuracy of $\pm 0.5\%$ can be achieved with very linear behaviour and rates ranging from 0.05K/min to 8K/min approximately.

The magnet in the PPMS is a superconducting solenoid composed of a niobium–titanium alloy embedded in copper. It sits on the outside of the probe, so it is always immersed in the liquid helium. The magnet is connected to a so-called persistent switch. The persistence switch is a small heater on the magnet wire that drives a section of the magnet non-superconducting. It allows the magnet controller to drive current through the magnet leads and change the magnetic field. When the heater is turned off the entire magnet can remain superconductor, which eliminates the need drive a current during constant field operation and reduce the boil-off rate of helium. This state is referred to as the persistent mode of the magnet. The PPMS offers the possibility of using a rotator probe that fits into the PPMS sample chamber to obtain information about angular dependence on electrical transport in a magnetic field. The samples are mounted on two special pucks that can be rotated along two different axes, respectively, perpendicular to the magnetic field. The rotator probe incorporates a thermometer just below the sample for precise temperature measurement.

3.3.2 Other systems used

Another of the systems used during this thesis was the Oxford Instrument He⁴ bath cryostat with a 18T superconducting magnet and a variable temperature insert (VTI) for 1.5K - 300K operation. The basic principle of operation is the same as in the PPMS although the design of the cryostat is different in some aspects. For example, instead of an impedance assembly, a needle valve is used to draw helium from the bath to the VTI. In addition, the system integrates a so-called lambda-point fridge to cool the magnet down to 2.2K and extend the magnetic field range. This fridge consists of a needle valve to control the flow of liquid helium and a chamber with a pumping line to reduce the vapour pressure above the liquid and hence cool it further down [67]. The liquid is drawn from the main helium bath which is separated from the lambda fridge by the main magnet support plate. Only a small proportion of the liquid in the main bath is cooled by the lambda plate, reducing the cost of operation. The Oxford cryostat also has a rotator probe so angular studies under a magnetic field are possible (along one axis perpendicular to the axis of the field).

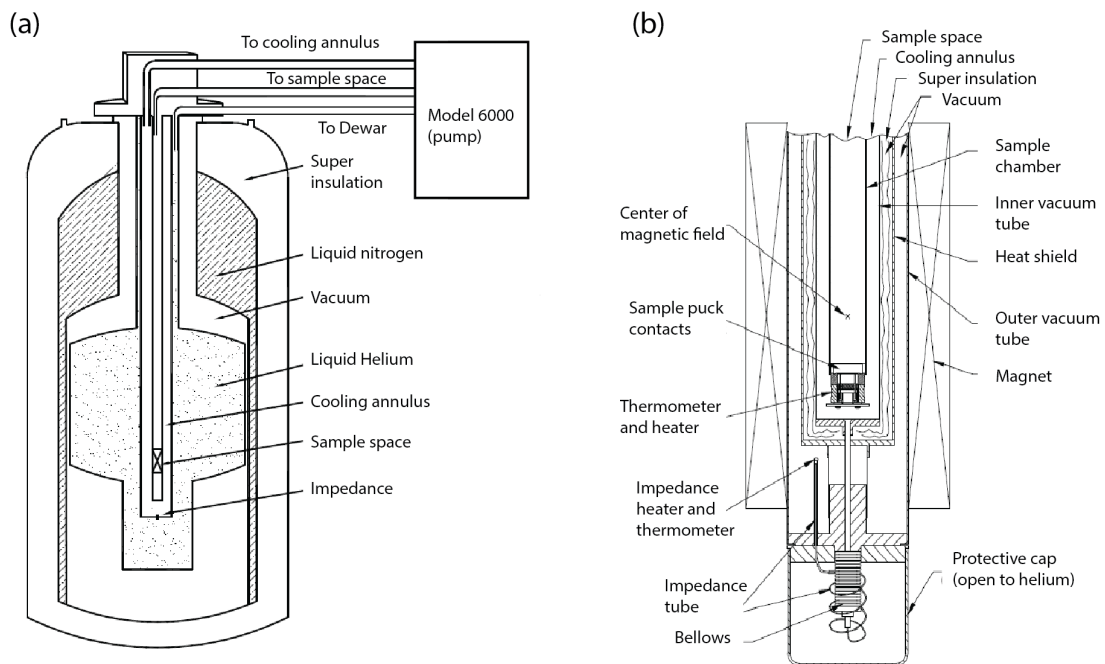


Figure 3.3: **Technical drawing of the PPMS system.** (a) Dewar cross section with gas and vacuum controls (b) Cross section of the probe with some of its major components. Adapted from [66].

Finally, a couple of experiments were performed in the Bluefors LD250 dilution refrigerator, which incorporates a 9T magnet. A detailed review of the working principle of a dilution refrigerator can be found in [68]. The main principle is approximately the following: when a mixture of He^3 and He^4 is cooled below a critical temperature, it separates into two phases. The lighter "concentrated phase" is rich in He^3 , and the heavier "dilute phase" is rich in He^4 . The concentration of He^3 in each phase is temperature-dependent. The evaporation of He^3 from the concentrated phase into the dilute phase is what provides the cooling power. Very roughly, the concentrated phase of the mixture is pretty much liquid He^3 , and the dilute phase is effectively He^3 gas. The evaporation of He^3 from the "liquid" phase to the "gas" phase cools the sample. A very important feature of the system used for this thesis is a two-axis rotator that was incorporated to the instrument, allowing to determine a 2D map the magnetoresistance along two different degrees of freedom.

3.4 X ray characterization

As mentioned previously in chapter 2, the alignment of crystalline samples via X ray techniques is a key preliminary step for the fabrication of microstructures. In this section I will outline the main procedures used for the X-ray characterization of the materials studied in this thesis.

3.4.1 MultiWire Laue back-reflection diffractometer

In the Laue back-reflection method a polychromatic X-ray source is used to irradiate a stationary single crystal and produce the desired diffraction pattern. Different atomic planes diffract different wavelengths of radiation, allowing multiple diffraction spots to be observed simultaneously in the Laue pattern and used for subsequent indexing. The great advantage of the Laue method is that a single pattern, since it is the result of the diffraction of many planes, clearly reflects the symmetry of the entire crystal and can thus be used to determine its orientation. The instrument used in this thesis was the MultiWire MWL120 diffractometer at the Institute of Physics in EPFL (see figure 3.4 (a)). The machine employs a tungsten tube to produce the polychromatic X-rays, and a collimator to direct them at the sample. After the X-rays are "back-scattered" from the sample, they are collected by a detector with an active area of 30cm×30cm. The main working parameters of the machine are the applied voltage, which determines the emission profile of the tungsten tube; and the applied current, which determines the number of X-rays produced. A higher voltage might produce more diffraction spots while a higher current tends to produce better defined patterns, however too high values of these parameters can also increase the background noise and diminish the lifetime of the tungsten tube. For this thesis, typical values of 20kV and 35mA (together with a 0.5 mm pinhole size collimator) were used to obtain diffraction patterns with good contrast. This instrument is typically operated to screen rather large single crystals that are fixed on a motorized goniometer using clay or some other glue. However, the single crystals studied in this thesis were usually too small to be mounted in this way and rotated *in situ* with the motorized goniometer since the alignment with the X-ray beam was constantly lost. More importantly, such a mounting procedure is not optimal when transferring the crystal to the FIB after the alignment is done. Ideally, the transfer should be made directly from one instrument to the other without the introduction of ill-defined variables like the thickness and irregularity of the glue droplet fixing the crystal, which could cause an undesired misalignment when cutting the crystal with the FIB. To avoid such effects, a manual goniometer was chosen to hold the sample (see figure 3.4 (b)), which in turn was already placed on the SEM stub used for the FIB. Figure 3.4 (c) shows an image of a sample mounted in this way, taken with the internal camera of the system.

Figure 3.5 outlines the typical procedure carried out for the alignment of a crystal, which in this case is the TSM TaAs. Translating the alignment angles obtained from the X-ray screening to the position parameters of the FIB stage is a crucial step in the fabrication process. To this end, a sapphire chip is placed next to the crystal of interest to serve as a clear reference when cutting the crystal with the FIB. These sapphire chips are also single crystals and their diffraction patterns can be used to check their orientation. Consequently, the first step in the alignment procedure is to orient the sapphire chip in a convenient manner, in the case of figure 3.5 (a) this means with one of its edges aligned horizontally, which is corroborated by the symmetrical diffraction pattern thus obtained (see figure 3.5 (b)). The TaAs diffraction pattern at this initial position is shown in figure 3.5 (c). TaAs has a tetragonal crystal structure and although the crystal are not always very regular, they tend to exhibit larger flat faces

along the (001) planes and some well defined edges along the [100] ([010]) directions. To take advantage of these features the crystal in figure 3.5 (a) was mounted with its larger flat faces parallel to the SEM stub and its straight edge as parallel as manually possible to the edge of the sapphire chip. The diffraction pattern presented in figure 3.5 (c) is consistent with the tetragonal structure and the expected rough orientation, showing a 4-fold symmetric pattern that is not yet completely centered. Figures 3.5 (d) and (e) show successive changes in the rotation and tilting angle of the goniometer until the crystal is finally oriented. The software QLaue was also used to analyse the diffraction patterns. This software simulates the scattering pattern of single crystals based on their lattice parameters. The simulated pattern is moved until it matches the initial pattern, like the one in figure 3.5 (a), and then it is moved again until it matches the desired orientation. The corresponding rotation and tilting angles can be compared to the actual ones obtained with the diffractometer, which typically resulted in extremely good agreement. These angles are then translated to the position parameters of the FIB stage using simple trigonometric relations.

3.4.2 SuperNova single crystal diffractometer

As mentioned in the previous section, the Laue back reflection method is not optimal for the characterization of single crystals that are small, which is commonly the case for many of the newly synthesised topological materials of interest. Moreover, the use of a polychromatic source makes it, in general, unsuitable for quantitative analysis and the determination of crystal structure and lattice parameters. To measure those properties the approach of applying a monochromatic source on a rotating crystal to obtain the diffraction patterns is usually much more advantageous. Taking this into consideration, the SuperNova single crystal diffractometer from Agilent Technologies (now Rigaku Oxford Diffraction), located at the Institute of Chemical Sciences and Engineering in EPFL (see figure 3.6 (a)), was also employed to characterize some of the samples studied in this thesis together with a procedure for sample mounting and transfer to the FIB that was optimized to achieve the best possible crystal orientation. The SuperNova diffractometer is particularly well suited for screening small crystals by optimizing, among other things, the production of a very bright and well focused X-ray beam. It is equipped with both copper (Cu) and molybdenum (Mo) monochromatic sources exhibiting their characteristic $K\alpha$ radiation of wavelength $\lambda = 1.54\text{\AA}$ and $\lambda = 0.71\text{\AA}$, respectively. However, the Mo source was always chosen for the crystal studied here since its more energetic X-rays can penetrate deeper into inorganic materials compared to their softer Cu-generated counterparts, increasing the sampled volume and facilitating the screening of thicker and/or strongly absorbing samples.

In the SuperNova diffractometer, the sample (a Cd_3As_2 crystal in this case) is mounted on a XRD magnetic holder with a metallic pin, as shown in figure 3.6 (b). As before with the Laue method, the translation of the orientation information to the FIB stage is of paramount importance. With this in mind a couple of steps were taken: a costume-made SEM stub with a small magnet was used to fit the XRD holder directly into the FIB after the X-ray screening,

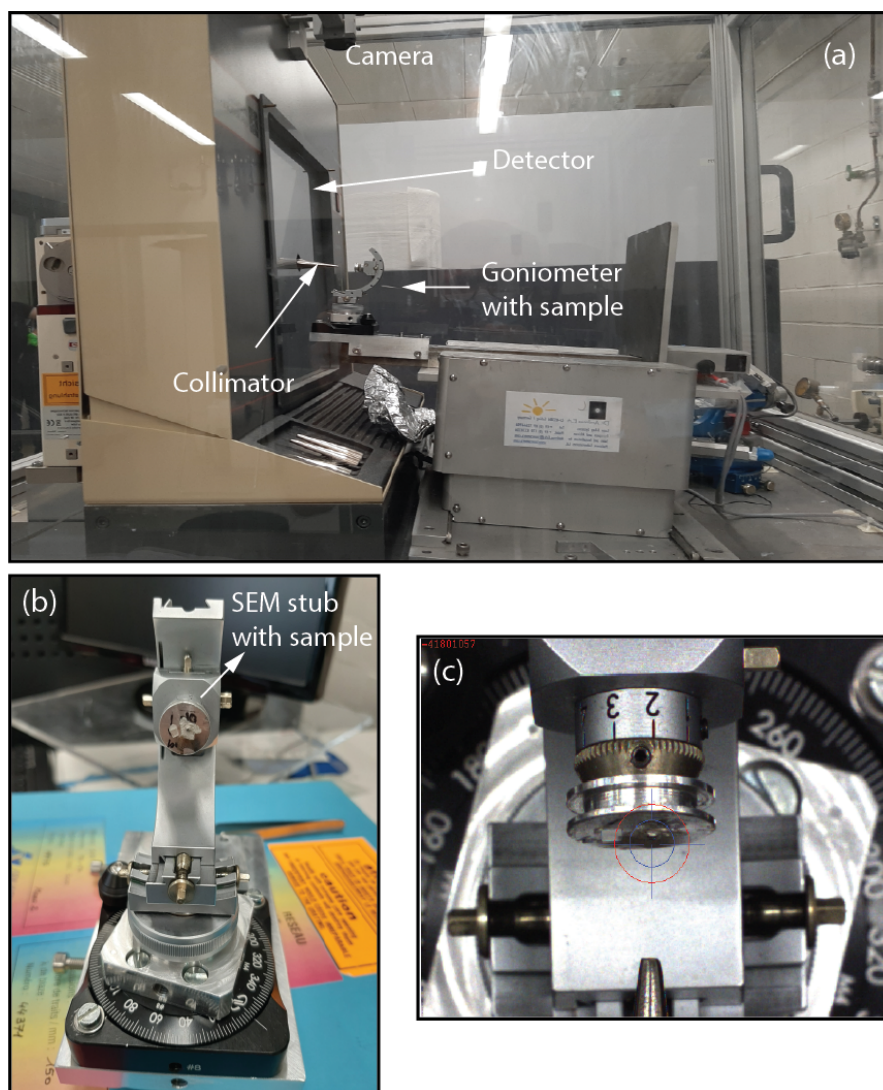


Figure 3.4: **MWL120 Multiwire back-reflection Laue system.** (a) Experimental set-up for crystal orientation. (b) Goniometer with sample mounted. (c) View of the sample inside the machine from the system's camera.

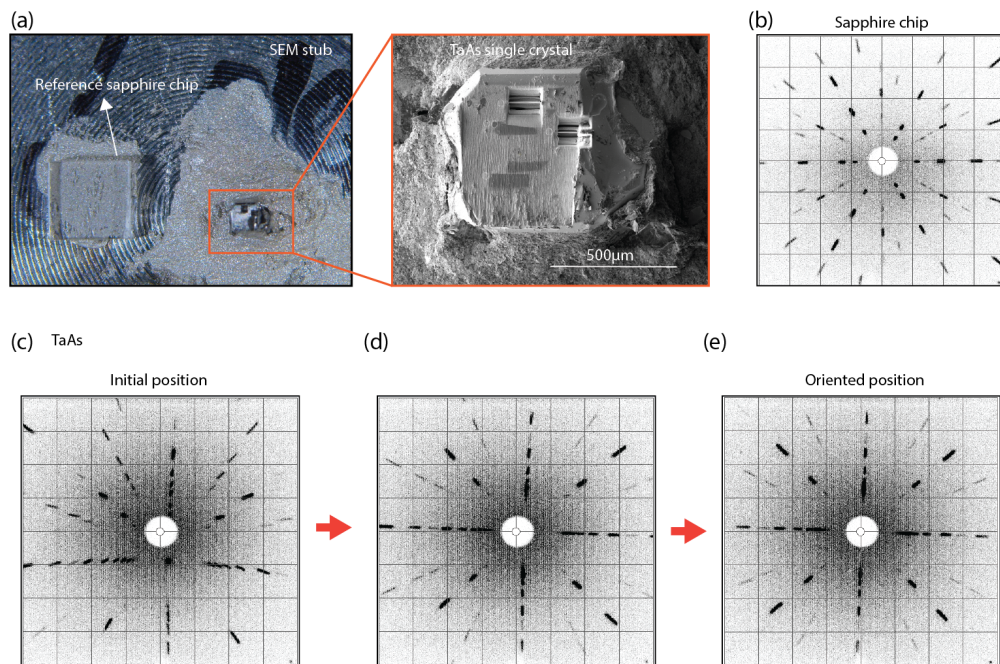


Figure 3.5: **Crystal orientation with the Laue system.** (a) As a reference, a sapphire chip is mounted next to the TaAs crystal to be oriented. (b) Diffraction pattern of the aligned sapphire chip. (c) Successive rotations to align the TaAs crystal.

the sample was mounted on the metallic pin using the conductive H20E epoxy to ground it properly to the FIB stage, and a vertical mark was previously milled into the metallic pin with the FIB (highlighted in figure 3.6 (b)) to serve as a reference when inserting back the crystal for final FIB cutting. In the final result of the screening, a total set of 360 frames (one frame per angle) was obtained showing the different crystallographic directions for every position of the crystal as it is rotated along the axis of the metallic pin. Figure 3.6 (c) highlights three of such frames, where the reference mark can also be seen. These "crystal movies" were analysed with the CrysAlis^{Pro} software, which also displays the crystal structure information. In the case of the Cd_3As_2 crystal of figure 3.6 (b) and (c), the results indicated a tetragonal unit cell with lattice parameters $a = 1.26\text{nm}$ and $c = 2.53\text{nm}$ consistent with the centrosymmetric space group $I4_1/acd$, which are in very good agreement with values reported previously for this compound[69, 70].

After the screening of the crystal is finished, it is taken directly to the FIB to cut the lamellae along the desired crystallographic directions. The vertical mark is used to translate the relevant orientation angles to the FIB stage position. In general, unless the position of the crystal in the metallic pin is very convenient for the desired crystallographic directions, the translation of these angles can be rather cumbersome and more importantly, after such translation is made, the final position of the crystal in the FIB might not be ideal for digging and polishing lamellae. Unfortunately, this problem is made worse by the use of the XRD magnetic holder inside the FIB since its size limits some of the stage movements to avoid crashing into the

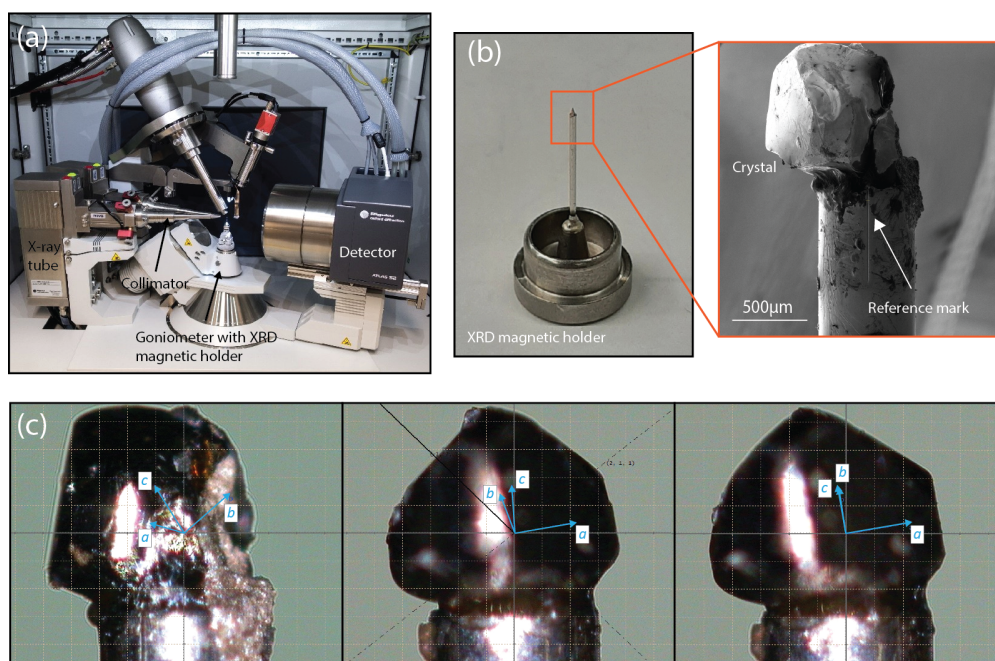


Figure 3.6: **Agilent SuperNova diffractometer system.** (a) Experimental set-up with main components of the instrument. (b) Mounting of a Cd_3As_2 macrocrystal for the determination of crystal orientation. (c) Crystal directions identified.

electron and ion columns. The strategy taken to avoid this issue altogether was to expose the desired crystallographic faces first by cutting large sections of the crystal with the FIB and then, after taking it out of the FIB, removing the crystal from the metallic pin and mounting it on a regular SEM stub with the desired face flat on the SEM surface. In this way, the lamellae can be prepared following the exact procedure described in 2.5.1. Moreover, the cut lamella can itself be screened to verify its orientation. This is shown in figure 3.7 for a PtSn_4 sample. The lamella is transferred *in situ* with the FIB to the metallic pin using the micromanipulator and FIB-induced deposition to attach it to a sharpened copper piece that had previously been fixed to the top of the pin (see figure 3.7 (a)). Figure 3.7 (b) shows the results of the screening, confirming that the lamella was cut along the desired crystallographic directions and exhibits the lattice parameters $a = 6.42\text{ nm}$, $b = 11.36\text{ nm}$ and $c = 6.38\text{ nm}$, consistent with the expected orthorhombic structure characteristic of this material [61].

3.5 Finite elements simulations

The finite element method (FEM) is a numerical technique used to find approximate solutions to boundary value problems for partial differential equations. It's become a standard tool of analysis in many fields of science and engineering given its ability to model very complex shapes to perform structural, thermal and electrical simulations, among many others. In this section I give a broad overview of the method, more detailed descriptions can be found

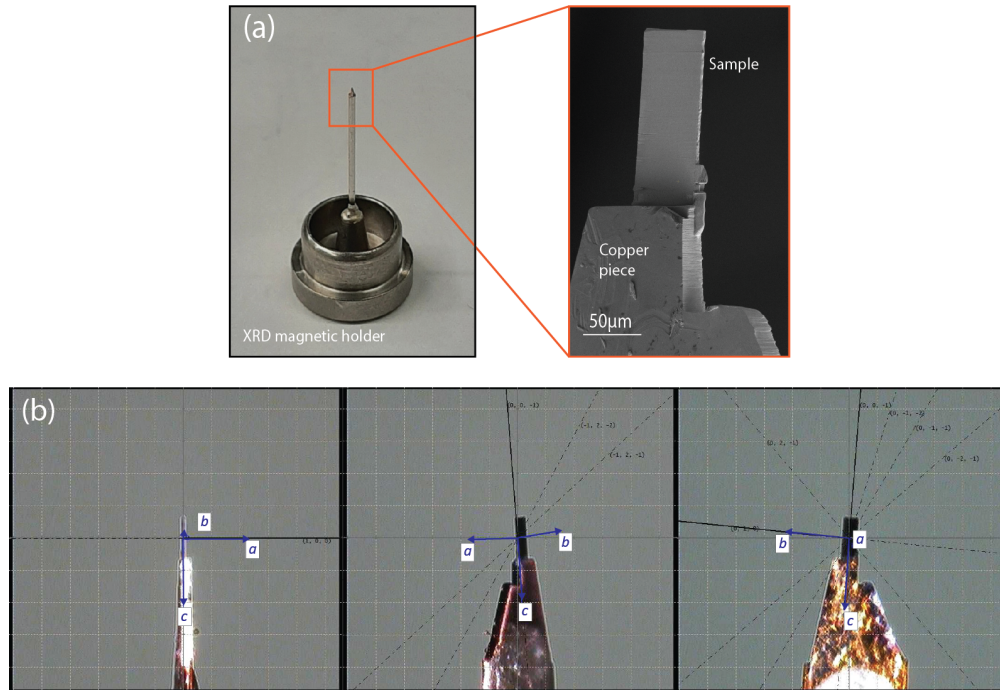


Figure 3.7: **X-ray characteritaion of a single crystalline lamella.** (a) Mounting of a PtSn₄ lamella for the determenation of its orientation. (b) Crystal directions identified.

in [71] and [72]. A key step in the FEM is the subdivision of a complicated geometry into simpler blocks called finite elements (see figure 3.8), which are connected at nodes on their boundaries. The collection of discretized elements and nodes is called the mesh and the process of its construction is called meshing. For each finite element an approximate solving function of to the global differential equation is found, which is dependent on the values held by the function at the nodes. The relationships between the nodes are then used to assemble all the elemental solutions into a solution over the whole geometry. The general algebraic equation to be solved can be written in the form:

$$\{F\} = [K]\{u\} \tag{3.6}$$

where $[K]$ is called the global stiffness matrix, F denotes the load vector and $\{u\}$ the unknown vector to be found, for example, the displacement. Most commercial algorithms solve this equation not by inverting the global stiffness matrix, which is rather computationally inefficient, but by using methods that approximate iteratively the vector $\{u\}$ like the conjugate vector gradient method.

For this thesis, mechanical and electrical simulations were performed using the FEM software COMSOL. A typical simulation of the electrical situation of a microstructure in a transport experiment is presented in figure 3.9. A geometry with the actual dimensions of the the microstructure is first constructed and a fine mesh is then used to solve the relevant elec-

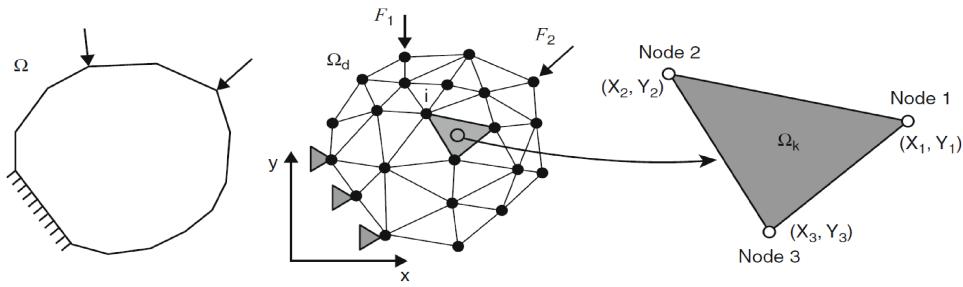


Figure 3.8: **Finite element method.** Discretization of a domain Ω into a partition Ω_d with triangular elements Ω_k , including forces and boundary conditions. Image taken from [73].

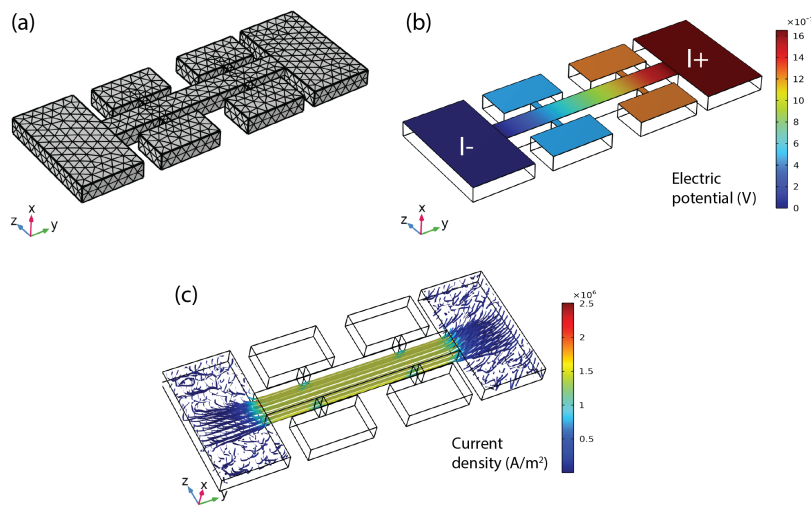


Figure 3.9: **COMSOL simulation of a microstructure** (a) A fine mesh is created to discretize the geometry of the microstructure. (b) Resulting electrostatic potential distribution after sourcing a current through one of the contacts. (c) Streamlines of the current density for the same simulation shown in (b), highlighting the uniformity of the current in the central bar of the microstructure.

tromagnetic equations numerically, given the desired boundary conditions (see figure 3.9 (a)). For example, in figure 3.9 (b), a current of $10 \mu\text{A}$ is injected from the top of one of the current contacts, while the other is kept grounded. For the simulations COMSOL allows to input the required materials' constants such as elastic moduli, electrical conductivity, thermal expansion coefficient, etc, or to sweep values of any given parameter like the components of a conductivity tensor, in case anisotropy studies are desired. From the simulations several quantities can be obtained like the electric potential distribution (see figure 3.9 (b)) or the streamlines of the current density (see figure 3.9 (c)), among many others, which can provide valuable information regarding the design of the microstructure.

4 Theoretical background

4.1 Introduction

It is a remarkable fact that the 100-year-old theory of quantum mechanics can still be expanded in often unexpected ways to explain new phenomena. The inclusion of topological concepts in the quantum mechanical theory of solids that began in the 1980's using toy models has been validated by the discovery of materials like graphene and TIs in the 2000's. In this chapter I will introduce some of the main concepts that have been developed to study topologically non-trivial states of matter, with emphasis on the description of topological effects in the transport properties of TSMs. After briefly reviewing some fundamental aspects of the band theory of solids, I will describe the characterization of band crossings using a topological index and the further classification of these crossings into Weyl and Dirac types. This characterization already represents an extension to gapless systems of the description initially applied to gapped systems like TIs. It is worth mentioning that such classifications are a very active field of research and new aspects in the topological identification of materials are still being explored. For example, recently the concept of quasi-symmetry was introduced to describe approximate symmetries that could stabilize band crossings by enforcing finite yet perturbatively small energy gaps [74]. Later in the chapter I will discuss the basic equations of electron dynamics under external magnetic fields, the theory of quantum oscillations and Weyl orbits and some of the transport characteristics of TSMs. The connection of some these phenomena to topology is particularly important since in an actual material both topologically trivial and non-trivial effects will be present at the same time and might even lead to similar features in their transport behaviour, e.g, additional phase factors in the quantum oscillation spectrum. Finally, I will discuss the concept of pseudo-fields induced by strain gradients in 3D Weyl systems. These pseudo-fields could provide a very convenient description of many physical effects in TSMs like the activation of the chiral anomaly or the redistribution of chiral charge, some of which have been observed in metamaterials but not in actual 3D materials.

4.2 Band theory fundamentals

At the heart of understanding the electronic properties of solids is a proper description of the behaviour of electrons inside the electric potential of the nuclei. In 1933 Sommerfeld and Bethe treated the problem quantum mechanically [75]. The solid was modelled as a potential well with infinite barriers at the surfaces and the movement of the electron, now treated as a wave, is determined by solving Schrödinger's equation. They found that the set of wave vectors \mathbf{k} associated with the electron wave functions forms a discrete set of values called the k -space or reciprocal space. In this space, the total number of states available for conduction is temperature dependent and can be calculated using a distribution $f(T, E)$ that computes how the charge carriers arrange in the available states, and a density of states (DOS) $D(E)$ that computes the number of states available per unit energy. In this fashion, the number of charge carriers per unit volume is given by:

$$n = \int_0^{\infty} D(E) f(T, E) dE \quad (4.1)$$

The density of states depends on the dimensionality of the system and the corresponding dispersion relation, that is, the $E(\mathbf{k})$ functional form. Since the electrons are fermions, subject to Pauli's principle, the distribution function is the Fermi-Dirac one:

$$f(T, E) = \frac{1}{e^{(E-\mu)/(k_B T)} + 1} \quad (4.2)$$

Within the approximation of free and independent particles, the electrons would fill all the k -states available up to a certain energy value called the chemical potential μ . At $T = 0$ this energy value is called the Fermi energy E_F and defines the constant energy surface known as the Fermi surface (FS), which characterizes the metallic state. Transport phenomena, including the flow of electric current, are dominated then by two mechanisms: the driving force of the external fields, like the electric field, and the dissipative effect of the scattering of carriers by phonons and defects of the crystal. Most of the charge carriers participating in the transport will be those close to the Fermi energy. When considering the periodicity of the atoms in a crystal, the overlap of the electrons' wave functions leads to the formation of energy bands $E_n(\mathbf{k})$, where n is the band index. Given the translational symmetry of the Hamiltonian $H(\mathbf{k})$ describing the system (a consequence of the periodicity of the electric potential of the atoms), the eigenfunctions can be described by a plane wave modulated by a periodic function $u_{n,k}(\mathbf{r})$, resulting in the so-called Bloch waves: $\psi_{n,k}(\mathbf{r}) = e^{i\mathbf{k}\cdot\mathbf{r}} u_{n,k}(\mathbf{r})$ [76, 77]. The relation $E_n(\mathbf{k})$ is also periodic in reciprocal space so we only need to consider the so-called first Brillouin zone (BZ). Based on the existence or not of an energy gap and the position of the chemical potential in the structure of $E_n(\mathbf{k})$, materials can be classified as insulators, semi-conductors and metals.

As mentioned in chapter one, the novel properties of TSMs are related to their linearly dispersive bands and the existence of crossing points or nodes (see figure 4.1). Electrons in

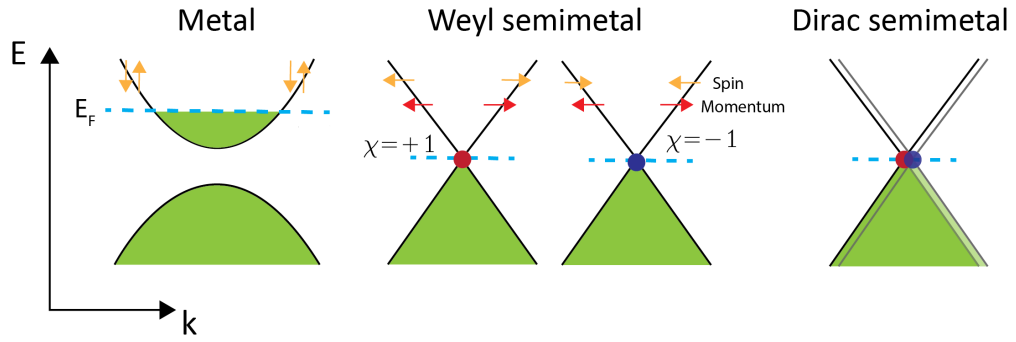


Figure 4.1: **Schematic band structure of a normal metal and Weyl and Dirac semimetals.** DSMs can be considered as the superposition of WSMs of opposite chirality, protected from mixing by crystal symmetries.

a normal metal such as copper move approximately like in free space, with an energy of $E(k) = (\hbar k)^2/2m$, where $\hbar k$ is the momentum and m is the effective mass. If a force is applied, for example, through the application of an electric field, the electrons populate states of higher momentum and experience a change in their group velocity, which is proportional to the slope of the band. This is the typical behaviour of a massive particle. TSMs on the other hand, by virtue of their linearly dispersive bands, have a fixed slope, which means that even if subjected to a force, they would still move with the same velocity. This is analogous to the behaviour of massless particles. Additionally, in regular metals there is no preferred relative direction between spin and momentum, with bands showing spin up and down degeneracy, whereas in TSMs chirality dictates a spin-momentum locking as schematically depicted in figure 4.1. Furthermore, the linear band structure of 3D TSMs also leads to a DOS $D(E) \propto E^2$ instead of the $D(E) \propto E^{1/2}$ characteristic of 3D parabolic bands, which naturally influences their transport behaviour. The reason why most materials don't exhibit linear touching bands is that, in general, bands tend to avoid crossing and open up a gap but gapless structures can still arise in some materials.

4.3 Band crossings and topological invariants

Under certain conditions there is the possibility of having band crossings in the structure of $E_n(\mathbf{k})$, that is, energy degeneracies. In general, Bloch states with the same symmetry cannot be degenerate at some arbitrary point in the BZ. Usually, when these bands approach each other, they hybridize and open up gap [78]. However, if there are other symmetries obeyed by the system's Hamiltonian, like crystal related symmetries such as rotations and reflections, these degeneracies can be stable. This is a general result from quantum mechanics, where one can classify the eigenstates of a given Hamiltonian according to how they transform under such symmetry operations. In this fashion, one can decompose the Hamiltonian into smaller representations, each of which corresponds to a given energy value. If those representations are not one dimensional, then its energy value is degenerate. This degeneracy can happen

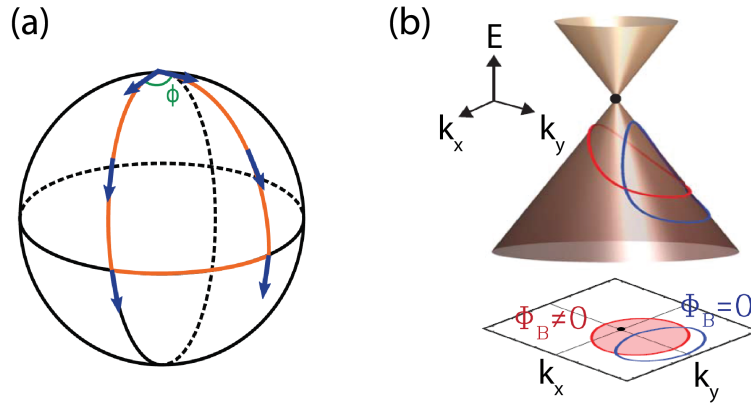


Figure 4.2: **Berry phase and paths in the Brillouin zone.** (a) Parallel transport of a vector on a closed path on a sphere rotates the vector by an angle ϕ . (b) Closed trajectories around a band crossing showing a non-trivial or trivial Berry phase Φ_B depending on whether the trajectories enclose or not. Adapted from [80].

either as a result of a fine-tuning of some parameter of the Hamiltonian (in which case it is called *accidental degeneracy*) or as a consequence of a larger symmetry not taken into account. A well known example is the classification of states of the hydrogen atom according to their angular momentum, which stems from the fact that the potential is centrally symmetric. In the case of solids, the band structure itself and the classification of states into Bloch waves is a consequence of the translational symmetry.

4.3.1 Berry phase

The basis to express the topological character of band crossings is the concept of the Berry phase, which is a general geometrical phase acquired by the wave function when traversing closed paths in parameter space [79]. To illustrate this phase, let's consider a closed path ζ on a sphere, as illustrated in figure 4.2 (a). If we choose a tangential vector and move it along ζ while keeping it locally parallel to itself, it will be rotated by an angle Φ when completing the path. This angle will depend on the geometry of the surface on which we move the vector so it is called a geometrical phase. Analogously, in solids, the Berry phase is a geometrical phase associated to the evolution of the wave function on a closed path over the BZ.

To define the Berry phase, consider a system described by a Hamiltonian that depends on time through a set of parameters represented by the vector $\mathbf{R}(t)$, that is, $H(\mathbf{R}(t))$. Let $E_i(\mathbf{R})$ be the eigenvalues of this Hamiltonian and $|\psi_i(\mathbf{R})\rangle$ its eigenfunctions. When $\mathbf{R}(t)$ undergoes a cyclic evolution such that $\mathbf{R}(0) = \mathbf{R}(T)$ over a certain closed path ζ , the corresponding eigenstate Ψ_n will remain an instantaneous eigenstate (this result is called the *adiabatic theorem* in quantum mechanics) but might pick up a geometrical phase factor such that its time evolution is given

by:

$$\Psi_n(t) = e^{\Phi_B(t)} \exp\left[\frac{-i}{\hbar} \int_0^t dt' E_n(\mathbf{R}(t'))\right] |\psi_n(\mathbf{R}(t'))\rangle \quad (4.3)$$

The factor in the exponential is the conventional dynamical phase, while Φ_B is called the Berry phase. It can be shown that the Berry phase is given by following path integral over ζ :

$$\Phi_B = \oint_{\zeta} i \langle \psi_{\mathbf{R}} | \nabla_{\mathbf{R}} | \psi_{\mathbf{R}} \rangle \cdot d\mathbf{R} = \oint_{\zeta} \mathbf{A}_{\mathbf{R}} \cdot d\mathbf{R} \quad (4.4)$$

Where $\mathbf{A}_{\mathbf{R}}$ is called the Berry connection. This quantity is analogous to the vector potential in electromagnetism and one can also define an equivalent magnetic field called the Berry curvature $\Omega = \nabla_{\mathbf{R}} \times \mathbf{A}_{\mathbf{R}}$. Recalling Stokes' theorem, we can turn the integral into a surface integral of the Berry curvature:

$$\Phi_B = \iint \Omega \cdot d^2\mathbf{R} \quad (4.5)$$

Using again the analogy with electromagnetism, one can conclude that this quantity is also gauge invariant. The application of this formalism to the case of solids is immediate: the eigenfunctions are the Bloch states $\psi_{n,k}(\mathbf{r}) = e^{i\mathbf{k}\cdot\mathbf{r}} u_{n,k}(\mathbf{r})$ and the time dependant parameter is the momentum \mathbf{k} . The surface of integration is taken as the entire BZ, which, given its translational symmetry can be map to a torus. With this expression for the Berry phase we can finally define our topological index, which is called the Chern invariant C :

$$C = \frac{1}{2\pi} \Phi_B \quad (4.6)$$

The Chern invariant is only well defined over the entire BZ for insulators, where there is an energy gap in the band structure. However, it can also be extended to cases where there is a degeneracy in the bands. In that case the surface of integration must enclose the corresponding crossing point and is typically taken to coincide with the FS. One can show that in the case of TSMs, each node is characterized by a Chern number of $C = \pm 1$, meaning that they behave as monopoles of Berry flux with a chirality that is determined by the sign of C [9, 81]. Closed trajectories that enclose the crossing points will then be characterized by a non-trivial Berry phase that can manifest itself in various magneto-oscillatory effects like in graphene [80, 82, 83] (see figure 4.2 (b)). Furthermore, as shown by Nielsen and Ninomiya [84], the total monopole charge in the BZ has to be zero, which implies that the band-crossing points always come in pairs of opposite chirality.

Different types of TSMs can be distinguished based on some of the characteristics of the band crossings, such as its degeneracy or co-dimension (whether the band degeneracy is a line or a point). Another possible classification is based on the nature of the band crossing, whether it is symmetry enforced or results from a band inversion due to spin-orbit coupling (SOC). Within this last classification I concentrate on two types of TSMs: Weyl semimetals (WSMs)

and Dirac (DSMs) semimetals.

4.3.2 Weyl semimetals

In a WSM, two non-degenerate bands cross at discrete points, called Weyl nodes, showing a linear dispersion relation in all directions. In the simplest case, there can appear two of these nodes in reciprocal space associated to a different chirality. This new quantum number describes whether the spin of the fermions is locked parallel or anti-parallel to their momentum. This number is a conserved quantity in these systems and constitutes a new degree of freedom to encode and process information. The Hamiltonian describing these chiral Weyl fermions is

$$H = \chi \hbar v_F \boldsymbol{\sigma} \cdot \mathbf{k} = \chi \hbar v_F \begin{bmatrix} k_z & k_x - i k_y \\ k_x + i k_y & -k_z \end{bmatrix} \quad (4.7)$$

where $\chi = \pm 1$ is the chirality, v_F is the Fermi velocity and $\boldsymbol{\sigma}$ are the Pauli matrices. The existence of WSMs is conditioned by the breaking of either time reversal symmetry (TRS), $H(\mathbf{k}, s) = H(-\mathbf{k}, -s)$, where s is the spin and \mathbf{k} the crystal momentum; or inversion symmetry (IS), $H(\mathbf{k}, s) = H(-\mathbf{k}, s)$ [9, 10, 85]. Otherwise, the energy bands would be doubly degenerate at each \mathbf{k} point, the two Weyl nodes would coincide, and since the corresponding electronic states would have the same symmetries, they would tend to annihilate each other and open up a gap [86]. Since one of these symmetries must be broken, Weyl nodes can appear in a generic point in momentum space, and their existence does not rely on any additional crystalline symmetry of the system. This means that as long as the nodes are not brought to coincidence they are topologically stable. Using angle-resolved photoemission spectroscopy (ARPES), a technique based on the photoelectric effect that can give information on the energy and momenta of surface electrons, WSMs have been found such as TaAs [87], TaP [88], NbAs [89] and NbP [90].

4.3.3 Dirac semimetals

DSMs are characterized by the presence of Dirac nodes where two doubly degenerate bands cross and disperse linearly in all directions. They require the presence of both TRS and IS and can be considered as the superposition of two Weyl nodes of opposite chirality. Since, in general, this would lead to the annihilation of the nodes, additional symmetries are needed to realize a stable Dirac node. In three dimensions, two mechanisms have been identified to give rise to stable Dirac nodes in solids: firstly, the presence of the so-called non-symmorphic symmetries (a symmorphic symmetry is one which leaves at least one point of the real space crystal invariant. They are essentially point group symmetries of the crystal, such as reflection and rotation), which enforces the occurrence of the Dirac node at a high symmetry point of the BZ [12]. This type of DSM has not been experimentally observed. The second kind of mechanism relies on band inversion, induced by SOC, in the presence of an n -fold rotational

symmetry axis. This happens because the bands crossing each other can be associated to a different rotation eigenvalue. Along the direction of the the rotational axis, and in the presence of TRS and IS, all two-fold degenerate bands with different rotational symmetry representation lead to a stable four-fold Dirac node, which is the case in Cd_3As_2 [91]. The excitations around the nodes can be represented by the following Hamiltonian:

$$H = \hbar v_F \begin{bmatrix} \sigma \cdot \mathbf{k} & 0 \\ 0 & -\sigma \cdot \mathbf{k} \end{bmatrix} \quad (4.8)$$

This is analogous to the low energy structure of graphene, which is described by a Dirac equation in two dimensions. ARPES measurements have also shown the existence of DSMs such as Na_3Bi [92], ZrTe_5 [93] and most prominently Cd_3As_2 [94–96].

4.3.4 Bulk-boundary correspondence

The theoretical treatment described before has allowed us to classify different states of matter based on their topological character and to realise that at the interface of regions with different topological indexes, there must necessarily exist conducting edge states. This principle is known as the bulk-boundary correspondence and has been very useful in understanding TIs and, perhaps most notably, the integer quantum Hall effect and related phenomena [97–99], where electrons can only conduct along $1D$ channels at the edge. In the case of TSMs, the Fermi arcs connecting the nodes of different chirality are those edge states, now present as $2D$ surface channels as shown schematically in figure 4.3 (a). This relation to the presence of chiral nodes is what makes them different to other surface states: they are topologically protected, meaning that they cannot be destroyed through small perturbations or impurities. The presence of Fermi arcs is one of the hallmarks for experimentally observing TSMs and they have been confirmed via ARPES in various WSMs such as NbAs , NbP and TaAs (see figure 4.3 (b)).

4.4 Electronic transport under external fields

In this thesis I am interested in probing the topological character of TSMs through electrical resistivity measurements, and since in these materials both topological and non-topological properties cohabit, it is important to review some of the main concepts describing the charge transport in solids and how they are modified by the presence of topological effects.

4.4.1 Drude model

Close to 1900, before the quantum theory of the solid was developed, Drude described the metallic conductivity of solids considering the charge carriers as particles of an ideal classical gas in the solid. Although this idea is an oversimplification of the conduction mechanism, it still provides a good description for many materials and it is often used to characterize their

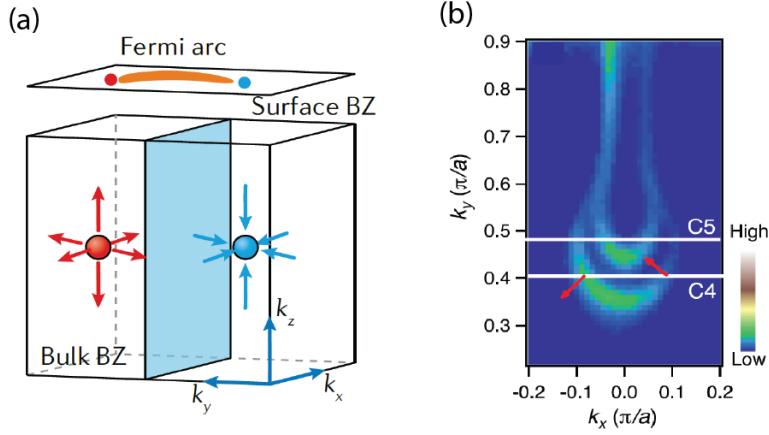


Figure 4.3: **Fermi arcs in Weyl semimetals.** (a) Fermi arcs can be viewed as the topologically protected states present between regions of different topological character. They appear as surface states connecting the projections of two Weyl nodes on the surface BZ. Taken from [13]. (b) ARPES results showing the existence of Fermi arcs in the WSM TaAs [100].

transport behaviour as a first approximation. For an ideal electron gas in an external electric field \mathbf{E} , the dynamics of the electrons is described by Newton's equation of motion:

$$m \frac{d\mathbf{v}}{dt} = -e\mathbf{E} - \frac{m\mathbf{v}_D}{\tau} \quad (4.9)$$

the dissipative effect of scattering is taken into account by the friction term $m\mathbf{v}_D/\tau$, where \mathbf{v}_D is called drift-velocity. Since v relaxes exponentially to its final value with a time constant τ after the external field \mathbf{E} is switched off, τ has the meaning of a relaxation or scattering time and can be considered the mean free time between successive collisions by the electron. For the stationary, one dimensional case ($dv/dt = 0$):

$$v_D = \frac{-e\tau}{m} E \quad (4.10)$$

so the current density in the direction of the field is:

$$j = -env_D = n\tau E = \frac{e^2 n \tau}{m} E \quad (4.11)$$

In this model n is the volume density of all free electrons and the mobility is defined as a proportionality constant between drift velocity and external field. The main result from Drude is that the electrical conductivity is given by:

$$\sigma_0 = j/E = \frac{e^2 n \tau}{m} \quad (4.12)$$

and the electron mobility, ν , becomes:

$$\nu = \frac{e\tau}{m} \quad (4.13)$$

4.4.2 Semi-classical equations of motion

In the same line of the Drude model, one can write semi-classical equations of motion for the electrons described by the Bloch waves and whose energies are given by the different bands of the solid. The main idea is to consider wave packets of Bloch waves that characterize a localized electron, such that the velocity is the group velocity of the wave packet and the momentum is the crystal momentum defined by $\hbar\mathbf{k}$. With these considerations one can write the following equations of motion in the presence of external electric \mathbf{E} and magnetic fields \mathbf{B} :

$$\hbar\dot{\mathbf{k}} = -e\mathbf{E} - e\mathbf{v} \times \mathbf{B} \quad (4.14)$$

$$\mathbf{v} = \frac{1}{\hbar} \nabla_{\mathbf{k}} E_n(\mathbf{k}) \quad (4.15)$$

Remarkably, it's possible to show that in topological materials the last equation is modified by adding the following term [81, 101–103]: $\dot{\mathbf{k}} \times \Omega$, where Ω is the Berry curvature defined in 4.3.1. The form of this term is analogous to the Lorentz force term in equation 4.14 associated to the presence of a magnetic field \mathbf{B} , which further supports the interpretation of the Berry curvature as a magnetic field in momentum space. The resultant anomalous velocity can be associated to a number of potential transport phenomena in TSMs, ranging from the anomalous Hall effect [104, 105], the chiral magnetic effect [106] and the presence of negative magnetoresistance [107, 108].

By calculating the rate of change of the group velocity and making an analogy with the classical case, the scalar mass m is formally replaced by an effective mass tensor, which in the simplest case reduces to $m^* = \hbar^2 / (d^2 E / dk^2)$. This is related to the curvature of the band, which means that m^* depends on \mathbf{k} and that, for example, flat bands represent heavy charge carriers. Interestingly, one can show that for linear bands, unlike their parabolic counterparts, $m^* \propto E$, meaning that as the chemical potential moves away from the band crossing, the mass of charge carriers increases. Of particular interest for this thesis is the effect of a magnetic field on the electron's movement. The corresponding term in the equation of motion is $-e\mathbf{v} \times \mathbf{B}$, indicating that the electrons move in a plane perpendicular to the magnetic field and along trajectories tangential to the Fermi surface. The period of these trajectories is connected to the energy dependence of the area, S , enclosed by the orbit in k -space:

$$T_c = \frac{\hbar^2}{eB} \frac{\partial S(E, k)}{\partial E} \quad (4.16)$$

This is more commonly written in terms of the cyclotron frequency:

$$\omega_c = \frac{2\pi}{T_c} = \frac{eB}{m^*} \quad (4.17)$$

where m^* is the effective mass.

4.4.3 Magnetoresistance basics

The term magnetoresistance (MR) refers to the change of electrical resistance when an external magnetic field is applied. The study of MR effects in metallic materials has a long history and detailed reviews and textbooks are available on this topic [77, 109–111]. In the following I will only describe some of the fundamental principles of this phenomenon. In the presence of an external magnetic field (assumed here along the \hat{z} direction), the Drude model can be used to calculate the conductivity of a material with a single charge carrier and a closed FS. Such conductivity is now described by the following tensor:

$$\sigma = \sigma_0 \begin{bmatrix} \frac{1}{1+(\omega_c\tau)^2} & \frac{-\omega_c\tau}{1+(\omega_c\tau)^2} & 0 \\ \frac{\omega_c\tau}{1+(\omega_c\tau)^2} & \frac{1}{1+(\omega_c\tau)^2} & 0 \\ 0 & 0 & 1 \end{bmatrix} \quad (4.18)$$

This tensor can be inverted using standard procedures to determine the corresponding resistivity tensor ρ :

$$\rho = \rho_0 \begin{bmatrix} 1 & \omega_c\tau & 0 \\ -\omega_c\tau & 1 & 0 \\ 0 & 0 & 1 \end{bmatrix} \quad (4.19)$$

where $\rho_o = 1/\sigma_o$. The off-diagonal element can be shown to simplify to $\rho_{xy} = -\rho_{yx} = B/ne$, which is the familiar expression for the Hall effect. The diagonal elements show no field dependence, that is, in this model there is no MR. In reality, most metals exhibit some MR, which typically can be associated to anisotropic FS's, causing electrons to have varying effective masses and/or different associated scattering times. In those cases, it is typically found that for weak magnetic fields, $\omega_c\tau \ll 1$, the MR grows proportional to B^2 ; but for strong fields, $\omega_c\tau \gg 1$, the MR saturates. Many semimetals like Bi [112, 113], and some TSMs [10, 12], exhibit a non-saturating MR with a quadratic field dependence. A classical model can reproduce this behaviour by also introducing holes as charge carriers and with the same density as that of electrons. In this two band model it can be shown that perfect charge compensation results exactly in a B^2 dependence of the MR. Such behaviour, together with the connection between MR and FS shape, has been treated numerically by solving the Boltzmann transport equation [114]. Figure 4.4 (a) shows the numerical results for the isotropic two band model. The degree of compensation is controlled by the Fermi energy E_F . For $E_F = 0eV$, i.e., perfect compensation, the dependence $MR \propto B^2$ is obtained, while for shifted values of E_F the nearly-compensated system leads to sub-quadratic MR dependence.

The situation changes completely if the FS has 2D or quasi-2D FS sheets capable of hosting open orbits since the two band model is no longer applicable. The numerical results for this case are presented in figure 4.4 (b), where an open sheet extending in the \hat{z} direction is modelled. When the current is applied along this same direction, the transverse MR exhibits a non-saturating behaviour for $\omega_c\tau \gg 1$, in stark contrast to the single, closed FS pocket case. When the current is applied along a direction perpendicular to the open orbit's direction, for

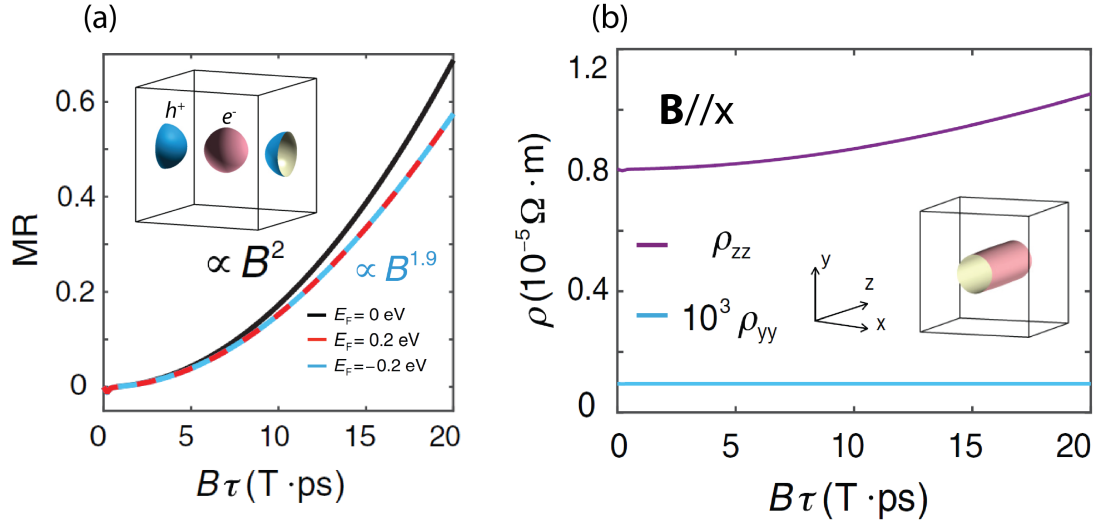


Figure 4.4: **Magnetoconductance and Fermi surface shape.** Numerical results from solving the Boltzmann transport equation. (a) Isotropic two-band model showing a quadratic field dependence of the MR for perfect compensation and a sub-quadratic dependence for imperfect compensation. (b) Isotropic open orbit FS showing a non-saturating transverse MR when the current is applied along the direction of the open orbits; and a small, saturating MR when it is applied in a direction perpendicular to the open orbits. Image adapted from [114].

example, along the \hat{y} direction, then a very small, saturating transverse MR is obtained. The connection between FS shape and MR has been used extensively to help map the FS of many metals and semimetals, and it's still an essential factor to consider when studying TSMs and trying to determine which of their properties can be accounted for using classical explanations and not more exotic topology-related effects.

4.4.4 Landau quantization

The previous description is not enough to characterize the full effect of magnetic fields on the quantum states of the electrons. In a magnetic field, the Schrödinger equation is no longer translational invariant in the directions perpendicular to the field, leading to the well known Landau quantization. In the Hamiltonian the canonical momentum \mathbf{p} must be replaced by $\mathbf{p} + e\mathbf{A}$, where \mathbf{A} is the vector potential such that $\mathbf{B} = \nabla \times \mathbf{A}$. The components of the vector k perpendicular to B are no longer good quantum numbers and the whole picture of energy bands is modified. For a non-relativistic fermion in 3D, with the field applied in the \hat{z} direction the new energy levels are those of a harmonic oscillator:

$$E_n = \left(n + \frac{1}{2}\right) \hbar\omega_c + \frac{\hbar^2 k_z^2}{2m} \quad (4.20)$$

Moreover, the area perpendicular to the field, S_{\perp} , enclosed by the electrons in k -space is quantized according to the Onsager's relation [115]:

$$S_{\perp}(E, k_{\parallel}) = (r + \gamma) \frac{2\pi B e}{h} \quad (4.21)$$

Where k_{\parallel} is the wave vector component parallel to the field, r is an integer and the parameter γ depends on the form of the dispersion relation. For a parabolic band with $E = \hbar^2 k^2 / 2m^*$ and the energy levels given by equation 4.20, one obtains $\gamma = 1/2$. Equation (4.21) indicates that for a constant magnetic field, S_{\perp} is the same for all values of k_{\parallel} . This means that the electrons' states are located on a concentric set Landau tubes, onto which the free electron k -states condense when a field is turned on. As the size of the orbit changes with field, increasing B expands these Landau levels (LLs) and they successively leave the Fermi surface at rate given by:

$$\Delta(1/B) = \frac{1}{B_n} - \frac{1}{B_{n+1}} = \frac{2\pi e}{h S_{extr}} \quad (4.22)$$

where only the extremal orbits are taken into account. This, in turn, corresponds to the frequency:

$$F = \frac{h S_{extr}}{2e\pi} \quad (4.23)$$

As the Landau levels cross the Fermi surface, the DOS oscillates with this frequency, which, in turn, causes oscillations in all the electronic related properties of the solid, usually referred to as quantum oscillations (QOs), including magnetization, resistivity, thermal conductivity and even sample's length. Since the frequency is related to the cross section of the Fermi surface perpendicular to the field, these oscillations are essential in understanding the shape of the Fermi surface.

In the case of TSMs, the Landau energy spectrum is completely different [116]. Choosing the Landau gauge, $\mathbf{A} = -By\hat{x}$ for a constant magnetic field B pointing in the \hat{z} direction and again replacing \mathbf{p} by $\mathbf{p} + e\mathbf{A}$, equation 4.7 takes the form:

$$H = \chi v_F \begin{bmatrix} p_z & (p_x - eBy) - ip_y \\ (p_x - eBy) + ip_y & -p_z \end{bmatrix} \quad (4.24)$$

This Hamiltonian acts on a two-component wave vector $\psi(\mathbf{r})$

$$\psi(\mathbf{r}) = \begin{bmatrix} \psi_1(\mathbf{r}) \\ \psi_2(\mathbf{r}) \end{bmatrix} \quad (4.25)$$

such that Schrödinger equation, $H\psi(\mathbf{r}) = E\psi(\mathbf{r})$, results in two equations relating $\psi_1(\mathbf{r})$ and $\psi_2(\mathbf{r})$:

$$\chi v_F p_z \psi_1(\mathbf{r}) + \chi v_F [(p_x - eBy) - ip_y] \psi_2(\mathbf{r}) = E \psi_1(\mathbf{r}) \quad (4.26)$$

$$\chi v_F[(p_x - eBy) + ip_y]\psi_1(\mathbf{r}) - \chi v_F(p_z)\psi_2(\mathbf{r}) = E\psi_2(\mathbf{r}) \quad (4.27)$$

Choosing $\chi = 1$ and substituting the second into the first equation above, one can obtain an expression for $\psi_1(\mathbf{r})$ only:

$$\begin{aligned} E^2\psi_1(\mathbf{r}) &= \{v_F^2 p_z^2 + v_F^2((p_x - eBy) + ip_y)((p_x - eBy) - ip_y)\}\psi_1(\mathbf{r}) \\ &= \{v_F^2 p_z^2 + v_F^2((p_x - eBy)^2 - i[(p_x - eBy), p_y] + p_y^2)\}\psi_1(\mathbf{r}) \\ &= \{v_F^2 p_z^2 + v_F^2((p_x - eBy)^2 - \hbar Be + p_y^2)\}\psi_1(\mathbf{r}) \\ &= \{v_F^2 p_z^2 + v_F^2((p_x - eBy)^2 + p_y^2) - v_F^2 \hbar Be\}\psi_1(\mathbf{r}) \end{aligned}$$

where I have used the canonical commutation relations for the momentum and position operators. The first two terms multiplying $\psi_1(\mathbf{r})$ on the right hand side of the equation are exactly the same as that of a three dimensional harmonic oscillator centered away from the origin and with the mass replaced by $1/2v_F^2$, so that the corresponding energy levels are the ones given by equation 4.20 (p_z commutes with the rest of the Hamiltonian so we can replace p_z by its eigenvalue $\hbar k_z$). The final term can be written as $-\hbar\omega_c/2$ and effectively shifts in energy all the Landau levels, guaranteeing that there is now a level crossing $E = 0$. Combining all these terms and taking into consideration the equivalent result when taking $\chi = -1$, the energy spectrum for the LL of a TSMs can be written as:

$$E_n = v_F sgn(n) \sqrt{2e\hbar|B||n| + \hbar^2 k_z^2} \quad (4.28)$$

where $n = 0, \pm 1, \pm 2, \pm 3, \dots$. In figure 4.5 some of the main differences between the Landau quantization between topologically trivial materials and TSMs are shown. Most remarkably, there exists a field independent zeroth LL ($n = 0$) that is locked at the band crossing point. As we shall see below, one of the main consequences of this fact is the manifestation of a new topological phase factor in quantum oscillations associated to the Berry phase.

4.4.5 Shubnikov-de Haas oscillations

The oscillations in resistivity coming from the Landau quantization are called Shubnikov-de Haas (SdH) oscillations. They can be described using the Lifshitz-Kosevich (LK) formalism, which in its simplest case predicts the following expression for the oscillatory part of the resistivity [117]:

$$\Delta\rho/\rho \propto R_S R_T R_D \cos[2\pi(F/B + \gamma - \delta)] \quad (4.29)$$

where δ is another phase factor that depends on the dimensionality of the system and $\delta = \pm 1/8$ in the 3D case. The factors R_T, R_D and R_S are damping factors of the quantum oscillations. The determination of the phase factor is of particular interest in topological materials since the Berry phase becomes relevant. Under a magnetic field, the cyclotron motion of the electrons around the nodes would induce a Berry phase that changes the phase of the quantum

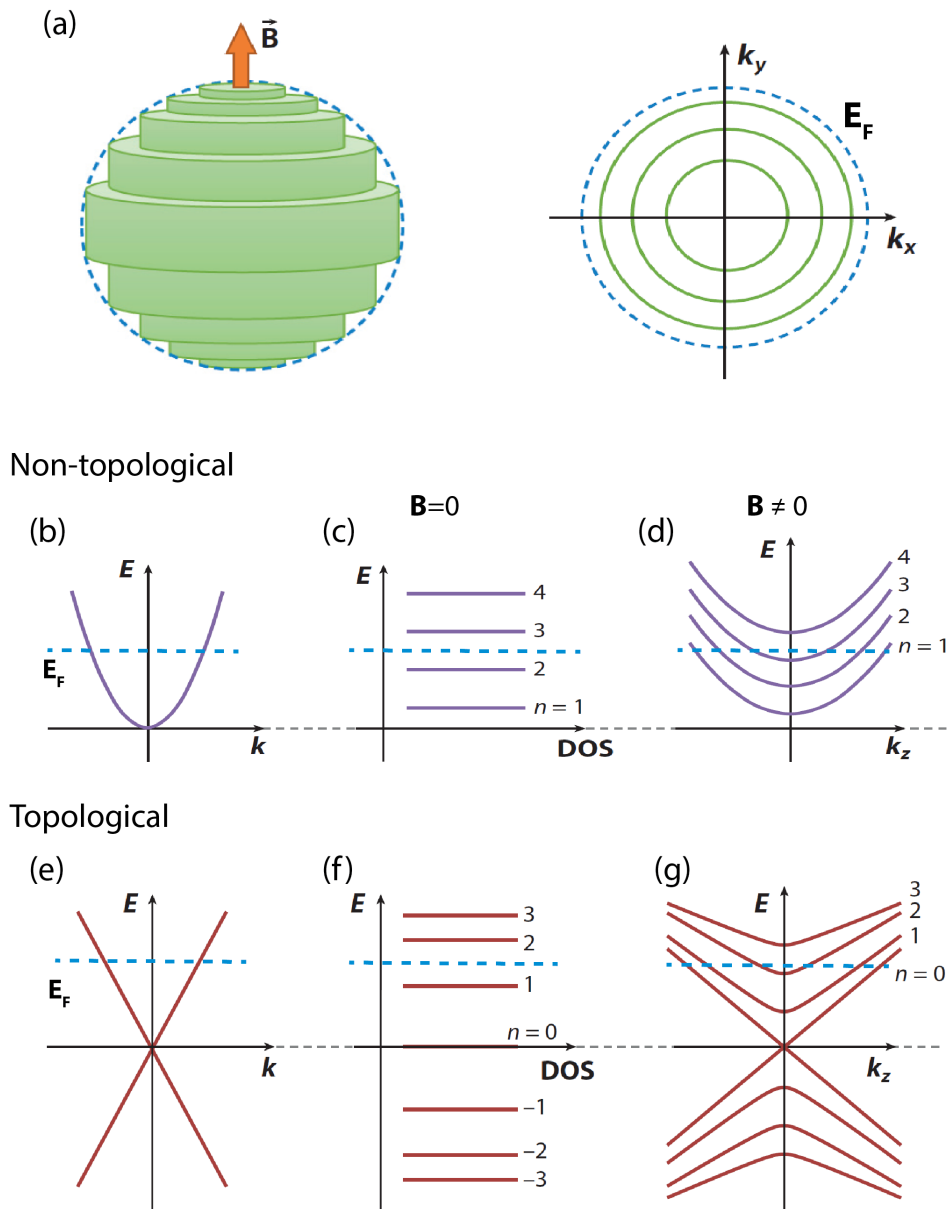


Figure 4.5: **Main differences between the Landau quantization of non-topological (parabolic band) and topological (linear band) fermions.** (a) Landau tubes intersecting a spherical Fermi surface. Dispersion relation for (b) normal and (c) topological electrons. Landau spectra for a 2D spinless (c) normal and (f) topological system. Landau dispersion relation for a 3D spinless (d) normal and (g) topological system with the field applied along the \hat{z} direction. Image adapted from [12].

oscillations. In their original work concerning the accidental degeneracy in the material LaRhIn₅, Sharlai and Mikitic [118] proposed that it was possible to write $\gamma = 1/2 - \Phi_B/2\pi$. For a linear band around a crossing point, one can show that $\Phi_B = \pi$, thus rendering $\gamma = 0$ for topological materials. However, this has proven to be an oversimplified picture in the case of 3D TSMs. More recent advances in the theory of band topology [119] have highlighted that there are additional phase factors coming from the contribution of orbital moments [120] and the Zeeman effect [121] that can make even topological trivial materials exhibit an experimental phase of π in their quantum oscillations spectrum.

It is worthwhile to describe in a bit more detail the damping parameters present in the LK formula. R_T describes the thermal broadening of the Fermi-Dirac distribution function as the temperature is increased. At $T \neq 0$ the depopulation of the LLs as they cross the Fermi level is not sharp but becomes smeared out. This leads to a decrease of the quantum oscillation's amplitude according to:

$$R_T = \frac{X}{\sinh X} \quad (4.30)$$

where:

$$X = \frac{2\pi^2 k_B T}{\hbar \omega_c} \approx 14.69 p m^* \frac{T}{B} \quad (4.31)$$

The effective mass m^* can be obtained from the fit of the temperature dependence of the oscillation's amplitude. R_D describes the effect of disorder and the corresponding finite relaxation time. In the presence of impurities, the LLs themselves will be broadened, also affecting the amplitude of the oscillations.

$$R_D = \exp\left(-\frac{\pi}{\omega_c \tau_q}\right) \quad (4.32)$$

High quality samples are required to observe QOs, which can be expressed by the condition that $\omega_c \tau_q \gg 1$, where τ_q is called the quantum relaxation time. It is important to distinguish this relaxation time from the transport relaxation time τ introduced in the Drude model. τ measures the motion of the particles along the electric field gradient, so it is largely unaffected by small angle scattering. On the other hand, τ_q is affected by scattering from all directions, so it is usually smaller than τ . Finally, R_S quantifies the correction due to the phase difference between the spin up and spin down sub-bands and can be written as:

$$R_S = \cos\left(\pi g \frac{m^*}{m_o}\right) \quad (4.33)$$

where m_o is the free electron mass and g the gyromagnetic ratio defined by the Zeeman splitting: $\Delta E = g \mu_B B$, μ_B being the Bohr magneton.

4.4.6 Weyl Orbits

The presence of symmetry protected nodes close to the Fermi level leads to new signatures in the transport response of TSMs and the so-called Weyl orbits are one of these signatures [35, 122, 123]. However, it is first necessary to see how these orbits distinguish themselves from other magneto-transport effects that are also part of the material's response. As mentioned before, in a normal metal, the application of a magnetic field \mathbf{B} quantizes the orbits of the bulk electrons, localizing them in the direction perpendicular to the field (see figure 4.6 (a)). For a given field, the electrons orbit the Fermi surface and, in the most general case, follow a helix trajectory in real space as they move along the direction of the applied field. Weyl orbits, on the other hand, not only involve the LLs in the bulk but also the Fermi arcs on the surface, as depicted schematically in figure 4.6 (b). This is very peculiar, since it's a combination of metallic bulk conductive states with Quantum Hall-like states in the surface. Moreover, given the linearity of the bulk bands and hence the constancy of the velocity (which is proportional to the slope of the bands), the electrons traversing the bulk experience zero Lorentz force and their trajectory in space is not a helix but the one shown in figure 4.6 (b). Nonetheless, these orbits are coherent and also lead to modulations of the DOS. For low energies, when the states are only populated near the nodes of a WSM, the chiral LLs are the ones taking part in the Weyl orbits. Since the Weyl orbits involve electrons traversing the bulk, the quantization condition is modified and includes a term that depends on the material's thickness. With this consideration, the peaks of these QOs happen at the fields given by:

$$\frac{1}{B_n} = \frac{e}{k_0 \hbar} \left[\frac{2\pi v_F \hbar}{\mu} (n + \gamma) - 2L_z \right] \quad (4.34)$$

where k_0 denotes the momentum space separation of the nodes, μ the chemical potential, γ is a constant of the order unity encoding low- n quantum effects, and L_z the device thickness. Like regular QOs, the ones coming from the Weyl orbits are periodic in $1/B$ with a frequency of $\mu k_0 / \pi v_F$. Even though the Weyl oscillations are periodic in $1/B$, they violate Onsager relation and they include a novel thickness dependant term. If the sample thickness is greater than the mean free path, these QOs will not be observed since quantum coherence will be lost. If the magnetic field points in the direction of the axis where the nodes are located, they will also disappear since the projection of the Weyl nodes will be zero. Additional factors could weaken the signal as well. For example, scattering from impurities and from chiral and non-chiral LLs (when the chemical potential is not exactly at the nodes). Experimental evidence for Weyl orbits have been reported. Moll et al [35] measured SdH oscillations on Cd₃As₂ FIB prepared microstructures of different thickness, down to 150 nm (see figure 4.6 (c) and (d)). In addition to the frequency of the bulk Fermi surface, they found an additional frequency of 61.5 T, consistent with the Weyl orbits extension, and whose amplitude decreased exponentially with increasing thickness. Furthermore, they found that if the sample has a triangular shape, the additional frequency disappears due to the destructive interference coming from different thickness-related phases. More recently, Zhang et al [124] measured the quantum Hall resistance on Cd₃As₂ wedge shaped samples and found a strong modulation

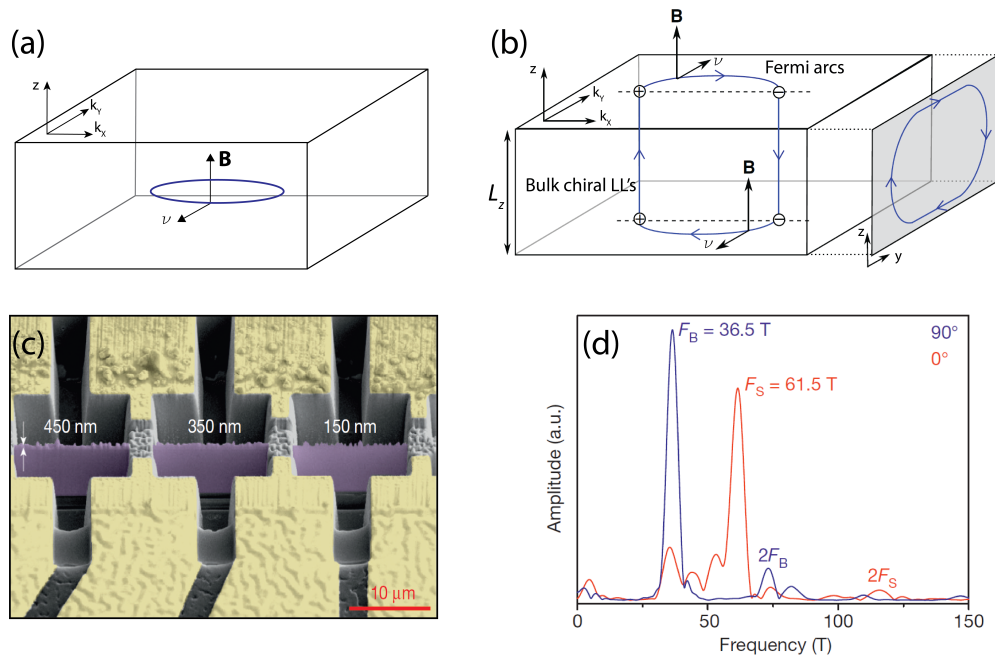


Figure 4.6: **Quantum oscillations from Weyl orbits.** (a) Localized electron orbits in a normal metal where a magnetic field \mathbf{B} is applied in the z direction. (b) Schematic of a Weyl orbit in mixed real/momentum space and real space [122]. These orbits extend through the material and also lead to DOS modulations. (c) Microstructures of different thickness investigated by Moll et al showing (d) conventional bulk QOs and additional, thickness dependant, QOs with a frequency of $61.5T$, which are associated to the Weyl orbits [35].

that can be explained in terms of the edge modes associated to the Weyl orbits.

4.5 Pseudo-magnetic fields induced by strain

Soon after graphene was discovered, it was realized that lattice distortions produced by strain gradients can couple to the electronic degrees of freedom as a gauge potential, much in the same way a vector potential is coupled to electric charges in electromagnetism[125]. The change in the hopping terms coming from a strain gradient in the lattice has the effect of displacing the Dirac nodes in momentum space, making the electrons behave as if they were in the presence of an emergent or pseudo magnetic field. A schematic picture of this phenomena is presented in figure 4.7 (a). This effect has been observed experimentally in the form of pseudo-Landau levels using scanning-tunneling microscopy, both in real [29] (see figure 4.7 (b)-(d)) and artificial graphene [30].

DSMs and WSMs are expected to show similar effects [126–128], which might open up the door to new technological applications of these materials requiring high magnetic fields that would be very difficult or impossible to attain by traditional means. A good review in the description of pseudo-fields in TSMs can be found in [31]. In this section, I give a brief reminder of this

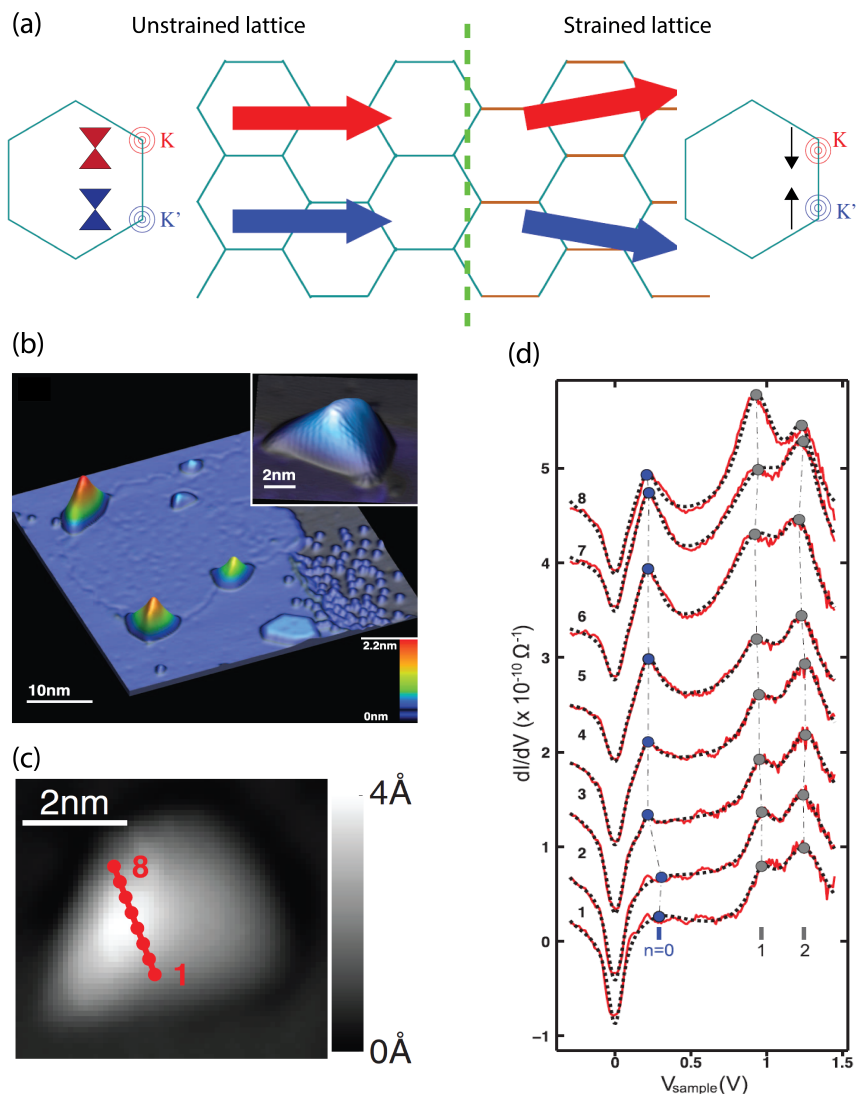


Figure 4.7: **Pseudo-magnetic fields in graphene.** (a) A distortion of the lattice changes the hopping between bonds. In regions where the distortion has different magnitudes, i.e, where there's a strain gradient, the shift of the Dirac nodes leads to a deflection of the electron trajectories. This is analogous to the effect of a magnetic field. Image taken from [30]. (b) STM image of a graphene monolayer patch with nanobubbles. (d) Sequence of eight dI/dV spectra taken in the line across the graphene nanobubble shown in (c). The peaks in dI/dV can be attributed to pLLs originating from a strain-induced pseudo-magnetic field. (b)-(d) are taken from [29].

concept and highlight one of its most consequential statements, as presented in [34]: that Fermi arcs can be thought of as the $n = 0$ pseudo-Landau level (pLL) of a pseudo-field confined to the surface boundary of a WSM. This provides a new way of thinking about topological surface states, which under the conventional formalism of topological band theory arise as the necessary edge states between two regions of different topological index [129]. As was mentioned before, the effect of strain in WSM can be modelled by including in the Hamiltonian a node separation \mathbf{k}_0 that is space dependant: $H = \pm \hbar v_F (\mathbf{k} \pm \mathbf{k}_0) \cdot \boldsymbol{\sigma}$, where the pseudo-magnetic field is given by $\mathbf{B}_5 = \nabla \times \mathbf{k}_0$. Notice that a constant \mathbf{k}_0 would lead to a null \mathbf{B}_5 . To illustrate a concrete example, let $\mathbf{b}(\mathbf{r}) = b^x(y)\hat{x}$. Since $\mathbf{b}(\mathbf{r})$ only depends on y , the corresponding \mathbf{B}_5 points in the \hat{z} direction. Consider the three profiles of $b^x(y)$ presented in the second row of figure 4.8, where l_1 and l_2 represent the boundaries of a WSM. The nodes' separation changes linearly over a certain distance so that \mathbf{B}_5 is constant and changes sign as indicated in the figure. The evolution of the profiles from left to right corresponds to reducing the region of change of the node's separation, eventually confining such region to the boundary of the WSM. The corresponding energy diagram, calculated from a lattice model Hamiltonian for WSMs, is shown in the first row of figure 4.8. Analogously to equation 4.28, a pseudo-magnetic field \mathbf{B}_5 along the \hat{z} direction produces pLL with energies $E_n = \pm v_F \sqrt{2e\hbar|B_5||n| + \hbar^2 k_z^2}$ and thus disperses along k_z only. This allows us to identify the flat parts of the energy diagrams in figure 4.8 with the pLL. Furthermore, we see that as the node's variation is confined to the jump between different boundaries, the $n \geq 1$ pLL disappear from the spectrum leaving only the $n = 0$ pLL, which is nothing more than the Fermi arc states characteristic of WSMs.

In 3D materials, pseudo-fields have been realized using acoustic and photonic metamaterials where pressure and light waves exhibit a linear dispersion relation that resembles that of a WSM [130, 131]. Cold atom systems have also been successful in emulating and manipulating effective gauge fields [132, 133] and there are proposals for synthetic realizations of axial gauge fields analogous to \mathbf{B}_5 [134]. In spite of these tantalizing results, experimental realizations and transport signatures of pseudo-fields in 3D WSMs remain elusive. Some studies have suggested that strain gradients near lattice defects and dislocations can be formulated as pseudo-magnetic fields and possibly result in detectable transport signatures [135, 136]. Other studies have suggested to concentrate on the boundaries between different WSMs, WSMs and insulators (topological or trivial) and even heterostructures formed from these interfaces to generate appreciable pseudo-fields [31]. However, no experiment has yet shown the viability of any of these approaches. The only relevant experimental result in this regard is the reported observation via scanning tunneling spectroscopy of strain-induced pseudo-magnetic fields in rippled regions of Re-doped MoTe_2 crystals [137]. Those ripples, whose origin is conjectured to be related to the cleavage of the crystals, remain fixed once the samples are prepared. In this sense, the main challenge in this kind of experiments is both to generate global strain gradients that are not confined to small regions of the sample and also to generate them in such a way that they are capable of fine-tuning in order to adjust the magnitude of the induced pseudo-fields.

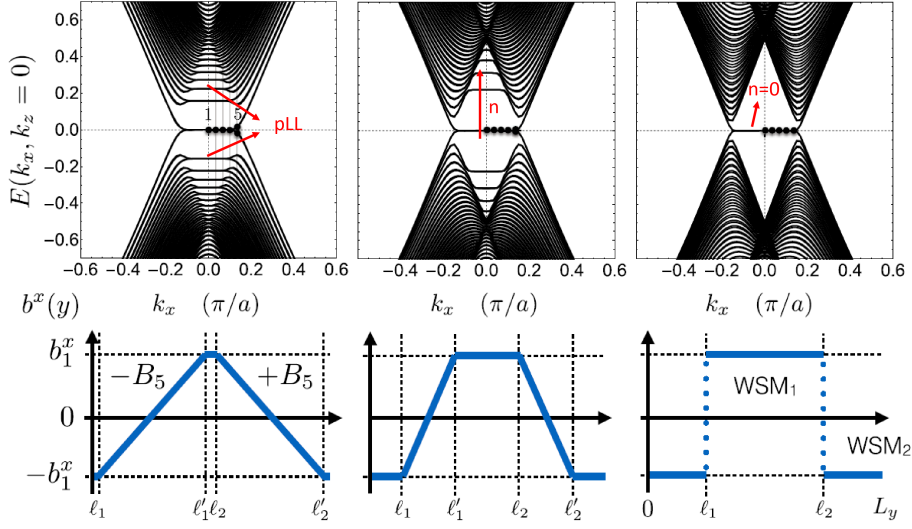


Figure 4.8: **Fermi arc states as the zeroth Landau level of a pseudo magnetic field.** Energy spectra (top row) of a WSM in the presence of a spatially varying node distance, $\mathbf{b}(\mathbf{r}) = b^x(y)\hat{x}$, with the profile shown in the second row. The flat regions of the energy curves correspond to the pseudo Landau levels (pLL) associated to \mathbf{B}_5 . Image taken from [34].

5 Mechanical bending set-up for microstructures

5.1 Introduction

The identification of novel physical phenomena in TSMs associated to the presence of strain gradients has prompted the development of new experimental techniques that try to offer a better control of the strain landscape that can be applied to this kind of materials. Most approaches to generate sizeable strain and strain gradients focus on 2D materials and thin films [138]. These approaches include, for example, biaxial strain from lattice mismatch [139], the use of flexible substrates such as polyimide films [140] and nanoindentation by atomic force microscopy tips [141]. In the case of the most prominent 2D TSM, graphene, some approaches are based on transferring the graphene membrane to nanopillars arrays [142] and precisely shaped nano-dots [143] and anti-dots [144], thus subjecting the membrane to a nonuniform distribution of strain. These complex strain fields acting on both graphene sublattices independently have been proposed to induce large and constant pseudo-magnetic fields [145, 146](see figure 5.1 (a)). The creation of uniform strain gradients has also been attempted in other kinds of nanostructures, for example, in long micro-wires that are bent using a glass tip [147] (see figure 5.1 (b)) or micro-fabricated constraining pillars [148]. In spite this variety of experimental techniques, none of them can be easily extended to apply large strain gradients in 3D materials. The techniques aimed at 2D materials and thin films rely fundamentally on having thin membranes as samples, obtained by exfoliation methods or grown by other processes like molecular beam epitaxy. Most of the time these techniques are not applicable to the 3D materials of interest and when they are, the resulting nanostructures tend to suffer from a reduction of sample quality. Similarly, techniques like the bending of long wires is limited by the availability of crystals that can be grown in this shape. In the case of 3D macrocrystals, uniaxial strain techniques have been used recently to obtain considerable strains of up to 0.73% [52]. However, as its name suggests, this technique is aimed at achieving homogeneous strains and although some strain inhomogeneity usually persists, the re-purposing of the uniaxial pressure rig for a controlled application of strain gradients would be practically impossible. Furthermore, the technique also requires relatively large samples of around 1 mm in length. This imposes an important limitation since large crystals

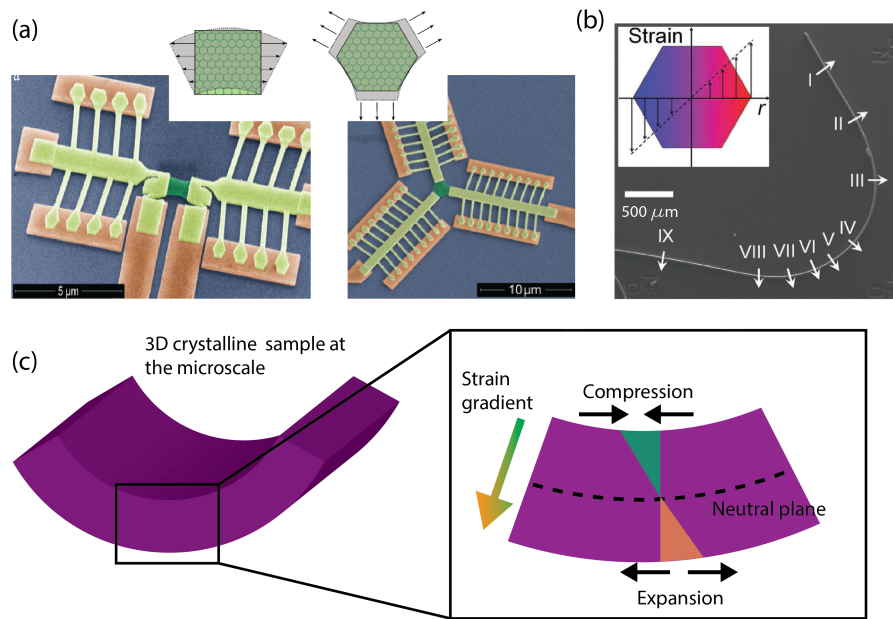


Figure 5.1: **Different approaches for producing strain gradients.** (a) False colour SEM image of graphene devices suspended from Au contacts. As the devices are cooled down the contraction of the Au beams is expected to produce the necessary complex strain distribution (shown in the inset) required for the observation of constant pseudo-magnetic fields. Image adapted from [146] (b) SEM image of bent microwires of the semiconducting material ZnO, showing a strain gradient through their cross section (highlighted in the inset). Figure taken from [147]. (c) A simple way to generate a strain gradient in 3D samples is by bending. The magnitude of the gradient will depend on the thickness of the sample and the bending angle.

cannot sustain high strain gradients before exceeding yield limits and plastically deforming or breaking. In this sense, any technique aiming at achieving large strain gradients in 3D crystalline materials must be applied at the micro or smaller scales.

In this chapter I present a technique developed during the course of this thesis to generate and control strain gradients at the micro and nanoscale in 3D crystalline samples, which are micro-machined using the FIB. The main idea is shown in figure 5.1 (c): bending a sample is a simple way to create a strain gradient whose magnitude can be adjusted by changing either the thickness of the sample or the angle of bending. In addition, by doing this at the microscale it is possible to apply such gradient in an elastic and reproducible way. I use the Dirac semimetal Cd_3As_2 as a test material for the technique given its simple electronic structure as well as the cleanliness of available crystals. Due to the small dimensions that are accessible in the FIB fabrication process, the magnitude of the attainable strain gradients can become quite significant but without resulting in rupture of the sample. The results conclusively demonstrate that nearly constant strain gradients exceeding $1.3\% \mu\text{m}^{-1}$ can be achieved at a surface strain value of $\approx 0.65\%$. The transport behaviour and quantum oscillation spectrum of the samples before and after maximum bending remains unchanged, suggesting that the bending procedure is done elastically, without irreversible structural consequences to the material itself. In the following section I will describe the sample design and fabrication process that were tailored for the bending experiments, followed by a presentation of the apparatus used for bending, which includes a bending without rotation version and a version fitted to a probe with a mechanical rotator such that the bent samples can be rotated in presence of a magnetic field. Finally, the section 5.4 presents the main conclusions and outlook. Many of the results of this chapter have already been published in Diaz et al, Journal of Physics D: Applied Physics 55 (2022), and some passages have been quoted verbatim from that reference.

5.2 Sample design and fabrication for bending experiments

The main goal in the design of the samples is to have the possibility of bending them by using a macroscopic, mechanical piezo-driven positioner and at the same time measure the resistance of sections of the sample that concentrate the bending and are subjected to the desired strain gradient. The design of the samples in the form of cantilevers is presented in figure 5.2 (a). The typical size of Cd_3As_2 crystals ($\approx 1\text{mm}$) and their often irregular shape precludes traditional lithography-based cantilever fabrication. Instead, FIB machining is used to carve lamellae from the parent crystals (as described in chapter 2), which are later used to fabricate the cantilevers. The cantilever starts with a large scale lamella of Cd_3As_2 whose thickness or shortest dimension points along the desired direction of strain gradient. In order to avoid bending the electrical contacts and the engagement point of the bending apparatus, a segment of the lamella is thinned down, dividing it into three sections along its long axis. The first one is composed of four thick platinum electrical contacts that are firmly connected to the substrate. They are followed by three thin flexures, the two outermost of which act as

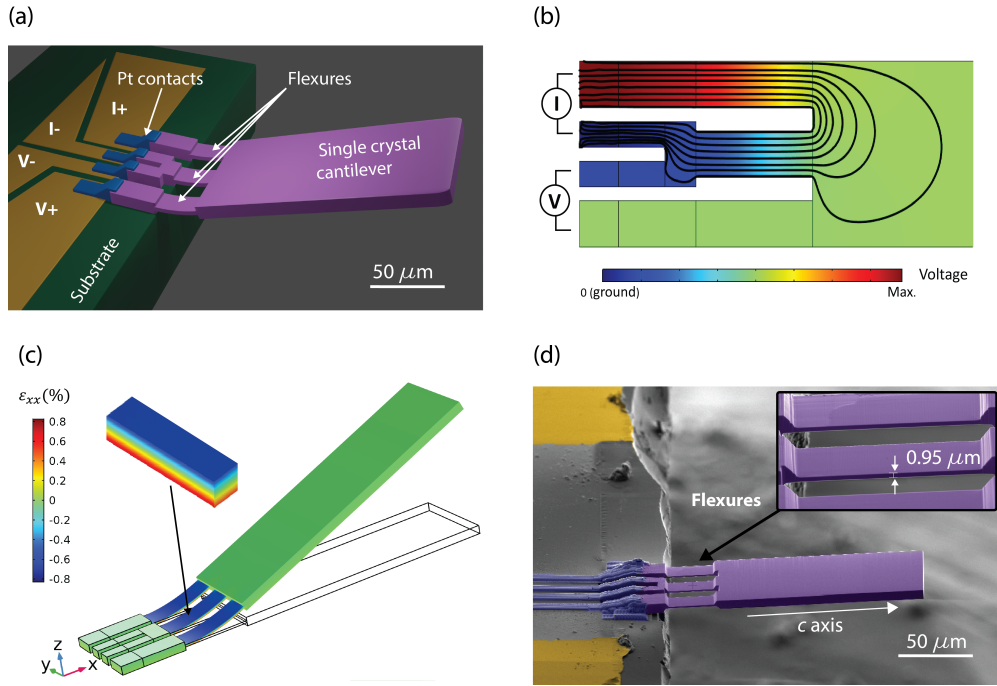


Figure 5.2: **Sample design for transport measurements under large strain gradients.** (a) Schematic diagram of a bending cantilever (purple) with electrical contacts that are Pt welded (blue) to a substrate with a Au layer on top (yellow). (b) Simulated potential distribution and current density streamlines. (c) Simulated strain ε_{xx} distribution for a maximum vertical displacement of $h = 60\mu\text{m}$ of the free end of the cantilever. (d) Scanning electron microscopy image of a FIB-fabricated Cd_3As_2 cantilever welded at the edge of a sapphire substrate.

current and voltage leads, while the central bar is the active part being measured. Finally, a long and thick free end of the cantilever is used to dock the positioner. A finite elements (FEM) simulation of the electrical situation for this sample design is presented in figure 5.2(b), showing the distribution of the electrical potential and the current density streamlines for Cd_3As_2 crystalline bars. The current density is approximately uniform in the central flexure and the thick part of the cantilever can be approximated as an equipotential given its much larger size. The thin flexures are important for two main reasons: i) the flexures concentrate the strain, minimizing the radius of curvature and maximizing the strain gradient. To confirm this statement, FEM simulations of the cantilever were performed applying a vertical displacement at the free end (see figure 5.2(c)). As expected for a simple beam under bending strain, the simulations showed that the strain ε_{xx} changes from its minimum (negative) value at the top to its maximum (positive) value at the bottom surface, crossing the neutral plane in the middle of the flexures; ii) the central active bar thickness must not exceed the mean free path of the material to maintain coherence of the Weyl orbits (which is about $1\mu\text{m}$ in these Cd_3As_2 crystals) [35]. Leaving the remaining cantilever thicker than this dimension ensures that the oscillatory signal from Weyl orbits only originates from the thin central flexure, whose resistance is the dominant term in the electrical signal. Figure 5.2 (d) shows a false-color SEM

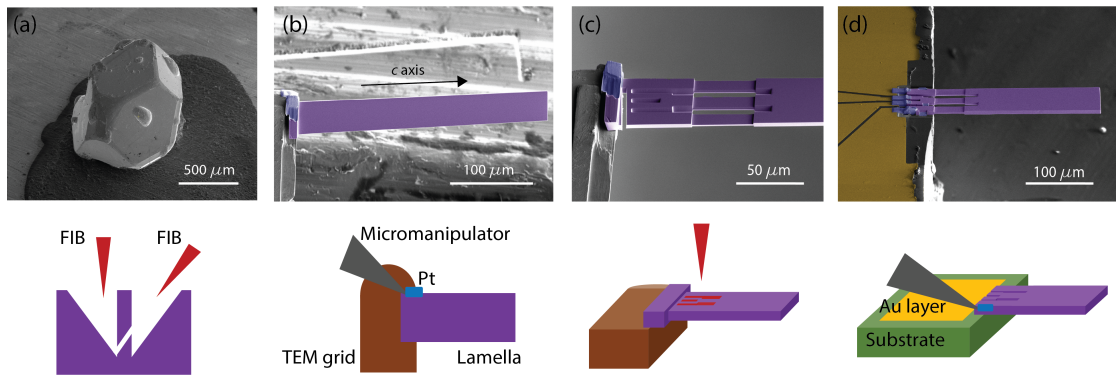


Figure 5.3: **Main steps in the fabrication of cantilevers.** (a) Oriented crystal from which rectangular lamellae are cut along the desired crystallographic directions. (b) The lamella (purple) is transferred to a grid (brown) where it is then polished. (c) The microstructuring is done while the lamella is attached to the grid. (d) The patterned cantilever is welded with platinum (blue) to the edge of a sapphire chip where gold contacts (yellow) are delineated with the FIB.

image of a finished Cd_3As_2 cantilever.

Next, I turn to the main stages of the FIB fabrication process, as shown in figure 5.3. Many of the steps and their corresponding guidelines are similar to the ones described in section 2.5.3 for the fabrication of free-standing microstructures, in particular, those related to handling the sample with the micromanipulator and transferring it onto a substrate. The devices reported here were machined using both Ga-ions and Xe-ions beams. From a Cd_3As_2 bulk crystal, whose crystallographic directions had been determined by X-ray diffraction, rectangular bars or lamellae of $\approx 250 \times 70 \times 7 \mu\text{m}^3$ dimensions were cut along the desired directions (see figures 5.3 (a) and (b)). Throughout the fabrication, a dwell time of $1 \mu\text{s}$ was used. The coarse cuts were performed with beam currents of 60 nA at 30 kV . Using the micromanipulator, the lamella was transferred *in situ* to a TEM grid, where it was carefully polished to guarantee smooth and parallel surfaces (see figure 5.3 (b)), and subsequently thinned down to its final dimensions (including the thinnest region where the flexures were located). This was achieved by using small currents and refining the tilting angle for polishing. For example, the lamella faces in figure 5.3 (c) were polished using 4 nA while the thinning down of the flexures was done using 300 pA . In both instances a tilting angle in the range of 53° - 53.5° was chosen.

After polishing, the TEM grid was flipped horizontally and the desired pattern was structured top-down with a current of 1 nA (figure 5.3 (c)). This relatively low current value, as well as having the sample on the TEM grid, minimizes the redeposition of sputtered material and allows for the creation of sharp, well defined features. Such structural precision is critical as the Weyl orbit phase depends on the thickness of the traversed bulk [122]. During this step, small bridges joining the current and voltage contacts were left uncut to secure the structural integrity of the sample during the transfer process. Finally, the structured cantilever was transferred to the edge of a sapphire chip and welded down by ion-assisted deposition

Devices	Thickness (μm)
Sample 1	0.95
Sample 2	0.88
Sample 3	1.92
Sample 4	1.71
Sample 5	1.77

Table 5.1: **Devices fabricated and the final thickness of their flexures.** These devices were fabricated using both the Ga-FIB and the P-FIB.

of Pt, forming both electric contacts to Au leads on the sapphire chip and solid mechanical connections (see figure 5.3 (d)). The small bridges left for structural stability were then cut and the regions between the four legs that act as electrical contacts were further exposed to the ion beam (using small currents of around 1nA) to eliminate any possible electrical shortcuts. The Au leads were made from a Au layer of around 200nm that was previously sputtered on the sapphire chip after carefully masking it with a Kapton tape. The goal of the masking is to have Au as close as possible to the edge where the cantilever is mounted. To avoid electrical shorts from the sputtering step, the edge and corresponding face of the sapphire chip is preemptively exposed to a large current with the ion beam ($>60\text{nA}$) until a clear, bright insulating surface is achieved, thus eliminating any possible electrical path. The region close to where the lamella is meant to be placed is also previously milled with the ion beam to have a well defined "landing" zone with a sharp Au layer (see figure 5.3 (d)). Table 5.1 summarizes the total number of samples fabricated and the final thickness of their flexures.

5.3 Bending apparatus

5.3.1 Bending without rotation

In this section I will describe the apparatus designed for bending without rotation of the sample with respect to the applied magnetic field. The main working principle is the following: a piezo-actuated pusher is used to bend the fabricated cantilevers. The mechanical motion is provided by an attocube linear nanopositioner with the capability of sub-micrometer step motion (premium line model ANPz51). Since this component is essential for the here presented technique, it is worthwhile to briefly review the working mechanism responsible for the stepping motion, which is based on the stick-slip phenomenon. This is shown in figure 5.4 (a). The attocube nanopositioners are driven via piezoceramics made from lead zirconite titanate (PZT) while the other components are made from highly pure titanium as it is light, nonmagnetic, and has a coefficient of expansion matching the piezo and other elements of the drive for reliable low temperature performance. The moving table in the nanopositioner is spring-clamped to a rod that serves as the driving element. The rod is moved by the piezoelectric ceramic. The clamping force and the coating on both sides of the frictional contact are carefully tuned for the respective environment. At the initial stage, where

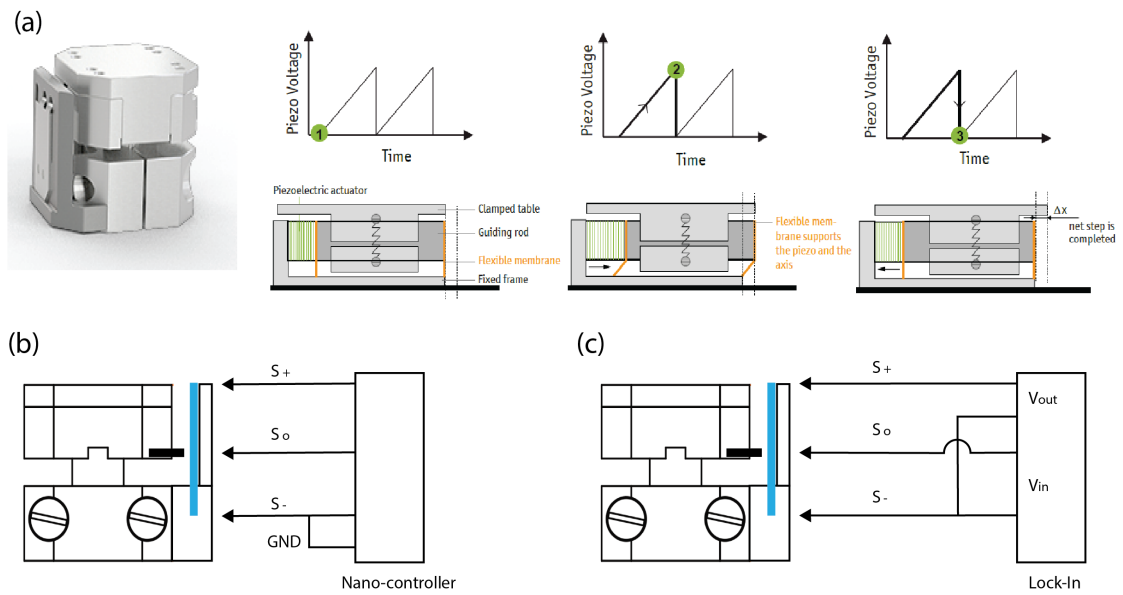


Figure 5.4: **Working mechanism of the attocube nano-positioners.** (a) Stepping procedure during movement, which is based on the stick-slip phenomenon. Resistive encoder reading using (b) the attocube nano-controller and (c) the lock-in amplifier. Figure (a) is taken from the attocube datasheet.

no voltage is applied to the piezo, the table is held in place by the friction with the driving element. In the next stage, a sawtooth shaped pulse is applied to the piezo. The table sticks to the driving element through friction and is moved over a distance that is proportional to the applied maximum voltage. Next, by applying a steep drop of the voltage pulse to the piezo, the driving element is accelerated very rapidly over a short period of time, so that the inertia of the movable table overcomes friction and slips. In this fashion, the table disengages from the driving element and remains nearly non-displaced. The net step Δx is now completed and the table remains fixed again at zero voltage. The driving of the nanopositioners is done with an attocube nano-controller where typical values of 20V-30V and 150 Hz-200Hz were used for the amplitude and frequency of the driving signal, respectively. The nano-controller can be controlled either directly from the front panel or, alternatively, with the help of the “DAISY” software provided by attocube. The model ANPz51 is equipped with a potentiometric encoder to read the platform position with a nominal resolution close to 300 nm at cryogenic temperatures. The standard connection to the nano-controller for the reading of the encoder is presented in figure 5.4 (b). The measurement is a three-point measurement of the potentiometer’s resistance, which is determined by the position of the sensor named S₀ in the figure and is in the k Ω range. The three wire configuration helps reducing the heat load and complexity in the resistance measurement. During the experiments I also used the connection shown in figure 5.4 (c) to read the encoder. The principle of the measurement is the same, but the lock-in amplifier is used instead of the nano-controller to read the voltage, V_{in}, from the potentiometer. In this configuration, a typical output voltage in the lock-in is

0.01V, and one of the lock-in channels is used to read the corresponding V_{in} voltage. The advantage of this set-up is a better control in the parameters for the measurement of the potentiometer's resistance, such that optimizing, for example, the time constant of the lock-in amplifier one can obtain a less noisy signal and hence a better resolution of the encoder's reading. Using this configuration, a resolution closer to 200-250 nm was obtained.

For the bending apparatus presented in this section, the transport measurements were performed in the PPMS coupled to the multi-channel lock-in amplifier. An AC excitation current of 50 μA at 177.77 Hz was applied to measure the flexure resistance in a four-probe geometry. The design to accommodate the nanopositioner together with the PPMS resistivity puck is presented in figure 5.5 (a). It includes two pieces: an external cage to fix the nanopositioner to the puck (grey), and a mobile top part fixed to the nanopositioner that is to serve as the "pushing" part (red). Both pieces were made from high purity titanium to match the nanopositioner's material. Figure 5.5 (b) shows the final design assembled together, with electrical contact pads that can be conveniently glued down on the top of the external case. A typical mounting of a sample is presented in figure 5.5 (c).

Key to obtaining a reliable bending motion of the cantilever is a properly designed mating piece on the pushing part. With this in mind, a silicon chip with a sharp FIB-carved edge of around 7 μm width is placed on the pushing part of the apparatus and glued down flat with a thin layer of GE varnish. In this way, an even, well defined contact line between bending edge and sample can be achieved. After this step, the pushing part is lowered down to a safe position and the chip with the bending cantilever is manually placed on the top of the external case at the necessary distance to the bending chip to guarantee the proper engagement of the sharp edge and the cantilever during the bending procedure. The chip with the bending cantilever is usually mounted using a thin layer of either GE varnish or vacuum grease. The latter has the advantage of not drying up quickly like GE varnish, allowing for a more precise positioning of the cantilever, but has the risk of evaporating or dispersing and potentially contaminating the sample. Whether using GE varnish or vacuum grease, it is very important to apply small amounts to avoid undesired residues from coming out of the sides and, most importantly, the front of the chip after pressing it down. Once the cantilever is fixed, the bending chip is moved upwards under the microscope to check for appropriate engagement with the cantilever and to measure the distance from the touching point to the edge of the sample's chip (necessary later to compute the bending angle). This design permits the positioning of the sample far away from the pusher when piezoactuation is not engaged (see figure 5.5 (d)). This is important to avoid any unknown strains from differential thermal conduction during temperature sweeps. In this fashion, the pusher is typically cooled down at a safe distance ($> 100\mu\text{m}$) below the cantilever. Once at base temperature, the pusher is slowly moved upwards to mechanically engage with the cantilever.

Although the main characterization of the Cd_3As_2 samples is presented in the next chapter, it is worthwhile to briefly discuss the transport behaviour when no bending is applied to the cantilevers. Figure 5.6 (a) shows a typical resistance vs temperature curve for the cantilever

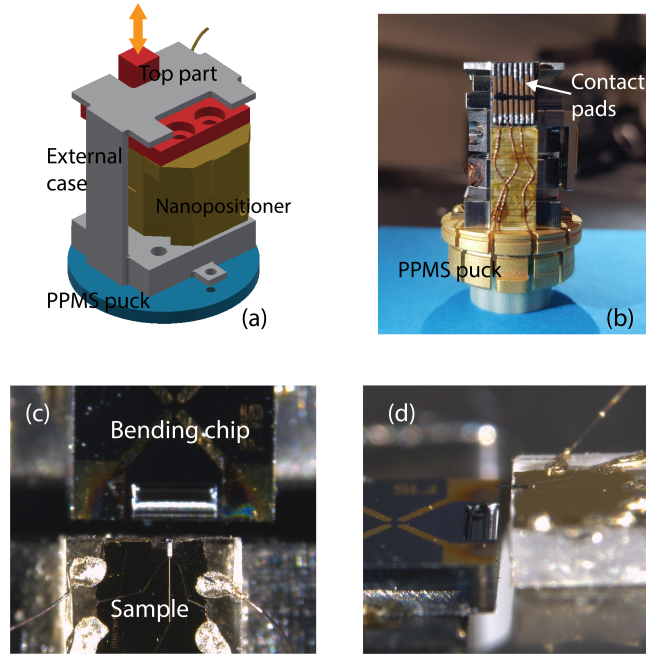


Figure 5.5: **Sample holder for the mechanical bending set-up.** (a) The external case and the top part were designed to mount the nanopositioner on the PPMS puck. (b) Assembled sample holder with contact pads. (c) and (d) show a typical mounting of the sample together with the bending chip.

samples with no bending. As can be seen there, the resistance decreases with temperature, signaling a metallic behaviour characteristic of Cd_3As_2 and consistent with the corresponding curves obtained for other microstructures of this material fabricated in the course of this thesis, as well as those reported in literature [35]. With the set-up described in this section, the magnetic field can only be applied in one direction, namely, in the direction out of the plane of the sample. The MR at 2K and up to 14T is presented in figure 5.6 (b). Clear SdH oscillations are visible, which sit on a background that is mostly linear from 2T onward. The MR at 14T, defined as $\text{MR} = 100\% \times [R(B) - R(B = 0)] / R(B = 0)$, is $\approx 1900\%$, a value that is consistent with the high MR characteristic of TSMs and with some reported values for Cd_3As_2 macrocrystals [149, 150]. To analyse the oscillatory behaviour of the MR curves, the non-oscillatory background is fitted with a polynomial of up to order six and subtracted from the original curves. The field range and exact order of the polynomial fit are optimized to avoid spurious oscillatory components in the signal after the background subtraction. The resulting oscillatory signal is quantitatively analyzed using a Fast Fourier Transform (FFT) algorithm implemented in a MATLAB code. Figure 5.6 (c) shows the resulting FFT spectrum using the field range from 5T to 11T. Two main frequencies are clearly present: one at $F_{\text{Bulk}} = 36\text{T}$ that is consistent with previous reports corresponding to the bulk Fermi surface; and a second frequency $F_{\text{Weyl}} = 61\text{T}$ that agrees well with those reported for the Weyl orbits [35, 151].

To check for the stability with time of the transport properties of the unbent cantilevers, several

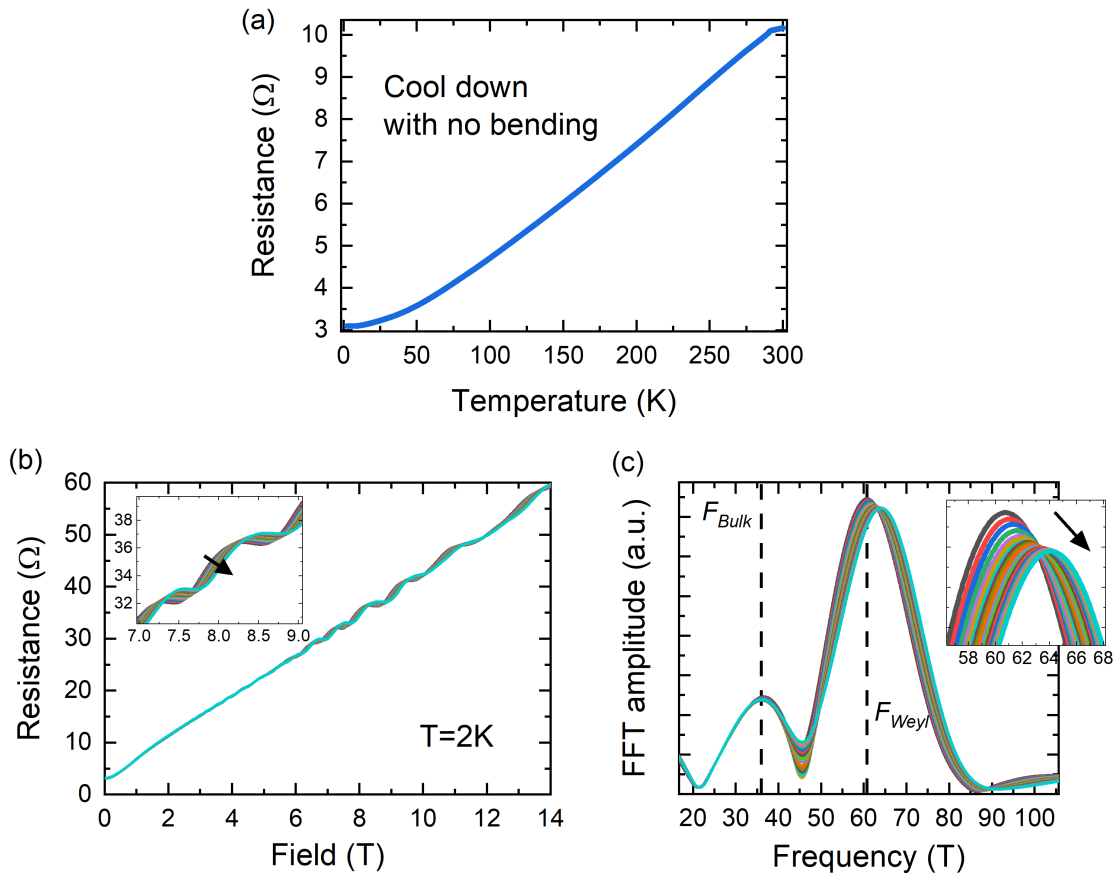


Figure 5.6: **Transport behaviour of Cd_3As_2 cantilevers without bending.** (a) Resistance vs temperature of the cantilevers showing a typical metallic behaviour. (b) Magnetoresistance vs field at 2K for several consecutive field sweeps taken roughly every hour. The inset highlights a drift in the curves with time. (c) FFT of the corresponding oscillatory part in (b) after a background subtraction. The inset highlights the corresponding drift in the peak of F_{Weyl} with consecutive runs.

measurements were made consecutively with a waiting time of about one hour between successive field sweeps. This diagnostic is of the utmost importance to establish a solid reference and to later differentiate clearly the effects coming from bending and not from other factors related to the apparatus. Figures 5.6 (b) and (c) show the MR and corresponding FFT spectrum of the consecutive measurements. The main observation is that a drift in the MR curves was detected, which translated into a drift of the F_{Weyl} peak in the FFT spectrum from 61T to higher values, eventually saturating around 64T-65T more than 36 hours after the initial field sweep. It was verified that this drift was not associated to any numerical artifact in the treatment of the data, for example, during the calculation of the FFT. The F_{Bulk} remains almost unchanged during this time, with less than a 0.5T shift in frequency. Although the origin of this drift is not clear, several other observations were made trying to shed some light into the matter. For example, it was observed that after warming up to around 100K-200K and cooling down again to 2K, one would typically obtain a F_{Weyl} peak closer to 61T, and then the drift to higher frequencies would start again until saturation. This could, for example, point to a relaxation process in the mechanical state of the cantilever, which after cooling down transitions slowly to its final equilibrium state. Another possibility considered had to do with thermal coupling of the sample in the set-up and the chance of some sort of thermal leakage or local heating. To test this possibility more Helium gas was released in the sample space at 4K with the aim of improving the thermal link to the sample. This did have a small effect in reducing the time for the saturation of F_{Weyl} , although the final value after saturation remained close to 65T. The current through the sample was also reduced to $5\mu\text{A}$ in case local current heating was present but no effect was observed after this change. To have a more definite picture of the physical situation and the origin of the drift in F_{Weyl} , further investigations are required to understand what happens microscopically when the cantilever is cooled down. Whatever the case, based on the observed F_{Weyl} drift, all subsequent measurement strategies using the bending apparatus always included initial field sweeps well separated in time to make sure that the final saturation in F_{Weyl} was reached.

A critical point in the technique described here is to detect the moment of contact between the pusher and the cantilever. This can be done by observing a change in the resistance of the sample at constant magnetic field. Given the extreme magnetoresistance typical of TSMs [12], a strong response of the resistance even to small angle changes between the field and the cantilever is expected. Indeed, a sharp anomaly signals the touching point followed by a strong decrease of the MR with increasing bending in the Cd_3As_2 cantilevers (see figure 5.7(b)). In combination with the displacement readout of the piezo drive, this allows to *in situ* calibrate the relative distance between cantilever and pusher.

One issue to be addressed with this experimental set-up is to avoid any kind of twisting of the cantilever as the nanopositioner moves upwards and bends the sample. To minimize this undesired effect, several strategies were taken. One of them was to place above the titanium top piece a sapphire chip with a silver wire of $25\mu\text{m}$ in diameter attached along its edge. The idea was to use the wire as a well defined contact region and given its rounded shape, reduce the effect of any tilting of the chip in the direction perpendicular to the edge. As it was difficult

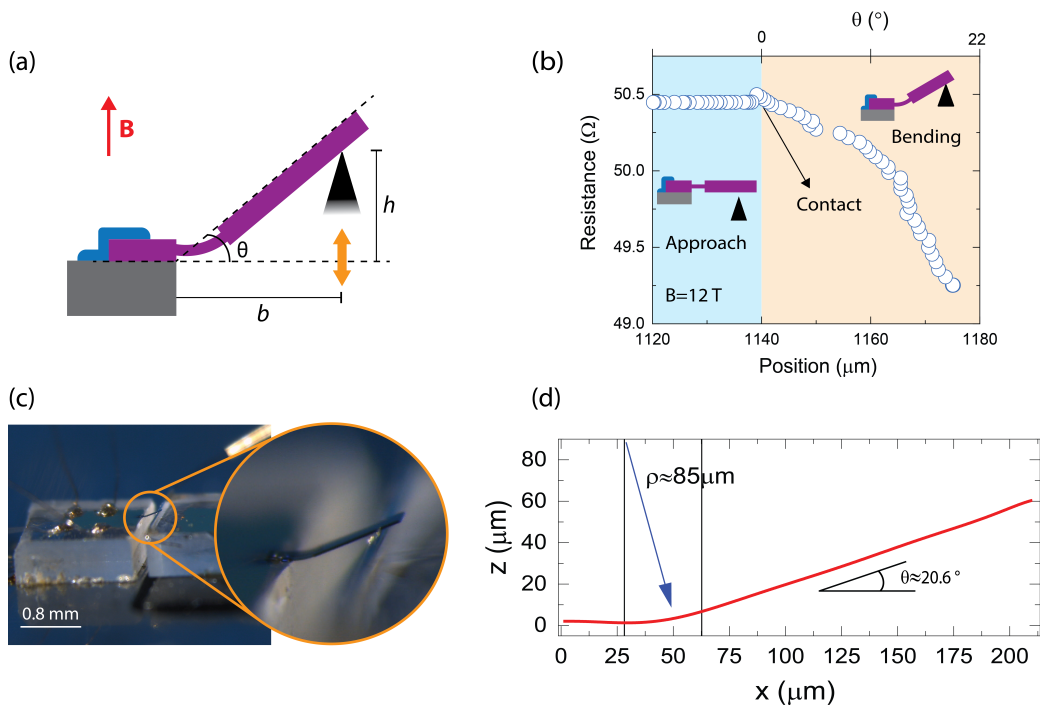


Figure 5.7: **Approach and bending procedure.** (a) Schematic diagram of the cantilever during bending (b) Approach and bending cycle as monitored via the change in the cantilever's magnetoresistance. (c) With this design we can elastically bend the cantilever by more than 20° . (d) Experimental profile of a bent cantilever, obtained from an optical image, showing the measured radius of curvature and corresponding bending angle.

to place the silver wire completely flat and straight, some tilting might have persisted. A second strategy was to fabricate a cantilever with a triangular end instead of a rectangular one. In this fashion, the contact with the cantilever would be at a very small point, making any tilting effects negligible. The risk in this case is to make the cantilever too flexible at the “paddle” section so that the bending is not confined to the thinner legs. In the end, the approach taken was to use a silicon chip with a very sharp FIB cut edge of around $7\ \mu\text{m}$ in width to bend the cantilever. In this way, a flat, well defined contact point can be achieved. Although a torsional motion is difficult to eliminate completely, this approach produced very good results both with rectangular and triangular shaped samples.

The bending angle θ is approximated by solving a numerical equation: $\tan(\theta) = (h + t / \cos(\theta)) / b$, where h is the nanopositioner’s height from the touching point, t is the thickness of the free end of the cantilever and b is the distance from the edge of the sapphire chip to the pushing part (figure 5.7(a)). One may approximate the mechanical situation using the simple relation from beam theory under bending strain: $1/\rho = \theta/d$, where ρ is the radius of curvature and d is the length of the sample’s central flexure [152]. This leads to a radius of curvature of $\rho \approx 79\ \mu\text{m}$ and a bending angle of $\theta = 21.7^\circ$ for the maximum nanopositioner’s height used, $h \approx 60\ \mu\text{m}$. These values are in good agreement with a direct analysis of the optical image of a bent cantilever with a similar h (figure 5.7(d)), from which we obtain a bending angle of $\theta \approx 20.6^\circ$ and a radius of curvature of $\rho \approx 85\ \mu\text{m}$. Using the expression for the strain on a thin beam $\varepsilon_{xx} = z/\rho$, one estimates the value of the strain gradient as $d\varepsilon_{xx}/dz = 1/\rho \approx 1.3\% \mu\text{m}^{-1}$. The value of the the surface strain is then calculated to be $\varepsilon_{xx} = 0.65\%$, which compares well with the value obtained in the finite element simulations (figure 5.2(c)). These simulations also suggest a rather uniform strain distribution on the flexures surfaces.

It is important to check for possible plastic deformation of the cantilever, especially given the substantial bending angles in the experiment. A first indication is given by a comparison of the MR at zero bending before and after bending to a large angle, $\theta = 21.7^\circ$ (figure 5.8(a)). Indeed, the curves overlap both in the low-field region, indicating an unchanged residual resistivity, as well as in the high-field region, supporting an unchanged value of $\omega_c\tau$ (ω_c : cyclotron frequency, τ : quasiparticle lifetime). This strongly suggests an unchanged defect landscape and, hence, an unchanged τ . The presence of quantum oscillations further provides insights into the quantum transport (figure 5.8(b)). The results of figure 5.8 were taken at 4K with an increased amount of Helium gas in the sample space and after making sure that no drift in F_{Weyl} was observed. As before, the oscillations are analyzed using the FFT in the field range from 5T to 11T, after subtracting a sixth-order polynomial background to remove the non-oscillatory part of the MR. No resolvable change in F_{Bulk} nor F_{Weyl} is observed after bending, suggesting that no effects like increase of quantum scattering time nor remnant deformation of the Fermi surface are produced by the application of the strain gradients. There is a subtle difference in the amplitude of F_{Weyl} peak that is compatible with differences in the subtracted polynomial background. These signatures together paint a consistent picture of elastic bending without plastic deformation. Under strong bending, the Weyl oscillation shifts to higher frequencies at reduced amplitude, while the bulk remains unchanged. It is intriguing

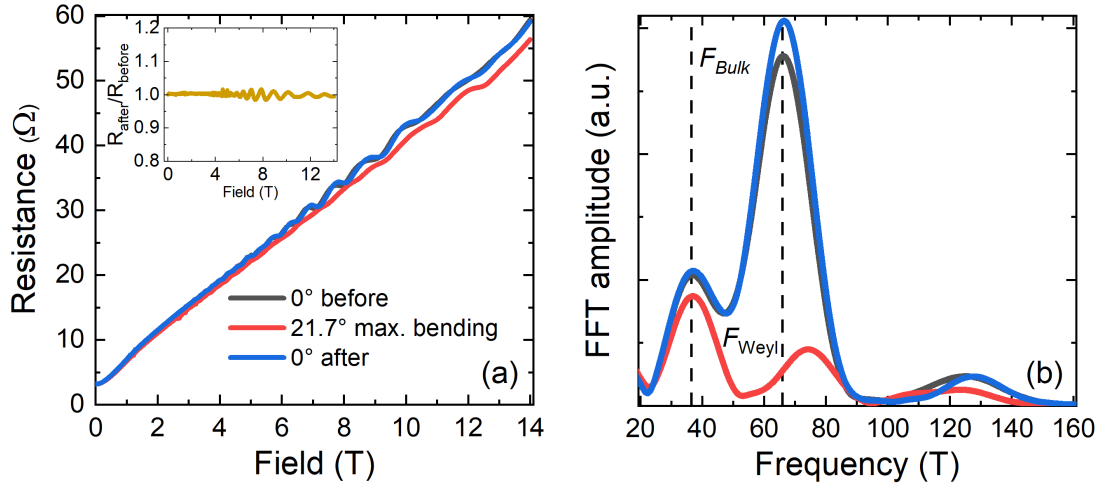


Figure 5.8: **Quantum oscillations before and after maximum bending.** (a) Resistance vs magnetic field at 4K and (b) the corresponding FFT spectrum after background subtraction. The inset in (a) shows the ratio between the magnetoresistance after and before maximum bending. The magnetic field direction is the same as the one depicted in figure 5.7(a).

to note that the direction of the frequency increase is compatible with theoretical predictions of pseudo-field effects in Cd_3As_2 [33]. These results will be discussed in more detail in the next chapter.

5.3.2 Probe for bending and rotation

The rotation of samples with respect to the applied magnetic field has become a standard capability in experimental set-ups given its importance in characterizing different physical phenomena like the change in shape and dimensionality of Fermi surfaces, the evolution of magnetoresistance or the identification of finite-size effects in nanostructures. In the context of pseudo-fields this capability is particularly pertinent since the change in the magnetic field direction with respect to the sample can lead to an amplitude modulation and a frequency variation of the Weyl orbits that is similar to the one predicted for the existence of strain-induced pseudo-fields [35]. Technically, this imposes the challenge of having a set-up with the capability to rotate and bend the samples at the same time, in contrast to the previous set-up where the magnetic field direction is kept fixed. To this end a probe with a mechanical rotator was fitted to accommodate a nanopositioner with which to perform the mechanical bending (see figure 5.9). This probe was built to be used with one of the available cryostats in the laboratory¹. Given the space constraints of the new probe, it was not possible to have a resistive encoder together with the nanopositioner to read its displacement during bending (the model ANPz30/HV was used, which is the smallest one manufactured by attocube).

¹Dr. Carsten Putzke, a postdoctoral member of the QMAT laboratory, was responsible for building the probe described in this sub-section

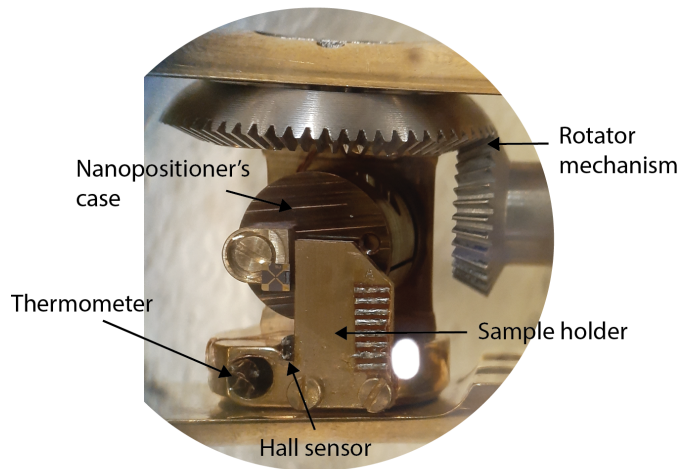


Figure 5.9: **Probe with mechanical rotator and attocube nanopositioner to perform bending experiments.** The probe is also equipped with a thermometer and a Hall sensor. Given the space constraints, it's not possible to have a nanopositioner with an encoder to read its position.

To quantify such a displacement I used a piezo-resistive cantilever from a torque magnetometry chip (see figure 5.10 (a)). The chip was cut to have only the longest available cantilever on the chip extending from the edge (see figure 5.10 (b)). Using a wire bonding machine, suitable electrical leads were attached to the contact pads to perform a resistance measurement. The idea is to use the cantilever as a displacement sensor by measuring the change in MR (at fixed temperature and magnetic field) when bending is done with a known vertical displacement. Such a measurement was done with the bending set-up described in the previous section, with which the calibration curve shown in figure 5.10 (c) was obtained. The approach adopted here was to use the torque cantilever as displacement sensor by mounting it together with the sample, as shown schematically in figure 5.10 (d), with the aim of engaging with both every time the bending procedure is initiated.

The final mounting and bending procedure carried out when using the rotator probe is presented in figure 5.11. The sample shown in figure 5.11 (a), referred to as Sample 2, is a different Cd_3As_2 sample to the one used for the previous case of bending without rotation. As in that case, a silicon chip is used to have a well defined edge to engage with both cantilevers (like before, the edge used to bend the sample has been sharpened with the FIB). A key point and one of the main difficulties with this approach is that the bending chip should touch first the piezo-resistive cantilever and then the sample, such that the full bending angle of the latter can be accounted for. To this end the torque cantilever had to be mounted upside down on a sapphire chip of the same kind used to mount the sample, so that both are roughly at the same height. After mounting, the bending chip is moved upwards under the microscope to check that it touches first the torque cantilever and then the sample.

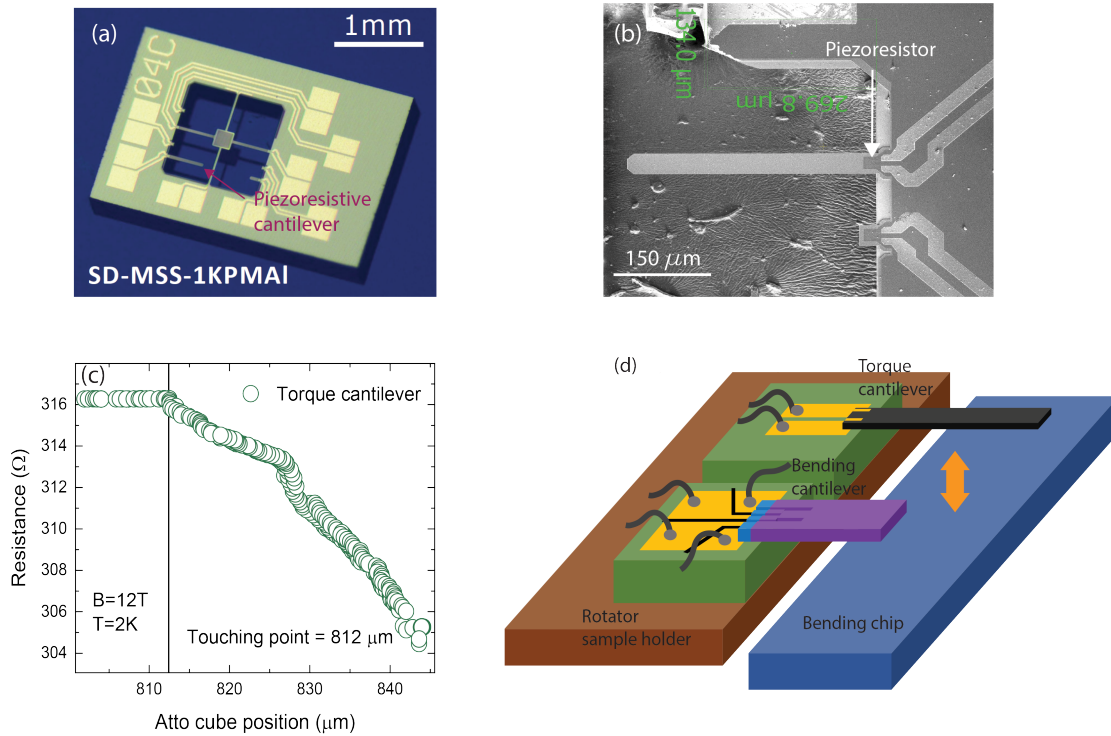


Figure 5.10: **Piezo-resistive cantilever from torque magnetometry chip.** (a) Original chip from NANOSENSORTM. (b) SEM image of the cantilever used as a displacement sensor. (c) Measured magnetoresistance vs displacement calibration curve of the torque cantilever at 2K and 12T. (d) Schematic diagram of the final mounting on the rotator probe including both torque and bending cantilevers.

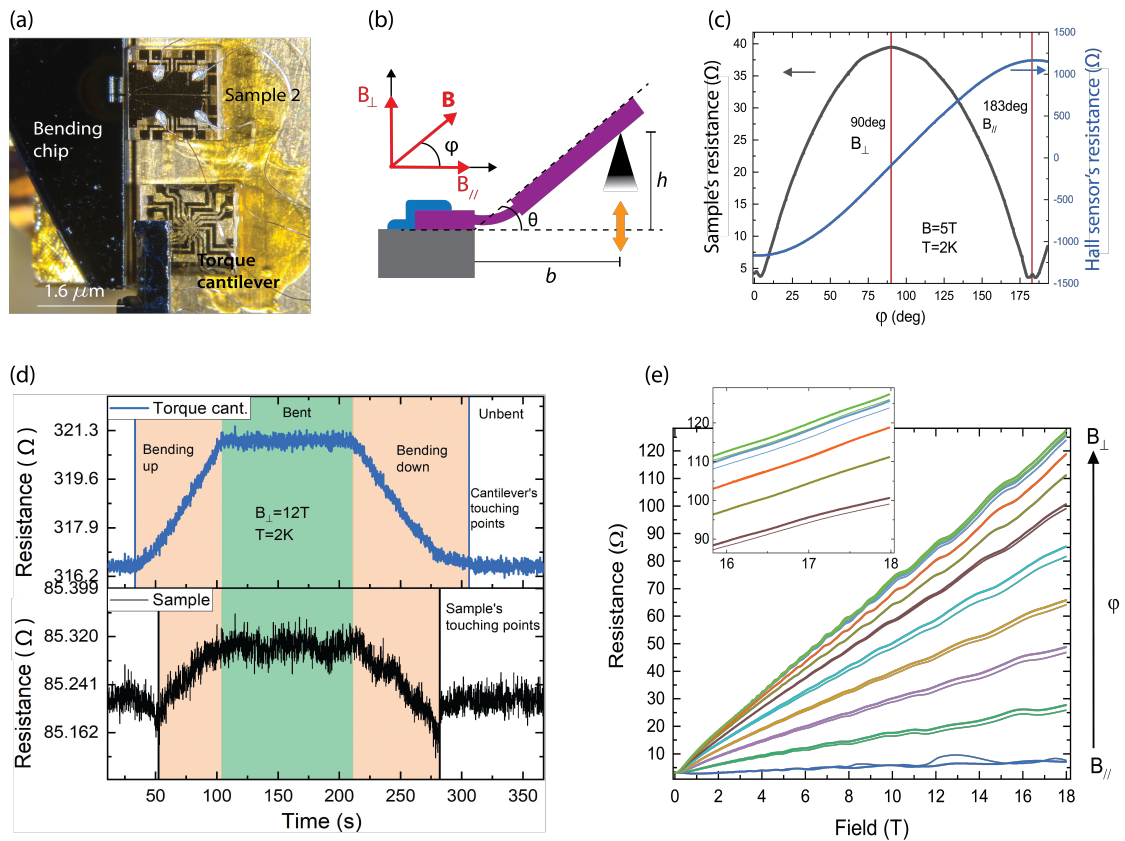


Figure 5.11: **Bending and rotation mounting and bending procedure.**(a) Mounting of the sample together with the torque cantilever. (b) Schematic diagram of the cantilever during bending and definition of the rotation angle φ . (c) Magnetoresistance vs φ for both cantilever and Hall sensor at 5T, highlighting the directions perpendicular, B_{\perp} , and parallel, B_{\parallel} , to the sample. (d) Approaching and bending procedure for both sample and torque cantilever. (e) Magnetoresistance vs field for the unbent (thick lines) and bent (thinner lines) sample at different rotation angles in steps of 10 degrees from B_{\parallel} to B_{\perp} .

The general procedure to approach the sample is exactly the same as in the bending without rotation case, with the additional step that first the right direction of the magnetic field must be determined, that is, the field must be perpendicular to the plane of the unbent sample. This is accomplished by a rotation under fixed field, as shown in figure 5.11 (b). The maximum and minimum in the MR of the sample, as well as the signal from the Hall sensor, clearly indicate when the field points in the directions perpendicular (denoted B_{\perp}) and parallel (denoted B_{\parallel}) to the unbent sample's plane, respectively (naturally, the MR of the sample is minimum when the field is parallel to the applied current). Once the B_{\perp} direction is determined, the approach is done with this field configuration (see figure 5.11 (c)). As in the bending without rotation case, the change in MR at low temperatures indicates the touching point with the bending chip, which in the experiment shown in figure 5.11 (c) clearly engages first with the torque cantilever and then with the sample. The figure also suggests that the bending is done reversibly since the torque cantilever and sample's resistances return to their initial unbent values after lowering the bending chip to disengage with both. One thing to notice in figure 5.11 (c) is that the MR of the torque cantilever increases with bending, in contrast to figure 5.10 (c) where it decreases. This is due to the fact that the cantilever is mounted upside down in the case of figure 5.11, as was mentioned before. The assumption here is that the MR behaves symmetrically with respect to the unbent value. With this consideration and from the MR value of the torque cantilever at the touching point of the sample and at the bent plateau shown in figure 5.11 (c), a vertical displacement of $13.3\mu\text{m}$ was estimated for the sample, which translates to a bending angle of $\theta \approx 5^{\circ}$.

Regarding the sample's behaviour, figure 5.11 (c) shows a slightly increasing MR with bending, instead of a decreasing one as exhibited by the sample used in the previous bending without rotation case. Although the exact reason for this is not clear, it's likely that in this case it happened due to a small angle mismatch when approaching the actual B_{\perp} direction during the bending procedure. This is consistent with the resistance value in the unbent state of the sample in figure 5.11 (c) being slightly lower than the corresponding one shown in figure 5.11 (d), $\approx 85.2\Omega$ vs $\approx 86.5\Omega$, respectively. That figure shows the field dependence of the MR for both the unbent (thin lines) and bent (thick lines) cases at different values of the rotation angle φ . Such a mismatch could originate from the mechanical backlash associated to every mechanical rotator, although in all the experiments carried out with this probe (including the results presented in figure 5.11) the rotation angles were always changed monotonically, either in an increasing or decreasing way, to avoid the rotator backlash when changing the direction of change. In general, whether the MR increases or decreases with bending during the approach procedure will depend on the exact shape of the MR vs rotation angle at the chosen values of field and temperature. In other words, it will depend on whether the MR decreases monotonically with respect to the rotation angle around the B_{\perp} direction or whether the MR value at B_{\perp} is not actually an absolute maximum. This last option is particularly likely if, for example, the amplitude of the quantum oscillations is relatively big around B_{\perp} . Such a situation is more clearly observed in figure 5.12, where the results for an additional test sample (Sample 3) are presented. Figure 5.12 (a) shows the MR vs rotation angle at 5T for both

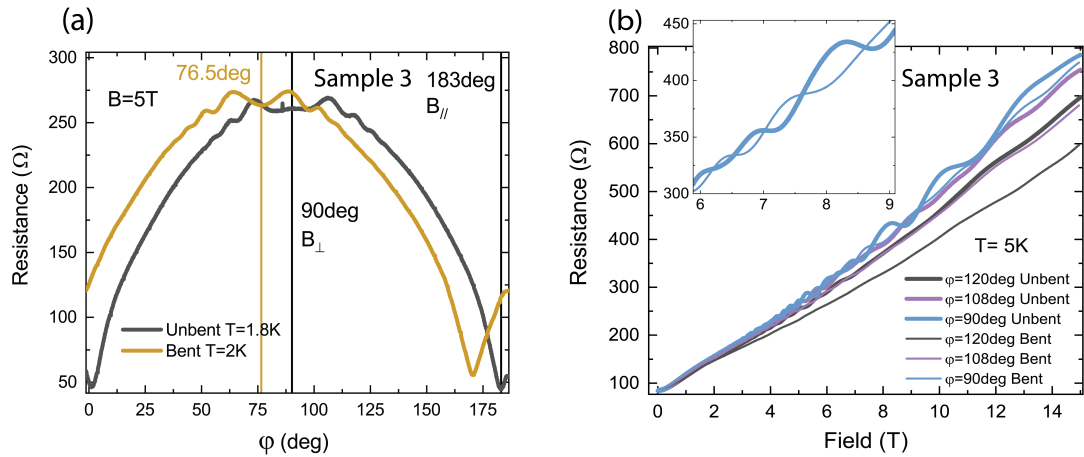


Figure 5.12: **Rotation and bending for sample 3.** (a) Magnetoresistance vs ϕ for both bent and unbent case. The bending angle for the bent case was $\theta \approx 25.5^\circ$ (b) Magnetoresistance vs field for the unbent (thick lines) and bent (thinner lines) sample. The inset highlights the behaviour at medium field range where there are field values for which the MR can be smaller or bigger for the bent case compared to the unbent case.

bent and unbent states. The bending angle for the case shown in that figure was estimated to be $\theta \approx 25.5^\circ$. As can be seen in figure 5.12 (a) the curve for the unbent state doesn't have an absolute maximum at the B_\perp direction. The corresponding curve for the bent case remains very similar in shape to the unbent one only that it's shifted down in angle around 13.5° . This results in angle ranges where the MR is expected to increase with respect to the unbent case, for example, from $\phi = 78^\circ$ to $\phi = 96^\circ$, and others where it is expected to decrease, for example, from $\phi = 100^\circ$ to $\phi = 177^\circ$. This behaviour is highlighted in the inset of figure 5.12 (b), where the field dependence of the MR for both the unbent (thin lines) and bent (thick lines) cases at different values of the rotation angle ϕ are shown (although the temperatures in figures 5.12 (a) and (b) are different, the MR doesn't vary much at low temperatures). As can be seen there, there are some field values, especially in the medium to low field range, for which the MR in the bent state is actually larger than in the unbent case. At higher field values, however, the tendency is to have a smaller MR with with bending, as exhibited by both samples 2 and 3. The main point to take away from the results of figures 5.11 and 5.12 is that the set-up for bending and rotation works well and that the results obtained for the test samples are consistent with what was presented in the previous section for the bending without rotation case. The focus in this section is on showing the feasibility of the set-up and not on the detailed analysis of the MR and quantum oscillations in the context of pseudo-fields, which will be done in the next chapter.

Although in the experiment shown in figure 5.11 (c) it was possible to bend the torque cantilever first and then the sample, this was not always the case in other experiments where different samples were used, including the one presented in figure 5.12. This in spite the check done under the microscope at room temperature. The reasons for such behaviour are

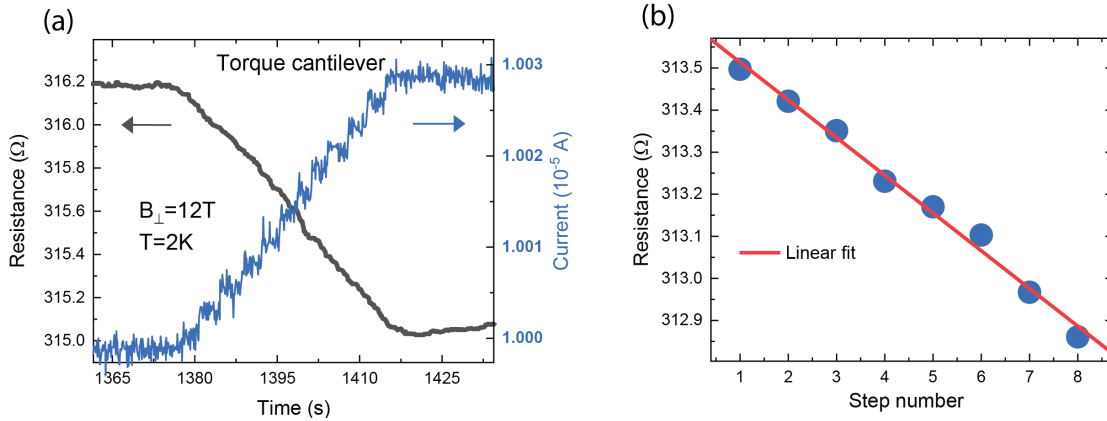


Figure 5.13: **Nanopositioner step size characterization.** (a) Magnetoresistance and current of the torque cantilever vs time during the bending procedure. Each bending step can be clearly observed as plateaus in the current curve. (b) Resistance values corresponding to each current plateau in (a) vs step number. The line is a linear fit from which a ratio of resistance change per step can be determined.

not entirely clear but it highlights the necessity to have a very precise control in the relative positioning of the torque cantilever and sample, which can be seen as the main challenge with this approach and one of the aspects to optimize in future applications. An alternative way to estimate the vertical displacement without the necessity to rely on the precise engagement of the bending chip is to characterize the step size of the nanopositioner in the conditions of field and temperature used during the bending process. This is shown in figure 5.13, where the same torque cantilever is bent in the probe at 2K and $B_{\perp} = 12\text{T}$ and using 177Hz and 30V for the control parameters of the nanopositioner. This time the torque cantilever was not mounted upside down but with the same configuration shown in figure 5.10 (c), which is why the MR decreases with increase bending. The main observation in figure 5.13 (a) is that it is possible to clearly resolve each step of the nanopositioner in the plateaus exhibited by the current applied to the torque cantilever as it is bent upwards. During this measurement no current regulation option in the lock-in amplifier was used since that would make the observations of the current plateaus more difficult. Such plateaus were not so clearly resolved in the resistance and because of that the current plateaus were used to associate each bending step with a resistance value. With this procedure the plot shown in figure 5.13 (b) was obtained, where using a linear fit a ratio of resistance change per step can be determined. Combined with a similar linear fit of the decreasing MR with increasing vertical displacement shown in figure 5.10 (c), this ratio can be used to finally obtain an estimation of $0.25\ \mu\text{m}$ per step taken. This value compares well with the nominal step size for the nanopositioner model, as claimed by attocube. In figure 5.10 (c), 50 steps were taken to bend the sample, which translates to $12.5\ \mu\text{m}$ of vertical displacement, a value that is also reasonably close to the one reported in the previous paragraph for sample 2. In the case of Sample 3, 200 steps upwards were taken, which translates to the aforementioned $\theta \approx 25.5^{\circ}$ of bending angle.

5.4 Conclusions and outlook

I have presented a set-up for the controlled application of large strain gradients on crystalline FIB-microstructured cantilevers of 3D TSMs that have been designed for transport measurements down to cryogenic temperatures. Despite the large deformation, transport evidences this to be well within the elastic limit. This experimental methodology and apparatus presents a first, crucial step towards the creation of pseudo-magnetic fields in 3D TSMs. Yet the versatility of the fabrication technique allows to apply this approach to a large variety of crystalline materials beyond the direct scope of effective magnetic fields. For example, strain gradients may tune further topological phenomena such as topological phase transitions and high order topological phases [153–157]. Furthermore, if strain gradients can produce additional effects beyond changing the position of the Weyl points, such as creating tilt gradients of the Weyl cones, it is possible that additional physical phenomena can be accessed [158, 159]. Current theoretical models assume weak strain gradients and that the overall shape of the strained objects remains almost unchanged. The results presented here clearly call for further theoretical studies of quantum states in TSMs under strong strain gradients that significantly distort the shape of the physical crystal. Thanks to the fabrication possibilities accessible with the FIB, other approaches for the application of strain to microstructures are also possible. For example, in the QMAT laboratory samples have been fabricated with a design similar to the one presented in this chapter but where a voltage is applied between the "paddle" section and a Au contact underneath it. The principle is to produce a mechanical bending from the associated capacitive force between the the paddle section and the Au contact. Preliminary results have shown that such bending is actually feasible, which could potentially simplify the apparatus necessary to attain large strain gradients. Not only strain gradients through bending could be explored, test microstructures with a small rectangular section subjected to a torsional deformation have also been fabricated. With strong strain gradient fields now controllably available in 3D solids, new ideas to create and control distorted quantum materials can be realized in the future.

6 Mechanical bending of Cd₃As₂ cantilevers

6.1 Introduction

This chapter summarizes my efforts to detect pseudo-fields in bent Cd₃As₂ cantilevers. These challenging experiments uncover that much is left to understand in the Landau quantization of crystals under strong lattice gradients. The complexity of this problem ultimately prevented an unambiguous identification of pseudo-field predictions based on simplified toy models applied to the complex data. These results, however, are very encouraging to advance the subject on both the theoretical and experimental side. In the following, I lay out the rationale that brought me to this conclusion.

The existence of pseudo-electromagnetic fields in 3D WSMs is predicted to give rise to a number of physical phenomena such as the enhancement of longitudinal conductivity [34, 160], collapse of pseudo-Landau levels [161], emergence of chiral magnetic waves [162], flow of quasi-1D currents circulating along dislocation lines [135, 163], magnetic focusing of chiral Weyl fermions at different spatial locations [164] and zero magnetic field quantum oscillations [165], among many others. In spite of this rich predicted phenomenology, the experimental verification of pseudo-electromagnetic fields in 3D WSMs remains elusive. In this chapter I investigate experimentally the model proposed by Pikulin and Ilan [33] to detect pseudo-magnetic fields by exploring their effect on the QOs coming from the Weyl orbits. The basic idea is depicted in figure 6.1. In the presence of both \mathbf{B} and \mathbf{B}_5 , the particles in the bulk move according to the total effective magnetic field acting on the Weyl nodes, which includes both the external and the strain-induced one: $\mathbf{B}_\chi = \mathbf{B} + \chi\mathbf{B}_5$, where $\chi = \pm 1$ denotes the chirality of the node. For example, for a strain profile such that the Weyl node separation is $\mathbf{k}_0(z) = (b_0 - B_5 z)\hat{y}$, a homogeneous pseudo-magnetic field results, $\mathbf{B}_5 = \nabla \times \mathbf{k}_0 = B_5 \hat{x}$. Assuming \mathbf{B} along the z direction (see figure 6.1), the effective length of the bulk part of the Weyl orbit increases from $2L$ to $L_{eff} = 2L\sqrt{1 + (B_5/B)^2}$ and the energy levels of the system are given by:

$$\varepsilon_n = \frac{2\pi v_F \hbar (n + \gamma) - k_0 \mu_0 l_B^2 \hbar}{L_{eff} + k_0 l_B^2} \quad (6.1)$$

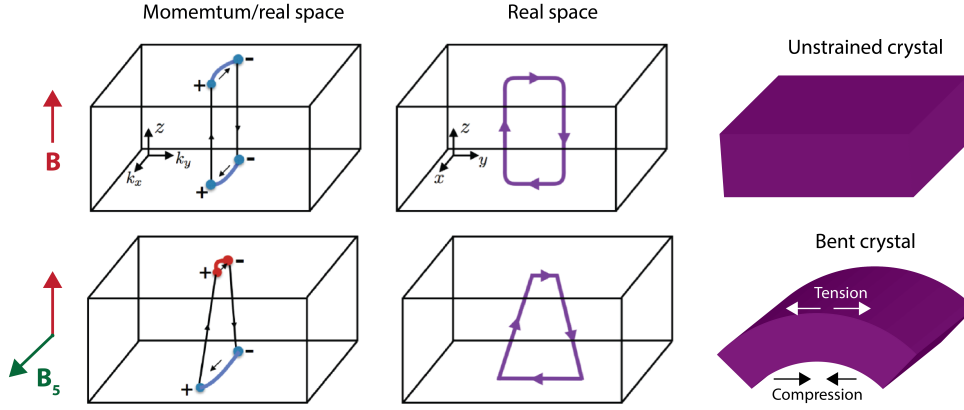


Figure 6.1: **Effect of pseudo-magnetic fields on the Weyl orbits.** When a magnetic field \mathbf{B} is applied in the z direction and a strain-induced pseudo field \mathbf{B}_5 is generated in the x direction, the top and bottom Fermi arcs change lengths and the bulk trajectories are tilted. The strain caused by bending the sample is a way to generate these pseudo-fields. Image adapted from [33].

where $l_B = \hbar/eB$ is the magnetic length, and μ_0 is a chemical potential offset that takes into account the variation of the Fermi arcs' length at finite chemical potential μ if the bulk FS projection takes up part of it [123]. Equation 6.1 dictates that under a varying magnetic field B , the n th energy level crosses the chemical potential and gives rise to peaks in the density of states, i.e, quantum oscillations, at fields B_n given by the condition $\varepsilon_n(B_n) = \mu$. The most important consequence of this is that the Weyl orbits' oscillations are not necessarily periodic in $1/B$ but the separation between the peaks, $\Delta(1/B)$, can become field, pseudo-field and thickness dependent. In the case of a small B_5 , the resultant peak separation is $\Delta(1/B) = 2\pi e/(S_k + \mu eLB_5^2/Bv_F)$, where $S_k = k_0(\mu + \mu_0)/v_F$ is the momentum space area enclosed by the Fermi arc section of the Weyl orbits. These oscillations are clearly not periodic in $1/B$. In the opposite case of $B_5 \gg B$, the peak separation is $\Delta(1/B) = 2\pi e/(S_k + 2\mu eLB_5/v_F)$, making the oscillations periodic in $1/B$ but with a higher frequency that scales with B_5 . Experimentally, one way to produce and detect pseudo-fields is by bending the sample in the presence of a varying external magnetic field \mathbf{B} , as shown schematically in figure 6.1. As already described in the previous chapter, bending causes compressive and tensile stresses that lead to strain gradients across the sample. By controlling how much the sample is bent, it is possible, in principle, to tune B_5 . In this fashion, transport measurements could reveal the effect of B_5 on the oscillatory signature of the Weyl orbits. A key point in this regard is the characteristic strength of the pseudo-magnetic field, which has been predicted to range from $B_5 \approx 0.3T$ for a twisted nanowire of Cd_3As_2 [160] to $B_5 \approx 15T$ for a thin film of the same material [165]. The numerical model presented in [165] is actually pertinent for the experimental set-up proposed in this thesis and can be used to calculate the predicted B_5 magnitude under bending. The situation described in the model is presented in figure 6.2. Following the pseudo-field formalism, the effect of the induced strain gradient is to modify the electron tunneling amplitudes in the model, which is treated by the introduction of a gauge potential, \mathbf{A} ,

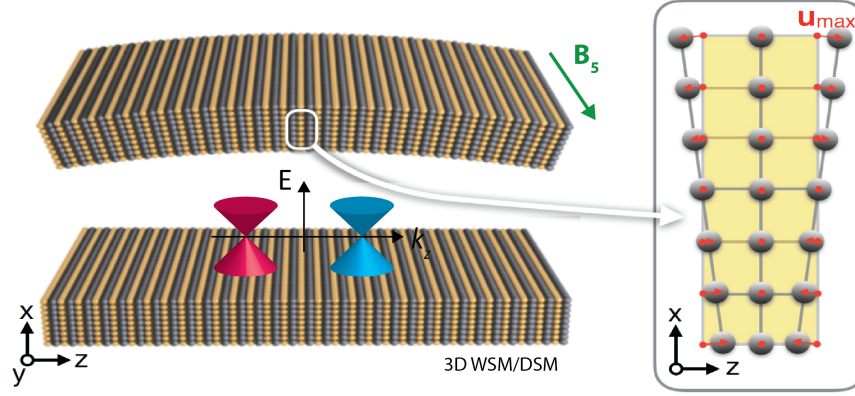


Figure 6.2: **Pseudo-magnetic field B_5 created in a bent slab of a WSM or DSM.** The corresponding numerical model suggests a magnitude of up to $B_5 \approx 8.6T$ for a bending angle of $\theta \approx 30^\circ$. Image adapted from [165].

whose components depend on the displacement field created by the bending (schematically depicted in figure 6.2). After inserting the relevant numerical constants for Cd_3As_2 , the final magnitude of $\mathbf{B}_5 = \nabla \times \mathbf{A}$ is estimated to be:

$$B_5 = (246T)2\theta t/L \quad (6.2)$$

where t is the thickness of the the sample, L its length and θ is the bending angle. For the bending angles available experimentally, up to $\theta \approx 30^\circ$, equation 6.2 predicts $B_5 \approx 8.6T$, which should be large enough to appreciably modify the Weyl orbits' extension, yet it would not necessarily become the dominant field scale (as in the limiting case $B_5 \gg B$) for the experimentally available external fields of up to 18T.

Having established the technique for the mechanical bending of FIB-fabricated cantilevers in the previous chapter, in this chapter I concentrate on the experimental findings of bending Cd_3As_2 cantilevers and discuss the potential presence of strain-induced pseudo-magnetic fields. I begin by describing in the next section the known electronic properties of the material Cd_3As_2 . The following section presents the main experimental results, starting with the angle dependence of the quantum oscillations from the cantilevers under zero strain, followed by the static bending experiments and finally the results for simultaneous bending and rotation. I end the chapter presenting the main conclusions and giving an outlook.

6.2 Cd_3As_2 material characteristics

In addition to the existence of the nodes, the observation of transport properties of TSMs, such as electrical and thermal conductivities, requires that the Fermi level be near such nodes, making the search for this kind of materials non trivial. After the theoretical predictions by Wang et al [91] that Cd_3As_2 might host 3D Dirac-like nodes at its Fermi level, there was a

renewed interest in the electronic characterization of this material. It had been studied in the past mostly because its high mobility of electrons: more than $10^4 \text{ cm}^2/\text{Vs}$ at room temperature and $10^6 \text{ cm}^2/\text{Vs}$ at low temperatures. The crystal structure of Cd_3As_2 is rather complex and the exact details are still a matter of research. Currently, it is believed to have a tetragonal unit cell of $a = b \approx 1.26 \text{ nm}$ and $c \approx 2.54 \text{ nm}$, showing no structural transition at lower temperatures [69]. This cell contains a total of 160 atoms, 96 Cd and 64 As (see figure. 6.3 (a)). Most evidence suggests a centrosymmetric space group: $I4_1/acd$. This observation, and the fact that Cd_3As_2 doesn't show any kind of permanent magnetism, guarantees the presence of both time reversal and inversion symmetry, ensuring that the Dirac nodes are not split into Weyl nodes. The theoretical predictions suggest a band structure like the one sketched in figure. 6.3 (b) and (c). Two 3D Dirac nodes are located on the tetragonal c axis, equidistant from the Brillouin zone center Γ at positions $\pm k_D$, and protected from gapping by the C_4 rotational symmetry of the crystal. Data collected by ARPES has shown clear evidence of conical bulk valence and conduction bands in Cd_3As_2 , as can be seen in figure 6.3 (d) and (e) [94–96, 166]. The measured values of E_D , the maximum energy distance between the bands (see figure. 6.3 (b)), are in the order of a hundred meV . This means that the bands are linearly dispersive only in a rather small energy window, making the appearance of topological effects susceptible to changes in the Fermi level due to defects or impurities. The Fermi surface of Cd_3As_2 consists of two small, almost spherical ellipsoids centred at the nodes [167, 168]. These measurements also reveal a large, non-saturating, linear MR [150, 169]. In general, the application of a magnetic field in transport measurements breaks time reversal symmetry, making the the Dirac nodes split into two Weyl nodes of different chirality.

6.3 Experimental results

6.3.1 Angle dependence of quantum oscillations without bending

In this section I present the results of the angle dependence measurements of MR under zero strain. The purpose of these experiments is twofold: first, to further characterize the samples by mapping the corresponding Fermi surface and identify any possible effect of the cantilever design and dimensions on the transport properties of Cd_3As_2 ; and second, to later compare the effect on the Weyl orbit's frequency of changing the direction of the external magnetic field versus that of increasing the magnitude of the strain-induced pseudo-magnetic fields. Both of them can lead to similar experimental features.

6.3.1.1 *In-plane* rotation

First, the results of the rotation studies where the field direction is changed *in the plane* of the large surfaces of the sample, that is, from the crystallographic [001] to the [100] direction, are considered. No Weyl orbits are expected nor observed in this field configuration due to the shape of the cantilever. Instead, the results form a baseline of bulk quantization and semi-

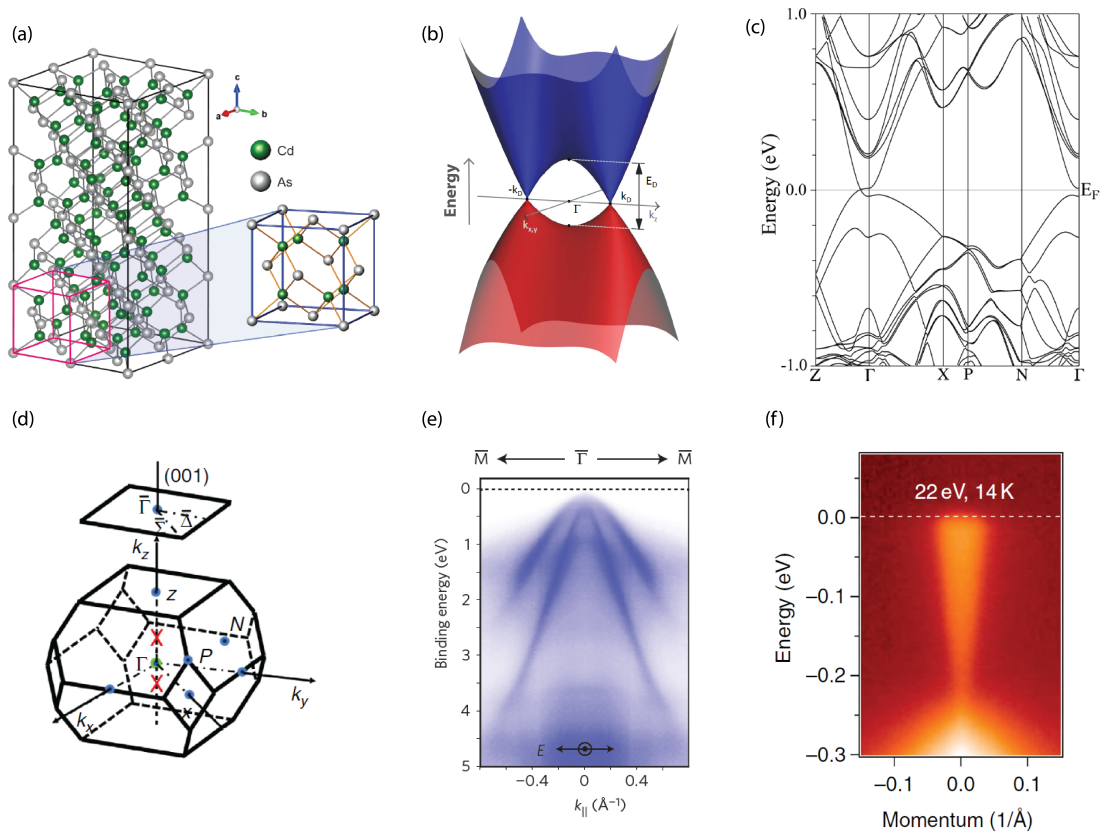


Figure 6.3: **Crystal structure and electronic characteristics of Cd_3As_2 .** (a) Tetragonal unit cell [170]. (b) Schematic view of the two 3D Dirac cones located on the tetragonal axis (z axis in this figure). (c) Band structure calculations along high symmetry directions across the Brillouin zone, which is shown in (d) [69]. The band crossing can be seen close to the Γ point. ARPES results showing conical valence bands (e) [166] and conduction bands (f) [94].

classical transport effects. Current is applied along the [001] direction. The first cantilever, sample 1, is shown in figure 6.4 (a). Figure. 6.4 (b) displays the resistance for different values of the rotation angle ϕ (defined in the inset of the same figure). The resistance shows a tendency to decrease as the field is changed from the [001] to the [100] direction. At 12 T, the resistance for $\phi = 90^\circ$ ($\mathbf{B} \perp \mathbf{I}$) is about half of that one for $\phi = 0^\circ$ ($\mathbf{B} \parallel \mathbf{I}$). The MR, as quantified by $100\% \times [R(B) - R(B=0)]/R(B=0)$, is positive for fields greater than 1 T, reaching at 14T MR= 186% and MR= 83% for $\phi = 0^\circ$ and $\phi = 90^\circ$, respectively. For fields smaller than 1 T, the MR shows a broad peak that is followed by a region of negative MR. This feature was previously reported for the thin Cd₃As₂ microstructures studied in [35], where it was associated to the so-called Knudsen effect that originates from the enhanced boundary scattering of strongly confined ballistic electrons [171]. Early calculations based on the free electron model [172] indicate that at the field value, B_{max} , where the MR maximum is located, the thickness of the device scales with the cyclotron radius, r_c , according to $t/r_c = LeB_{max}/v_F m^* = 0.55$. This theoretical relation has described quite well the behaviour of quantum GaAs/AlGaAs heterostructure wires [173]. Using such relation with $B_{max} \approx 0.1 T$ and the experimentally determined parameters for the current microstructure, it's possible to estimate a thickness of $t \approx 1.2 \mu m$.

Regarding the oscillatory behaviour of the signal, figure 6.4 (c) shows $\Delta\rho/\rho$ as a function of $1/B$ after the background subtraction of a polynomial of order six. These curves exhibit clear, single frequency QOs associated to the bulk Landau quantization, which is further confirmed by their FFT spectra. This is consistent with the expectation that for fields applied in the plane of the cantilever, no signal from the Weyl orbits should be observed. When the field points in the [100] direction, the projections of the Dirac nodes are located on the surfaces separated by the width of the central leg, which is about 10 μm . This distance between nodes' projections is already too large for the formation of Weyl orbits, and grows further upon increasing the angle ϕ . The corresponding angle dependence of the bulk frequency is shown in figure 6.4 (d) and its variation suggests an ellipsoidal Fermi surface, albeit an almost spherical one. Applying Onsager's relation and assuming a spherical cross section, one can calculate $k_{F,min} = \sqrt{2eF_{bulk,min}/\hbar} = 3.21 \times 10^8 m^{-1}$. Similarly, assuming an ellipsoidal cross section one can calculate $k_{F,max} = 2eF_{bulk,max}/\hbar k_{F,min} = 3.59 \times 10^8 m^{-1}$, from which one obtains $k_{F,min} \approx 0.89 k_{F,max}$.

To determine the effective mass of the charge carriers, I studied the change of the QOs amplitude with temperature for the field direction $\mathbf{B} \parallel [100]$. The MR curves for different temperatures are shown in figure 6.5 (a). As expected, the MR increases with temperature, although only slightly, and the amplitude of the QOs decreases. This last observation is more evident in figure. 6.5 (b) and (c), where the oscillatory components and its corresponding FFT spectra are respectively shown for different temperatures. Figure 6.5 (d) displays the change in the amplitude of the FFT peak centered at $F_{bulk} = 37.3 T$ with temperature, which follows very well the LK formalism (equation 4.30). The procedure to perform the fit is to choose as the value of B in equation 4.31 the inverse of the $1/B$ average between the two limits of the field interval used to calculate the FFT, that is, $B_{ave} = [(1/B)_{ave}]^{-1} = [(1/2)(1/B_1 + 1/B_2)]^{-1}$, where B_2 and B_1 are

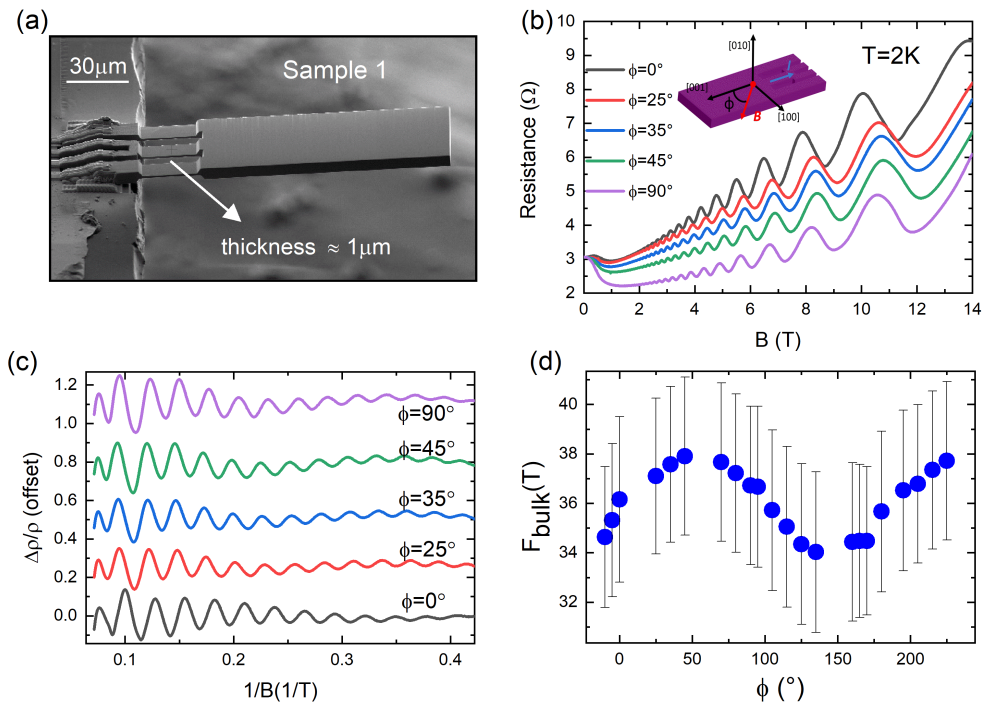


Figure 6.4: **Quantum oscillations of Sample 1 for *in-plane* rotation.** (a) SEM image of Sample 1. (b) Magnetoresistance at $T=2\text{K}$ for different values of the rotation angle ϕ . The inset shows the definition of ϕ . (c) Oscillatory component $\Delta\rho/\rho$ vs $1/B$ for different rotation angles. (d) Angular dependence of the bulk oscillation frequency F_{bulk} . Error bars are the HWHM of the FFT peaks.

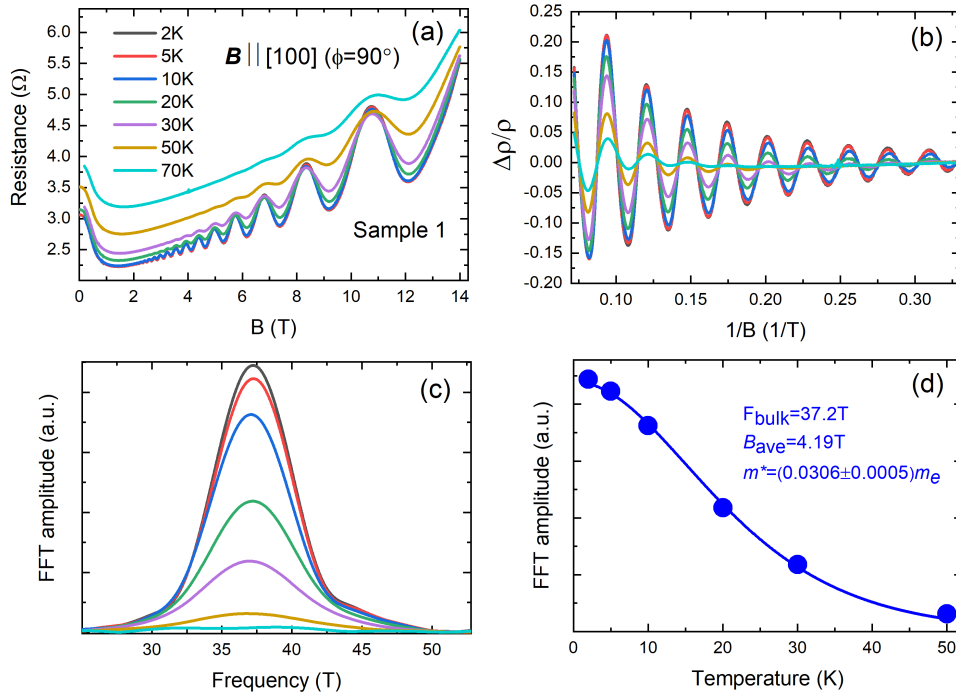


Figure 6.5: **Quantum oscillations at different temperatures for the field direction $B \parallel [100]$.** (a) Magnetoconductance and (c) oscillatory component $\Delta\rho/\rho$ vs $1/B$ for the temperatures indicated in (a). (c) Temperature dependence of the FFT spectra of the SdH oscillations. (d) Temperature dependence of the corresponding FFT peak amplitude at $F_{\text{bulk}} = 37.2\text{ T}$. The fitting with the LK formula is denoted by the solid line.

the upper and lower fields used for the FFT. This procedure is justified as $1/B$ is not rapidly changing in the high field window chosen for the analysis. From this fit, an effective mass of $m^* = (0.031 \pm 0.001)m_e$ is obtained, which is consistent with reports in literature [35, 168, 174]. Furthermore, such a low effective mass consistently shows that the Fermi level is effectively close to the node since in a TSM the effective mass is actually energy dependant. One can see this by re-writing equation 4.16 for the effective mass as $m^* = \frac{\hbar^2}{2\pi} \frac{\partial S(E, k)}{\partial E}$. In the case of a TSM with a Fermi energy $E_F = \hbar v_F k_F$ and a circular cross sectional area $S(E_F, k_F) = \pi k_F^2 = \pi E_F^2 / \hbar^2 v_F^2$, it follows that $m^* = E_F / v_F^2$, so that lower masses are expected as E_F is closer to the position of the nodes. This famous result has been well established in the 2D DSM graphene [125].

With the information obtained from the previous experiments it is possible to quantify some parameters characterizing the transport properties of the device (see table 6.1). Assuming an average bulk frequency of $\langle F_{\text{bulk}} \rangle = 36\text{ T}$ and a spherical Fermi surface with extremal area $S = \pi k_F^2$, one can use Onsager's relation to calculate $k_F = \sqrt{2e\langle F_{\text{bulk}} \rangle / \hbar} = 3.31 \times 10^8\text{ m}^{-1}$. From this, the Fermi velocity results in $v_F = \hbar k_F / m^* = 1.25 \times 10^6\text{ m s}^{-1}$. The Fermi energy above the Dirac point is given by $E_F = \hbar v_F k_F \approx 272\text{ meV}$. The bulk carrier density can also be calculated

Devices	$\langle F_{bulk} \rangle$ (T)	v_F (m/s)	m^* (m_e)	$n(10^{17} cm^{-3})$	E_F (eV)	$\nu(m^2/Vs)$
Sample 1	36	1.25×10^6	0.031	24.5	272	4
Sample 3	17	1.22×10^6	0.023	8.1	184	5.5

Table 6.1: **Main parameters of the two principal samples discussed.** m_e is the bare electron mass. $\langle F_{bulk} \rangle$ refers to the average. The values of Sample 3 were measured previous to its thinning down. m^* was measured for fields $\mathbf{B} \parallel [100]$.

using $n = 2k_F^3/3\pi^2 = 2.45 \times 10^{18} cm^{-3}$, which is very similar to values reported in literature [35, 167, 168]. From the the geometrical dimensions of the device and the extrapolated value of the MR at low fields excluding the Knudsen peak, the low temperature resistivity is calculated to be $\rho_0 \approx 65 \mu\Omega cm$. Within the Drude model, the corresponding value of the mobility is $\nu = 1/\rho_0 ne = 4 m^2/Vs$. All these values are consistent with those typically reported in literature for Cd₃As₂. From the mobility, one can estimate the bulk transport mean free path, $l = \nu m^* v_F / e \approx 0.9 \mu m$, which is in agreement with the value reported in [35] and the fact that this sample clearly exhibits Weyl oscillations.

6.3.1.2 c-axis rotation

Next, the field is rotated from the [001] to the [010] direction, as depicted in the inset of figure 6.6 (a). This rotation is much richer in physics, as we do expect the Weyl orbits to dominate the spectrum for magnetic fields perpendicular to the cantilever. Compared to the *in-plane* results of the previous section, the MR clearly grows much larger for fields tending to the [010] direction ($\varphi = 90^\circ$). At 14T, MR=1793% for $\varphi = 90^\circ$, about 20 times larger than the MR for $\varphi = 0^\circ$. Like the in the *in-plane* case, a Knudsen peak is observed for fields lower than 1T but it quickly disappears with increasing angle and for $\varphi > \approx 6^\circ$ the MR becomes positive over the whole field window. As the field is tilted from the [001] to the [010] direction, the motion of the electrons in the plane perpendicular to the field is less affected by the small thickness of the channel and the scattering is again dominated by bulk scattering, resulting in the usual large MR observed in bulk crystals. The FFT of the oscillatory component of the MR is presented in figure 6.6 (b). For values of φ close to 90° the amplitude of the F_{Weyl} peak becomes comparable to the amplitude of F_{bulk} . The angle dependence of F_{bulk} and its corresponding amplitude are presented in figure 6.6 (c). The variation of F_{bulk} confirms the ellipsoidal shape identified in the *in-plane* rotation. Figure 6.6 (d) shows the angle dependence of F_{Weyl} and its FFT amplitude. F_{Weyl} shrinks in amplitude relatively quickly and it's only appreciable in the range $80^\circ < \varphi < 105^\circ$ following the expected $1/\cos(\varphi)$ dependence around $\varphi = 90^\circ$ ($1/\sin(\varphi)$ in this case according to how the angle φ was defined).

Overall, the results presented in this and the previous section suggest that the transport characteristics exhibited by the cantilevers, including quasi-spherical Fermi surfaces, small effective mass of charge carriers, energy dependent effective mass and no apparent gap opening for magnetic fields tilted away for the [001] direction, are all consistent with the known properties of bulk and previously measured microstructures of Cd₃As₂. Furthermore,

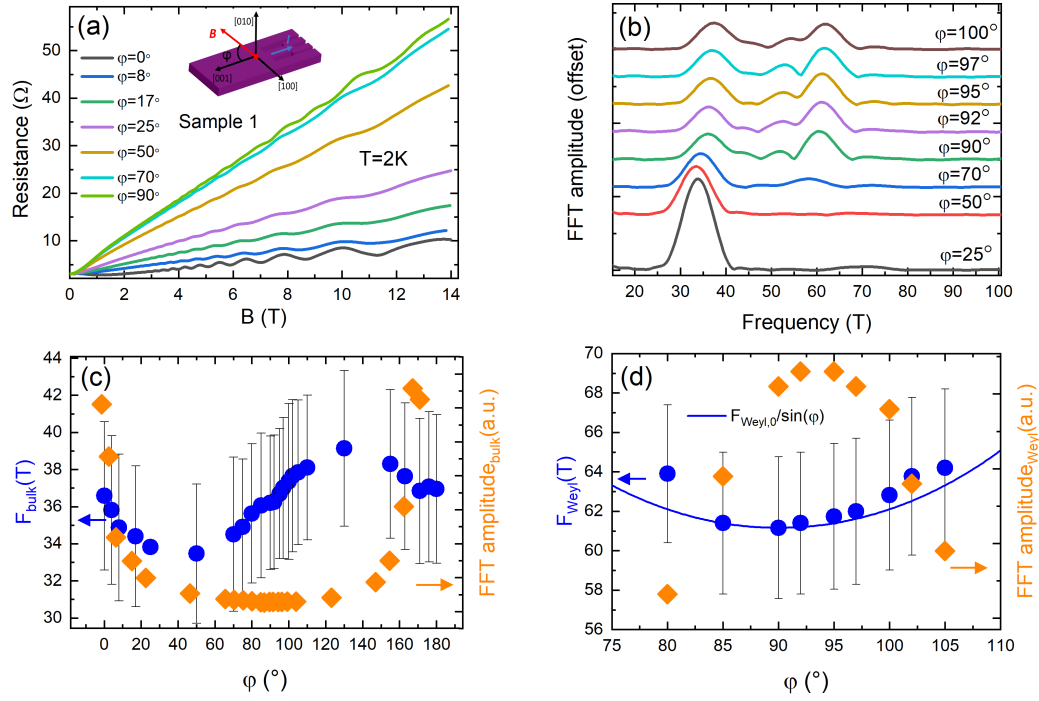


Figure 6.6: **Quantum oscillations of Sample 1 for c -axis rotation.** (a) Sample 1 magnetoresistance at $T=2\text{K}$ for different values of the rotation angle φ . The inset shows the definition of φ . (b) FFT spectra of the SdH oscillations obtained from (a) after the background subtraction. (c) Angular dependence of the bulk oscillation frequency F_{bulk} and its amplitude and (d) the same for the surface oscillation frequency F_{Weyl} . Error bars are the HWHM of the FFT peaks.

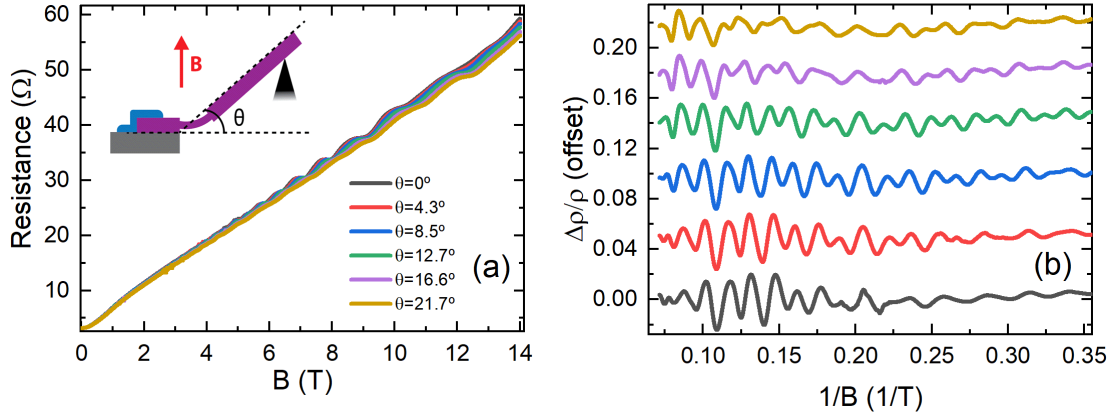


Figure 6.7: **Quantum oscillations of Sample 1 during static bending.**(a) Magnetoresistance at 4K for different values of the bending angle θ . (b) oscillatory component $\Delta\rho/\rho$ vs $1/B$ for the same values of θ as in (a).

the size-dependent features in the MR of the cantilevers can also be associated to known phenomena, namely the Knudsen effect and, most importantly for this thesis, the Weyl orbits.

6.3.2 Bending without rotation

Having established the field and angle dependence of the MR, the results of bending without rotation are discussed next. The promising results clearly demonstrate that Landau quantization is quite exotic and indeed compatible with pseudo-fields, yet the quantum system is extremely complex and at present alternative explanations for the data cannot be excluded, preventing the unambiguous identification of pseudo-fields at this point. Figure 6.7 (a) displays the field dependence of the resistance for different bending angles θ . Clear QOs are visible, which sit on a background that is mostly linear from 1T onward. This agrees well with the reports of large an linear MR in Cd_3As_2 , which is hypothesized to arise from chemical potential disorder [37, 175]. This linearity doesn't seem to be altered by bending. The weak decrease of MR with increasing bending angle, used to detect the touching point, is also clearly visible.

The oscillatory components $\Delta\rho/\rho$ of the MR curves (see figure 6.7 (b)) suggest the presence of at least two different oscillations, as it's expected for this cantilever configuration, a lower frequency one associated to F_{bulk} and a higher frequency one associated to F_{Weyl} . A windowed FFT analysis reveals that the oscillations with F_{bulk} are more dominant at lower fields whereas F_{Weyl} becomes more prominent at higher fields. This is self-consistently confirmed by fitting the data to the LK form. As shown in figure 6.8 (a), at zero bending a good LK fit can be found using only a single frequency $F_{bulk} = 36.8T$ for fields up to $\approx 4.5T$. Similar fits, even including a second frequency, get much worse as the field range is increased to include higher fields. One has to note here how non-trivial this is. The full LK fitting takes into account all phenomena usually arising in Landau quantized metals, hence its failure is pointing to unusual physics.

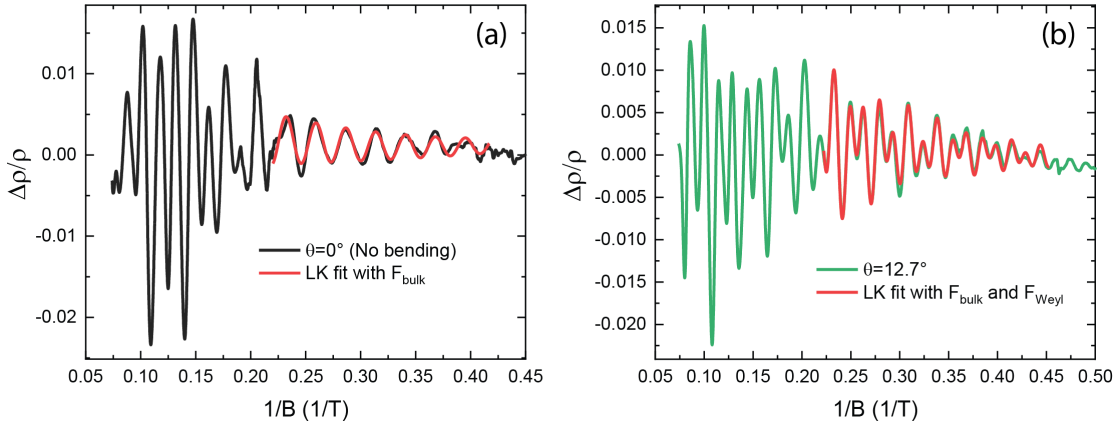


Figure 6.8: **LK fitting of quantum oscillations for unbent and bent Sample 1.** $\Delta\rho/\rho$ vs $1/B$ and its corresponding LK fitting for (a) $\theta = 0^\circ$ and (b) $\theta = 12.7^\circ$. Good LK fittings are typically obtained only in the low magnetic field region, up to approx. $B=5T$.

Figure 6.8 (b) shows a similar procedure for the $\Delta\rho/\rho$ curve with a bending angle $\theta = 12.7^\circ$. In this case again, a good LK at low fields was found using two main frequencies, $F_{\text{bulk}} = 36.8T$ and $F_{\text{Weyl}} = 66.5T$ but, as before, no such fit is satisfactory for the whole field range. This situation is not entirely surprising since the LK formalism describes the oscillations that result from the bulk quantization of the FS without considering any contribution from surface states nor mixing of bulk and surface states, which are the constituents of the Weyl orbits. One might consider to subtract the low-field LK fits from the entire field range, in an attempt to reduce the complexity by removing known bulk physics from the data. These attempts were unsuccessful, which is not surprising given the bulk/surface nature of the Weyl process. The self-consistent quantum mechanical solution combines them together, such that the coexistence of unaffected bulk oscillations with the Weyl process is an unlikely, oversimplified scenario.

This unusual field-dependence was investigated by restricted window FFT analyses. Figure 6.9 shows the FFT for two different field windows: (a) (3T - 14T) and (b) (5T - 11T). In both cases the two main peaks associated to F_{bulk} and F_{Weyl} are clearly resolved. However, while F_{bulk} remains fixed for all bending angles at around 37T using both windows, F_{Weyl} evolves differently in each case: it remains virtually fixed at around 67T for the first window but consistently shifts to higher frequencies with increasing bending angle when using the second window, which, as mentioned in the previous paragraph, sits on a field range where the Weyl orbits are more prominent. In a usual metal, the electronic spectrum itself is field independent, and the sole role of the magnetic field is to Landau-quantize the spectrum. Its failure here shows that the magnetic field itself does alter the electronic spectrum, which can arise from multiple mechanisms, some associated with topology and some with pseudo-fields. First, the presence of pseudo-fields necessarily causes non-periodic quantization. B_5 sets an intrinsic field scale, separating a low field ($B \gg B_5$) and a high field ($B \ll B_5$) region. In the cross-over region, $B \simeq B_5$, the Landau level positions are necessarily non-periodic in

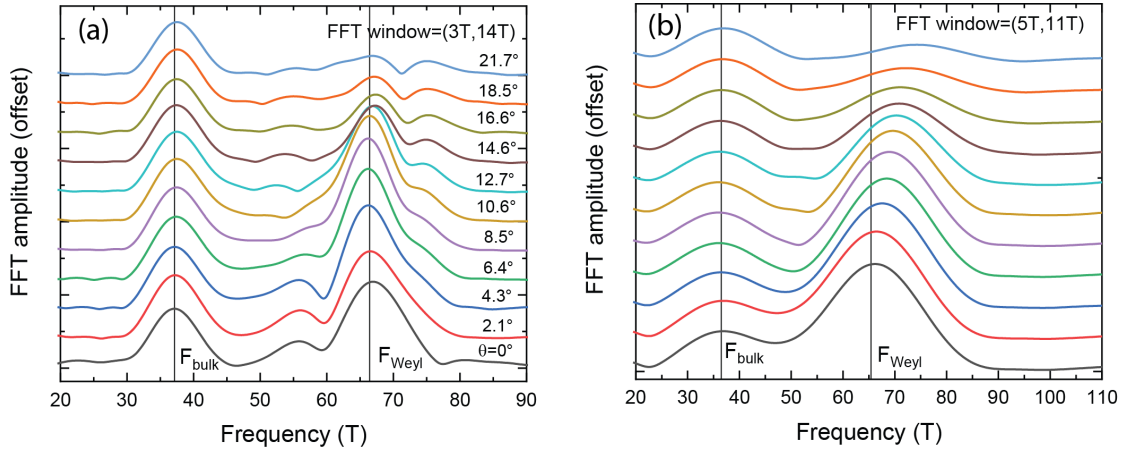


Figure 6.9: **FFT of quantum oscillations for static bending experiments.** FFT of the oscillatory part $\Delta\rho/\rho$ of the MR for different bending angles, using a FFT window of (a) (3T, 14T) and (b) (5T, 11T).

$1/B$. Alternatively, a second mechanism for deviations from ideal $1/B$ periodicity in the Weyl orbits' oscillations has been linked to so-called non-adiabatic corrections originating from the field-induced tunneling between Fermi arc states and bulk states as the quasi-particles approach the Weyl nodes [35]. These corrections are related to a magnetic breakdown not captured by the LK formalism and lead to a shift to lower frequencies in the spectral weight of the main F_{Weyl} peak. This results in a broader, asymmetric peak with further additional structure at lower frequencies. Similar features are also observed in figure 6.9 (a) for Sample 1. Further mechanisms for field-dependence include strain from magneto-striction, the field-dependence of the chemical potential as we are close to the quantum limit, and field-dependent effective masses given the linear Dirac spectrum. While the results are compatible with pseudo-fields, the complexity of the experimental situation and the possibility of these other bending-induced frequency shifts precludes me from making this identification.

The increase of F_{Weyl} with bending is a promising observation predicted by pseudo-fields, however the real situation deviates significantly from the idealized strain profile theoretically considered. The large gradients that are necessary come with a significant distortion of the cantilever upon bending. At high angles, it is not a straight beam anymore, and the local variation of the magnetic field angle w.r.t. the bent cantilever section is important since F_{Weyl} is expected to change according to the $1/\cos(\theta')$ relation, where θ' is the angle between the magnetic field and surface normal. Increasing the bending angle θ also increases the angle between the magnetic field and the different sections of the bent part of the lamella, which necessarily contributes to any change in the observed evolution of the F_{Weyl} peak. Figure 6.10 contrasts the variation of F_{Weyl} from rotation alone in the unbent state to that of the pure bending state without any change in nominal field angle. Figure 6.10 (a) shows the proportional change in F_{Weyl} for both experiments using the FFT window of (5T - 11T), where $\Delta F_{\text{Weyl}} = F_{\text{Weyl}}(\theta') - F_{\text{Weyl},0}$, with $F_{\text{Weyl}}(\theta' = 0^\circ) \equiv F_{\text{Weyl},0}$ and θ' is either the rotation or

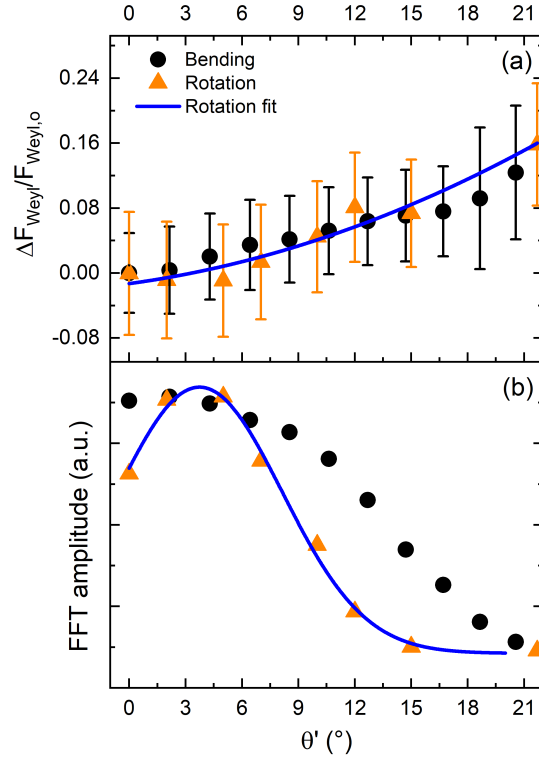


Figure 6.10: **Comparison of the F_{Weyl} change from static bending and rotation.** Angular dependence of the amplitude of F_{Weyl} (a) and of the relative change of F_{Weyl} (b) for the static bending and the c -axis rotation experiment, where $\Delta F_{\text{Weyl}} = F_{\text{Weyl}}(\theta') - F_{\text{Weyl}}(\theta' = 0^\circ)$ and $F_{\text{Weyl}}(\theta' = 0^\circ) \equiv F_{\text{Weyl},0}$. The variable θ' refers to either the rotation or bending angle. A FFT window of (5T - 11T) was used.

bending angle.

This similarity may cause the impression that the entire bending dependence of F_{Weyl} may be explained solely by the inherent variation of field angle. However, a quantitative analysis suggests a more nuanced picture. To model the impact of angle variation the basic assumption is that each infinitesimal part of the sample exhibits a Weyl orbit whose frequency is associated with the angle θ' between the magnetic field (whose direction is kept fixed) and the surface normal to that particular part of the sample (see figure.6.11 (a)). Each infinitesimal part would then exhibit an oscillatory process at $F_{\text{Weyl}}(\theta')$. The final response f of the sample is calculated as a simple angle average:

$$f = \frac{1}{\theta'_{\max} - \theta'_{\min}} \int_{\theta'_{\min}}^{\theta'_{\max}} A(\theta') G(F_{\text{Weyl}}(\theta')) d\theta' \quad (6.3)$$

The frequency shift and amplitude decrease of the F_{Weyl} peak is taken from the experimental fits presented in figure 6.10 for the c -axis experiments. Each peak is modelled as a Gaussian G

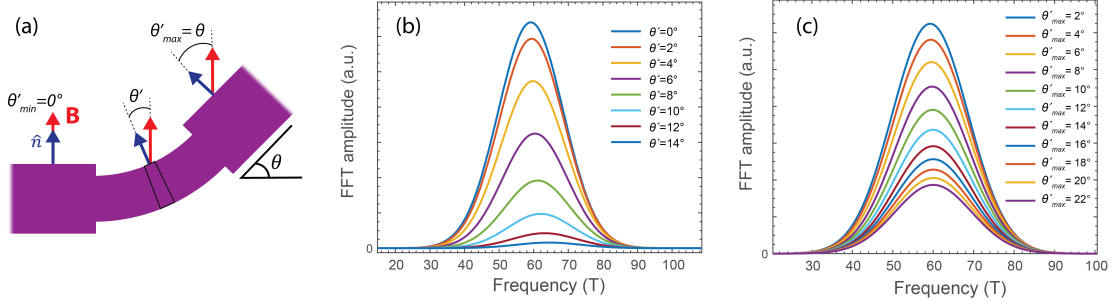


Figure 6.11: **A simple model for the evolution of F_{Weyl} during bending.** (a) Sample during bending where each infinitesimal section has a normal surface vector at an angle θ' with respect to the magnetic field B . (b) Simulated Gaussian F_{Weyl} peaks for different values of θ' , whose evolution in amplitude and frequency is taken from the experimental fit from the rotation experiments (figure 6.10). (c) Results of the model described in equation 6.3 for different values of θ'_{max} , which is equivalent to the bending angle θ , and θ'_{min} , which is always taken as zero.

with an angle dependent amplitude $A(\theta')$ and peak center $F_{Weyl}(\theta')$. Figure 6.11 (b) shows the isolated peaks following this evolution for different values of the angle θ' . The result of the integration for several values of maximum bending angle θ'_{max} (which is equivalent to the bending angle θ used in the bending experiments) is shown in figure 6.11 (c) (θ'_{min} is always taken as zero). As can be seen there, the final Weyl peak position is very similar to that of the $\theta' = 0^\circ$ peak. This is a consequence of the fact that only the peaks around $\theta' = 0^\circ$ have an appreciable amplitude, and those corresponding to higher angles die away quickly, making their influence almost negligible. The final maximum amplitude is also shown to decrease as the peak profile is made broader. In this fashion, one could think about the influence of the rotation effect on the Weyl orbits during the bending of the sample as extending only to a very small angle range around the $\theta' = 0^\circ$ peak. This picture suggests that the clear shift in F_{Weyl} observed during the bending experiments is not primarily affected by the pure rotation contribution. Essentially, the amplitude suppression under bending is much weaker than one would expect from rotation alone. It is clear that the segments at high effective angle (large θ') under bending similarly will have a negligible impact on the transport. The key difference, however, is that the bending gradient is present even close to the base of the cantilever, at $\theta' \sim 0$. The modification of the spectrum there must be at the origin of the observed peak shift.

6.3.3 Bending and rotation

To further probe the relation of bending and rotation, a miniaturized version of the bender was constructed that is compatible with an *in situ* rotator. Unfortunately, Sample 1 degraded over time and could not be remeasured. In view of this, and for the sake of reproducibility, I fabricated additional devices from different crystals using the same design and crystallographic orientation as Sample 1. Figure 6.12 shows the results for the device referred to as Sample 3.

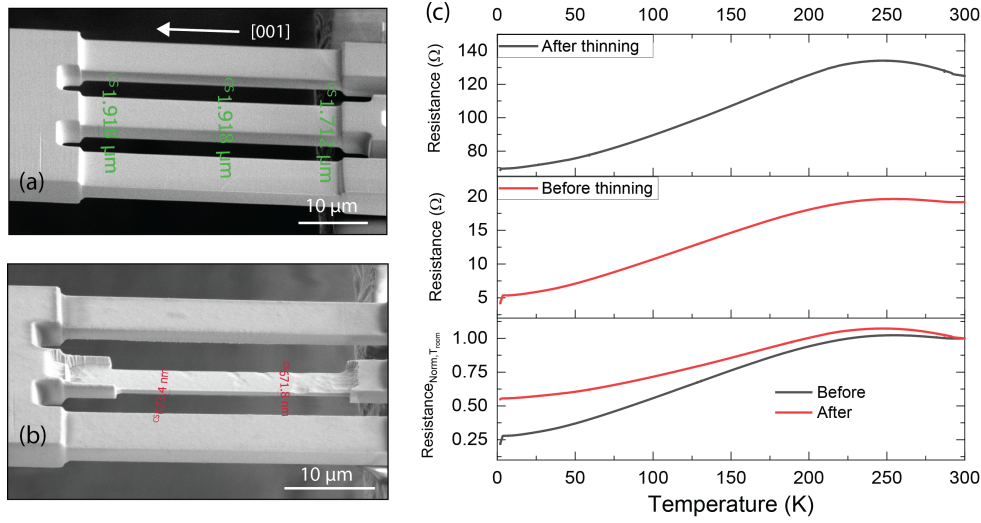


Figure 6.12: **Thinning down of Sample 3.** (a)-(b) SEM images of Sample 3 after thinning it down with the FIB using top irradiation with a very small current. (c) Resistance vs temperature for Sample 3 before and after thinning, including a comparison of the normalized curves using the resistances at room temperature as references.

Initially, the thickness of Sample 3 was not optimal to clearly resolve the F_{Weyl} peak. Thanks to the versatility of the FIB micro-fabrication technique, this issue can be addressed quickly by thinning the sample down using a very small current and carefully irradiating the central leg from the top. The result of this procedure is shown in figures 6.12 (a) and (b). The resistance vs temperature before and after thinning is shown in figure 6.12 (c). The thinned-down sample exhibits a higher resistance, as expected, but the behaviour is still metallic with a similar overall shape of the curve before thinning. The normalized curves also show a comparatively higher resistance for the thinned-down case, especially at lower temperatures, a result that is consistent with the observed behaviour of other thinned-down TSMs [59]. Prior to thinning, Sample 3 was characterized and some of its main parameters are presented in table 6.1.

The rotation studies under zero bending for the thinned-down Sample 3 are presented in figure 6.13. The sample was rotated 30° around the B_\perp ($\mathbf{B} \parallel [010]$) direction as indicated in the inset of figure 6.13 (a) (same experimental configuration as the one described already in section 5.3.2). Similar to the results of section 6.3.1.2, the background MR is very close to linear, over which the QOs are superimposed, and it tends to decrease as the field is tilted away from the B_\perp direction. The oscillatory components $\Delta\rho/\rho$ are presented in figure 6.13 (b). They clearly contain several frequencies and, like before, can be better fitted by the LK formalism with two main frequencies in lower field ranges. This range actually shrinks as the the field is tilted away from the B_\perp direction and the onset of the non-LK region is pushed to lower fields. The corresponding FFT for each $\Delta\rho/\rho$ curve is shown in figure 6.13 (c) using a window of (2.5T - 6T). One of the main FFT peaks sits at around 45T for $\mathbf{B} \parallel B_\perp$ and is consistent with the expected evolution of the F_{Weyl} peak with rotation angle (see figure 6.13 (d)). The value of

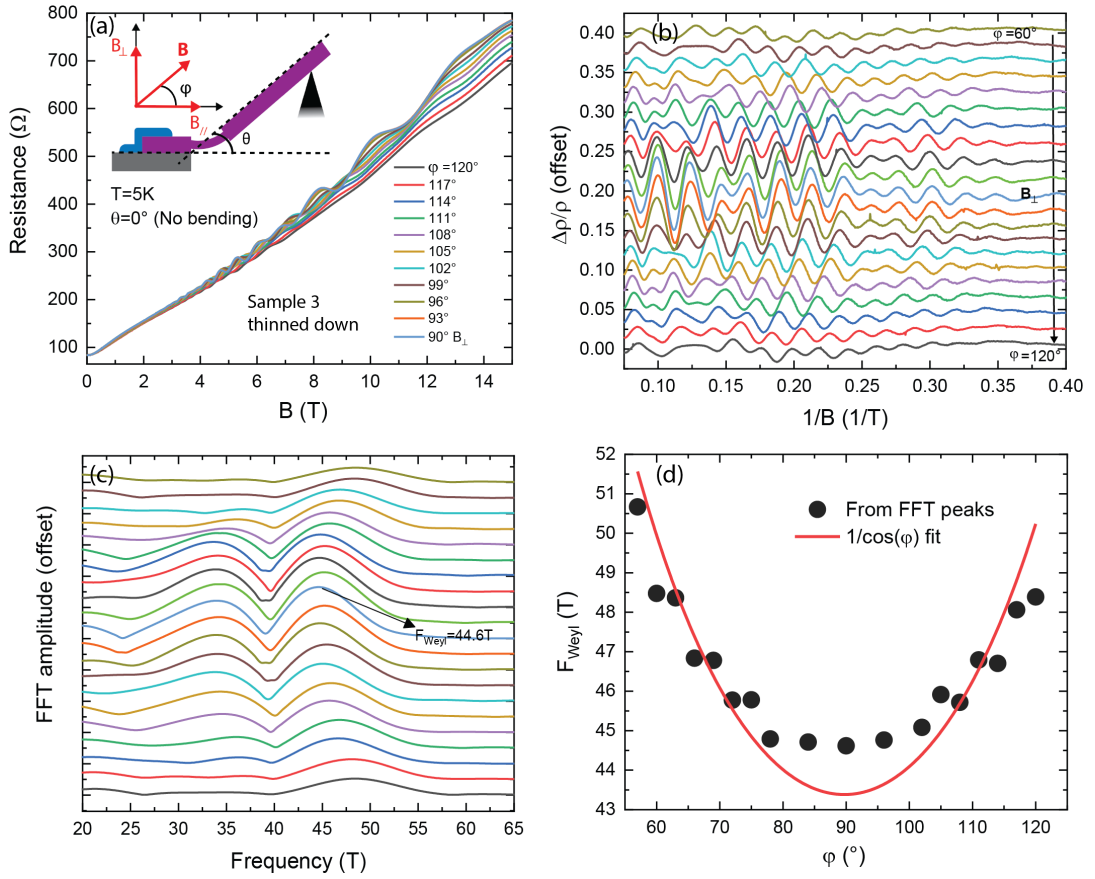


Figure 6.13: **Quantum oscillations of the thinned down sample 3 at zero bending.** (a) Magnetoresistance at $T=5\text{K}$ for no bending the indicated values of the rotation angle φ . The inset shows the definition of φ and the bending angle θ (same as depicted already in chapter five). (b) Oscillatory component $\Delta\rho/\rho$ vs $1/B$ for different rotation angles and (c) the corresponding FFT spectra. (d) Angular dependence of F_{Weyl} .

$F_{\text{Weyl}} \approx 45\text{T}$ also compares well with the expected one for Sample 3 of $F_{\text{Weyl}} \approx 40\text{T}$, obtained from the relation $F_{\text{Weyl}} = \mu k_0 / \pi e v_F$, where the chemical potential $\mu = 184\text{meV}$ determined for sample 3 before thinning has been used. Similar observations to the ones discussed above are also obtained when using a larger FFT window of (2.5T - 15T).

The rotation studies for a bending angle of $\theta = 25^\circ$ are presented in figure 6.14. The overall behaviour of the $\Delta\rho/\rho$ set of curves is very similar to the zero bending case, with the only difference that it is symmetric not around the B_\perp field direction ($\varphi = 90^\circ$) but around $\varphi \approx 75^\circ - 80^\circ$. This is consistent with the results of figure 5.12 (a) showing the angle dependency of the MR at a fixed field $B=5\text{T}$ for this very same bending angle. Figure 6.14 (b) highlights the F_{Weyl} evolution with rotation angle extracted from the FFT of the curves in figure 6.14 (a). Once again, the general behaviour is comparable to the zero bending case, showing also a relatively flat angular region around which $F_{\text{Weyl}} \approx 46\text{T}$, which is only slightly higher than the $F_{\text{Weyl}} \approx 45\text{T}$ for zero bending. This result is at odds with the expected behaviour deduced

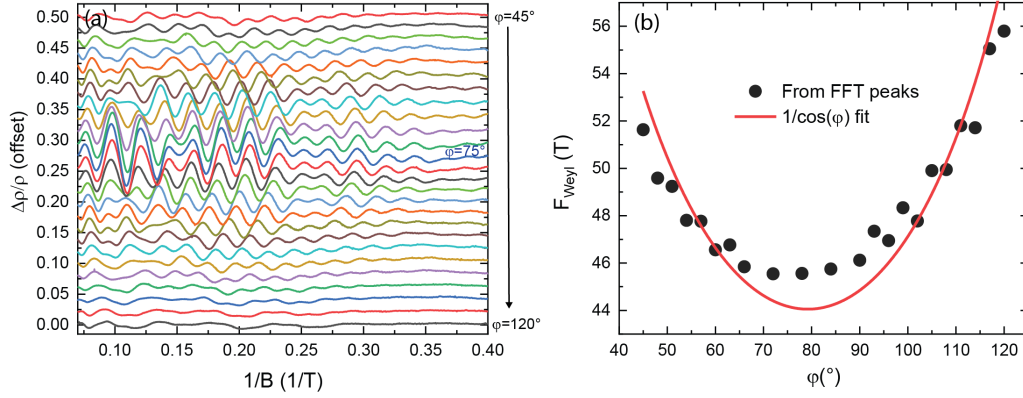


Figure 6.14: **Quantum oscillations of the thinned down sample 3 with a bending angle $\theta = 25^\circ$.** (a) Oscillatory component $\Delta\rho/\rho$ vs $1/B$ for different rotation angles and (b) angular dependence of F_{Weyl} from its FFT peak.

from the simple model discussed in figure 6.11. That model suggests that the dominant F_{Weyl} comes from the cantilever section whose surface normal is parallel to the field, for any given rotation angle φ of the field. Assuming that the Weyl orbits are affected uniformly by the strain gradients along the bent section of the cantilever, one should then expect a fixed F_{Weyl} peak for all rotation angles. The experimental results, however, point to a F_{Weyl} evolution similar to the $1/\cos(\varphi)$ dependence observed in the zero bending case. To avoid any spurious effect coming from the use of the FFT, whose F_{Weyl} peak is susceptible to changes depending on the chosen window, figure 6.15 shows for three different bending angles the $\Delta\rho/\rho$ curves around which the corresponding set of curves is symmetrical (like the one at $\varphi \approx 75^\circ$ in figure 6.14 (a)). There, it is evident that the frequency content is the same for all bending angles and that, apart from a very small change in the phase of the quantum oscillations, all the curves overlap almost perfectly.

6.4 Conclusions and outlook

In the work presented in this chapter I have applied large bending strain gradients on FIB-fabricated cantilevers of the DSM Cd_3As_2 and studied the evolution of Weyl orbits in search for experimental signatures of the theorized pseudo-magnetic fields. Although some features of the complex data are consistent with the existence of such fields, the application of the basic theoretical models available doesn't seem to reproduce important aspects of the experimental situation and corresponding data, making it difficult to unambiguously assert the presence of strain-induced pseudo-magnetic fields. Furthermore, even within the available models, simple alterations in some of the numerical parameters needed can lead to significant reductions of up to 1/30 of the initially calculated magnitude of B_5 [165], suggesting that their effect in the periodicity of Weyl orbits could be almost negligible. Additionally, the modification due to strain gradients of other band parameters, like the Fermi velocity, might have a bigger

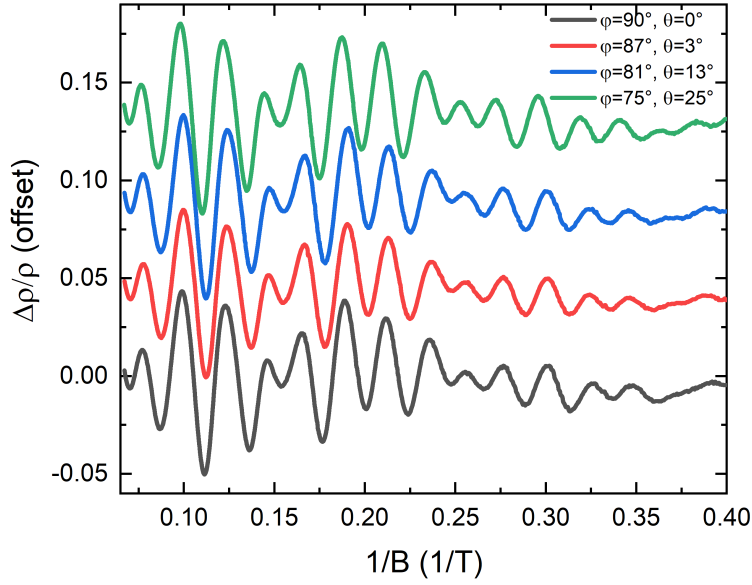


Figure 6.15: **Quantum oscillations of thinned down sample 3 for different bending and rotation angles.** The $\Delta\rho/\rho$ curves correspond to the rotation angle around which the corresponding set of curves looked more symmetrical.

influence than previously thought. One possible way forwards is to look for other materials with more favorable parameters for the creation of B_5 where Weyl orbits can also be clearly resolved. Unfortunately, as of today, Cd₃As₂ is the only material where unequivocal evidence of Weyl orbits has been reported, although tantalizing results also suggest the existence of these orbits in nanoribbons of WTe₂[176] and thin films of SrRuO₃[177]. In the search for Weyl orbits' signatures from additional materials, during this thesis I attempted to use the Ga-FIB to thin-down samples of NbAs to dimensions comparable with its mean free path ($\approx 100nm$). Although working devices were fabricated, they were heavily affected by the known differential sputtering phenomenon in this material [59], as well as potential Ga implantation, both of which significantly alter the surface of the sample.

Another important lesson to extract from the experiments here presented is the necessity to better understand the Weyl orbits themselves and to devise a formalism akin to the LK one for bulk quantum oscillations. In particular, the evolution of the Weyl orbits in high magnetic fields is of great interest since it could provide information on the theorized localization of the orbits on the surface of the sample from a certain critical value of the field called the mixing field [122]. The sensitivity of this field to strain gradients might be a way to detect pseudo-fields. During this thesis I prepared some preliminary samples for high field experiments but unfortunately such measurements had to be cancelled due to the Covid-19 pandemic.

7 Transport measurements in PtSn₄ microstructures

7.1 Introduction

With the material challenges posed by Cd₃As₂, the next step was to look for other topological materials that may host Weyl orbits. The main requirement is a high mobility and high cleanliness. The Dirac semimetal PtSn₄ appeared as a promising candidate as both Dirac bulk nodes as well as a Dirac node line associated to surface states were recently uncovered by ARPES [41]. Some studies have supported the topological nature of this material by, for example, determining a nontrivial Berry phase from dHvA quantum oscillations [178], and observing the existence of the giant planar Hall effect induced by the chiral anomaly [179]. While it turned out that PtSn₄ is too strongly dominated by bulk bands to show appreciable transport signatures of Weyl orbits, the microstructure measurements solved a long-standing puzzle about the nature of its extreme magnetoresistance. The fine field-angle studies presented here were able to unambiguously identify a semi-classical origin for its MR.

One of the most interesting characteristics of topologically non-trivial matter is its response to magnetic fields, with non-magnetic materials like Cd₃As₂ [36], WTe₂ [180], ZrSiS [181], and NbSb₂ [182] often exhibiting extremely large magnetoresistance (XMR) in the order of 10⁵%-10⁶% at helium temperatures. Before its topological character was discovered, PtSn₄ had already been of great interest precisely because of its XMR of $\approx 5 \times 10^5\%$ with no appreciable saturation up to 14T at 1.8K [61]. These values of XMR are very rare for high carrier-density metals like PtSn₄ and are considerable larger than those associated to the well-known phenomena of colossal magnetoresistance (CMR) in transition-metal oxides [183] and giant magnetoresistance (GMR) in ferromagnetic heterostructures [184, 185], and hence have great potential for technological applications like magnetic field sensors and magnetic data storage. It's worth mentioning that such a strong response to magnetic fields is not expected to happen in most metallic materials, where typical values of MR are in the few percent, and whose origin can usually be understood by semi-classical models of transport considering deviations of a simple free electron gas. In contrast, the microscopic origin of the XMR observed in topological materials is still an intense field of research, with several mechanisms proposed as

potentially responsible. Electron-hole compensation is a known semi-classical mechanism, particularly relevant in semimetals like WTe₂ [180], that can give rise to non-saturating MR in two-band systems due to the vanishing of their Hall fields and the resultant back-flow of charge carriers [111]. In materials with strong spin-orbit coupling, magnetic-field driven changes of the Fermi surface form another class of mechanisms. These will be particularly effective if a band-structure anomaly such as a van-Hove singularity [186] or a topological band-crossing point exist close to the Fermi surface [181]. Especially in Dirac systems, the loss of time-reversal symmetry in magnetic fields necessitates a transition into a Weyl material, which has been argued to suppress a topological back-scattering protection [36]. Even more exotic ideas are discussed in interacting systems, such as the field-induced formation of excitonic insulators [187, 188] or parallel conductance in topological surface states [189]. In the case of PtSn₄, more recent studies have reported somewhat contrasting results, claiming, on the one hand, that neither carrier compensation nor the Dirac arc node surface states are the primary source of XMR [190], while, on the other hand, suggesting that a combination of carrier compensation and a mixture of *d-p* orbital texture are the origins of the XMR [191].

In this chapter, I explore the transport properties of the first FIB-machined microstructures of the material PtSn₄, with particular emphasis on their magnetoresistive behaviour. As already mentioned in previous chapters, the use of the FIB allows for a much better signal to noise ratio thanks to the reduction in cross section of the fabricated microstructures. This is a significant advantage for an extremely good conductor like PtSn₄ whose voltage signal might be difficult to measure without inducing Joule heating via large applied currents. Furthermore, the FIB also offers excellent control over the fabrication of devices of precise dimensions and along the desired crystallographic axes, which can be a key factor when investigating the origin of MR. The results presented here highlight the role of the Fermi surface shape in the measured MR for currents applied along the main crystallographic axes. In particular, the observation of saturated transverse MR points to the formation of open orbits on specific branches of the FS. This consequently suggests a semi-classical mechanism like imperfect electron-hole compensation as a likely candidate for the origin of the XMR typically observed in PtSn₄. In the next section I briefly discuss the known electronic properties of the material PtSn₄. Next, in section 7.3 I present the main experimental results, including the observation of both sub-quadratic field dependence of the MR as well as MR saturation depending on the direction of the applied current. An additional magneto-oscillatory effect known as Sondheimer oscillations (SO) is also reported, a phenomenon never observed before in PtSn₄ macrocrystals. Finally, section 7.4 summarizes the work.

7.2 PtSn₄ material characteristics

PtSn₄ crystallizes in an orthorhombic structure with lattice parameters $a = 6.418\text{\AA}$, $b = 11.366\text{\AA}$ and $c = 6.384\text{\AA}$ and with the Sn-Pt-Sn layers stacked along the b axis (see figure 7.1(a)) [192, 193]. This layer structure is visible in the single crystals, which typically exhibit large flake-like features extending on the ac plane and stacked along the b axis, as shown in figure

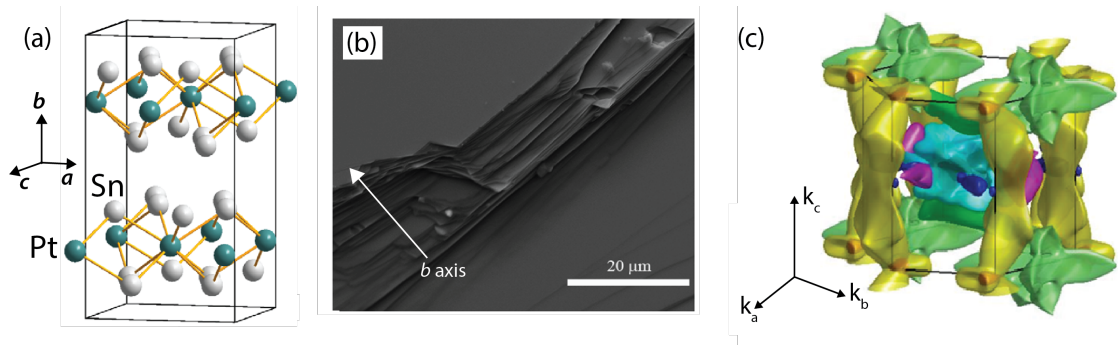


Figure 7.1: **Crystal structure and electronic characteristics of PtSn₄**. (a) Orthorhombic unit cell. (b) Typical layer structure of the crystals [196]. (c) Calculated Fermi surface [194].

7.1 (b). The electronic behaviour is characterized by a very complex Fermi surface (see figure 7.1 (c)), excellent conduction at low temperature ($\rho(2K) \sim 0.04 \mu\Omega.cm$), extreme purity with residual-resistivity ratios ($RRR = \rho(300K)/\rho(2K)$) of around 1000 and an estimated mean free path of around $3 \mu m$ at 2K [61]. Hall voltage measurements suggests the presence of highly mobile electron-like and hole-like charge carriers, with the former dominating the conduction at low temperatures. PtSn₄ also exhibits a largely suppressed thermal conductivity under an applied magnetic field along the *b* axis [194], which is attributed to the different transport behaviour of both charge carriers under a magnetic field. The crystals used in this chapter were grown out of a Sn-rich binary melt as described in [195] and were provided by the group of prof. Paul Canfield from the Ames National Laboratory at Iowa State University.

7.3 Experimental results

7.3.1 Magnetoresistance and Kohler scaling

Figure 7.2 (a) shows the initial microstructure fabricated with two sets of voltage probes along the *c* crystallographic direction. The sample was made using lamellae extracted with the P-FIB from aligned single crystals, whose crystallographic directions were determined by XRD (following the procedure already described in sections 2.5 and 3.4). For this particular sample the sputtered layer was made from Pd since its chemical similarity to Pt was thought to improve the contact resistance. Subsequent samples were fabricated using the more common option of Au for the sputtered layer, obtaining in both cases contact resistances in the order or a couple of Ohms. Initially, some surface roughness appeared when removing the Pd layer with the Ga-FIB but this artifact was later avoided by using smaller voltage and current parameters during the sputtered-layer removal step (around 5kV and 200pA). Figure 7.2 (b) shows the measured resistivity as a function of temperature for both available voltage channels. The signals from both channels are almost identical and the values and overall behaviour of the measured resistivities match very well those reported for macroscopic single crystals [61]. However, the RRR values obtained, while still suggesting a very clean system, are not as high

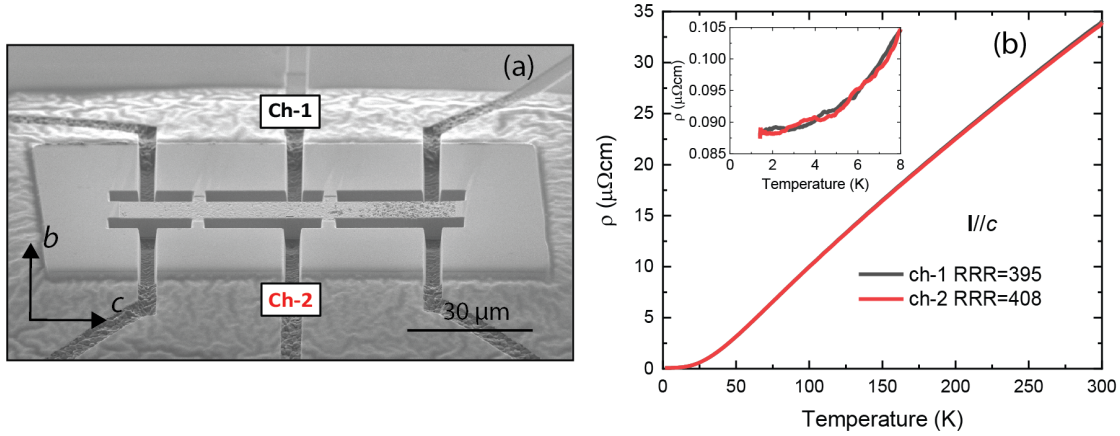


Figure 7.2: **Glue-mounted PtSn_4 microstructure.** (a) SEM image of the fabricated sample. (b) Resistivity vs temperature for both voltage channels available. The inset highlights the resistivity at low temperatures.

as those reported for macroscopic single crystals. The difference comes mainly from the low temperature resistivity values, which are systematically larger in the microstructures. This is not surprising since the geometrical dimensions of the microstructure are comparable to the reported mean free path ($\approx 3 \mu\text{m}$ [61]) so additional boundary scattering is expected to appear.

The transverse MR (as defined as $\text{MR} = 100 \times [R(B) - R(B = 0)] / R(B = 0)$) of the microstructure at different temperatures and along the field directions $\mathbf{B} \parallel a$ and $\mathbf{B} \parallel b$ is presented in figure 7.3. Once again, the overall behaviour matches well the observed one in macrocrystals. For all field and temperature ranges measured, an unsaturated XMR was obtained. At 1.5K and 14T, an XMR of $\approx 1.1 \times 10^5\%$ and $\approx 7.2 \times 10^4\%$ was observed for $\mathbf{B} \parallel a$ and $\mathbf{B} \parallel b$, respectively. This is consistent with the fact that at high fields the cyclotron radius shrinks well below the dimensions of the microstructure so the bulk behaviour is recovered. The MR falls quickly with temperature, dropping to $\approx 378\%$ and $\approx 430\%$ at 40K and 14T for $\mathbf{B} \parallel a$ and $\mathbf{B} \parallel b$, respectively. The MR at different temperatures is typically analyzed using Kohler's rule, which states that it should exhibit a scaling behaviour of the form $\text{MR} = f(B/\rho_0)$, where $\rho_0 = \rho(T, B = 0)$ and f is usually a power law. It can be shown that $B/\rho_0 \propto l/r = \omega_c \tau$, where l is the mean free path, r the cyclotron radius, ω_c the cyclotron frequency and τ the scattering time. B/ρ_0 then quantifies how many orbits the charge carriers can make before being scattered. The physical content of the Kohler's scaling is that the MR can be fully explained by orbital effects with a field-independent scattering time, in which case the MR vs B/ρ_0 curves at different temperatures should overlap with each other. The corresponding Kohler plots for the microstructure for field directions $\mathbf{B} \parallel a$ and $\mathbf{B} \parallel b$ are shown in figures 7.3 (c) and (d), respectively. In both cases the MR data seems to collapse into a single curve, which exhibits a sigmoidal shape similar to the one reported previously for both PtSn_4 [61] and its isostructural compound PdSn_4 [190]. The high field/low temperature region appears as well characterized by a power law with $\text{MR} \propto (B/\rho_0)^{1.8}$ and $\text{MR} \propto (B/\rho_0)^{1.7}$ for $\mathbf{B} \parallel a$ and $\mathbf{B} \parallel b$, respectively. In [190], it is argued that

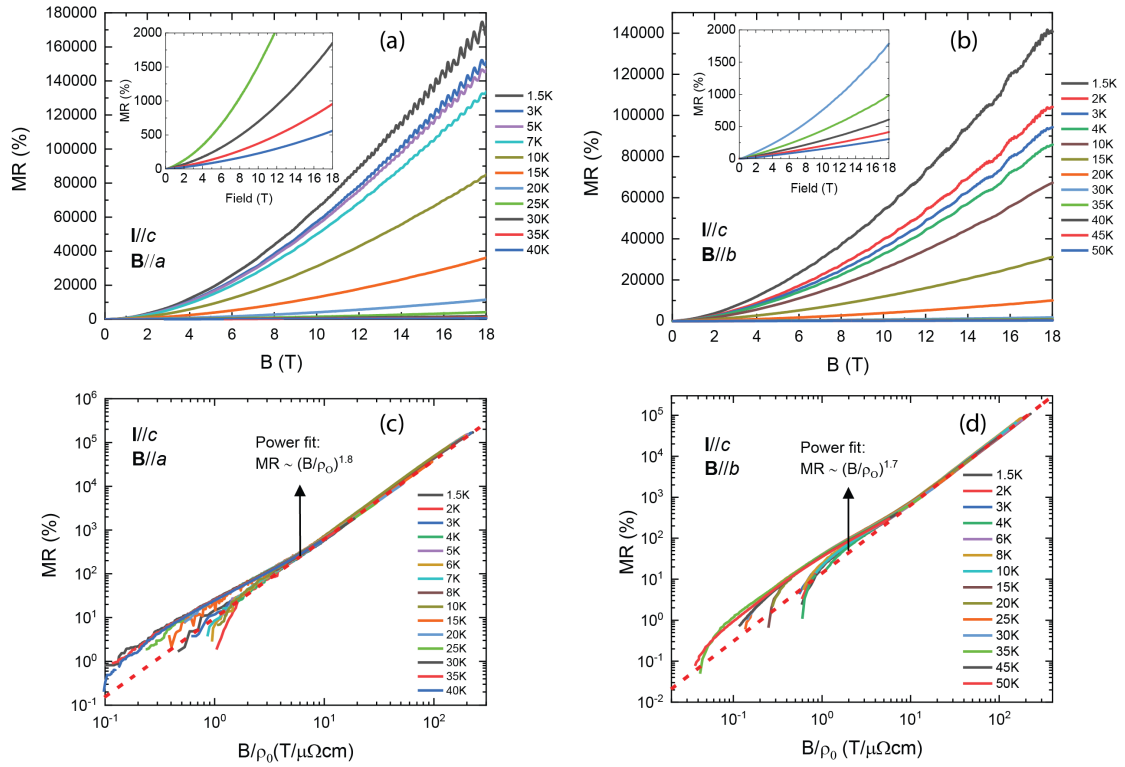


Figure 7.3: **Transverse magnetoresistance as a function of temperature and field magnitude and direction.** MR for (a) $\mathbf{B} \parallel a$ and (b) $\mathbf{B} \parallel b$ at the indicated temperatures. The insets (a) and (b) show the MR at higher temperatures. Kohler plots of the MR for for (c) $\mathbf{B} \parallel a$ and (d) $\mathbf{B} \parallel b$. The insets (c) and (d) show the Kohler scaling at higher temperatures.

the beginning of the low field/high temperature region signals the transition from the $\omega_c \tau \gg 1$ condition to the $\omega_c \tau \ll 1$ one and that the collapse of the MR data into this "generalized" Kohler scaling points to the same underlying physics for both regimes.

The high quality of the microstructure is also evident in the clear SdH oscillations observed in the MR curves. The corresponding oscillatory components and their FFT are presented in figure 7.4 (a) and (b) for $\mathbf{B} \parallel a$ and $\mathbf{B} \parallel b$, respectively. The complexity of the FS is once again revealed in the considerable number of resolved FFT peaks. Although a mapping of the FS is not the main purpose of this work, some of the main peaks and their corresponding effective masses m^* are reported in table 7.1. The peaks and their associated effective masses are consistent with previously reported ones [61, 197] originating from closed electron and hole pockets.

7.3.2 Resistivity anisotropy

Given the flake-like structure of PtSn₄, with the thinnest dimension along the b crystallographic axis, measurements of the resistivity along this direction are difficult to perform in

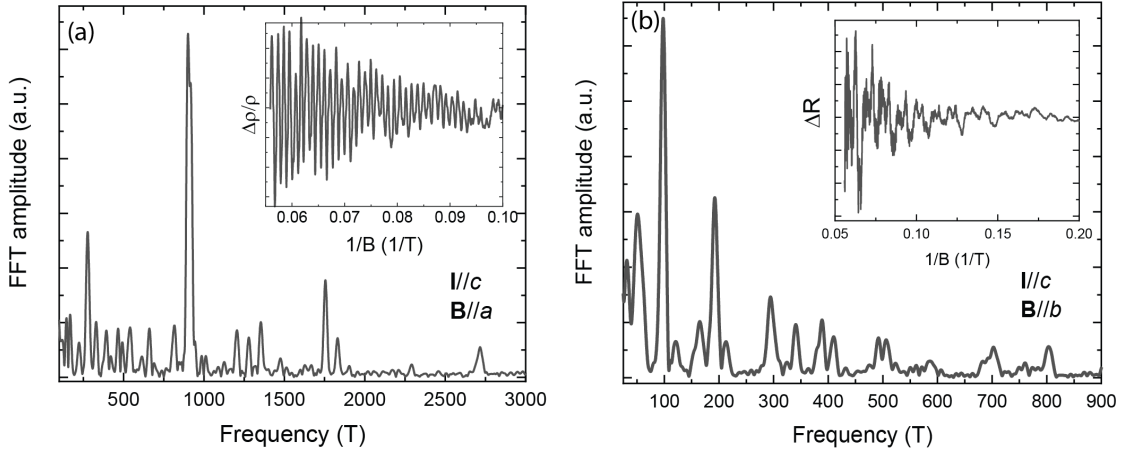


Figure 7.4: **Shubnikov-de Haas oscillations for two different field directions.** FFT spectra of the SdH oscillations at 1.5K for (a) $\mathbf{B} \parallel a$ and (b) $\mathbf{B} \parallel b$, with some of the main FFT peaks highlighted. The insets (a) and (b) show the oscillatory components of the MR after background subtraction.

$\mathbf{I} \parallel c$			$\mathbf{I} \parallel a$					
$\mathbf{B} \parallel a$			$\mathbf{B} \parallel b$			$\mathbf{B} \parallel c$		
	Freq. (T)	m^*/m_e		Freq. (T)	m^*/m_e		Freq. (T)	m^*/m_e
F1	276	0.27	F1	98	0.24	F1	95	0.21
F2	330	0.37	F2	192	0.23	F2	108	0.21
F3	660	0.51	F3	293	0.05	F3	264	0.27
F4	900	0.40	F4	340	0.26	F4	288	0.32
F5	912	0.39	F5	390	0.26	F5	514	0.27
F6	1750	0.94	F6	1560		F6	1023	0.39
						F7	2552	

Table 7.1: **Main experimental SdH frequencies and corresponding cyclotron effective masses.** m_e is the bare electron mass. The case $\mathbf{I} \parallel a$, $\mathbf{B} \parallel c$ is taken from the measurements of the sample presented in figure 7.10.

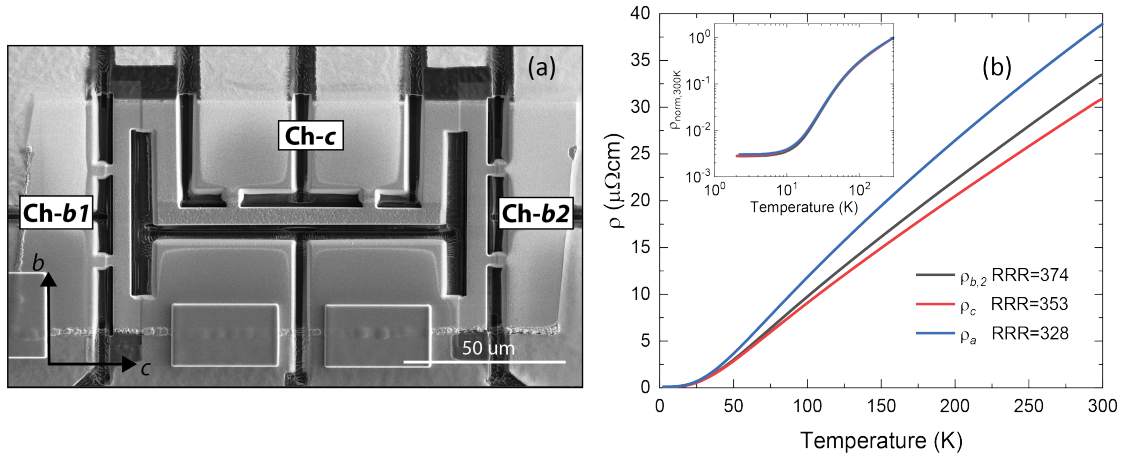


Figure 7.5: **Temperature dependence of the resistivity along different crystallographic directions.** (a) SEM image of the fabricated sample. (b) Resistivity vs temperature for currents applied along all three main crystal axes. ρ_a was measured in the microstructure presented in figure presented in figure 7.10. The inset in (b) shows the normalized resistivities $\rho(T)/\rho(300K)$.

macrocrystals. In fact, the only report of this measurement that I am aware of claims a value of $\rho_b \approx 3800 \mu\Omega cm$ at room temperature, about 10 times larger than the values of ρ_a and ρ_c reported in the same study [198]. The values of ρ_a and ρ_c reported in that study are themselves around 10 times larger than the ones typically found in the literature, which might point to defective samples or experimental flaws. In any case, the question of whether such a large anisotropy actually exists remains relevant since it would have important consequences for the general transport behaviour of PtSn_4 . To tackle this question a so called "U" microstructure was fabricated using the P-FIB featuring voltage probes along the b and c crystallographic directions (see figure 7.2 (a)). Figure 7.2 (b) shows the measured resistivity as a function of temperature for all main three crystal axes, where the one associated to axis a was measured using an additional free-standing microstructure to be discussed in the next section. The values of the different resistivities suggest that the electronic behaviour of PtSn_4 is rather isotropic, in spite of its layered structure and complex FS branches. The resistivities do show some differences, specially in the higher temperature range, but still compare well with the values typically reported in literature ($\approx 30 \mu\Omega cm - 40 \mu\Omega cm$ for currents applied in the ab plane). Furthermore, the normalized resistivity curves $\rho(T)/\rho(300K)$ overlap almost perfectly, indicating a consistent and unified metallic behaviour. The origin of the high temperature discrepancies remains unclear but factors like strain might be at play, with some studies suggesting a sensitivity of room temperature resistivity to pressure in the isostructural compound PdSn_4 [199].

The transverse MR of the channels with $\mathbf{I} \parallel b$ has a similar behaviour to the one of the channels with $\mathbf{I} \parallel c$, namely, a background MR $\propto \approx B^{1.8}$ with clear superimposed SdH oscillations whose frequency content is consistent with the results for the other current directions with

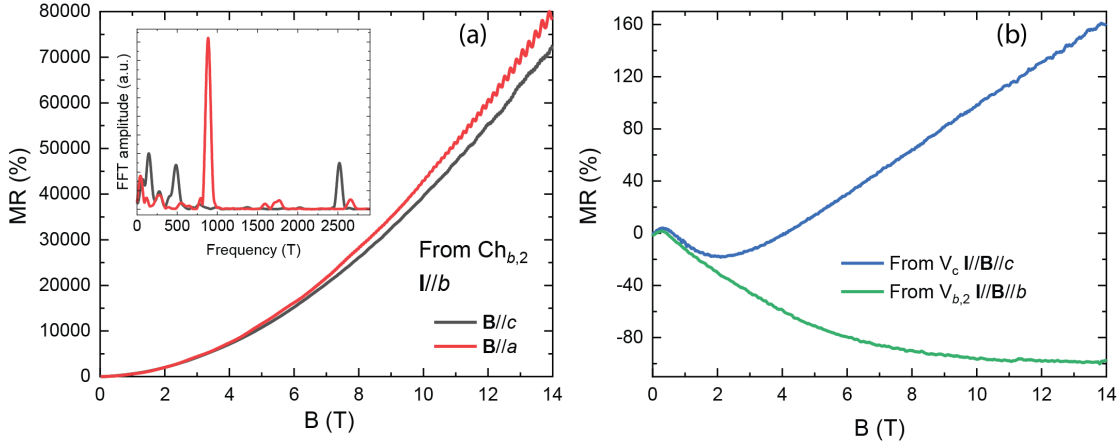


Figure 7.6: **Magnetoresistance as a function of field magnitude and direction from the "U" structure at 2K.** (a) Transverse MR for $\mathbf{B} // a$ and $\mathbf{B} // c$. The inset shows the FFT of the corresponding oscillatory part of the MR. (b) Longitudinal MR for $\mathbf{I} // b$ and $\mathbf{I} // c$.

same field configuration (see figure 7.6 (a)). The longitudinal MR for both $\mathbf{I} // c$ and $\mathbf{I} // b$ is presented in figure 7.6 (b), where clear regions of negative MR can be observed at low fields. The shape of the longitudinal MR curves has some similarities with the ones reported for other materials like ZrSiS [181] and GdPtBi [200] where it was associated to the presence of the chiral anomaly. However, such a curve could also be interpreted based on the Knudsen effect originating from the enhanced boundary scattering of strongly confined electrons in very clean systems [171].

7.3.3 Sondheimer oscillations

In addition to the $1/B$ -periodic SdH oscillations, another kind of magneto-oscillatory behaviour was also observed in all the PtSn₄ microstructures studied in this work, namely, B -periodic oscillations known as Sondheimer oscillations [201, 202]. Figure 7.7 (a) shows the MR in the low field regime of the "U" microstructure after a background subtraction was performed using a second degree polynomial. Clearly resolved B -periodic oscillations appear in all the channels measured. SOs were detected in longitudinal voltage channels as well as in Hall-voltage channels (when available in the microstructure). The physical origin of the SO is schematically depicted in figure 7.7(b). Unlike the space localized, quantum coherent electron states that give rise to the SdH oscillations, the states responsible for the SO move in semi-classical helical trajectories with a net velocity along the magnetic field B . The magnitude of B determines the helical radius and hence how many revolutions the electron completes while moving from one surface to the other in the microstructure. For certain values of B , the movement is commensurate with the distance between surfaces, that is, there will be an integer number of revolutions. In that case, the charge carrier performs no net motion along the channel, and hence is semi-classically localized. However, if the number of revolutions is non-integer, a net motion exists, de-localizing the carriers and resulting in

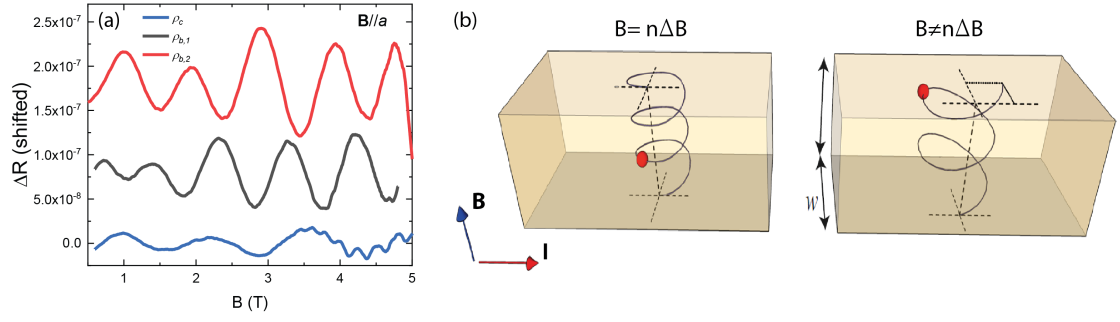


Figure 7.7: **Sondheimer oscillations in a PtSn₄ microstructure.** (a) B-periodic oscillations in the low field regime of the "U" microstructure MR curves at 2K after a background subtraction. (b) Schematic depiction of the Sondheimer effect. Image adapted from [203].

oscillatory longitudinal and transverse magnetotransport behaviour[203].

The period of the SOs can be determined by calculating the ratio of two quantities: the time it takes to travel the thickness d of the microstructure, $t_d = d/v_{\parallel}$; and the time it takes to complete one full cyclotron revolution, $\tau_c = 2\pi/\omega_c = 2\pi m^*/eB$, where v_{\parallel} is the velocity component parallel to the magnetic field. For some field values, an integer number n of revolutions is completed within the channel, $t_d/\tau_c = n$, which happens periodically with a period ΔB of:

$$\Delta B = \frac{2\pi m^* v_{\parallel}}{ed} \quad (7.1)$$

this expression establishes one of the main characteristic of the SOs, namely, a linear dependency of the oscillation frequency and the thickness of the device perpendicular to the magnetic field.

SOs can be used to extract information about the relevant scattering mechanisms in the microscopic conduction process, in particular, they can be used to extract a value of the transport mean free path and identify the appropriate conduction regime. Recently, this has been done very successfully in the material WP₂ [203], where the SOs were used as a quantitative probe of the inelastic scattering mean free path and the identification of the relevant FS parts contributing states to the SOs. Although this FS identification is more complicated in the case of PtSn₄, given its complexity, it is still interesting to probe the scattering mechanisms in such a clean material. Unlike QOs from bulk quantization, SOs do not depend on self-interference of electron waves and therefore do not require quantum coherence. They persist up to higher temperatures, limited only by the bulk transport mean free path l (instead of the quantum one). As l decreases with increasing temperature, it can be shown that the amplitude of SO diminishes as $e^{-d/l}$ [204], which can be used to determined l :

$$\frac{1}{l} = -\frac{1}{d} \ln \frac{A(T)}{A(0)} \quad (7.2)$$

where, $A(T)$ is the SO amplitude at temperature T and $A(0)$ is determined by extrapolation.

To probe the SOs in PtSn₄ and the linear dependence of their frequency on the device thickness, a "staircase" microstructure with several sections of different thickness was fabricated (see figure 7.8(a) and (b)). This design allows for the simultaneous measurement of each section using both Hall and longitudinal voltage contacts. I present the preliminary results obtained from this sample as its behaviour regarding SOs exemplifies and encapsulates the behaviour of the other microstructures fabricated for this work. Figure 7.8 (c) shows the measured MR from the longitudinal contacts after a background subtraction and for different angles of the applied magnetic field. B -periodic oscillations are clearly observed, which extend only for a narrow angle range of $\approx 5^\circ$ around the perpendicular field configuration $\mathbf{B} \parallel c$ ($\theta = 90^\circ$). At high fields, the curves also exhibit the onset of conventional SdH oscillations. Figure 7.8 (d) shows the FFT of the curves in figure 7.8 (c) at $\mathbf{B} \parallel c$. The extracted SOs frequency $F = 1/\Delta B$ is plotted against the channel thickness in figure 7.8 (c), clearly revealing a linear dependency.

Figure 7.9 (a) shows the temperature dependence of the SOs. From the FFT peak, the corresponding amplitude suppression with temperature is presented in figure 7.9 (b). The data is fitted with an expression of the form $A(T) = A_1 / (1 + \exp(\frac{T-c_1}{c_2}))$, which describes the data very well and from which the extrapolated amplitude value $A(0)$ can be determined. Following equation 7.2, the bulk mean free path is then calculated for each section of different thickness and plotted against temperature in figure 7.9 (c). Although some differences exist in the values of l associated to each thickness, a decent match and similar overall behaviour is observed, especially for higher temperatures. The value of $l \approx 40\mu\text{m}$ at 2K is considerably larger than the reported value of $l \approx 3\mu\text{m}$ at the same temperature determined for macrocrystals using the expression $l = \hbar(3\pi^2/n^2)^{1/3}/e^2\rho_0$, where n is the charge carrier concentration and ρ_0 the resistivity at low temperatures [61, 205]. At 12K, the estimated $l \approx 2\mu\text{m}$ is much smaller than the $l \approx 30\mu\text{m}$ reported in [196] at 13K, which was estimated from the resistivities vs temperature curves at fixed magnetic fields.

7.3.4 Suppression of magnetoresistance

As already mentioned before, a free-standing microstructure of PtSn₄ was fabricated to account for potential strain effects (see figure 7.10 (a)). This microstructure was fabricated following the procedure already described in section 2.5.3 and incorporates voltage probes along the crystallographic a direction. The resistivity vs temperature curves are presented in figure 7.10 (b), showing a metallic behaviour consistent with the behaviour of macrocrystals and the other microstructures already presented in this work, and the high crystalline quality of the devices as reflected in the RRR values.

The transverse MR behaviour of the free-standing microstructure is presented in figure 7.11. Figure 7.11 (a) shows the temperature dependence of the resistivity for $\mathbf{B} \parallel c$ and field magnitudes of $B = 0\text{T}$, 4T, 8T and 14T. Once again, the overall behaviour is consistent with what has been reported for macrocrystals. Above 50K the resistivity shows a weak dependence on magnetic fields. Between 50K and 10K, $\rho(T)$ increases rather rapidly and below 10K, where

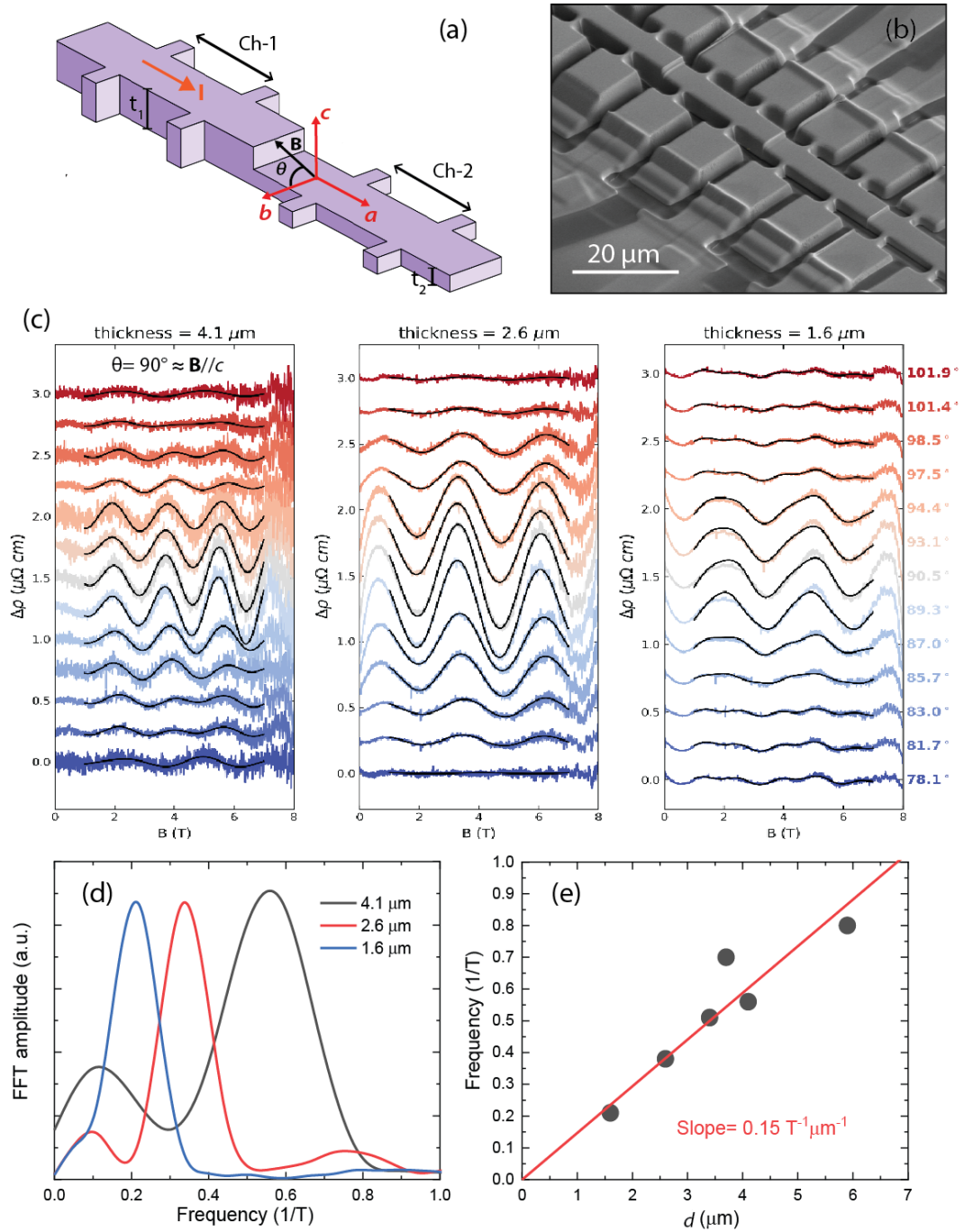


Figure 7.8: **Staircase structure designed for SOs experiments.** (a) Schematic representation of the sample's design and the rotation of the magnetic field. (b) SEM image of the fabricated sample. (c) Oscillatory component of the low field signals coming from the sections of different thicknesses $d = 4.1 \mu\text{m}, 2.6 \mu\text{m}$ and $1.6 \mu\text{m}$. (d) FFT of the curves in (c) for the field configuration $\mathbf{B} \parallel c$. (e) Dependence of the SOs frequency on the channel thickness d . The solid line indicates a linear fit.

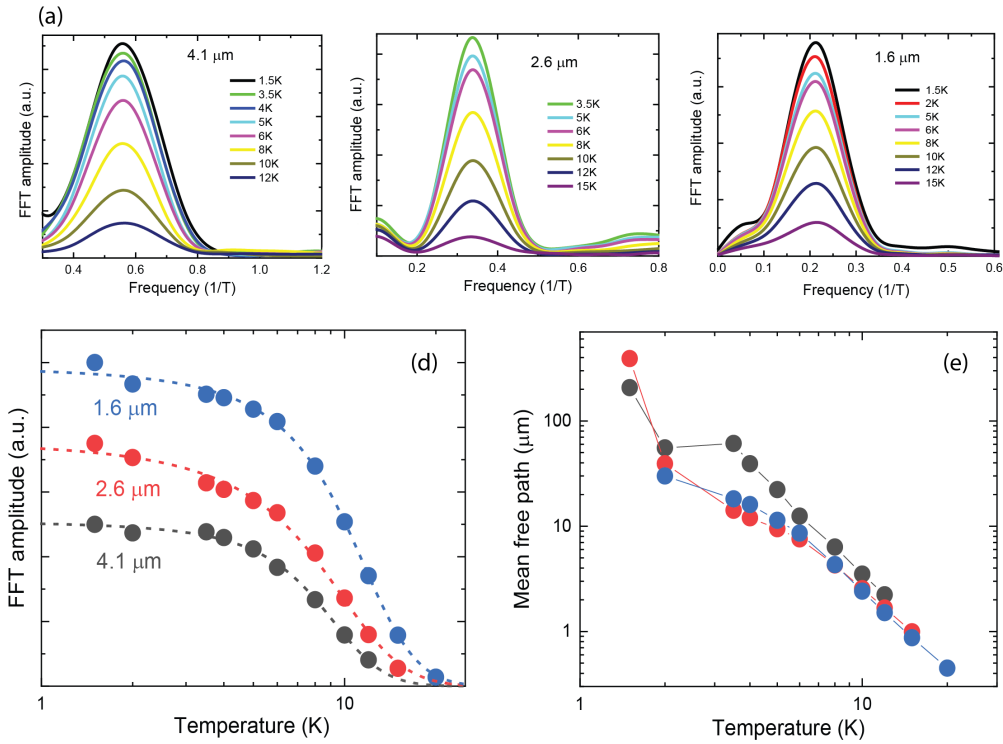


Figure 7.9: **Mean free paths extracted from Sondheimer oscillations.** (a) FFTs of the SOs at different temperatures for thicknesses $d = 4.1 \mu\text{m}, 2.6 \mu\text{m}$ and $1.6 \mu\text{m}$. (b) Temperature dependence of the SOs amplitude for the indicated thicknesses. The dashed lines are fits used to extrapolate to the amplitude at zero temperature $A(0)$. (c) Mean free paths calculated for the same thicknesses shown in (b) using equation 7.2.

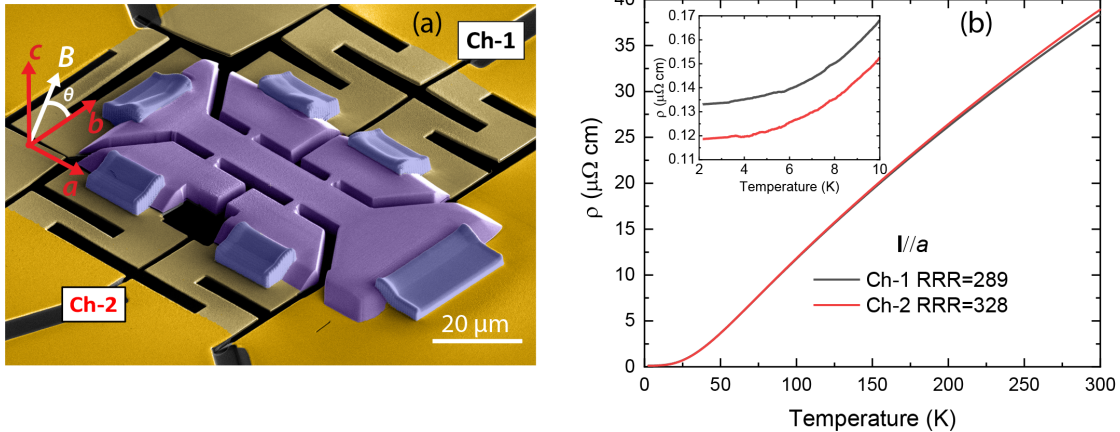


Figure 7.10: **Free-standing microstructure.** (a) SEM image of the fabricated sample and magnetic field configuration in the experiment. (b) Resistivity vs temperature for both voltage channels available. The insets in (b) show the resistivity at low temperatures.

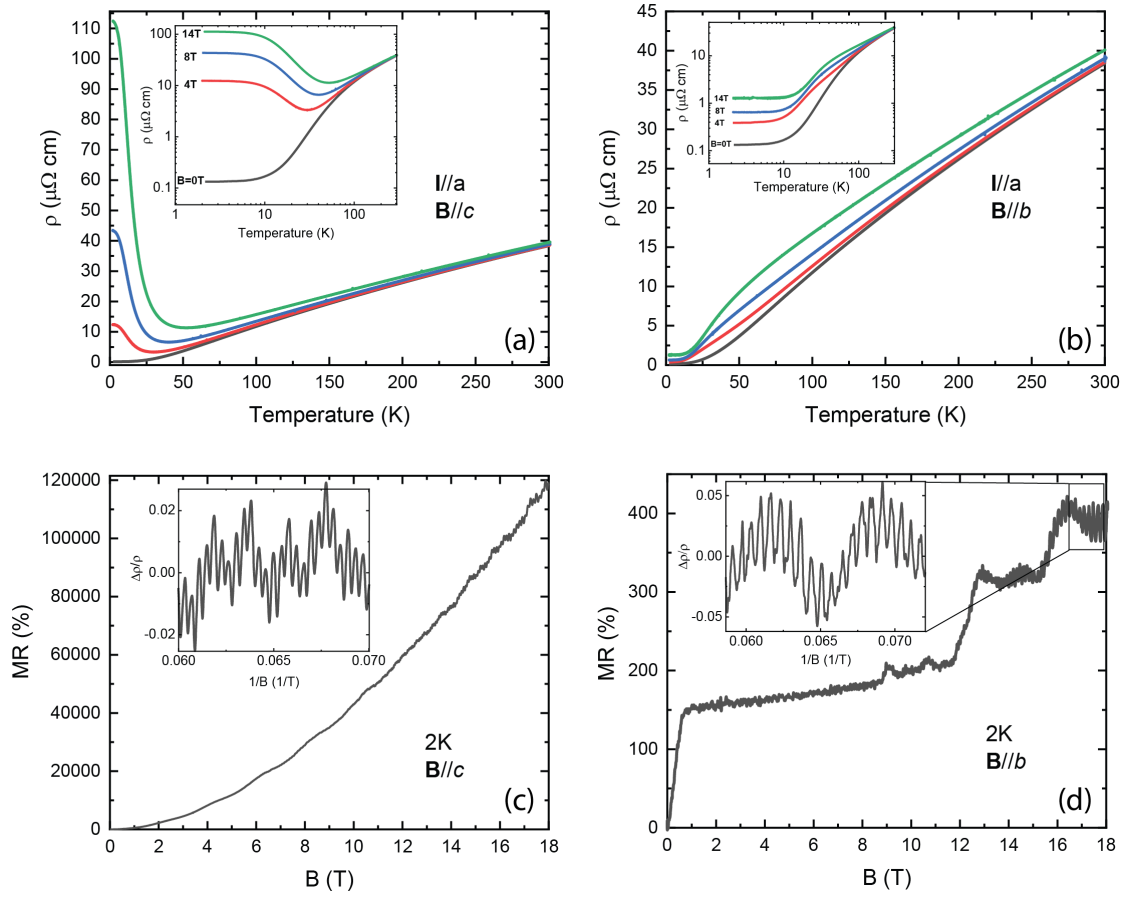


Figure 7.11: **Magnetoresistance as a function of field magnitude and direction for the free-standing microstructure.** Temperature-dependent resistivity for fixed fields applied along (a) $\mathbf{B} \parallel c$ and (b) $\mathbf{B} \parallel b$. The insets (a) and (b) show the same data in a log-log scale. Magnetoresistance field dependency at 2K for fields applied along (c) $\mathbf{B} \parallel c$ and (d) $\mathbf{B} \parallel b$. The insets (c) and (d) highlight the SdH oscillations. (e) and (f) FFT spectra from the oscillatory components of (c) and (d), respectively.

$\rho(T)$ saturates at zero field, it also saturates to a constant value. Similarly, the field dependence of the MR for $\mathbf{B} \parallel c$ behaves as expected (see figure 7.11 (c)): the background MR grows quickly in a nearly quadratic fashion, with superimposed SOs as well as SdH oscillations, whose frequency content matches well the observed one for the other microstructures.

Contrarily, the behaviour for $\mathbf{B} \parallel b$ is remarkably different to what's been reported so far for PtSn₄. Figure 7.11 (b) shows the temperature dependence of the resistivity for $\mathbf{B} \parallel b$ and field magnitudes of $B=0T$, 4T, 8T and 14T. As for the $\mathbf{B} \parallel c$ case, above 50K the resistivity increases only slightly with field but, unlike before, there is no region of rapid increase in resistivity at low temperatures, instead, $\rho(T)$ saturates below 10K without ever reaching large values of MR. This behaviour is also observed in the field dependence of the MR (see figure 7.11 (d)). Instead of the expected $MR \propto \approx B^{1.8}$ growth, we observe an initial small increase up to

$\approx 1\text{T}$, followed by a plateau that extends to around 12T where the MR saturates to an almost field-independent value of ≈ 175 . For higher fields, the MR increases in a step-wise fashion, and the SdH oscillations start to become appreciable. At 14T , $\text{MR} \approx 300$, less than 400 times what's been reported in previous studies for the same $\mathbf{B} \parallel b$ field direction [61].

To further explore the observed suppression of the MR when $\mathbf{B} \parallel b$, figure 7.12 (a) shows the transverse MR at fixed fields as a function of rotation angle θ . In the experiment, the field always remains in the bc plane, i.e., in the transverse configuration. The MR exhibits two clear dips, a small one when $\mathbf{B} \parallel c$ and a much more pronounced one when $\mathbf{B} \parallel b$, around which the MR quickly grows as the field is increased. When this kind of MR is presented in a polar plot, it exhibits a characteristic butterfly shape that has also been reported in materials like PdSn₄ [206] and ZrSiS [207]. The field dependence of the MR for field directions close to $\mathbf{B} \parallel b$ is presented in figure 7.12 (b). For fields up to $\approx 1\text{T}$, all the curves coalesce and show the same initial small surge but as the field increases they begin to diverge significantly. Only the curves within a very narrow angle range of less than 2° around the $\mathbf{B} \parallel b$ direction exhibit MR suppression, while the others grow quickly and in a manner closer to the previously observed sub-quadratic behaviour. This sensitivity to field orientation is one of the reasons why MR suppression was not observed before in PtSn₄ macrocrystals, although in [196], for example, the resistivity vs temperature curves at fixed values of the magnetic field, applied along the b axis, already showed a much smaller low temperature MR than in other studies (albeit in crystals of poorer quality, $\text{RRR} \approx 70$). Similarly, the analogous resistivity curves for the compound PdSn₄ reported in [206] also showed a very weak dependence on the applied magnetic field.

For higher field values, the MR curves of figure 7.12 (b) start to show appreciable SdH oscillations, whose FFT is presented in figure 7.12 (c). The same curves that exhibit a suppressed MR, also exhibit two dominant peaks: $F_1 \approx 1480\text{T}$ and $F_2 \approx 1590\text{T}$. The amplitudes of these peaks quickly diminishes as the field is tilted away from the $\mathbf{B} \parallel b$ direction, as indicated in figure 7.12 (d) where such amplitudes are plotted as a function of the MR value at 17T . It's important to mention that a frequency around $F \approx 1590\text{T}$ was identified in macrocrystals of PtSn₄ through dHvA oscillations and associated to an extremal orbit from a closed FS branch centered in the BZ [197]. This orbit persists for fields tilted away from the $\mathbf{B} \parallel b$ direction, which strongly suggests that it can't be the origin of the quickly vanishing frequencies F_1 and F_2 .

To investigate the potential existence of suppressed MR in a macrocrystal and rule out a possible finite-size-related cause, I prepared a single crystal for transport measurements in the traditional four-point configuration with manually attached wires and current applied along the ac plane (see figure figure 7.13 (a)). The crystal has the typical flake-like shape of PtSn₄, with its shortest dimension along the b axis (thickness of around $100\mu\text{m}$). It was cut with the P-FIB from a larger crystal that had two sharp, almost perpendicular edges, assumed to be the a and c directions. To ensure the best possible orientation with respect to the magnetic field in the transport experiments, the crystal is mounted in a two-axis rotator incorporated in the Bluefors LD250 dilution refrigerator (see figure 7.13 (b)).

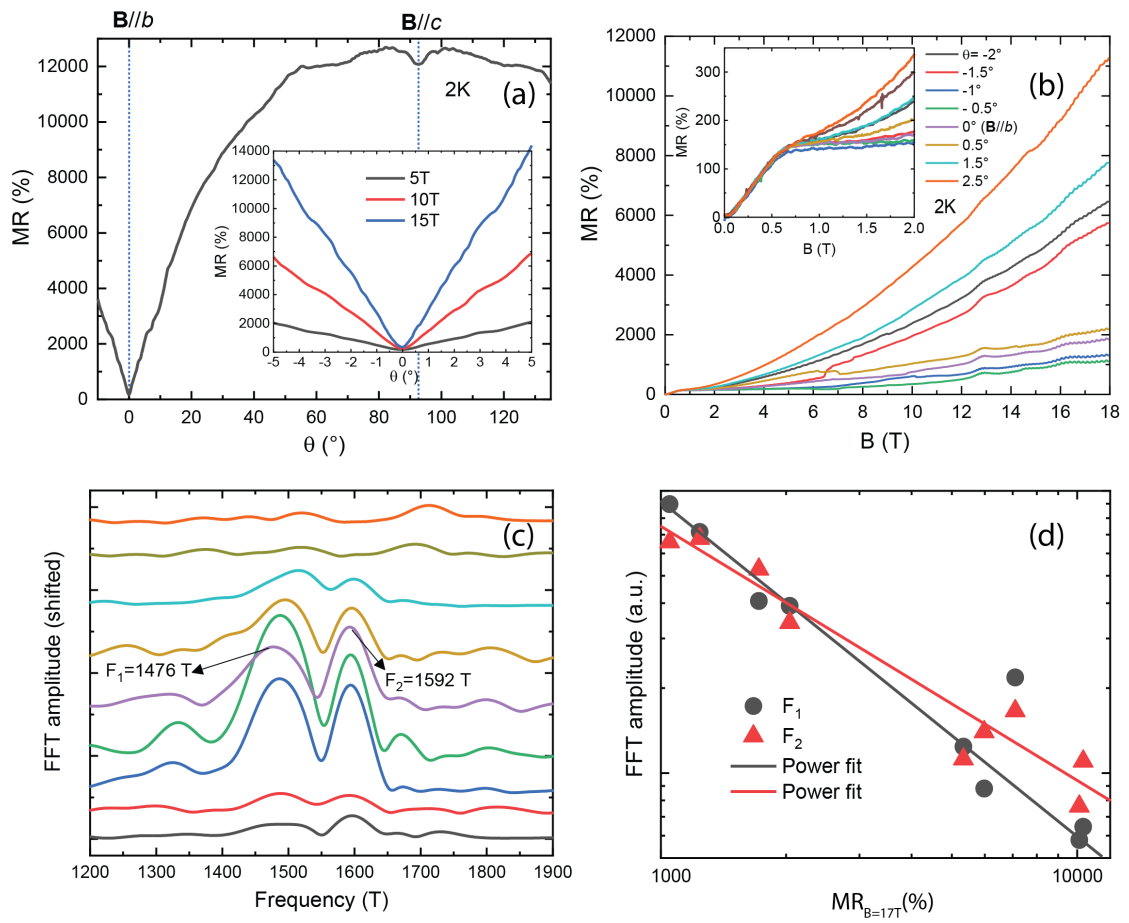


Figure 7.12: **Magnetoresistance around $B//b$.** (a) MR vs rotation angle at fixed field. The rotation angle is defined in figure 7.10 (a). (b) MR around $B//b$. The inset shows the MR at low fields. (c) Corresponding FFT spectra from the oscillatory components of (b). (d) FFT amplitude of the main two frequencies highlighted in (c) as a function of the MR value at 17T. ($I//a$ always)

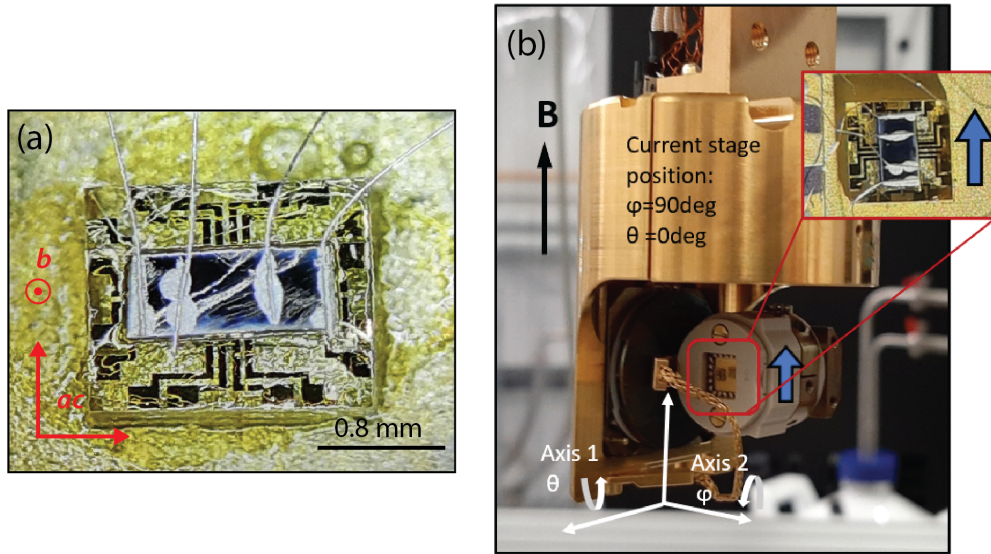


Figure 7.13: **Two-axis rotation study of a PtSn_4 macrocrystal.** (a) Electrical contacts and mounting of the crystal. (b) Atto-cube two axis rotation probe in the Bluefors LD250 dilution refrigerator.

The results of the measurements at 0.5K are presented in figure 7.14. Figure 7.14 (a) shows the MR vs the rotation angle φ at fixed values of $B=5\text{T}$ and $\theta = 90^\circ$. The MR curve clearly shows a considerable dip when $\mathbf{B} \parallel b$, similar to what had been observed before in the previous microstructure but no as pronounced in magnitude, and has the same overall butterfly shape. Analogous curves of the MR for fixed θ and scanning φ are combined to obtain the two dimensional mapping of the MR presented in figure 7.14(b). Such figure clearly shows a persistent minimum in the MR when $\mathbf{B} \parallel b$, no matter the value of θ . For some angles the MR map shows asymmetries around this minimum that could be due to the influence of Hall-like voltages. Similarly, MR turns negative for configurations close to the $\mathbf{B} \parallel \mathbf{I}$ condition, which was also observed before for microstructures but clearly is dominated by current inhomogeneity effects known as current jetting [208, 209].

The phenomenon of MR suppression was not only observed in the free-standing microstructure but also in the "staircase" microstructure originally designed for studying SO (figure see figure 7.8). Figure 7.15 (a) shows the transverse MR angle dependence at low temperature and fixed field of $B=5\text{T}$, revealing once more the huge drop in MR when $\mathbf{B} \parallel b$ for all the sections of different thickness. The corresponding field dependence of the MR for such field configuration is presented in figure 7.15 (b). The suppression of MR is observed in all measured sections, with the curves exhibiting the same overall features described before for the free standing microstructure. In particular, the plateau of almost constant MR is manifest in all cases. The evolution with temperature of the MR is also shown in figure 7.15 (b). As the temperature grows, the initial step feature and the following plateau are turned into monotonously increasing curves. This evolution, specially for temperatures below $\approx 20\text{K}$, is clearly incompatible

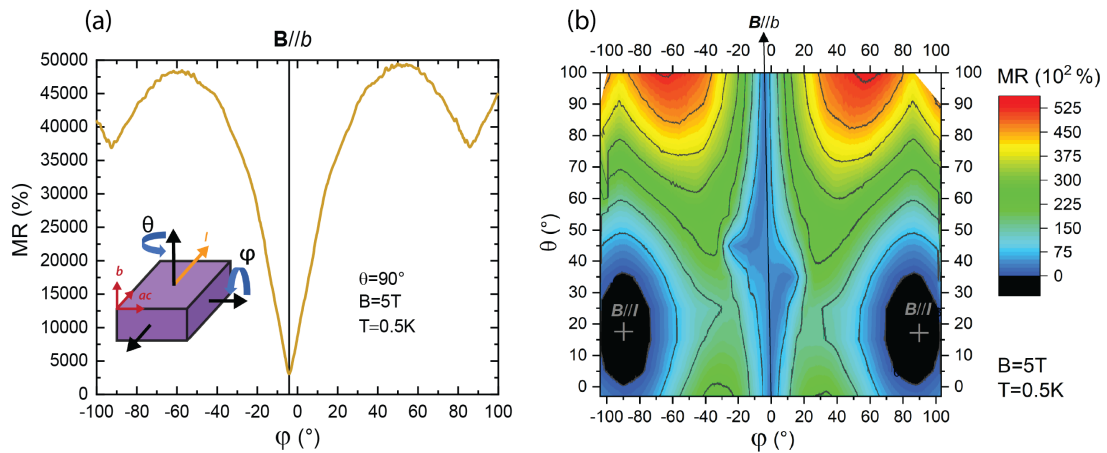


Figure 7.14: **Angular dependence of the magnetoresistance at 0.5K of a PtSn₄ macrocrystal.** (a) MR vs rotation angle φ at fixed θ . The inset shows the definition of both rotation angles φ and θ . (b) 2-d map of the MR at 5T.

with any kind of Kohler scaling, which suggests a completely different physical mechanism as the origin of the observed MR curves at low temperatures.

To look into the possible origin of the observed MR suppression, the band and FS structure was investigated. The calculations are presented in figure 7.16 and were performed by the collaborating post-doctoral researcher Dr. Qun Yang from the Max Planck institute for chemical physics of solids, in Dresden, Germany. Consistent with previous studies, the complexity of the FS and the multiple sheets of both electron and hole type that cross the Fermi level are revealed. Regarding the FS branches, one located at the boundary of the BZ stands out, as it connects to the next zone and effectively extends across both along the c axis. This branch is highlighted in figure 7.16 (c). It has the shape of a deformed cylinder-like tube and for the field direction $\mathbf{B} \parallel b$ it can actually host open orbits (also highlighted in figure 7.16 (c)). In contrast to closed ones, in open orbits the charge carriers cannot complete any revolution on the the FS so they do not give rise to quantum oscillations as no frequency can be associated with them. The orbits shown in figure 7.16 (c) are the only open orbits on this complex Fermi surface. Furthermore, the corresponding FS branch has two narrow necks on the $k_z = \pi/c$ and $k_z = 0$ planes of the BZ, which act as pinhole-collimators in k -space (see figures 7.16 (d) and (e)). This means that only for field configurations very close to $\mathbf{B} \parallel b$ the open orbits exist, as any other field orientation closes them when they miss the constrictions. We associate this very selective physical mechanism to the observed behaviour in the MR for fields close to $\mathbf{B} \parallel b$.

The effect of open orbits on the MR can be understood qualitatively in the following way: for open orbits extending along the z axis in the presence of a magnetic field parallel to the y axis, only the average velocity v_x remains appreciable and constant when $\omega_c \tau \gg 1$. This means that the corresponding resistivity tensor component ρ_{xx} saturates and leads to a suppressed MR for currents applied along that direction. On the other hand, it can be shown that the very

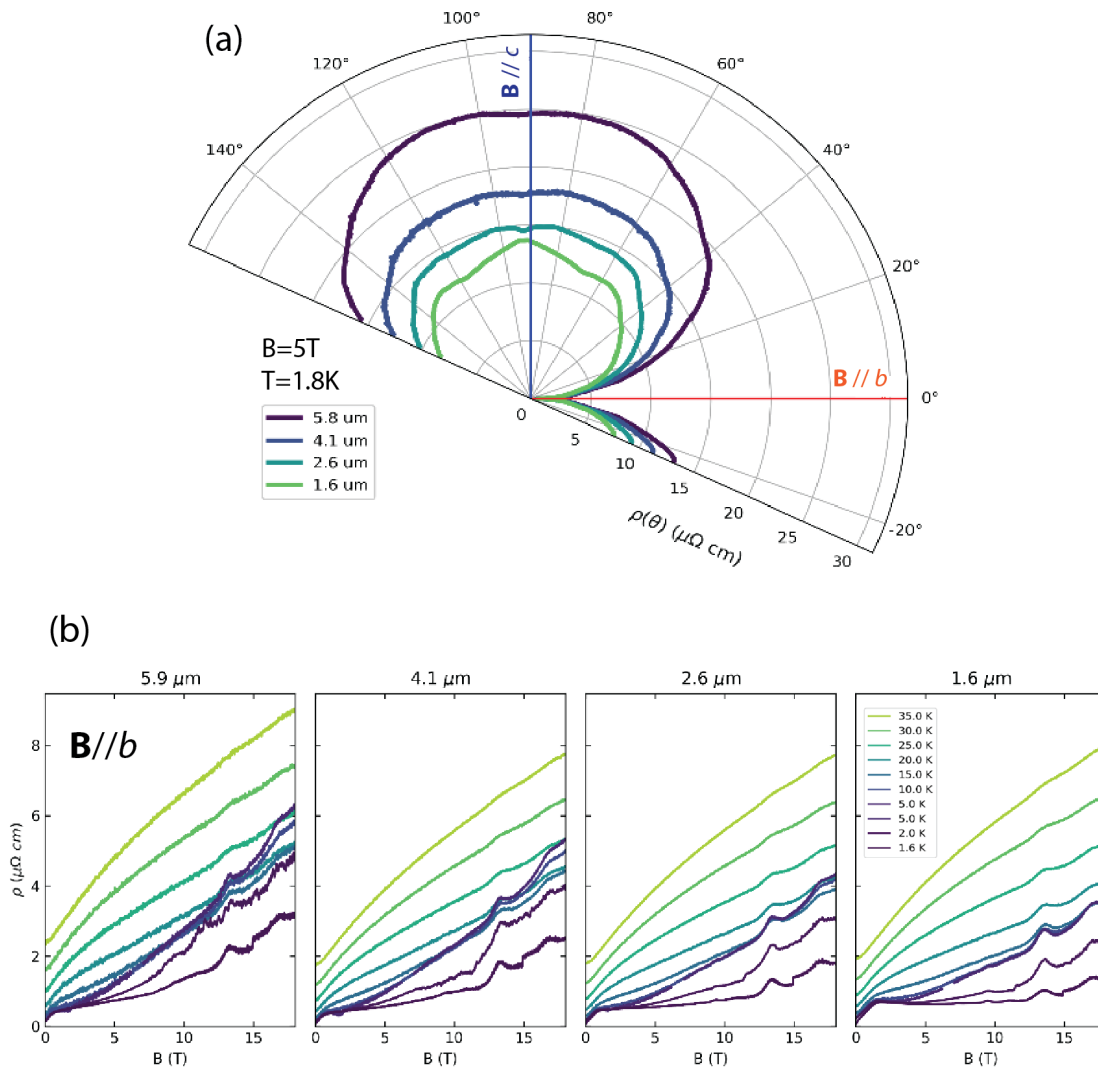


Figure 7.15: Magnetoresistance as a function of temperature and field magnitude and direction for the staircase microstructure. (a) MR vs rotation angle at 5T and 2K. (b) Resistivity vs field for the indicated temperatures along the field direction $\mathbf{B} // b$ ($\mathbf{I} // a$ always).

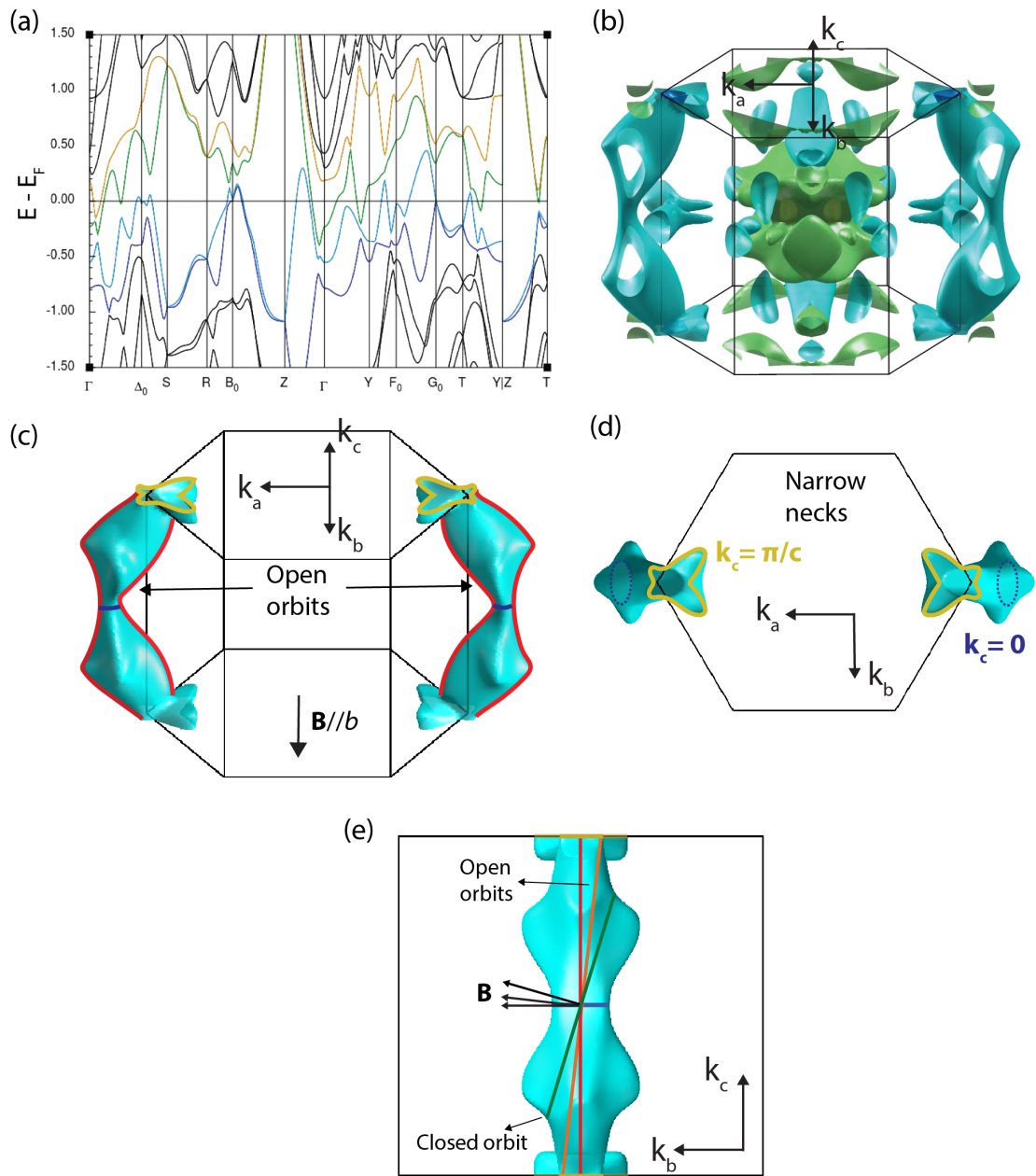


Figure 7.16: **Band structure and Fermi surface of PtSn₄.** (a) Band dispersion along high symmetry directions highlighting the different bands crossing the Fermi level. (b) Calculated Fermi surface. (c) FS branch extending along the BZ and capable of hosting the delineated open orbits. (d) Top view of the BZ highlighting the two narrow neck sections of the FS branch. (e) Open and closed orbits from different magnetic field directions. Only fields within a small angle range around $\mathbf{B} // b$ lead to open orbits.

small average velocity v_z results in a significant resistivity component ρ_{xx} , which increases quadratically with magnetic field for currents applied along the same direction [110]. In PtSn₄, the condition $\omega_c\tau \gg 1$ is already reached at small magnetic fields, and the lack of closed orbital motion for $\mathbf{B} \parallel b$ then leads to a saturation of the transverse MR, as these states are unaffected by further increases of the magnetic field. The saturation of the transverse MR for currents not running along the direction of the open orbits is a well known phenomenon [110] and has been nicely reproduced in recent numerical models based on the Boltzmann transport theory [114], as discussed in section 4.4.3 and shown in the corresponding figure 4.4. This mechanism also explains why the MR suppression was not observed in the microstructure presented in figure 7.2 since in that case the current was applied along the c axis, that is, parallel to the direction of the open orbits, a configuration that is not conducive to transverse MR saturation. This could also explain why the MR suppression observed in the macrocrystal of figure 7.14 is not as sharp as the one of the free standing microstructure, since the condition $\mathbf{I} \parallel a$ is satisfied to a much higher degree (thanks to the FIB microfabrication) in the latter.

7.4 Conclusions and outlook

In this chapter I have investigated the transport properties of FIB-fabricated microstructures as well as macrocrystals of the TSM PtSn₄. There are two main conclusions that change the way we think about charge transport in this material. First, the experiments presented in this chapter unequivocally demonstrate semi-classical effects at the origin of the unusually large and non-saturating magnetoresistance. No exotic correlated or topological features have to be invoked to explain it. This problem bears resemblance to the magic angles in elementary metals such as Ag or Cu, for which MR is lost. Similarly, the conditions for these angles arise from the open orbits defined by the touching points of their otherwise free-electron like Fermi surfaces. The real physical question is why such a complex crystal, with such a complex Fermi surface, is so clean as to show $\omega_c\tau \gg 1$ physics at such low magnetic fields. The observation of Sondheimer oscillations in the microstructures is fully consistent with this physics. Second, PtSn₄ is clearly identified as a hidden 2D system, yet with the two-dimensionality rotated by 90° compared to the crystallographic Pt planes. Naively, one might expect a 2D, cylinder like Fermi surface arising from these planes, yet that is not the case. Instead, a cylindrical Fermi surface is formed in the (ac) -plane, perpendicular to the natural layers of the crystal. This serves as a most interesting reminder that in densely packed intermetallic crystals, physical "layers" can be highly misleading when the electronic spectrum is considered.

8 Summary and outlook

In this chapter I present a brief summary of the results obtained during the course of this thesis and provide an outlook on the possible next research directions.

The first point I would like to emphasize is the *coming of age* of the focused ion beam as a microfabrication technique for novel 3D quantum materials. As the pool of materials investigated by this technique grows and its advantages and limitations become clearer, the enormous potential of FIB-machining is steadily being harnessed to reveal valuable physical insights and fabricate technologically relevant prototype devices. Part of this potential stems from the compatibility of the FIB approach with many other techniques and experimental tools, which can be exploited to explore electrical transport (and other properties) under previously unattainable regimes.

In chapter 5 I take advantage of this compatibility to design an experimental set-up aimed at applying strain gradients to FIB-machined, 3D crystalline cantilevers while simultaneously measuring their transport properties. The strain gradients are created by bending the cantilevers with a mechanical nano-positioner whose vertical displacement can be controlled to tune the desired magnitude of the strain gradients. The results conclusively show that strain gradients of $1.3\% \mu\text{m}^{-1}$ can be easily attained without inducing elastic deformations and while maintaining quantum coherence. The set-up is applicable to any material that can be microfabricated with the FIB. Furthermore, the sample design is compatible with other fixed bending mountings, for example, by using a small diameter wire on a chip as a bending edge. In this way, and since the bent section of the sample remains exposed, other techniques like angle-resolved photo-emission spectroscopy (ARPES) or scanning tunnelling microscopy (STM) could, in principle, be applied to the same sample that is characterized by transport measurements. One of the aspects to investigate further in the presented experimental set-up has to do with the microscopic state of the sample while bending at low temperatures. Considering that the set-up is compatible with any conventional cryostat, optical cryostats with a transparent window suited for direct optical inspection and spectroscopic instrumentation can be a promising way forwards. The approach of combining commercially available nano-positioners with FIB-fabricated samples opens up new ways to explore other strain gradient

configurations by, for example, twisting the sample. In this sense, I hope that the results of chapter 5 are only the beginning of a promising experimental strategy.

The experiments discussed in chapter 6 explore the effects of bending on cantilevers of the Dirac semimetal Cd_3As_2 . This set of experiments represent an initial step in the investigation of transport properties of 3D TSMs under Landau quantization and large strain gradients. The theorized strain-induced pseudo-magnetic fields and their influence on the Weyl orbits' frequency are investigated. The difficulty in interpreting the complex experimental data within the available models for the combined presence of bulk quantization, Weyl orbits and presumably pseudo-fields prevents me from clearly identifying certain experimental features with the existence of strain-induced pseudo-fields, and points to a richer underlying physics that is not yet understood completely. Important aspects to consider are the possible refinement of the coupling constants used in the numerical models for Cd_3As_2 , which might be overestimating the magnitude of the pseudo-fields, as well as the inclusion of other experimentally relevant aspects like a varying direction of the magnetic field on the strained sample, which might affect the spatial extension of the Weyl orbits on different parts of the sample and potentially alter their constructive interference and overall signal. In this sense, it is also important to recognize that further understanding of the Weyl orbits themselves is necessary as there are still several open questions regarding their behaviour and proper theoretical description. For example, one of these questions is related to the influence of the chemical potential μ in the value of F_{Weyl} . In principle, it should vary according to $F_{\text{Weyl}} = \mu k_0 / \pi v_F e$. However, there is no systematic study of this relation and some results reported in [151] on nanoplates of Cd_3As_2 of low charge carrier density seem to deviate from it. Manipulating the chemical potential by gating, as it has been done in Cd_3As_2 nanowires [210] could be a way forwards in this regard.

Chapter 7 focuses on the magneto-transport properties of the Dirac nodal arc semimetal PtSn_4 . This material stands out as a multi-band, high carrier density semimetal that exhibits a extremely large magnetoresistance (XMR) whose microscopic origin has been object of considerable debate. The applicability of the FIB microfabrication technique to this material is soundly established in the chapter as the overall transport behaviour of the microstructures is consistent with the bulk behaviour of macroscopic samples and indicates no significant loss of crystalline quality nor chemical contamination. With the help of the FIB, microstructures with active channels along all the main crystallographic directions are fabricated. This makes it possible to identify principal field directions for which a transverse MR with sub-quadratic field dependence and Kohler-like scaling is observed. Similarly, a field direction displaying a suppressed transverse MR with no Kohler-like scaling is also identified. From examinations of the Fermi surface (FS), this suppression of MR is explained by the existence of singular open electronic orbits on sheets of the FS. Such orbits can be formed only within a small angle interval of the identified field configuration. This mechanism points to a semi-classical origin for the observed XMR in this material without the need of invoking more exotic topological or correlated electron theories.

The research on topological semimetals continues to expand in exciting ways and although many challenges remain in this field, ranging from better material realizations to deeper understanding of their fundamental properties, a growing number of theoretical and experimental approaches have emerged in response. In this regard, I hope that the work presented in this thesis serves as a modest encouragement to meet such challenges and hopefully drive the field in fruitful directions.

Publications

J. Diaz, C. Putzke, X. Huang, A. Estry, J. G. Analytis, D. Sabsovich, A. Grushin, R. Ilan & P. J. W. Moll. Bending strain in 3D topological semi-metals. *Journal Of Physics D: Applied Physics*. **55**, 084001 (2022).

C. Guo, L. Hu, C. Putzke, **J. Diaz**, X. Huang, K. Manna, F. R. Fan, C. Shekhar, Y. Sun, C. Felser, B. A. Bernevig & P. J. W. Moll. Quasi-symmetry-protected topology in a semi-metal. *Nature Physics*, **18**, 813 (2022).

X. Huang, C. Putzke, C. Guo, **J. Diaz**, M. König, H. Borrmann, N. Nair, J. G. Analytis & P. J. W. Moll. Magnetic electron collimation in three-dimensional semi-metals. *npj Quantum Materials*. **5**, 1-7 (2020).

X. Huang, C. Guo, C. Putzke, **J. Diaz**, K. Manna, C. Shekhar, C. Felser & P. J. W. Moll. Non-linear Shubnikov-de Haas oscillations in the self-heating regime. *Applied Physics Letters*. **119**, 224101 (2021).

Y. Lai, K. Wei, G. Chappell, **J. Diaz**, T. Siegrist, P. J. W. Moll, D. Graf, and R. E. Baumbach. Tuning the structural and antiferromagnetic phase transitions in UCr_2Si_2 : Hydrostatic pressure and chemical substitution. *Physical Review Materials*, **4**, 075003 (2020).

M. van Delft, Y. Wang, C. Putzke, J. Oswald, G. Varnavides, C. A. C. Garcia, C. Guo, H. Schmid, V. Süß, H. Borrmann, **J. Diaz**, Y. Sun, C. Felser, B. Gotsmann, P. Narang & P. J. W. Moll. Sondheimer oscillations as a probe of non-ohmic flow in WP2 crystals. *Nature Communications*, **12**, 4799 (2021).

Bibliography

- ¹Q. Niu, D. J. Thouless, and Y. S. Wu, “Quantized Hall conductance as a topological invariant”, *Physical Review B* **31**, 10.1103/PhysRevB.31.3372 (1985).
- ²D. J. Thouless, M. Kohmoto, M. P. Nightingale, and M. Den Nijs, “Quantized hall conductance in a two-Dimensional periodic potential”, *Physical Review Letters* **49**, 405–408 (1982).
- ³C. K. Chiu, J. C. Teo, A. P. Schnyder, and S. Ryu, “Classification of topological quantum matter with symmetries”, *Reviews of Modern Physics* **88**, 1–63 (2016).
- ⁴X. G. Wen, “Colloquium: Zoo of quantum-topological phases of matter”, *Reviews of Modern Physics* **89**, 1–17 (2017).
- ⁵P. Narang, C. A. Garcia, and C. Felser, “The topology of electronic band structures”, *Nature Materials* **20**, 293–300 (2021).
- ⁶X. L. Qi and S. C. Zhang, “Topological insulators and superconductors”, *Reviews of Modern Physics* **83**, 1057 (2011).
- ⁷A. H. Castro Neto, F. Guinea, N. M. Peres, K. S. Novoselov, and A. K. Geim, “The electronic properties of graphene”, *Reviews of Modern Physics*, 10.1103/RevModPhys.81.109 (2009).
- ⁸B. Yan and C. Felser, “Topological Materials: Weyl Semimetals”, 10.1146/annurev-conmatphys-031016-025458 (2016).
- ⁹N. P. Armitage, E. J. Mele, and A. Vishwanath, “Weyl and Dirac semimetals in three-dimensional solids”, *Reviews of Modern Physics* **90**, 15001 (2018).
- ¹⁰S. Wang, B. C. Lin, A. Q. Wang, D. P. Yu, and Z. M. Liao, “Quantum transport in Dirac and Weyl semimetals: a review”, *Advances in Physics: X* **2**, 518–544 (2017).
- ¹¹B. Bradlyn, J. Cano, Z. Wang, M. G. Vergniory, C. Felser, R. J. Cava, and B. A. Bernevig, “Beyond Dirac and Weyl fermions: Unconventional quasiparticles in conventional crystals”, *Science* **353**, 10.1126/science.aaf5037 (2016).
- ¹²J. Hu, S.-Y. Xu, N. Ni, and Z. Mao, “Transport of Topological Semimetals”, *Annual Review of Materials Research* **49**, 207–252 (2019).
- ¹³M. Z. Hasan, G. Chang, I. Belopolski, G. Bian, S. Y. Xu, and J. X. Yin, “Weyl, Dirac and high-fold chiral fermions in topological quantum matter”, *Nature Reviews Materials* **6**, 784–803 (2021).

- ¹⁴B. A. Bernevig, C. Felser, and H. Beidenkopf, “Progress and prospects in magnetic topological materials”, *Nature* 2022 603:7899 **603**, 41–51 (2022).
- ¹⁵A. Burkov, “Topological semimetals”, *Nature Materials* **15**, 1145–1148 (2016).
- ¹⁶C. W. Beenakker and H. van Houten, “Quantum Transport in Semiconductor Nanostructures”, *Solid State Physics - Advances in Research and Applications*, 10.1016/S0081-1947(08)60091-0 (1991).
- ¹⁷A. Q. Wang, X. G. Ye, D. P. Yu, and Z. M. Liao, “Topological Semimetal Nanostructures: From Properties to Topotronics”, *ACS Nano* **14**, 19 (2020).
- ¹⁸E. Zhang, Y. Liu, W. Wang, C. Zhang, P. Zhou, Z. G. Chen, J. Zou, and F. Xiu, “Magnetotransport Properties of Cd₃As₂ Nanostructures”, *ACS Nano* **9**, 8843–8850 (2015).
- ¹⁹H. Pan, K. Zhang, Z. Wei, B. Zhao, J. Wang, M. Gao, L. Pi, M. Han, F. Song, X. Wang, B. Wang, and R. Zhang, “Quantum oscillation and nontrivial transport in the Dirac semimetal Cd₃As₂ nanodevice”, *Applied Physics Letters* **108**, 10.1063/1.4948654 (2016).
- ²⁰P. J. Moll, “Focused Ion Beam Microstructuring of Quantum Matter”, *Annual Review of Condensed Matter Physics* **9**, 147–162 (2017).
- ²¹I. Utke, P. Hoffmann, and J. Melngailis, “Gas-assisted focused electron beam and ion beam processing and fabrication”, *Journal of Vacuum Science & Technology B: Microelectronics and Nanometer Structures* **26**, 1197 (2008).
- ²²J. H. Chu, J. G. Analytis, K. De Greve, P. L. McMahon, Z. Islam, Y. Yamamoto, and I. R. Fisher, “In-plane resistivity anisotropy in an underdoped iron arsenide superconductor”, *Science*, 10.1126/science.1190482 (2010).
- ²³C. W. Hicks, D. O. Brodsky, E. A. Yelland, A. S. Gibbs, J. A. N. Bruin, M. E. Barber, S. D. Edkins, K. Nishimura, S. Yonezawa, Y. Maeno, and A. P. Mackenzie, “Strong Increase of T_c of Sr₂RuO₄ Under Both Tensile and Compressive Strain”, *Science* **344**, 283–285 (2014).
- ²⁴Y. Nii, T. Nakajima, A. Kikkawa, Y. Yamasaki, K. Ohishi, J. Suzuki, Y. Taguchi, T. Arima, Y. Tokura, and Y. Iwasa, “Uniaxial stress control of skyrmion phase”, *Nature Communications*, 10.1038/ncomms9539 (2015).
- ²⁵C. W. Nicholson, M. Rumo, A. Pulkkinen, G. Kremer, B. Salzmänn, M.-L. Mottas, B. Hildebrand, T. Jaouen, T. K. Kim, S. Mukherjee, K. Ma, M. Muntwiler, F. O. von Rohr, C. Cacho, and C. Monney, “Uniaxial strain-induced phase transition in the 2D topological semimetal IrTe₂”, *Communications Materials*, 10.1038/s43246-021-00130-5 (2021).
- ²⁶C. Zhao, M. Hu, J. Qin, B. Xia, C. Liu, S. Wang, D. Guan, Y. Li, H. Zheng, J. Liu, and J. Jia, “Strain Tunable Semimetal–Topological-Insulator Transition in Monolayer 1T′-WTe₂”, *Physical Review Letters* **125**, 046801 (2020).
- ²⁷V. Bhardwaj, A. Bhattacharya, S. Srivastava, V. V. Khovaylo, J. Sannigrahi, N. Banerjee, B. K. Mani, and R. Chatterjee, “Strain driven emergence of topological non-triviality in YPdBi thin films”, *Scientific Reports* | **123**, 7535 (2020).

- ²⁸J. Mutch, W. C. Chen, P. Went, T. Qian, I. Z. Wilson, A. Andreev, C. C. Chen, and J. H. Chu, “Evidence for a strain-tuned topological phase transition in ZrTe₅”, *Science Advances* **5**, 10.1126/SCIADV.AAV9771 (2019).
- ²⁹N. Levy, S. A. Burke, K. L. Meaker, M. Panlasigui, A. Zettl, F. Guinea, A. H. Castro Neto, and M. F. Crommie, “Strain-induced pseudo-magnetic fields greater than 300 tesla in graphene nanobubbles”, *Science*, 10.1126/science.1191700 (2010).
- ³⁰K. K. Gomes, W. Mar, W. Ko, F. Guinea, and H. C. Manoharan, “Designer Dirac fermions and topological phases in molecular graphene”, *Nature* **483**, 306–310 (2012).
- ³¹R. Ilan, A. G. Grushin, and D. I. Pikulin, “Pseudo-electromagnetic fields in 3D topological semimetals”, *Nature Reviews Physics* **2**, 29–41 (2020).
- ³²T. Liu, D. I. Pikulin, and M. Franz, “Quantum oscillations without magnetic field”, *Physical Review B*, 10.1103/PhysRevB.95.041201 (2017).
- ³³D. I. Pikulin and R. Ilan, “Bulk-boundary quantum oscillations in inhomogeneous Weyl semimetals”, *New Journal of Physics* **22**, 013035 (2020).
- ³⁴A. G. Grushin, J. W. Venderbos, A. Vishwanath, and R. Ilan, “Inhomogeneous weyl and dirac semimetals: Transport in axial magnetic fields and fermi arc surface states from pseudo-landau levels”, *Physical Review X* **6**, 1–20 (2016).
- ³⁵P. J. Moll, N. L. Nair, T. Helm, A. C. Potter, I. Kimchi, A. Vishwanath, and J. G. Analytis, “Transport evidence for Fermi-arc-mediated chirality transfer in the Dirac semimetal Cd₃As₂”, *Nature* **535**, 266–270 (2016).
- ³⁶T. Liang, Q. Gibson, M. N. Ali, M. Liu, R. J. Cava, and N. P. Ong, “Ultrahigh mobility and giant magnetoresistance in the Dirac semimetal Cd₃As₂”, *Nature Materials* **14**, 280–284 (2015).
- ³⁷M. M. Parish and P. B. Littlewood, “Non-saturating magnetoresistance in heavily disordered semiconductors”, *Nature* **426**, 162–165 (2003).
- ³⁸A. Abrikosov, “Quantum magnetoresistance”, *Physical Review B - Condensed Matter and Materials Physics* **58**, 2788–2794 (1998).
- ³⁹F. Jerzembeck, H. S. Røising, A. Steppke, H. Rosner, D. A. Sokolov, N. Kikugawa, T. Scaffidi, S. H. Simon, A. P. Mackenzie, and C. W. Hicks, “The superconductivity of Sr₂RuO₄ under c-axis uniaxial stress”, *Nature Communications* **13**, 1–11 (2022).
- ⁴⁰M. D. Bachmann, G. M. Ferguson, F. Theuss, T. Meng, C. Putzke, T. Helm, K. R. Shirer, Y. S. Li, K. A. Modic, M. Nicklas, M. König, D. Low, S. Ghosh, A. P. Mackenzie, F. Arnold, E. Hassinger, R. D. McDonald, L. E. Winter, E. D. Bauer, F. Ronning, B. J. Ramshaw, K. C. Nowack, and P. J. Moll, “Spatial control of heavy-fermion superconductivity in CeIrIn₅”, *Science* **366**, 221–226 (2019).
- ⁴¹Y. Wu, L. L. Wang, E. Mun, D. D. Johnson, D. Mou, L. Huang, Y. Lee, S. L. Bud’ko, P. C. Canfield, and A. Kaminski, “Dirac node arcs in PtSn₄”, *Nature Physics* **12**, 667–671 (2016).
- ⁴²A. Rigort and J. M. Plitzko, “Cryo-focused-ion-beam applications in structural biology”, *Archives of Biochemistry and Biophysics* **581**, 122–130 (2015).

- ⁴³N. S. Smith, W. P. Skoczylas, and S. M. Kellogg, “High brightness inductively coupled plasma source for high current focused ion beam applications”, *Citation: Journal of Vacuum Science & Technology B: Microelectronics and Nanometer Structures Processing, Measurement, and Phenomena* **24**, 2902 (2006).
- ⁴⁴S. M. Vitale and J. D. Sugar, “Using Xe Plasma FIB for High-Quality TEM Sample Preparation”, *Microscopy and Microanalysis* **28**, 646–658 (2022).
- ⁴⁵T. L. Burnett, R. Kelley, B. Winiarski, L. Contreras, M. Daly, A. Gholinia, M. G. Burke, and P. J. Withers, “Large volume serial section tomography by Xe Plasma FIB dual beam microscopy”, *Ultramicroscopy* **161**, 119–129 (2016).
- ⁴⁶B. W. Ward, J. A. Notte, and N. P. Economou, “Helium ion microscope: A new tool for nanoscale microscopy and metrology”, *Journal of Vacuum Science & Technology B: Microelectronics and Nanometer Structures* **24**, 2871 (2006).
- ⁴⁷J. M. De Teresa, ed., *Nanofabrication. Nanolithography techniques and their applications*. (IOP Publishing, 2020).
- ⁴⁸N. S. Smith, J. A. Notte, and A. V. Steele, “Advances in source technology for focused ion beam instruments”, *MRS Bulletin* **39**, 329–335 (2014).
- ⁴⁹C. S. Kim, S. H. Ahn, and D. Y. Jang, “Review: Developments in micro/nanoscale fabrication by focused ion beams”, *Vacuum* **86**, 1014–1035 (2012).
- ⁵⁰C. A. Volkert and A. M. Minor, “Focused Ion Beam Micromachining”, *MRS bulletin* **32**, 389–399 (2007).
- ⁵¹M. Y. Ali, W. Hung, and F. Yongqi, “A review of focused ion beam sputtering”, *International Journal of Precision Engineering and Manufacturing* **11**, 157–170 (2010).
- ⁵²P. Li, S. Chen, H. Dai, Z. Yang, Z. Chen, Y. Wang, Y. Chen, W. Peng, W. Shan, and H. Duan, “Recent advances in focused ion beam nanofabrication for nanostructures and devices: Fundamentals and applications”, *Nanoscale* **13**, 1529–1565 (2021).
- ⁵³J. F. Ziegler, “Srim-2003”, *Nuclear Instruments and Methods in Physics Research, Section B: Beam Interactions with Materials and Atoms* **219-220**, 1027–1036 (2004).
- ⁵⁴J. M. De Teresa, R. Cárdoaba, A. Fernández-Pacheco, O. Montero, P. Strichovanec, and M. R. Ibarra, “Origin of the difference in the resistivity of as-grown focused-ion- and focused-electron-beam-induced Pt nanodeposits”, *Journal of Nanomaterials* **2009**, 10.1155/2009/936863 (2009).
- ⁵⁵M. D. Bachmann, “Manipulating Anisotropic Transport and Superconductivity by Focused Ion Beam Microstructuring”, PhD thesis (Cham, Switzerland, 2020).
- ⁵⁶M. Cantoni and L. Holzer, “Advances in 3D focused ion beam tomography”, *MRS Bulletin* **39**, 354–360 (2014).
- ⁵⁷J. Liu, R. Niu, J. Gu, M. Cabral, M. Song, and X. Liao, “Effect of Ion Irradiation Introduced by Focused Ion-Beam Milling on the Mechanical Behaviour of Sub-Micron-Sized Samples”, *Scientific Reports* **10**, 1–8 (2020).

- ⁵⁸R. Kelley, K. Song, B. Van Leer, D. Wall, and L. Kwakman, “Xe+ FIB Milling and Measurement of Amorphous Silicon Damage”, *Microscopy and Microanalysis* **19**, 862–863 (2013).
- ⁵⁹M. D. Bachmann, N. Nair, F. Flicker, R. Ilan, T. Meng, N. J. Ghimire, E. D. Bauer, F. Ronning, J. G. Analytis, and P. J. Moll, “Inducing superconductivity in Weyl semimetal microstructures by selective ion sputtering”, *Science Advances* **3**, 10.1126/sciadv.1602983 (2017).
- ⁶⁰X. Huang, C. Guo, C. Putzke, M. Gutierrez-Amigo, Y. Sun, M. G. Vergniory, I. Errea, D. Chen, C. Felser, and P. J. Moll, “Three-dimensional Fermi surfaces from charge order in layered CsV₃Sb₅”, *Physical Review B* **106**, 1–6 (2022).
- ⁶¹E. Mun, H. Ko, G. J. Miller, G. D. Samolyuk, S. L. Bud’Ko, and P. C. Canfield, “Magnetic field effects on transport properties of PtSn 4”, *Physical Review B - Condensed Matter and Materials Physics* **85**, 1–12 (2012).
- ⁶²X. Huang, C. Putzke, C. Guo, J. Diaz, M. König, H. Borrmann, N. L. Nair, J. G. Analytis, and P. J. Moll, “Magnetic electron collimation in three-dimensional semi-metals”, *npj Quantum Materials* 2020 5:1 **5**, 1–7 (2020).
- ⁶³Z. Instruments, *Principles of lock-in detection and the state of the art*, 2016.
- ⁶⁴X. Huang, “Anisotropic and nonlinear transport in microstructured 3D topological semimetals”, PhD thesis (EPFL, 2022).
- ⁶⁵SynkTek AB, *MCL1-540. Multi-Channel Lock-in Amplifier Measurement System Instruction Manual*. Sweden, 2017.
- ⁶⁶Q. Design, *Physical Property Measurement System. Hardware Manual*. 2004.
- ⁶⁷N. H. Balshaw, *Practical Cryogenics. An Introduction to Laboratory Cryogenics*. (Oxford Instruments Superconductivity Limited, 2001).
- ⁶⁸F. Pobell, *Matter and Methods at Low Temperatures* (Springer, 2007).
- ⁶⁹M. N. Ali, Q. Gibson, S. Jeon, B. B. Zhou, A. Yazdani, and R. J. Cava, “The crystal and electronic structures of Cd₃As₂, the three-dimensional electronic analogue of graphene”, *Inorganic Chemistry* **53**, 4062–4067 (2014).
- ⁷⁰Z.-G. Chen, C. Zhang, Y. Zou, E. Zhang, L. Yang, M. Hong, F. Xiu, and J. Zou, “ Scalable Growth of High Mobility Dirac Semimetal Cd₃As₂ Microbelts ”, *Nano Letters* **15**, 5830–5834 (2015).
- ⁷¹J. N. Reddy, *Introduction to the Finite Element Method* (McGraw-Hill Education, 2019).
- ⁷²R. D. Cook, D. S. Malkus, M. E. Plesha, and R. J. W. Witt, *Concept and Applications of Finite Element Analysis*, 4th editio (John Wiley & Sons, 2002), p. 733.
- ⁷³A. E. Tekkaya and C. Soyarslan, *Finite Element Method* (Springer, Berlin, Heidelberg, Berlin, Heidelberg, 2019), pp. 677–683.
- ⁷⁴C. Guo, L. Hu, C. Putzke, J. Diaz, X. Huang, K. Manna, F. R. Fan, C. Shekhar, Y. Sun, C. Felser, C. Liu, B. A. Bernevig, and P. J. Moll, “Quasi-symmetry-protected topology in a semi-metal”, *Nature Physics* **18**, 813–818 (2022).

- ⁷⁵B. H. Sommerfeld A., *Elektronentheorie der Metalle. In: Aufbau Der Zusammenhängenden Materie. Handbuch der Physik, vol 24/2.* (Springer, Berlin, Heidelberg, 1933).
- ⁷⁶F. Bloch, “Über die Quantenmechanik der Elektronen in Kristallgittern”, *Zeitschrift für Physik*, 10.1007/BF01339455 (1929).
- ⁷⁷Von N. W. Ashcroft; N. D. Mermin, *Solid State Physics* (Saunders College, Philadelphia, 1976).
- ⁷⁸J. von Neumann and E. P. Wigner, “Über merkwürdige diskrete Eigenwerte”, *Physikalische Zeitschrift* (1929).
- ⁷⁹M. Berry, “Quantal phase factors accompanying adiabatic changes”, *Proceedings of the Royal Society of London. A. Mathematical and Physical Sciences*, 10.1098/rspa.1984.0023 (1984).
- ⁸⁰F. Ghahari, D. Walkup, C. Gutiérrez, J. F. Rodriguez-Nieva, Y. Zhao, J. Wyrick, F. D. Natterer, W. G. Cullen, K. Watanabe, T. Taniguchi, L. S. Levitov, N. B. Zhitenev, and J. A. Stroscio, “An on/off Berry phase switch in circular graphene resonators”, *Science* **356**, 845–849 (2017).
- ⁸¹D. Xiao, M. C. Chang, and Q. Niu, “Berry phase effects on electronic properties”, *Reviews of Modern Physics*, 10.1103/RevModPhys.82.1959 (2010).
- ⁸²K. S. Novoselov, A. K. Geim, S. V. Morozov, D. Jiang, M. I. Katsnelson, I. V. Grigorieva, S. V. Dubonos, and A. A. Firsov, “Two-dimensional gas of massless Dirac fermions in graphene”, *Nature*, 10.1038/nature04233 (2005).
- ⁸³K. S. Novoselov, E. McCann, S. V. Morozov, V. I. Fal’ko, M. I. Katsnelson, U. Zeitler, D. Jiang, F. Schedin, and A. K. Geim, “Unconventional quantum Hall effect and Berry’s phase of 2π in bilayer graphene”, *Nature Physics* **2**, 177–180 (2006).
- ⁸⁴H. B. Nielsen and M. Ninomiya, “Absence of neutrinos on a lattice: (I). Proof by homotopy theory”, *Nuclear Physics B* **185**, 20–40 (1981).
- ⁸⁵B. Yan and C. Felser, “Topological Materials: Weyl Semimetals”, *Annual Review of Condensed Matter Physics*, 10.1146/annurev-conmatphys-031016-025458 (2017).
- ⁸⁶B. J. Yang and N. Nagaosa, “Classification of stable three-dimensional Dirac semimetals with nontrivial topology”, *Nature Communications* **5**, 10.1038/ncomms5898 (2014).
- ⁸⁷S. Y. Xu, I. Belopolski, N. Alidoust, M. Neupane, G. Bian, C. Zhang, R. Sankar, G. Chang, Z. Yuan, C. C. Lee, S. M. Huang, H. Zheng, J. Ma, D. S. Sanchez, B. K. Wang, A. Bansil, F. Chou, P. P. Shibayev, H. Lin, S. Jia, and M. Z. Hasan, “Discovery of a Weyl fermion semimetal and topological Fermi arcs”, *Science*, 10.1126/science.aaa9297 (2015).
- ⁸⁸S.-Y. Xu, I. Belopolski, D. S. Sanchez, C. Zhang, G. Chang, C. Guo, G. Bian, Z. Yuan, H. Lu, T.-R. Chang, P. P. Shibayev, M. L. Prokopovych, N. Alidoust, H. Zheng, C.-C. Lee, S.-M. Huang, R. Sankar, F. Chou, C.-H. Hsu, H.-T. Jeng, A. Bansil, T. Neupert, V. N. Strocov, H. Lin, S. Jia, and M. Z. Hasan, “Experimental discovery of a topological Weyl semimetal state in TaP”, *Science Advances* **1**, e1501092 (2015).

- ⁸⁹S. Y. Xu, N. Alidoust, I. Belopolski, Z. Yuan, G. Bian, T. R. Chang, H. Zheng, V. N. Strocov, D. S. Sanchez, G. Chang, C. Zhang, D. Mou, Y. Wu, L. Huang, C. C. Lee, S. M. Huang, B. Wang, A. Bansil, H. T. Jeng, T. Neupert, A. Kaminski, H. Lin, S. Jia, and M. Z. Hasan, “Discovery of a Weyl fermion state with Fermi arcs in niobium arsenide”, *Nature Physics*, 10.1038/nphys3437 (2015).
- ⁹⁰S. Souma, Z. Wang, H. Kotaka, T. Sato, K. Nakayama, Y. Tanaka, H. Kimizuka, T. Takahashi, K. Yamauchi, T. Oguchi, K. Segawa, and Y. Ando, “Direct observation of nonequivalent Fermi-arc states of opposite surfaces in the noncentrosymmetric Weyl semimetal NbP”, *Physical Review B*, 10.1103/PhysRevB.93.161112 (2016).
- ⁹¹Z. Wang, H. Weng, Q. Wu, X. Dai, and Z. Fang, “Three-dimensional Dirac semimetal and quantum transport in Cd₃As₂”, *Physical Review B - Condensed Matter and Materials Physics*, 10.1103/PhysRevB.88.125427 (2013).
- ⁹²Z. K. Liu, B. Zhou, Y. Zhang, Z. J. Wang, H. M. Weng, D. Prabhakaran, S. K. Mo, Z. X. Shen, Z. Fang, X. Dai, Z. Hussain, and Y. L. Chen, “Discovery of a three-dimensional topological dirac semimetal, Na₃Bi”, *Science*, 10.1126/science.1245085 (2014).
- ⁹³H. Xiong, J. A. Sobota, S. L. Yang, H. Soifer, A. Gauthier, M. H. Lu, Y. Y. Lv, S. H. Yao, D. Lu, M. Hashimoto, P. S. Kirchmann, Y. F. Chen, and Z. X. Shen, “Three-dimensional nature of the band structure of ZrTe₅ measured by high-momentum-resolution photoemission spectroscopy”, *Physical Review B*, 10.1103/PhysRevB.95.195119 (2017).
- ⁹⁴M. Neupane, S. Xu, R. Sankar, N. Alidoust, G. Bian, C. Liu, I. Belopolski, T. R. Chang, H. T. Jeng, H. Lin, A. Bansil, F. Chou, and M. Z. Hasan, “Observation of a topological 3D Dirac semimetal phase in high-mobility Cd₃As₂”, *Nature Communications* **5**, 1–8 (2013).
- ⁹⁵S. Borisenko, Q. Gibson, D. Evtushinsky, V. Zabolotnyy, B. Büchner, and R. J. Cava, “Experimental realization of a three-dimensional dirac semimetal”, *Physical Review Letters* **113**, 1–5 (2014).
- ⁹⁶H. Yi, Z. Wang, C. Chen, Y. Shi, Y. Feng, A. Liang, Z. Xie, S. He, J. He, Y. Peng, X. Liu, Y. Liu, L. Zhao, G. Liu, X. Dong, J. Zhang, M. Nakatake, M. Arita, K. Shimada, H. Namatame, M. Taniguchi, Z. Xu, C. Chen, X. Dai, Z. Fang, and X. J. Zhou, “Evidence of topological surface state in three-dimensional dirac semimetal Cd₃As₂”, *Scientific Reports* **4**, 1–6 (2014).
- ⁹⁷K. V. Klitzing, G. Dorda, and M. Pepper, “New method for high-accuracy determination of the fine-structure constant based on quantized hall resistance”, *Physical Review Letters*, 10.1103/PhysRevLett.45.494 (1980).
- ⁹⁸M. König, S. Wiedmann, C. Brüne, A. Roth, H. Buhmann, L. W. Molenkamp, X. L. Qi, and S. C. Zhang, “Quantum spin hall insulator state in HgTe quantum wells”, *Science*, 10.1126/science.1148047 (2007).
- ⁹⁹C. Z. Chang, J. Zhang, X. Feng, J. Shen, Z. Zhang, M. Guo, K. Li, Y. Ou, P. Wei, L. L. Wang, Z. Q. Ji, Y. Feng, S. Ji, X. Chen, J. Jia, X. Dai, Z. Fang, S. C. Zhang, K. He, Y. Wang, L. Lu, X. C. Ma, and Q. K. Xue, “Experimental observation of the quantum anomalous Hall effect in a magnetic topological Insulator”, *Science*, 10.1126/science.1234414 (2013).

- ¹⁰⁰B. Q. Lv, S. Muff, T. Qian, Z. D. Song, S. M. Nie, N. Xu, P. Richard, C. E. Matt, N. C. Plumb, L. X. Zhao, G. F. Chen, Z. Fang, X. Dai, J. H. Dil, J. Mesot, M. Shi, H. M. Weng, and H. Ding, “Observation of Fermi-Arc Spin Texture in TaAs”, *Physical Review Letters* **115**, 1–5 (2015).
- ¹⁰¹M. C. Chang and Q. Niu, “Berry Phase, Hyperorbits, and the Hofstadter Spectrum”, *Physical Review Letters* **75**, 1348 (1995).
- ¹⁰²G. Sundaram and Q. Niu, “Wave-packet dynamics in slowly perturbed crystals: Gradient corrections and Berry-phase effects”, *Physical Review B* **59**, 14915 (1999).
- ¹⁰³J.-H. Zhou, H. Jiang, Q. Niu, J.-R. Shi, and., “Topological Invariants of Metals and the Related Physical Effects”, *Chinese Physics Letters* **30**, 027101 (2013).
- ¹⁰⁴P. Goswami and S. Tewari, “Axionic field theory of (3+1)-dimensional Weyl semimetals”, *Physical Review B - Condensed Matter and Materials Physics* **88**, 245107 (2013).
- ¹⁰⁵A. A. Zyuzin and A. A. Burkov, “Topological response in Weyl semimetals and the chiral anomaly”, *Physical Review B - Condensed Matter and Materials Physics* **86**, 115133 (2012).
- ¹⁰⁶M. C. Chang and M. F. Yang, “Chiral magnetic effect in a two-band lattice model of Weyl semimetal”, *Physical Review B - Condensed Matter and Materials Physics* **91**, 115203 (2015).
- ¹⁰⁷D. T. Son and B. Z. Spivak, “Chiral anomaly and classical negative magnetoresistance of Weyl metals”, *Physical Review B - Condensed Matter and Materials Physics* **88**, 104412 (2013).
- ¹⁰⁸A. A. Burkov, “Chiral Anomaly and Diffusive Magnetotransport in Weyl Metals”, *Physical Review Letters* **113**, 247203 (2014).
- ¹⁰⁹M. I. Kaganov and I. M. Lifshits, “Electron theory of metals and geometry”, *Soviet Physics - Uspekhi* **22**, 904–927 (1979).
- ¹¹⁰A. B. Pippard, *Magnetoresistance in Metals* (Cambridge University Press, New York, 1989).
- ¹¹¹J. Singleton, *Band theory and electronic properties of solids*. (Oxford University Press, 2001).
- ¹¹²P. B. Alers and R. T. Webber, “The magnetoresistance of bismuth crystals at low temperatures”, *Physical Review* **91**, 1060–1065 (1953).
- ¹¹³A. Collaudin, B. Fauqué, Y. Fuseya, W. Kang, and K. Behnia, “Angle dependence of the orbital magnetoresistance in bismuth”, *Physical Review X* **5**, 1–15 (2015).
- ¹¹⁴S. Zhang, Q. Wu, Y. Liu, and O. V. Yazyev, “Magnetoresistance from Fermi surface topology”, *Physical Review B* **99**, 1–12 (2019).
- ¹¹⁵L. Onsager, “Interpretation of the de Haas-van Alphen effect”, *The London, Edinburgh, and Dublin Philosophical Magazine and Journal of Science*, 10.1080/14786440908521019 (1952).
- ¹¹⁶T. Ando, “Physics of graphene zero-mode anomalies and roles of symmetry”, in *Progress of theoretical physics supplement* (2008).
- ¹¹⁷D. Shoenberg, *Magnetic Oscillations in Metals* (Cambridge University Press, 1984).

- ¹¹⁸G. P. Mikitik and Y. V. Sharlai, “Manifestation of berry’s phase in metal physics”, *Physical Review Letters* **82**, 2147–2150 (1999).
- ¹¹⁹A. Alexandradinata, C. Wang, W. Duan, and L. Glazman, “Revealing the Topology of Fermi-Surface Wave Functions from Magnetic Quantum Oscillations”, *Physical Review X* **8**, 11027 (2018).
- ¹²⁰Y. Gao, Q. Niu, and D. Vanderbilt, “Zero-field magnetic response functions in Landau levels”, *Proceedings of the National Academy of Sciences of the United States of America* **114**, 7295–7300 (2017).
- ¹²¹L. M. Roth, “Semiclassical theory of magnetic energy levels and magnetic susceptibility of bloch electrons”, *Physical Review*, 10.1103/PhysRev.145.434 (1966).
- ¹²²A. C. Potter, I. Kimchi, and A. Vishwanath, “Quantum oscillations from surface Fermi arcs in Weyl and Dirac semimetals”, *Nature Communications* **5**, 1–6 (2014).
- ¹²³Y. Zhang, D. Bulmash, P. Hosur, A. C. Potter, and A. Vishwanath, “Quantum oscillations from generic surface Fermi arcs and bulk chiral modes in Weyl semimetals”, *Scientific Reports* **6**, 1–6 (2016).
- ¹²⁴C. Zhang, Y. Zhang, X. Yuan, S. Lu, J. Zhang, A. Narayan, Y. Liu, H. Zhang, Z. Ni, R. Liu, E. S. Choi, A. Suslov, S. Sanvito, L. Pi, H. Z. Lu, A. C. Potter, and F. Xiu, “Quantum Hall effect based on Weyl orbits in Cd₃As₂”, *Nature* **565**, 331–336 (2019).
- ¹²⁵A. H. Castro Neto, F. Guinea, N. M. Peres, K. S. Novoselov, and A. K. Geim, “The electronic properties of graphene”, *Reviews of Modern Physics*, 10.1103/RevModPhys.81.109 (2009).
- ¹²⁶A. Cortijo, Y. Ferreirós, K. Landsteiner, and M. A. H. Vozmediano, “Elastic Gauge Fields in Weyl Semimetals”, *Phys. Rev. Lett.* **115**, 177202 (2015).
- ¹²⁷H. Shapourian, T. L. Hughes, and S. Ryu, “Viscoelastic response of topological tight-binding models in two and three dimensions”, *Physical Review B - Condensed Matter and Materials Physics*, 10.1103/PhysRevB.92.165131 (2015).
- ¹²⁸C. X. Liu, P. Ye, and X. L. Qi, “Chiral gauge field and axial anomaly in a Weyl semimetal”, *Physical Review B - Condensed Matter and Materials Physics*, 10.1103/PhysRevB.87.235306 (2013).
- ¹²⁹B. A. Bernevig and T. L. Hughes, *Topological insulators and topological superconductors* (Princeton University Press, Princeton, 2013).
- ¹³⁰V. Peri, M. Serra-Garcia, R. Ilan, and S. D. Huber, “Axial-field-induced chiral channels in an acoustic Weyl system”, *Nature Physics* 2019 15:4 **15**, 357–361 (2019).
- ¹³¹H. Jia, R. Zhang, W. Gao, Q. Guo, B. Yang, J. Hu, Y. Bi, Y. Xiang, C. Liu, and S. Zhang, “Observation of chiral zero mode in inhomogeneous three-dimensional Weyl metamaterials”, *Science*, 10.1126/science.aau7707 (2019).
- ¹³²J. Dalibard, F. Gerbier, G. Juzeliunas, and P. Öhberg, “Colloquium: Artificial gauge potentials for neutral atoms”, *Reviews of Modern Physics*, 10.1103/RevModPhys.83.1523 (2011).

- ¹³³M. Aidelsburger, “Artificial gauge fields and topology with ultracold atoms in optical lattices”, *Journal of Physics B: Atomic, Molecular and Optical Physics* **51**, 193001 (2018).
- ¹³⁴S. Roy, M. Kolodrubetz, N. Goldman, and A. G. Grushin, “Tunable axial gauge fields in engineered Weyl semimetals: semiclassical analysis and optical lattice implementations”, *2D Materials* **5**, 024001 (2018).
- ¹³⁵H. Sumiyoshi and S. Fujimoto, “Torsional Chiral Magnetic Effect in a Weyl Semimetal with a Topological Defect”, *Physical Review Letters* **116**, 1–6 (2016).
- ¹³⁶M. N. Chernodub and M. A. Zubkov, “Chiral anomaly in Dirac semimetals due to dislocations”, *Physical Review B* **95**, 1–16 (2017).
- ¹³⁷S. Kamboj, P. S. Rana, A. Sirohi, A. Vasdev, M. Mandal, S. Marik, R. P. Singh, T. Das, and G. Sheet, “Generation of strain-induced pseudo-magnetic field in a doped type-II Weyl semimetal”, *Physical Review B* **100**, 115105 (2019).
- ¹³⁸S. Deng, A. V. Sumant, and V. Berry, “Strain engineering in two-dimensional nanomaterials beyond graphene”, *Nano Today* **22**, 14–35 (2018).
- ¹³⁹Z. H. Aitken and R. Huang, “Effects of mismatch strain and substrate surface corrugation on morphology of supported monolayer graphene”, *Journal of Applied Physics*, 10.1063/1.3437642 (2010).
- ¹⁴⁰B. Lorenzi, Y. Tsurimaki, A. Kobayashi, M. Takashiri, and S. V. Boriskina, “Self-powered broadband photo-detection and persistent energy generation with junction-free strained Bi₂Te₃ thin films”, *Optics Express*, 10.1364/oe.399040 (2020).
- ¹⁴¹V. Harbola, S. Crossley, S. S. Hong, D. Lu, Y. A. Birkhölzer, Y. Hikita, and H. Y. Hwang, “Strain Gradient Elasticity in SrTiO₃ Membranes: Bending versus Stretching”, *Nano Letters*, 10.1021/acs.nanolett.0c04787 (2021).
- ¹⁴²Y. Jiang, J. Mao, J. Duan, X. Lai, K. Watanabe, T. Taniguchi, and E. Y. Andrei, “Visualizing Strain-Induced Pseudomagnetic Fields in Graphene through an hBN Magnifying Glass”, *Nano Letters* **17**, 2839–2843 (2017).
- ¹⁴³C. C. Hsu, M. L. Teague, J. Q. Wang, and N. C. Yeh, “Nanoscale strain engineering of giant pseudo-magnetic fields, valley polarization, and topological channels in graphene”, *Science Advances*, 10.1126/sciadv.aat9488 (2020).
- ¹⁴⁴P. Nigge, A. C. Qu, Lantagne-Hurtubise, E. Mårzell, S. Link, G. Tom, M. Zonno, M. Michiardi, M. Schneider, S. Zhdanovich, G. Levy, U. Starke, C. Gutiérrez, D. Bonn, S. A. Burke, M. Franz, and A. Damascelli, “Room temperature strain-induced Landau levels in graphene on a wafer-scale platform”, *Science Advances*, 10.1126/sciadv.aaw5593 (2019).
- ¹⁴⁵F. Guinea, M. I. Katsnelson, and A. K. Geim, “Energy gaps and a zero-field quantum hall effect in graphene by strain engineering”, *Nature Physics* **6**, 30–33 (2010).
- ¹⁴⁶C. S. Downs, A. Usher, and J. Martin, “Towards observation of pseudo-magnetic fields in suspended graphene devices”, *Journal of Applied Physics* **119**, 10.1063/1.4950879 (2016).
- ¹⁴⁷X. Han, L. Kou, Z. Zhang, Z. Zhang, X. Zhu, J. Xu, Z. Liao, W. Guo, and D. Yu, “Strain-gradient effect on energy bands in bent ZnO microwires”, *Advanced Materials* **24**, 4707–4711 (2012).

- ¹⁴⁸X. Fu, G. Jacopin, M. Shahmohammadi, R. Liu, M. Benameur, J. D. Ganière, J. Feng, W. Guo, Z. M. Liao, B. Deveaud, and D. Yu, “Exciton drift in semiconductors under uniform strain gradients: Application to bent ZnO microwires”, *ACS Nano* **8**, 3412–3420 (2014).
- ¹⁴⁹J. Cao, S. Liang, C. Zhang, Y. Liu, J. Huang, Z. Jin, Z. G. Chen, Z. Wang, Q. Wang, J. Zhao, S. Li, X. Dai, J. Zou, Z. Xia, L. Li, and F. Xiu, “Landau level splitting in Cd3As2 under high magnetic fields”, *Nature Communications* **6**, 1–6 (2015).
- ¹⁵⁰L. P. He, X. C. Hong, J. K. Dong, J. Pan, Z. Zhang, J. Zhang, and S. Y. Li, “Quantum transport evidence for the three-dimensional dirac semimetal phase in Cd3As2”, *Physical Review Letters*, 10.1103/PhysRevLett.113.246402 (2014).
- ¹⁵¹C. Zhang, A. Narayan, S. Lu, J. Zhang, H. Zhang, Z. Ni, X. Yuan, Y. Liu, J. H. Park, E. Zhang, W. Wang, S. Liu, L. Cheng, L. Pi, Z. Sheng, S. Sanvito, and F. Xiu, “Evolution of Weyl orbit and quantum Hall effect in Dirac semimetal Cd₃As₂”, *Nature Communications* **8**, 1–8 (2017).
- ¹⁵²L. D. Landau, E. M. Lifshitz, J. B. Sykes, W. H. Reid, and E. H. Dill, “Theory of Elasticity: Vol. 7 of Course of Theoretical Physics”, *Physics Today*, 10.1063/1.3057037 (1960).
- ¹⁵³A. L. Szabó, R. Moessner, and B. Roy, “Strain-engineered higher-order topological phases for spin-32 Luttinger fermions”, *Physical Review B*, 10.1103/PhysRevB.101.121301 (2020).
- ¹⁵⁴R. Battilomo, N. Scopigno, and C. Ortix, “Tuning topology in thin films of topological insulators by strain gradients”, *Physical Review B*, 10.1103/PhysRevB.100.115131 (2019).
- ¹⁵⁵W. Jiang, S. Zhang, Z. Wang, F. Liu, and T. Low, “Topological Band Engineering of Lieb Lattice in Phthalocyanine-Based Metal–Organic Frameworks”, *Nano Letters* **20**, 1959–1966 (2020).
- ¹⁵⁶W. Jiang, D. J. P. De Sousa, J.-P. Wang, and T. Low, “Giant Anomalous Hall Effect due to Double-Degenerate Quasiflat Bands”, *Physical Review Letters* **126**, 10.1103/PhysRevLett.126.106601 (2021).
- ¹⁵⁷H. Huang, W. Jiang, K.-H. Jin, and F. Liu, “Tunable topological semimetal states with ultraflat nodal rings in strained YN”, *Physical Review B* **98**, 10.1103/PhysRevB.98.045131 (2018).
- ¹⁵⁸K. Landsteiner, “Notes on anomaly induced transport”, *Acta Phys. Pol. B* **47**, 2617 (2016).
- ¹⁵⁹J. Gooth, A. C. Niemann, T. Meng, A. G. Grushin, K. Landsteiner, B. Gotsmann, F. Menges, M. Schmidt, C. Shekhar, V. Süß, R. Hühne, B. Rellinghaus, C. Felser, B. Yan, and K. Nielsch, “Experimental signatures of the mixed axial–gravitational anomaly in the Weyl semimetal NbP”, *Nature* 2017 547:7663 **547**, 324–327 (2017).
- ¹⁶⁰D. I. Pikulin, A. Chen, and M. Franz, “Chiral anomaly from strain-induced gauge fields in dirac and Weyl semimetals”, *Physical Review X* **6**, 1–20 (2016).
- ¹⁶¹V. Arjona, E. V. Castro, and M. A. Vozmediano, “Collapse of Landau levels in Weyl semimetals”, *Physical Review B* **96**, 1–5 (2017).
- ¹⁶²E. V. Gorbar, V. A. Miransky, I. A. Shovkovy, and P. O. Sukhachov, “Second-order chiral kinetic theory: Chiral magnetic and pseudomagnetic waves”, *Physical Review B* **95**, 1–12 (2017).
- ¹⁶³Y. Ferreira, Y. Kedem, E. J. Bergholtz, and J. H. Bardarson, “Mixed Axial-Torsional Anomaly in Weyl Semimetals”, *Physical Review Letters* **122**, 56601 (2019).

- ¹⁶⁴E. V. Gorbar, V. A. Miransky, I. A. Shovkovy, and P. O. Sukhachov, “Pseudomagnetic lens as a valley and chirality splitter in Dirac and Weyl materials”, *Physical Review B* **95**, 241114 (2017).
- ¹⁶⁵T. Liu, D. I. Pikulin, and M. Franz, “Quantum oscillations without magnetic field”, *Physical Review B* **95**, 1–8 (2017).
- ¹⁶⁶Z. K. Liu, J. Jiang, B. Zhou, Z. J. Wang, Y. Zhang, H. M. Weng, D. Prabhakaran, S.-k. Mo, H. Peng, P. Dudin, T. Kim, M. Hoesch, Z. Fang, X. Dai, Z. X. Shen, D. L. Feng, Z. Hussain, and Y. L. Chen, “A stable three-dimensional topological Dirac semimetal Cd₃As₂”, **13**, 677–681 (2014).
- ¹⁶⁷T. Liang, Q. Gibson, M. N. Ali, M. Liu, R. J. Cava, and N. P. Ong, “Ultrahigh mobility and giant magnetoresistance in the Dirac semimetal Cd₃As₂”, **14**, 3–7 (2015).
- ¹⁶⁸Y. Zhao, H. Liu, C. Zhang, H. Wang, J. Wang, Z. Lin, Y. Xing, H. Lu, J. Liu, Y. Wang, S. M. Brombosz, Z. Xiao, S. Jia, X. C. Xie, and J. Wang, “Anisotropic fermi surface and quantum limit transport in high mobility three-dimensional dirac semimetal Cd₃As₂”, *Physical Review X* **5**, 1–9 (2015).
- ¹⁶⁹J. Feng, Y. Pang, D. Wu, Z. Wang, H. Weng, J. Li, X. Dai, Z. Fang, Y. Shi, and L. Lu, “Large linear magnetoresistance in Dirac semimetal Cd₃As₂ with Fermi surfaces close to the Dirac points”, **081306**, 1–5 (2015).
- ¹⁷⁰I. Crassee, R. Sankar, W. L. Lee, A. Akrap, and M. Orlita, “3D Dirac semimetal Cd₃As₂: A review of material properties”, *Physical Review Materials* **2**, 1–15 (2018).
- ¹⁷¹M. J. M. de Jong and L. W. Molenkamp, “Electron High-Mobility”, *Physical Review B* **51**, 389–402 (1995).
- ¹⁷²E. Ditlefsen and J. Lothe, “Theory of size effects in electrical conductivity”, *Philosophical Magazine* **14**, 759–773 (1966).
- ¹⁷³T. J. Thornton, M. L. Roukes, A. Scherer, and B. P. Van De Gaag, “Boundary scattering in quantum wires”, *Physical Review Letters* **63**, 2128 (1989).
- ¹⁷⁴M. Uchida, Y. Nakazawa, S. Nishihaya, K. Akiba, M. Kriener, Y. Kozuka, A. Miyake, Y. Taguchi, M. Tokunaga, N. Nagaosa, Y. Tokura, and M. Kawasaki, “Quantum Hall states observed in thin films of Dirac semimetal Cd₃As₂”, *Nature Communications* **8**, 10.1038/s41467-017-02423-1 (2017).
- ¹⁷⁵A. Narayanan, M. D. Watson, S. F. Blake, N. Bruyant, L. Drigo, Y. L. Chen, D. Prabhakaran, B. Yan, C. Felser, T. Kong, P. C. Canfield, and A. I. Coldea, “Linear magnetoresistance caused by mobility fluctuations in n -doped Cd₃As₂”, *Physical Review Letters* **114**, 1–5 (2015).
- ¹⁷⁶P. Li, Y. Wen, X. He, Q. Zhang, C. Xia, Z. M. Yu, S. A. Yang, Z. Zhu, H. N. Alshareef, and X. X. Zhang, “Evidence for topological type-II Weyl semimetal WTe₂”, *Nature Communications* **8**, 8–15 (2017).

- ¹⁷⁷U. Kar, A. K. Singh, Y. T. Hsu, C. Y. Lin, B. Das, C. T. Cheng, M. Berben, S. Yang, C. Y. Lin, C. H. Hsu, S. Wiedmann, W. C. Lee, and W. L. Lee, “The thickness dependence of quantum oscillations in ferromagnetic Weyl metal SrRuO₃”, *npj Quantum Materials* **8**, 10.1038/s41535-023-00540-3 (2023).
- ¹⁷⁸Y. J. Wang, D. D. Liang, M. Ge, J. Yang, J. X. Gong, L. Luo, L. Pi, W. K. Zhu, C. J. Zhang, and Y. H. Zhang, “Topological nature of the node-arc semimetal PtSn₄ probed by de Haas-van Alphen quantum oscillations”, *Journal of Physics Condensed Matter* **30**, 10.1088/1361-648X/aab254 (2018).
- ¹⁷⁹J. Yan, X. Luo, J. J. Gao, H. Y. Lv, C. Y. Xi, Y. Sun, W. J. Lu, P. Tong, Z. G. Sheng, X. B. Zhu, W. H. Song, and Y. P. Sun, “The giant planar Hall effect and anisotropic magnetoresistance in Dirac node arcs semimetal PtSn₄”, *Journal of Physics Condensed Matter* **32**, 10.1088/1361-648X/ab851f (2020).
- ¹⁸⁰M. N. Ali, J. Xiong, S. Flynn, J. Tao, Q. D. Gibson, L. M. Schoop, T. Liang, N. Haldolaarachchige, M. Hirschberger, N. P. Ong, and R. J. Cava, “Large, non-saturating magnetoresistance in WTe₂”, *Nature* **514**, 205–208 (2014).
- ¹⁸¹R. Singha, A. K. Pariari, B. Satpati, and P. Mandal, “Large nonsaturating magnetoresistance and signature of nondegenerate Dirac nodes in ZrSiS”, *Proceedings of the National Academy of Sciences of the United States of America* **114**, 2468–2473 (2017).
- ¹⁸²K. Wang, D. Graf, L. Li, L. Wang, and C. Petrovic, “Anisotropic giant magnetoresistance in NbSb₂”, *Scientific Reports* **4**, 10.1038/srep07328 (2014).
- ¹⁸³A. P. Ramirez, “Colossal magnetoresistance”, *Journal of Physics Condensed Matter* **9**, 8171–8199 (1997).
- ¹⁸⁴M. N. Baibich, J. M. Broto, A. Fert, F. N. Van Dau, F. Petroff, P. Eitenne, G. Creuzet, A. Friederich, and J. Chazelas, “Giant magnetoresistance of (001)Fe/(001)Cr magnetic superlattices”, *Physical Review Letters* **61**, 2472–2475 (1988).
- ¹⁸⁵G. Binasch, P. Grünberg, F. Saurenbach, and W. Zinn, “Enhanced magnetoresistance in layered magnetic structures with antiferromagnetic interlayer exchange”, *Physical Review B* **39**, 4828–4830 (1989).
- ¹⁸⁶Y. Xu, F. Herman, V. Granata, D. Destraz, L. Das, J. Vonka, S. Gerber, J. Spring, M. Gibert, A. Schilling, X. Zhang, S. Li, R. Fittipaldi, M. H. Fischer, A. Vecchione, and J. Chang, “Magnetotransport of dirty-limit van Hove singularity quasiparticles”, *Communications Physics* **4**, 6–11 (2021).
- ¹⁸⁷D. V. Khveshchenko, “Magnetic-field-induced insulating behavior in highly oriented pyrolytic graphite”, *Physical Review Letters* **87**, 206401–1–206401–4 (2001).
- ¹⁸⁸Y. Kopelevich, J. C. Pantoja, R. R. Da Silva, and S. Moehlecke, “Universal magnetic-field-driven metal-insulator-metal transformations in graphite and bismuth”, *Physical Review B - Condensed Matter and Materials Physics* **73**, 1–7 (2006).
- ¹⁸⁹Y. Y. Wang, Q. H. Yu, P. J. Guo, K. Liu, and T. L. Xia, “Resistivity plateau and extremely large magnetoresistance in NbAs₂ and TaAs₂”, *Physical Review B* **94**, 1–6 (2016).

- ¹⁹⁰N. H. Jo, Y. Wu, L. L. Wang, P. P. Orth, S. S. Downing, S. Manni, D. Mou, D. D. Johnson, A. Kaminski, S. L. Bud'Ko, and P. C. Canfield, "Extremely large magnetoresistance and Kohler's rule in PdSn₄: A complete study of thermodynamic, transport, and band-structure properties", *Physical Review B* **96**, 1–13 (2017).
- ¹⁹¹X. Luo, R. C. Xiao, F. C. Chen, J. Yan, Q. L. Pei, Y. Sun, W. J. Lu, P. Tong, Z. G. Sheng, X. B. Zhu, W. H. Song, and Y. P. Sun, "Origin of the extremely large magnetoresistance in topological semimetal PtSn₄", *Physical Review B* **97**, 1–8 (2018).
- ¹⁹²B. Künnen, D. Niepmann, and W. Jeitschko, "Structure refinements and some properties of the transition metal stannides Os₃Sn₇, Ir₅Sn₇, Ni_{0.402(4)}Pd_{0.598}Sn₄, α -PdSn₂ and PtSn₄", *Journal of Alloys and Compounds* **309**, 1–9 (2000).
- ¹⁹³G. Li, C. Fu, W. Shi, L. Jiao, J. Wu, Q. Yang, R. Saha, M. E. Kamminga, A. K. Srivastava, E. Liu, A. N. Yazdani, N. Kumar, J. Zhang, G. R. Blake, X. Liu, M. Fahlman, S. Wirth, G. Auffermann, J. Gooth, S. Parkin, V. Madhavan, X. Feng, Y. Sun, and C. Felser, "Dirac Nodal Arc Semimetal PtSn₄: An Ideal Platform for Understanding Surface Properties and Catalysis for Hydrogen Evolution", *Angewandte Chemie* **131**, 13241–13246 (2019).
- ¹⁹⁴C. Fu, S. N. Guin, T. Scaffidi, Y. Sun, R. Saha, S. J. Watzman, A. K. Srivastava, G. Li, W. Schnelle, S. S. P. Parkin, C. Felser, and J. Gooth, "Largely Suppressed Magneto-Thermal Conductivity and Enhanced Magneto-Thermoelectric Properties in PtSn₄", *Research* **2020**, 1–8 (2020).
- ¹⁹⁵P. C. Canfield and Z. Fisk, "Growth of single crystals from metallic fluxes", *Philosophical Magazine B* **65**, 1117–1123 (1992).
- ¹⁹⁶A. N. Perevalova, S. V. Naumov, S. M. Podgornykh, E. B. Marchenkova, V. V. Chistyakov, J. C. Huang, and V. V. Marchenkov, "Features of the electronic transport of topological semimetal PtSn₄ and WTe₂ single crystals", *AIP Advances* **12**, 10–14 (2022).
- ¹⁹⁷T. Yara, M. Kakihana, K. Nishimura, M. Hedo, T. Nakama, Y. Ōnuki, and H. Harima, "Small Fermi surfaces of PtSn₄ and Pt₃In₇", *Physica B: Condensed Matter* **536**, 625–633 (2018).
- ¹⁹⁸M. Inamdar, M. Kriegisch, L. Shafeek, A. Sidorenko, H. Müller, A. Prokofiev, P. Blaha, and S. Paschen, "Quantum oscillations in ultra pure PtSn₄", *Solid State Phenomena* **194**, 88–91 (2013).
- ¹⁹⁹B. Zhang, C. An, Y. Zhou, X. Chen, Y. Zhou, C. Chen, Y. Yuan, and Z. Yang, "Structural and electrical transport properties of Dirac-like semimetal PdSn₄ under high pressure", *Chinese Physics B* **28**, 10–16 (2019).
- ²⁰⁰M. Hirschberger, S. Kushwaha, Z. Wang, Q. Gibson, S. Liang, C. A. Belvin, B. A. Bernevig, R. J. Cava, and N. P. Ong, "The chiral anomaly and thermopower of Weyl fermions in the half-Heusler GdPtBi", *Nature Materials* **15**, 1161–1165 (2016).
- ²⁰¹E. H. Sondheimer, "The Influence of a Transverse Magnetic Field on the Conductivity of Thin Metallic Films", *Physical Review* **80**, 401 (1950).
- ²⁰²V. L. Gurevich, "Oscillations in the conductivity of metallic films in magnetic field", *Soviet Physics JETP* **35(8)**, 464–470 (1959).

- ²⁰³M. R. van Delft, Y. Wang, C. Putzke, J. Oswald, G. Varnavides, C. A. Garcia, C. Guo, H. Schmid, V. Süß, H. Borrmann, J. Diaz, Y. Sun, C. Felser, B. Gotsmann, P. Narang, and P. J. Moll, “Sondheimer oscillations as a probe of non-ohmic flow in WP2 crystals”, *Nature Communications* **12**, 1–9 (2021).
- ²⁰⁴H. Sato, “Phonon-limited mean free path in the Sondheimer oscillation of aluminum”, *Journal of Low Temperature Physics* **38**, 267–275 (1980).
- ²⁰⁵C. Fu, T. Scaffidi, J. Waissman, Y. Sun, R. Saha, S. J. Watzman, A. K. Srivastava, G. Li, W. Schnelle, P. Werner, M. E. Kammanga, S. Sachdev, S. S. P. Parkin, S. A. Hartnoll, C. Felser, and J. Gooth, “Thermoelectric signatures of the electron-phonon fluid in PtSn4”, arXiv preprint: 1802.09468 (2018).
- ²⁰⁶C. Q. Xu, W. Zhou, R. Sankar, X. Z. Xing, Z. X. Shi, Z. D. Han, B. Qian, J. H. Wang, Z. Zhu, J. L. Zhang, A. F. Bangura, N. E. Hussey, and X. Xu, “Enhanced electron correlations in the binary stannide PdSn 4: A homologue of the Dirac nodal arc semimetal PtSn 4”, *Physical Review Materials* **1**, 1–8 (2017).
- ²⁰⁷M. N. Ali, L. M. Schoop, C. Garg, J. M. Lippmann, E. Lara, B. Lotsch, and S. S. Parkin, “Butterfly magnetoresistance, quasi-2D Dirac fermi surface and topological phase transition in ZrSiS”, *Science Advances* **2**, 1–8 (2016).
- ²⁰⁸R. D. Reis, M. O. Ajeesh, N. Kumar, F. Arnold, C. Shekhar, M. Naumann, M. Schmidt, M. Nicklas, and E. Hassinger, “On the search for the chiral anomaly in Weyl semimetals: The negative longitudinal magnetoresistance”, *New Journal of Physics* **18**, 10.1088/1367-2630/18/8/085006 (2016).
- ²⁰⁹F. Arnold, C. Shekhar, S. C. Wu, Y. Sun, R. D. Dos Reis, N. Kumar, M. Naumann, M. O. Ajeesh, M. Schmidt, A. G. Grushin, J. H. Bardarson, M. Baenitz, D. Sokolov, H. Borrmann, M. Nicklas, C. Felser, E. Hassinger, and B. Yan, “Negative magnetoresistance without well-defined chirality in the Weyl semimetal TaP”, *Nature Communications* **7**, 1–7 (2016).
- ²¹⁰L. X. Wang, C. Z. Li, D. P. Yu, and Z. M. Liao, “Aharonov-Bohm oscillations in Dirac semimetal Cd3As2 nanowires”, *Nature Communications* **7**, 1–7 (2016).

Jonás Díaz

Curriculum Vitae

Av. Alexandre Vinet 37
Lausanne, Switzerland
☎ +41 78 704 69
✉ jonasjd90@gmail.com
in [LinkedIn](#) [Skype](#)



Education

- 2018–present **Doctoral candidate in Material Science & Engineering**, *École Polytechnique Fédérale de Lausanne*, Lausanne (EPFL), Switzerland.
Advisor: Philip Moll
Thesis: Strain Gradients and Magnetoresistance in Microstructured 3D Topological Semimetals
- 2013–2016 **Master of Physics**, *Universidad Simón Bolívar (USB)*, Caracas, Venezuela.
Advisor: Gloria Buendía
Thesis: Kinetic Monte Carlo simulations of two catalytic reactions: CO oxidation and NO reduction
- 2006–2013: **Bachelor of Physics**, *Universidad Simón Bolívar*, Caracas, Venezuela.
Advisors: Estrella Laredo and Alfredo Bello
Thesis: Dielectric Properties of PLA/NTC Nanocomposites

Research Experience

- 2018–present **Laboratory for Quantum Materials (QMAT)**, *École Polytechnique Fédérale de Lausanne*, Lausanne, Switzerland.
- 2017 – 2018 **Microstructured Quantum Matter Group (MQM)**, *Max Planck Institute for Chemical Physics of Solids (MPI-CPFS)*, Dresden, Germany.
- 2014 – 2016 **Condensed Matter and Computational Physics Group**, *Universidad Simón Bolívar*, Caracas, Venezuela.
- 2011 – 2013 **Amorphous and Crystalline Materials Physics Laboratory.**, *Universidad Simón Bolívar*, Caracas, Venezuela.

Professional Expertise

- Software Programming and data analysis: Matlab, Origin
Instrument automation: LabVIEW
Finite element simulations: COMSOL
Mechanical design: Inventor 3D CAD
- Experimental techniques Nanofabrication: Focused ion beam (FIB), Scanning electron microscopy (SEM), Sputter deposition
Cryogenics: Physical properties measurement system (PPMS), Oxford Instrument He⁴ cryostat with 18T magnet

Material characterization: AC Lock-in amplifier , X-ray diffraction

Teaching Experience

- 2021–2022 **Superconducting electronics: A materials perspective**, EPFL, Masters course, Graduate teaching assistant.
- 2020 **Magnetic torque of quantum materials**, EPFL, Undergraduate semester project, Supervisor of bachelor student.
- 2014–2016 **Introductory Mechanics, Introductory Electromagnetism and Modern Physics Laboratory**, USB, Undergraduate courses, Lecturer.
- 2010–2011 **Linear Algebra and Introductory Mechanics**, USB, Undergraduate courses, Undergraduate teaching assistant.

Publications

- 2022 **J. Diaz**, C. Putzke, X. Huang, A. Estry, J. G. Analytis, D. Sabsovich, A. G. Grushin, R. Ilan, and P. J.W. Moll. Bending strain in 3D topological semi-metals. *Journal of Physics D: Applied Physics*, volume 55, 2022.
- 2022 C. Guo, L. Hu, C. Putzke, **J. Diaz**, X. Huang, K. Manna, F. Fan, C. Shekhar, Y. Sun, C. Felser, C. Liu, B. A. Bernevig, and P. J.W. Moll. Quasi-symmetry-protected topology in a semi-metal. *Nature Physics*, volume 18, pages 813–818. Springer US, 2022.
- 2021 M. R. van Delft, Y. Wang, C. Putzke, J. Oswald, G. Varnavides, C. A.C. Garcia, C. Guo, H. Schmid, V. Süß, H. Borrmann, **J. Diaz**, Y. Sun, C. Felser, B. Gotsmann, P. Narang, and P. J.W. Moll. Sondheimer oscillations as a probe of non-ohmic flow in WP2 crystals. *Nature Communications*, volume 12, pages 1–9. Springer US, 2021.
- 2021 X. Huang, C. Guo, C. Putzke, **J. Diaz**, K. Manna, C. Shekhar, C. Felser, and P. J.W. Moll. Non-linear Shubnikov-de Haas oscillations in the self-heating regime. *Applied Physics Letters*, volume 119. AIP Publishing LLC, 2021.
- 2020 Y. Lai, K. Wei, G. Chappell, **J. Diaz**, T. Siegrist, P. J.W. Moll, D. Graf, and R. E. Baumbach. Tuning the structural and antiferromagnetic phase transitions in UCr₂Si₂: Hydrostatic pressure and chemical substitution. *Physical Review Materials*, volume 4, pages 1–8. American Physical Society, 2020.
- 2020 X. Huang, C. Putzke, C. Guo, **J. Diaz**, M. König, H. Borrmann, N. L. Nair, J. G. Analytis, and P. J.W. Moll. Magnetic electron collimation in three-dimensional semi-metals. *npj Quantum Materials* 2020 5:1, volume 5, pages 1–7. Nature Publishing Group, feb 2020.
- 2018 **J. Diaz** and G.M. Buendía. A model for the catalytic reduction of NO with CO and N desorption. *Physica A: Statistical Mechanics and its Applications*, volume 491, pages 13–27, feb 2018.
- 2013 E. Laredo, A. Bello, **J. Diaz**, M. Grimau, D. Martinez-Tong, D. Wu, and L. Wu. Effect of cold-crystallization on the AC and DC conductive properties of polylactide biocomposites with carboxylic or neat large aspect ratio MWCNT. *Polymer Composites*, volume 34, pages 67–76, jan 2013.